SEISMIC STRUCTURE ACROSS THE ACTIVE SUBDUCTION ZONE OF WESTERN CANADA

by

GEORGE DANIEL SPENCE

M.Sc. The University Of British Columbia, 1976
B.Sc.(Hon.) The University Of Calgary, 1971

A THESIS SUBMITTED IN PARTIAL FULFILMENT OF

THE REQUIREMENTS FOR THE DEGREE OF

DOCTOR OF PHILOSOPHY

in

THE FACULTY OF GRADUATE STUDIES

Department Of Geophysics And Astronomy

We accept this thesis as conforming

to the required standard

THE UNIVERSITY OF BRITISH COLUMBIA

July 1984

In presenting this thesis in partial fulfilment of the requirements for an advanced degree at the University of British Columbia, I agree that the Library shall make it freely available for reference and study. I further agree that permission for extensive copying of this thesis for scholarly purposes may be granted by the head of my department or by his or her representatives. It is understood that copying or publication of this thesis for financial gain shall not be allowed without my written permission.

Department of Geophysics & Astronomy

The University of British Columbia
2075 Wesbrook Place
Vancouver, Canada
V6T 1W5

Date July 6, 1984

For their constant support and concern, I dedicate this thesis to my parents, George D. Spence and Dian Spence.

ABSTRACT

The Vancouver Island Seismic Project (VISP) was conducted in 1980 to study the structure of the subducting oceanic Juan de Fuca plate and the overriding continental America plate. The principal seismic refraction line (line I) was a 350 km onshore-offshore profile perpendicular to the continental margin. An array of 32 receivers was located on the America plate on the mainland and across Vancouver Island, and extended offshore with 3 ocean bottom seismometers (OBS's). Two shots were fired at the eastern end of the line, and 17 shots were located along the westernmost 100 km of the profile. Control for the interpretation of the onshore-offshore profile was provided by a reversed refraction profile along the length of Vancouver Island (McMechan and Spence 1983) and by the marine refraction profile recorded on the OBS's (Waldron 1982). To aid in the modeling of the seismic structure of this complex region, two practical techniques have been developed and applied in the interpretation of line I.

The first procedure was an iterative inversion technique for traveltimes from explosions in which shots at several locations are recorded on the same set of receivers. Traveltimes for the initial model and for subsequent iterations are computed using two-dimensional ray tracing. The model is represented by one or more blocks in which the velocity, the velocity gradient, and specified boundary positions are allowed to vary. Perturbations to the parameters are then determined simultaneously using a damped least squares method.

Second, a fast, efficient algorithm based on asymptotic ray theory has been developed for the calculation of synthetic seismograms through two-dimensional media. The same ray tracing scheme is used as in the traveltime inversion method, in which the velocity model is represented by large polygonal blocks, each with a uniform velocity gradient. Simple analytic expressions are thus used for both the ray tracing and for the amplitude computations. Amplitudes may be calculated for head waves, refractions, pre-critical and wide-angle reflections, surface reflections and multiples.

The traveltime inversion procedure and synthetic seismogram algorithm were both applied in the interpretation of the onshore-offshore profile. The major features of the refraction structural model are as follows: (1) The oceanic lithosphere dips at 3° or less beneath the continental slope, so the bend in the subducting slab occurs landward of the foot of the slope. (2) The subducting crust dips at 14-16° beneath the continental shelf until it passes beneath the continental Moho at 37 km depth below western Vancouver Island. (3) An upper mantle reflector may correspond to the base of the subducting lithosphere. (4) A segment of high-velocity material above the downgoing crust, with velocity 7.7 km/s and depth range ~20-25 km, may represent a remnant of subducted lithosphere, perhaps detached when the subduction zone jumped westward to its present position.

TABLE OF CONTENTS

LIST OF TABLES

LIST OF FIGURES

ACKNOWLEDGEMENTS

First and foremost, I want to thank my wife Marla, who did nearly all the typing and final diagram preparation for this thesis. But mostly I want to tender my sincere thanks for her unwavering moral support, which meant so much to me. And having completed her own doctoral thesis in the not so distant past, she provided a sterling example of someone who had survived.

Throughout my research I have had the distinct advantage of having two supervisors, Dr. R.M. Clowes and Dr. R.M. Ellis. I am grateful to them for their enthusiastic encouragement and advice, so critical in defining the direction of one's research. I should also like to thank Ron and Bob in general for the overall project design and for the opportunity to participate (rather heavily!) in organizing the logistics of the field program. While Ron was on sabbatical, Bob in particular provided the needed guidance for my organizational endeavors. Similarly, while Bob was on sabbatical, Ron provided stimulus during interpretation stages of the thesis, as well as advice in the writing of the synthetic seismogram routine. Finally, I felt I could almost always count on Ron to uplift my spirits by graciously declining to be the victor in most of our darts matches.

Discussions with Ken Whittall, especially related to the synthetic seismogram routine, are greatly appreciated. Perhaps the greater part of this thesis should be dedicated to Ken's ray tracing code, since much of my work was based upon it. I also appreciate talks with David Waldron concerning his marine

interpretation, and I am indeed grateful that his interpretation was completed in time to provide control for mine. As well, I am thankfull and constantly amazed that George McMechan was able to bring the majority of his interpretation to completion,including write-up, within a six week period. My gratitude also goes to Bob Meldrum, who I feel is the true core of the seismology group in matters of instrumentation and related field projects. In addition, Bob provided the greater part of the motivation for our long-standing semi-regular noon hour French sessions, which not only were rewarding in themselves but also supplied a needed break from the deadening effects of geophysics. Merci, Bob.

Data acquisition for the Vancouver Island Seismic Project (VISP) was only possible through the joint effort of many individuals and organizations. For the marine phase of the project, the participation of personnel from the Pacific Geoscience Centre was indispensable. It was particularly a privilege to work with Dr. Roy Hyndman, both during the organization of the marine operation and at later stages in discussing my interpretation. OBS's were supplied by the Pacific Geoscience Centre and the Atlantic Geoscience Centre. Grateful acknowledgement is also made to the Department of Fisheries and Oceans Canada for the use of the ship CSS Vector and to the Canadian Forces through the Defense Research Establishment Pacific for the CFAV Endeavour. The assistance of the Fleet Diving Unit, Pacific Maritime Command, who detonated the explosives at sea, is especially appreciated. The onshore phase of the project could not have been undertaken without the participation of members of the CO-CRUST group, who provided

equipment, scientific, organizational and financial contributions. In particular, the efforts of the nearly 30 people who took part in the field program are gratefully acknowledged. We are also indebted to the following forest companies on Vancouver Island for providing access to their areas of operation, advice on access and safety and detailed maps for station location: Rayonier Canada Ltd., MacMillan Bloedel Ltd., Canadian Forest Products Ltd., Tahsis Co. Ltd., Crown Zellerbach Canada Ltd., B.C. Forest Products Ltd., and Western Forest Industries Ltd.

Personal financial support was provided by a Postgraduate Scholarship from the Natural Sciences and Engineering Research Council (NSERC) and by an H.R. MacMillan Family Fellowship from the University of British Columbia. Principal support for the field program was provided by contract OSU80-00137 from the Earth Physics Branch of Energy, Mines and Resources Canada and from NSERC operating grants of the participants. Analysis has been supported by NSERC operating grants A2617 and A7707 to R.M. Ellis and R.M. Clowes, respectively.

CHAPTER 1. INTRODUCTION

In August 1980, CO-CRUST [1] conducted the Vancouver Island Seismic Project (VISP), a series of refraction and reflection seismic experiments that utilized both land-based and ocean bottom seismographs (OBS's) with explosive and airgun energy sources.

This dissertation concerns the interpretation of the principal refraction profile of the experiment, for which the purpose was to obtain a seismic structural section to upper mantle depths from the oceanic Juan de Fuca plate to the inland volcanic arc of the continental America plate (Fig. 1.1). Together with other geophysical studies such as seismicity, gravity, heat flow and magnetics, a seismic velocity model plays a major role in understanding the contemporary tectonics and plate interaction complexities of the region. The development of a seismic/tectonic model has two important practical implications. First, there is the potential for the tectonic model to be applied in the exploration for hydrocarbon resources on the continental shelf, or for mineral resources on Vancouver Island and in the Coast Range. In the past, the distribution of mineral deposits was considered to be somewhat haphazard; but today the tectonic setting is seen as a major controlling factor in the location of mineral resources, and methods are being

[1] CO-CRUST (Consortium for Crustal Reconnaisance using Seismic Techniques) included in 1980 participants from the Earth Physics Branch (Ottawa), Pacific Geoscience Centre, Atlantic Geoscience Centre, and the Universities of Alberta, British Columbia, Manitoba, Saskatchewan, and Western Ontario.

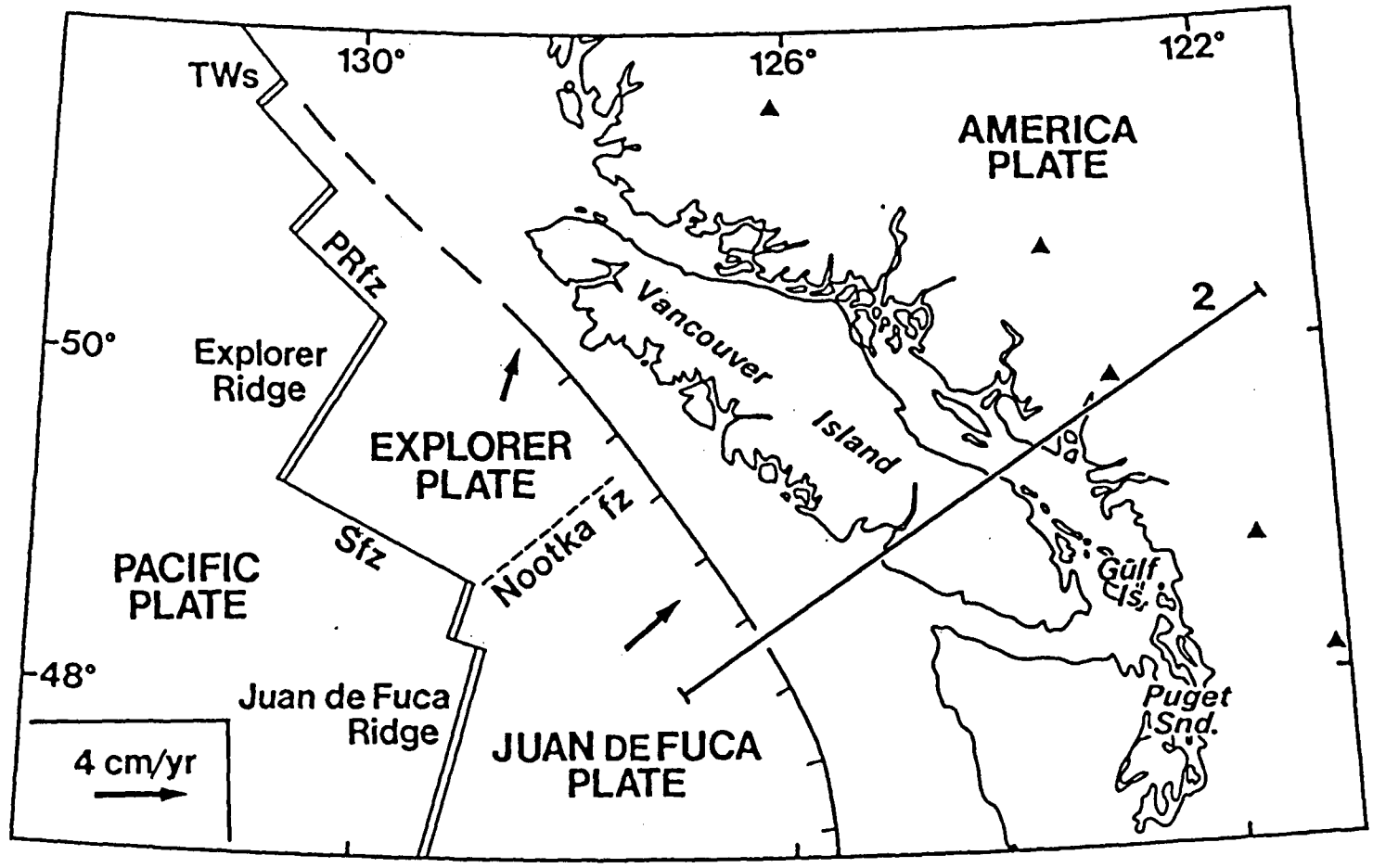

FIG. 1.1. Tectonic map of the southern British Columbia continental margin showing the main lithospheric boundaries and plate motions relative to North America. Quaternary volcanoes are indicated by solid triangles and profile 2 is the location of the gravity model cross section across southern Vancouver Island as shown in Fig. 1.2. TWs = Tuzo Wilson seamount; PRfz = Paul Revere fracture zone; Sfz = Sovanco fracture zone.

developed which use the tectonic setting as a guide to exploration (Rona 1980; Mitchell and Garson 1981). The second significant application of a seismic/tectonic model is in the assessment of earthquake risk, which affects not only areas of high population density, but also areas of low population density where facilities related to energy development may be placed. The tectonic model is necesssary for understanding the seismicity pattern and thus the processes generating large earthquakes. As well, a realistic velocity model is required specifically for the accurate location of the earthquakes themselves.

1.1 Tectonic Setting

In the Vancouver Island region the plate tectonic regime is convergent, with the oceanic Juan de Fuca and Explorer plates being subducted obliquely beneath the continental America plate (Fig. 1.1). Based on magnetic anomaly patterns, the present perpendicular convergence rates are about 3 cm/year for the Juan de Fuca-America and less than 2 cm/year for the Explorer-America plates (Riddihough 1977). The difference is accommodated by left-lateral strike-slip movement along the Nootka fault zone between the Explorer and Juan de Fuca plates (Hyndman et al. 1979). In terms of absolute plate motions fixed to a hot spot frame of reference, it is possible that the Explorer plate has stopped subducting in an absolute sense (Riddihough 1981). Thus, both the Explorer and Juan de Fuca plates are to some extent being over-ridden by the southwestward motion of the America plate.

The present structure at the western margin of the America plate is controlled by the past plate tectonic history at that margin, in which episodes of subduction may have alternated with periods of strike-slip motion (Riddihough 1982a). Recently, modifications to plate tectonic theory have introduced an additional factor. New evidence suggests that western North America has grown by the piecemeal addition of blocks of lithosphere (variably called microplates, terranes, exotic terranes or allochthonous terranes), some of which have been carried thousands of kilometers from their sites of origin. A terrane is recognized by its unique stratigraphy relative to neighboring terranes and the craton, by different faunas compared to those on the craton, and in some cases by paleomagnetic results which indicate that they have been rotated or displaced in latitude.

Among the best recognized terranes is the dispersed Wrangellia block, pieces of which are now in southeast Alaska, the Queen Charlotte Islands, Vancouver Island, and eastern Oregon (Jones et al. 1977). On Vancouver Island, middle Paleozoic volcanic rocks (the Sicker Group) which are characteristic of island arcs are overlain by up to 6000 m of basaltic pillow lavas, flows, pillow breccias and minor sediments of the upper Triassic Karmutsen Formation (Muller 1977). Paleomagnetic results from the Karmutsen show that Vancouver Island has moved northward relative to the North American craton by at least 1300 km, and possibly as much as 4900 km, since the late Triassic (Yole and Irving 1980). The Karmutsen basalt probably represents rifting related to the

commencement of northward movement. It is proposed that Wrangellia was accreted by mid-Cretaceous time, and since then has been fragmented by thrusting and translation along intraplate strike-slip faults (Coney et al. 1980).

The growth of western North America by terrane accretion is complex and poorly understood. It has been suggested that exotic terranes have modern analogs in some of the large oceanic plateaus, seamounts and volcanic ridges, which comprise about 10% of the ocean floor (Ben-Avraham et al. 1981). Many of the plateaus are comparable to continents in thickness and density, and would resist subduction on collision with a continental margin. It is likely that thrust faulting would be associated with the collison process, and the end result would be new crust thickened to continental proportions (Jones et al. 1982). Perhaps the present structure of Vancouver Island, as part of the Wrangellia terrane, reflects such a history.

1.2 Geophysical Studies

It is generally accepted that subduction has occurred along Canada's western margin over the last several million years, and that it is currently occurring. Riddihough and Hyndman (1976) reviewed the relevant geological and geophysical data which support the case for subduction. The geological information includes a sedimentary-filled margin trench, compressive deformation of sediments along the continental slope, and the active andesitic volcanism of the Cascade mountains. The geophysical evidence includes the classic magnetic lineations on the Juan de Fuca plate, the high-low pattern of the gravity

field at the continental margin, the change in heat flow from low values above the downgoing plate to high values near the volcanic arc, and the local seismicity. A comprehensive geophysical review of the western Canada continental margin was presented by Keen and Hyndman (1979).

Rogers (1983) has described the seismicity pattern for the Vancouver Island/Puget Sound region and has produced seismotectonic models to account for it. A strong concentration of seismicity occurs within the Puget Sound area. This localization is possibly the result of phase changes in the descending lithosphere in association with the bend in the continental margin at the latitude of Puget Sound (Rogers 1983). Several large earthquakes have taken place beneath central Vancouver Island, near a line corresponding to the extension of the Nootka fault zone. However, they may in fact not be directly related to motion along the Nootka fault zone because the character of the seismicity under Vancouver Island is different from that in the ocean basin where the fault zone is defined. Rather, Rogers (1983) argued that the large earthquakes are due to the interaction of the Explorer plate with the America plate. Since the Explorer may have stopped subducting in an absolute sense (Riddihough 1981) and is being over-ridden by the America plate, the Explorer may produce upward pressure on the overlying America plate. This interaction would be expected to be greatest near the southern boundary of the Explorer plate where it is thickest.

The seismicity, particularly in the Puget Sound region, is divided into two distinct groups - a shallow one with depths

less than 30 km, and a deeper one where the depths range from about 40 to 70 km. The depth distribution and location of earthquake hypocenters were greatly improved with the establishment in 1970 of the dense network of seismographs in the Puget Sound region by the University of Washington. In a compilation of the earthquake data by Crosson (1981), the deeper zone of seismicity was seen to be distributed along a classic Benioff zone, dipping under the continent at 11°. The Washington network was recently expanded westward with 11 permanent stations in the Olympic Peninsula, and the results of Taber (1983) improved the delineation of the Benioff zone. With the recent upgrading of the Canadian Earthquake Data File by Rogers (1983), a similar distribution of earthquakes was seen in the southern Vancouver Island and southern Georgia Strait region, where the Benioff zone was observed dipping at 12° to the northeast.

Geodetic data also have provided direct support for current subduction. In a precise levelling survey over a 70 year period across western Washington, a pattern of uplift on the outer coast and subsidence further inland is considered to be consistent with the subduction of the Juan de Fuca plate under North America (Ando and Balazs 1979). The same pattern continues northward into the Vancouver Island region (Riddihough 1982b). The question then remains whether the subduction is occurring in a seismic or an aseismic mode. Ando and Balazs (1979) argue that aseismic subduction is implied by their down-to-the-continent crustal tilt and by the lack of any large thrust earthquakes in Washington and Oregon in historical time (the past 140 years).

Aseismic slip is also suggested by the energy release calculations of Hyndman and Weichert (1983), who showed that the earthquake rate for Puget Sound was at least a factor of 10 less than that expected from the convergence rate. However, evidence contrary to aseismic slip comes from geodetic strain measurements in Washington by Savage et al. (1981), who found an accumulation of compressive strain perpendicular to the continental margin. The direction of strain accumulation is consistent with subduction of the Juan de Fuca plate, but the strain rate implies that large thrust earthquakes should be expected, which is difficult to reconcile with the evidence for aseismic subduction.

Riddihough (1979) carried out detailed modelling of the gravity field across the British Columbia and Washington margins. His structural model along profile 2 (Fig. 1.1) is shown in Figure 1.2. In the construction of this section, seismic control from reflection, refraction, and surface wave interpretations were used where available. Based on thermal arguments, he further assumed that the deepest earthquake hypocenters in the southern Strait of Georgia - Puget Sound area (50-70 km) cannot lie beneath the downgoing plate and that beneath the volcanic chain the depth to the top of the downgoing oceanic lithosphere is close to 100 km, as has been found for other active margins (Barazangi and Isacks 1976).

The seismic constraints placed on Mohorovicic (Moho) depths in the model of Figure 1.2 require further comment. Control point 1 was determined from the seismic refraction interpretations of Clowes and Malecek (1976) and Keen and

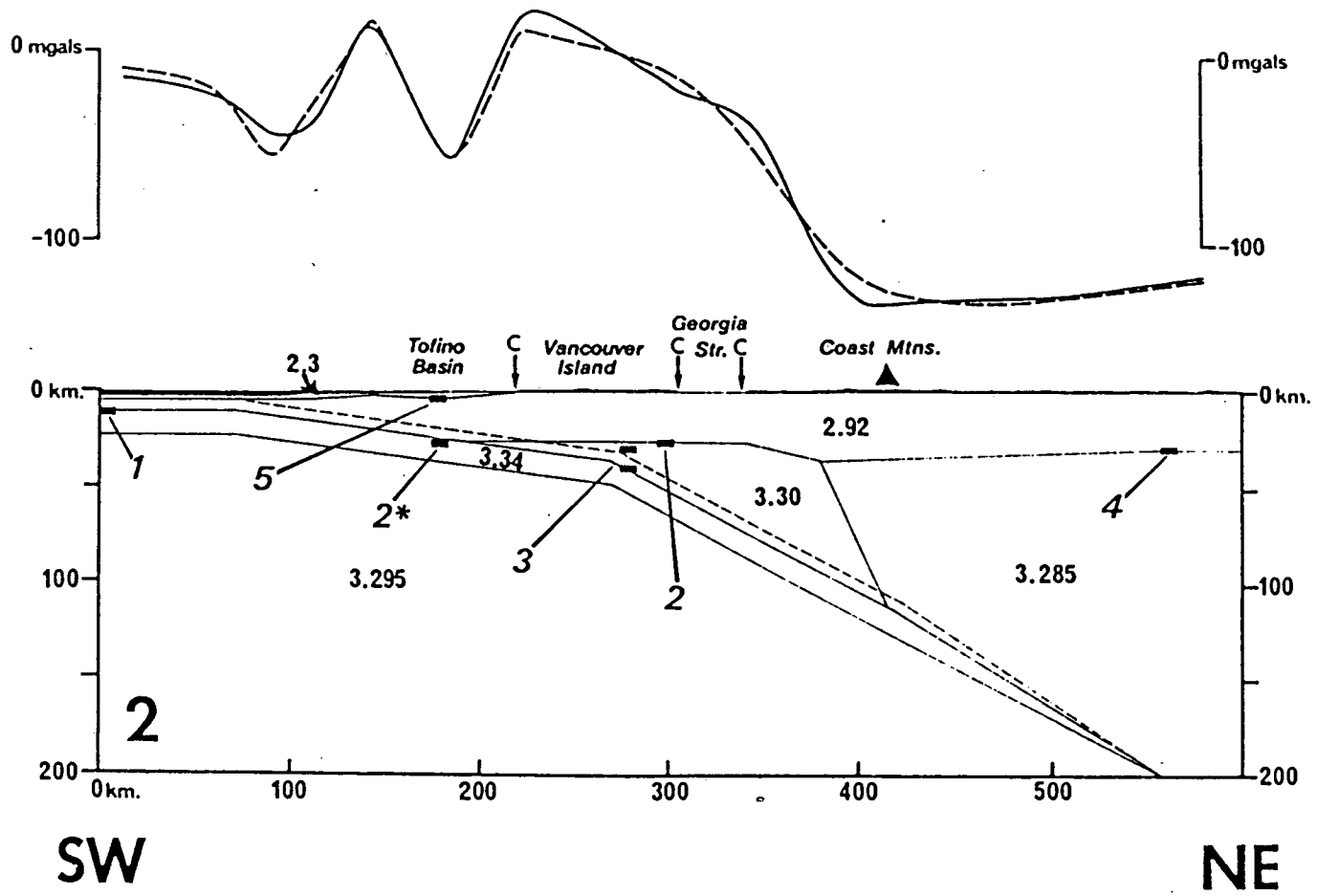

FIG. 1.2. Gravity model cross section across southern Vancouver Island (from Riddihough 1979). Gravity profiles are free over sea and Bouguer over land; solid = observed, dash = calculated. Densities are in grams per cubic centimetre. Note: 1 mGal = 10^{-5} m/s^2. Bars are seismic control points; numbers are sources: (1)Clowes and Malecek (1976), Keen and Barrett (1971); (2) and (2)Tseng (1968); (3)Wickens (1977); (4)White et al. (1968); (5)Shouldice (1971).

Barrett (1971). Unfortunately, the profiles for these interpretations are located at significant distances from the profile of Figure 1.2 and in different tectonic environments; the Clowes and Malecek (1976) study is located in the complex Explorer Ridge - Sovanco fracture zone region 200 km to the northwest, whereas the Keen and Barrett (1971) profiles lie off the northwest corner of Figure 1.1. However, Au and Clowes (1982) have interpreted refraction data located near the Nootka fault zone and on the Juan de Fuca plate, and the depth assigned at control point 1 is in agreement with their results. For control point 4 at the northeastern end of the profile, the depth to the continental Moho was determined by the refraction profile of White et al. (1968). Subsequently, Berry and Forsyth (1975) interpreted reversed seismic sections from southern Vancouver Island to the British Columbia interior, and in the eastern segment of their model the Moho depth is generally consistent with the Moho depth obtained by White et al. (1968). Berry and Forsyth (1975) also suggested that there is a change in structure between Vancouver Island and the mainland that is associated with the existence of a scattering zone beneath the eastern part of the Strait of Georgia.

Seismic control at points 2, 2*, and 3 beneath Vancouver Island (Fig. 1.2) is less stringent. Control point 3 of Wickens (1977) is based on the inversion of a rather scattered set of surface wave phase velocities. Depth errors for the boundaries are difficult to determine, but an error of ±4 km could be assigned as an optimistic estimate. The bounds are somewhat arbitrary; using the resolution matrix obtained in the

generalized inverse procedure, Wickens (1977) defined his bounds as the distance off the diagonal required to obtain an arbitrary 10% drop-off in amplitude. Interpretation of the refraction analysis of Tseng (1968), control points 2 and 2*, has presented some difficulty. The highest velocities observed, even for source-receiver separations in excess of 300 km, are 7.1±0.1 km/s for a layer with the upper boundary near 30 km. However, the gravity data require densities near 3.3 g cm^{-3} at this depth, a value which is normally characteristic of the upper mantle rather than the lower crust. Riddihough (1979) considered this problem and suggested that the probable conditions above the downgoing lithosphere of low temperature, high pressure, and hydrous environment may result in the formation of unusual metamorphic facies with the required high density and low P-wave velocity characteristics.

In summary, adequate seismic models exist of the oceanic and continental crusts to constrain the end points of the gravity model in Figure 1.2. Beneath Vancouver Island, only weak constraints are provided by the surface wave data, and P-wave velocities generally characteristic of the upper mantle have not been observed. However, arguments such as those of Riddihough (1979) mentioned above, which rationalize the apparent conflict between the low P-wave velocity determined from seismic data and high density required by the gravity interpretation, have been made.

1.3 The Vancouver Island Seismic Project (VISP)

In light of the evidence outlined in the previous section, there seems little doubt of the existence of a subducting lithospheric slab under Vancouver Island. The purpose of the Vancouver Island Seismic Project was to determine if seismic refraction and reflection methods could provide more details of the subduction zone structure. This dissertation presents an interpretation of the project's principal refraction line, in which shots in the deep ocean were recorded on onshore stations on Vancouver Island and the mainland. Constraints have been provided by other lines of the experiment, for which the interpretations have been presented elsewhere (McMechan and Spence 1983; Waldron 1982). Because of their relevance to the complete interpretation of the onshore-offshore line, a description of these profiles and of the significant points in their interpretation will also be described here.

1.3.1 Program description

Details of the full refraction and reflection program, including instrument characteristics, shooting and recording geometries, and a discussion of errors in timing and site location, are to be found in Ellis and Clowes (1981) and Ellis et al. (1983). A brief description of the portions of the program relevant to this thesis is given below.

The refraction program consisted of four profiles; two of them are shown in Figure 1.3. Line I extended across Vancouver Island from the volcanic arc to the deep ocean, and line IV was

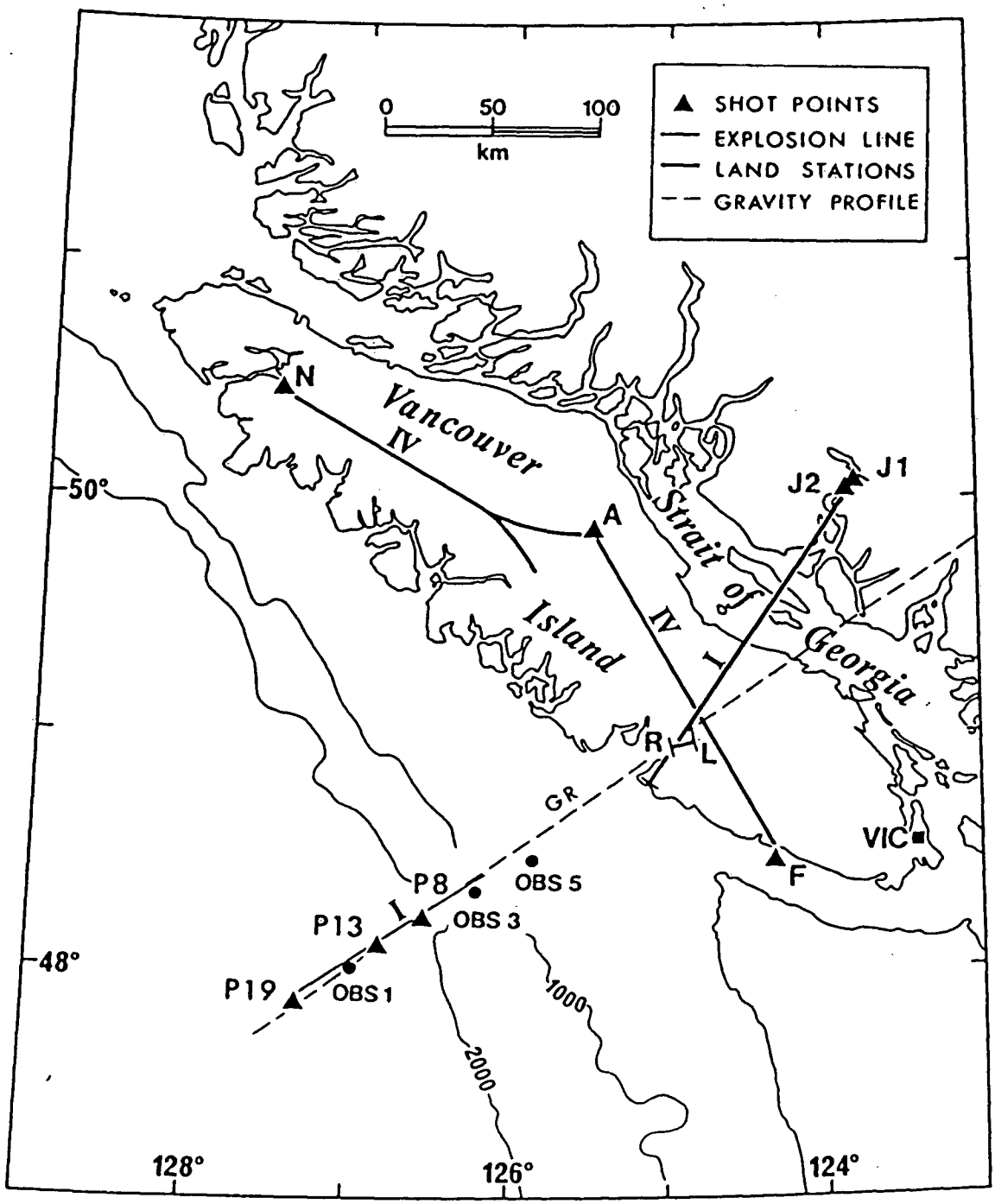

FIG. 1.3. Location map showing refraction lines I and IV, reflection line (RL), and the gravity profile (GR). Bathymetry is in metres.

shot along the length of Vancouver Island approximately parallel to the continental margin. Two additional lines along strike were also shot: line II in the deep ocean, using explosives and airgun sources into OBS's, and line III on the mid-continental shelf using an airgun source only. Interpretation of lines II and III has not yet been completed.

For line I, up to 32 land seismographs were deployed along a 160 km recording line on Vancouver Island, on islands in the Strait of Georgia, and on the British Columbia mainland. In addition, 4 OBS's were deployed in the offshore region, although only data from the 3 OBS's shown in Figure 1.3 have been interpreted (Waldron 1982). Two 825 kg shots (J1 and J2), separated by approximately 7 km, were shot at the eastern end of the profile, and a series of 17 shots ranging from 200 to 825 kg, designated as the P series, were fired over the continental slope and ocean basin into the land and marine detectors. Eighteen additional 50 kg charges were detonated for recordings on the OBS's alone. Finally, a continuous seismic profile (CSP) using a 5 L airgun was recorded along the marine portion of line I, and a 32 L airgun was fired along profiles over each OBS, to determine sedimentary structure, basement depth, and upper crustal structure.

For line IV, 38 land seismographs were distributed along the 150 km section N-A in Figure 1.3 and shots of 900, 900 and 1800 kg were detonated at N, A and F, respectively. The seismographs were then located along the A-F section of line IV to obtain recordings from 1800, 900 and 900 kg shots at N, A and F.

The reflection program was composed of two phases. The first was a 10 km 1200% common depth point explosion survey (RL in Fig. 1.3), designed to test whether coherent reflections to upper mantle depths could be obtained. In the second phase, a 5 km reflection spread deployed perpendicular to the coast remained stationary and in the adjacent inlet a 32 L airgun was detonated along a 10 km end-on profile to test the feasibility of obtaining deep reflection data using an airgun source. Positive results from the reflection experiment were obtained and have been reported in Clowes et al. (1983a).

1.3.2 Interpretation of line IV

Analysis of line IV along the axis of Vancouver Island has been done by McMechan and Spence (1983), and their results were also summarized in Ellis et al. (1983). The two-dimensional structure interpreted by McMechan and Spence (1983) is shown in Figure 1.4.

The most significant features of their interpretation are:

(1) The upper 20 km of the model is relatively well constrained. The velocity increases from ~5.4 km/s at the surface to 6.4 km/s at 2 km depth. The velocity then increases to 6.75 km/s at 16 km depth, where a discontinuity is present and the velocity jumps to 7 km/s.

(2) There is an anomaly in the structure just south of shotpoint A at ~23 km depth (Fig. 1.4), where a localized region of mantle-type velocity (7.8 km/s) is imbedded within the lower crust. McMechan and Spence (1983) speculated that the high velocity anomaly could be a remnant of a subducted slab.

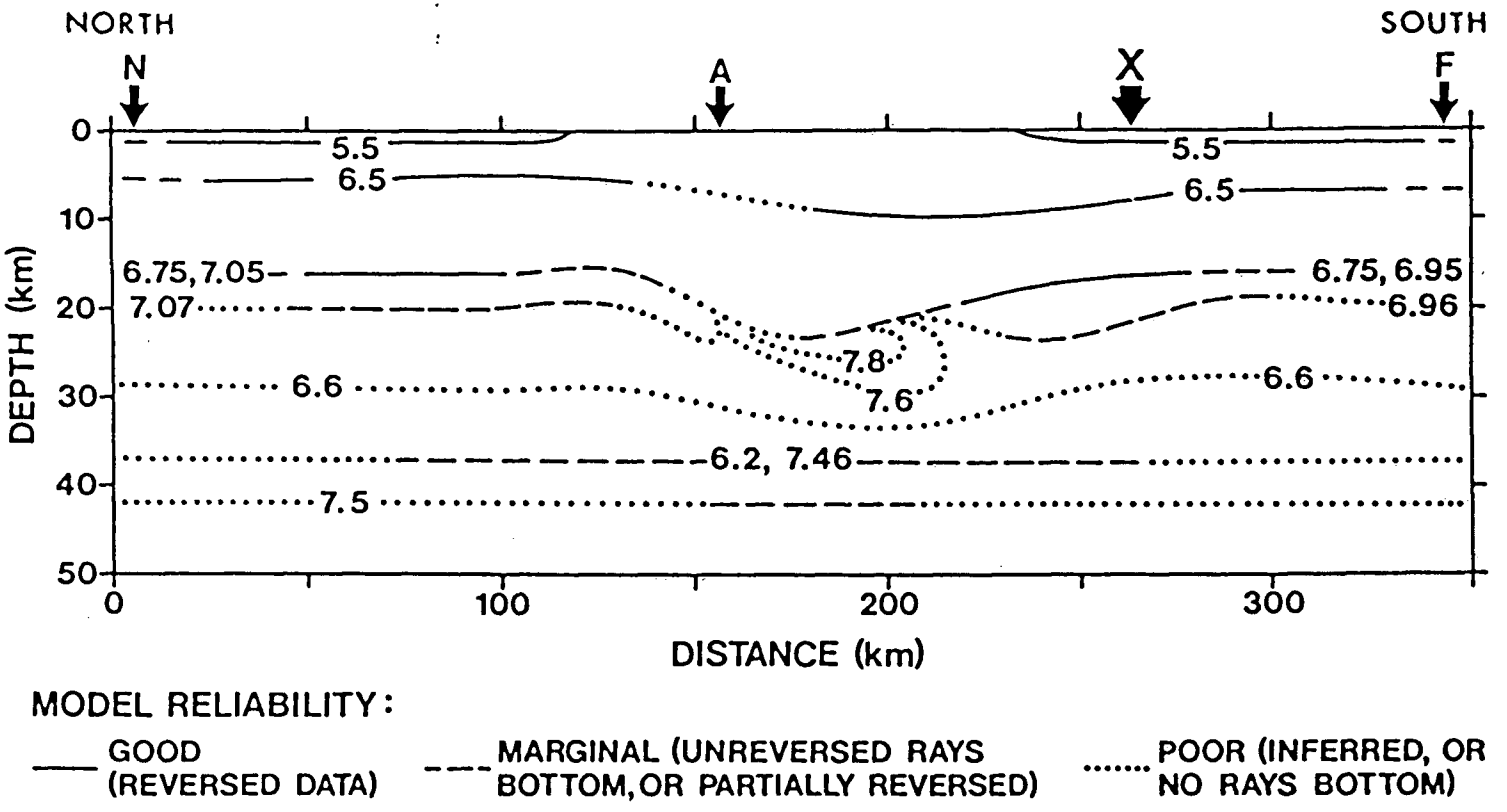

FIG. 1.4. Velocity-depth structure interpreted from data of line IV. Shot point locations are indicated by N, A and F; intersection with line I by X. Velocities (in km/s) are shown at boundaries; where two values are provided these are the velocities above and below the boundary; velocity gradients between boundaries are linear. Reliability of the contours is indicated by line types. Alternative interpretations are shown in Fig. 1.5. (Adapted from McMechan and Spence 1983).

(3) The structure of the lower crust and upper mantle is only weakly constrained. Three laterally homogeneous models of the lower crust and mantle (Fig. 1.5) were considered by McMechan and Spence (1983). Their preferred interpretation (model 2 in Fig. 1.5) contained a low velocity zone throughout the lower crust and an upper mantle velocity of 7.5 km/s at 37 km depth.

1.3.3 Interpretation of marine line I : OBS 1 to OBS 5

Data recorded on OBS's 1, 3 and 5 from the sequence of marine detonations on line I (Fig. 1.3) yield velocity information about the oceanic crust as it begins to subduct under the continental shelf. The two-dimensional velocity model interpreted by Waldron (1982) is shown in Figure 1.6. The near-surface structure was provided by continuous seismic profiling along line I and by airgun data recorded on the OBS's, while the deeper structure was determined by the explosion data on the OBS's.

The CSP section provides information on the basement structure beneath the ocean basin, and thus on sediment thicknesses. The basement west of the continental slope is seen to be dipping at 1.4° towards the continent. Some multichannel reflection profiles run by Chevron Standard Limited indicate that the basement continues to dip beneath the continental rise.

The airgun data on OBS 1, which is located in the deep ocean basin, define the structure to the mid-crust at almost 4 km depth, where the velocity is more than 6 km/s. This contrasts with the results from airgun data on OBS's 3 and 5 on the continental slope, where the maximum velocity of 3 km/s

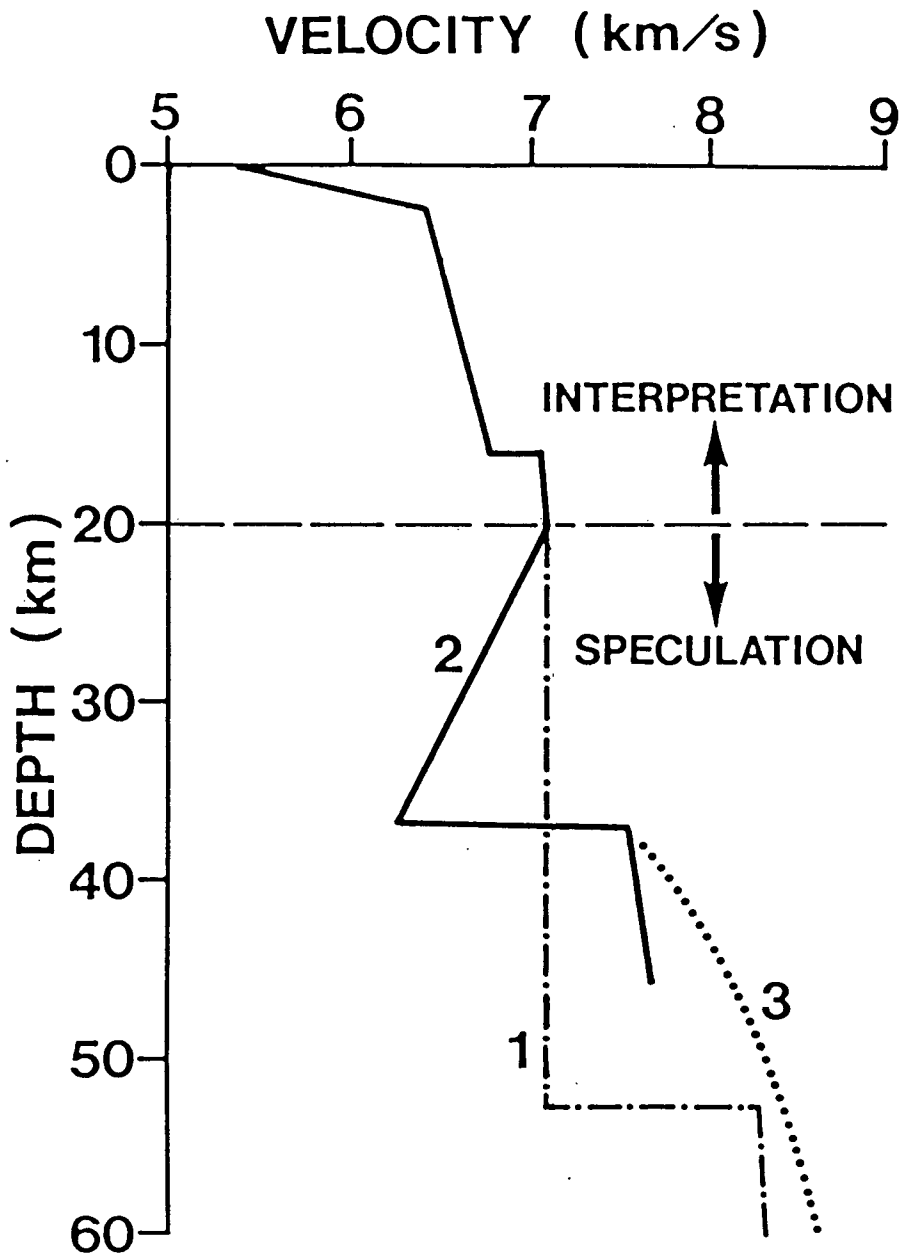

FIG. 1.5. Alternative velocity-depth models for line IV. The preferred interpretation is profile 2, but structure below 20 km is poorly constrained.

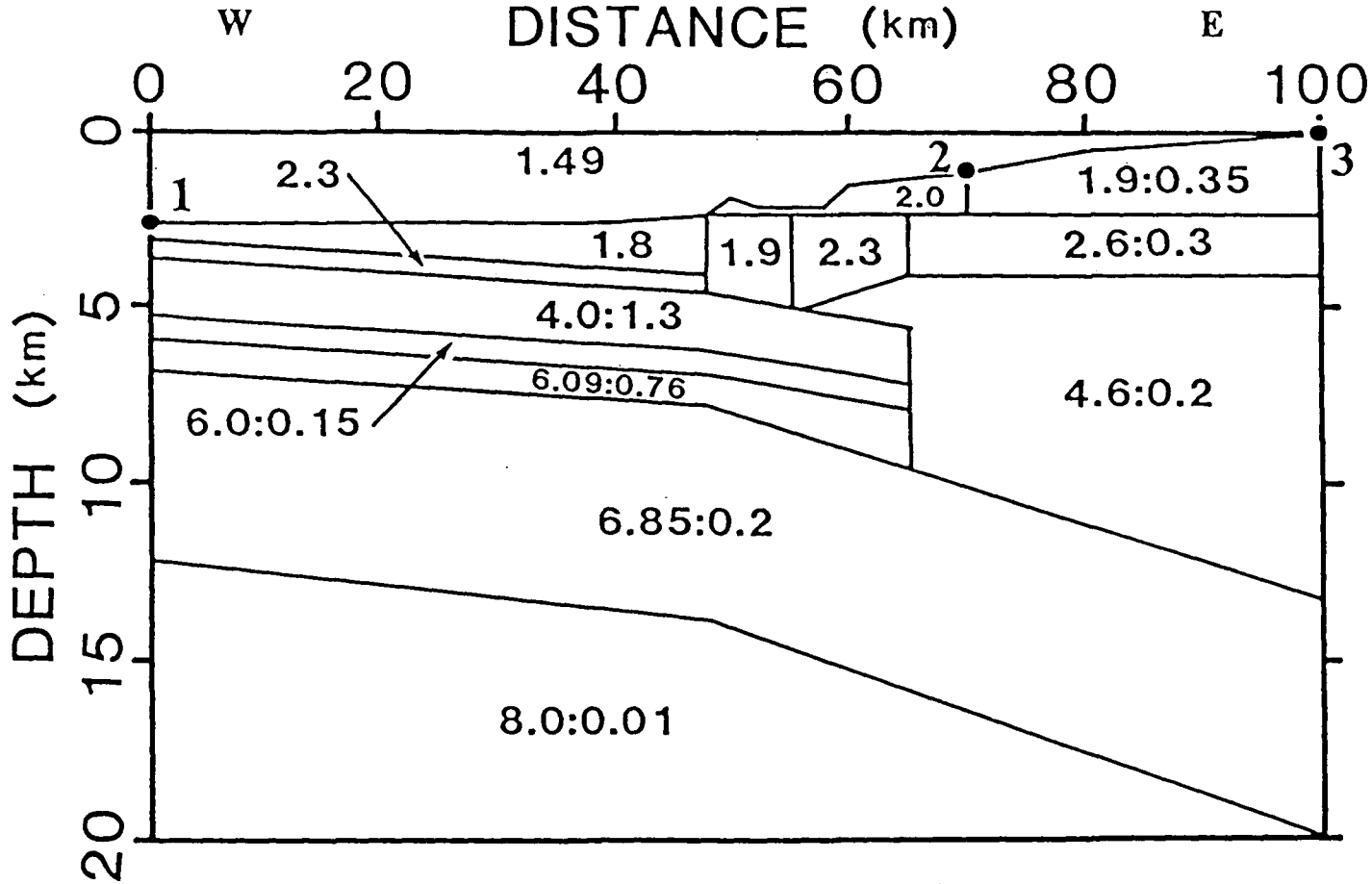

FIG. 1.6. Final velocity structure for the continental margin along the marine portion of line I, interpreted from data on OBS's 1,3 and 5. Dots show the locations of the OBS's. Velocities (in km/s) are given for the top of each region, followed after the colon by the velocity gradient (in km/s/km) if one was used (from Waldron 1982).

indicates that only sediments are being penetrated; as well, the sedimentary velocities are higher than under OBS 1. The structure is constrained down to about 2 km depth by the airgun data on OBS 3, and down to almost 3 km depth for OBS 5.

The marine explosions recorded on OBS 1 form the most diagnostic dataset for determining the sub-sedimentary oceanic velocity structure down to the Moho. The assumption was made that the entire crust beneath the ocean is dipping at the same 1.4° angle as the dip of the basement, which was observed on the CSP data. The interpretation includes a Moho at 9 km depth below OBS 1, and a 5 km constant velocity gradient region in the lower crust within which the velocity increases from about 6.8 to 8.0 km/s. The velocity at the Moho was not well constrained by the marine data,but no velocity discontinuity was required.

The velocity structure under the continental slope and shelf, as determined by data from OBS's 3 and 5, is not as well constrained as beneath the ocean basin. Since only shallow sedimentary information was available from the OBS airgun data and basement was not observed, a trade-off existed between sedimentary velocity and basement dip. Thus, an assumption had to be made concerning the dip of the basement and the boundaries below it; but presumably the dip beneath the slope and shelf is at least as great as the dip beneath the ocean basin.

The explosions recorded on OBS 5 do provide velocity information for the material above the subducting oceanic crust. The main feature of the dataset is that the apparent velocity remains near 5 km/s out to a distance of >30 km from the OBS, whereas the apparent velocity for OBS's 3 and 1 reaches 6 km/s

at offsets of <20 km. This implies that the higher velocity layers are deeper in the region of OBS 5; i.e. there is an unusual thickness of material with an intermediate velocity of about 5 km/s. The inferred position of this intermediate velocity block agrees well with that of a mid-Miocene melange proposed by Snavely and Wagner (1981) on the basis of multichannel reflection data collected by the U.S. Geological Survey.

1.4 Outline of the thesis

The main concern of this thesis is the interpretation of the onshore-offshore portion of line I (Fig. 1.3). However, a major contribution of the thesis has also been the development of techniques to carry out the interpretation.

To provide two-dimensional information along the profile, 17 shots had been fired at different locations above the continental slope and deep ocean basin, and were recorded on up to 32 stations on Vancouver Island and the mainland. It was thus necessary to find a model which simultaneously fit the large number of traveltimes corresponding to many different shot/receiver combinations. At present, the only practical method of calculating traveltimes through two-dimensional media is by ray tracing, and the ray tracing scheme of Whittall and Clowes (1979) has proven itself to be both flexible and efficient. Thus, a method was developed which incorporated the Whittall and Clowes (1979) ray tracer in a least-squares inverse scheme to find velocity models from seismic refraction data. This method is described in Chapter 2 of the thesis. It provides

an objective means of finding ray trace parameters such that the traveltime data are fit in a least-squares sense, and reduces the need for the large number of trial-and-error perturbations usually involved in ray trace modelling. However, its major limitation is that a trial-and-error procedure, based on subjective decisions about the nature of the ray paths between shot and receivers, is still required to find a starting model. It is possible that different starting models may even have different parameterizations, which thus implies variable forms of the final model.

In addition to the traveltime information, the amplitudes of seismic refraction data also place constraints on the velocity structure of the earth. It is clear that the structure beneath the onshore-offshore line I is strongly two-dimensional, since oceanic crust is considerably thinner than continental crust. Thus, as described in Chapter 3, a synthetic seismogram routine for laterally-varying media was developed. It is based on asymptotic ray theory (ART), using the practical, efficient ray tracing algorithm of Whittall and Clowes (1979). Although other two-dimensional ART routines already existed (e.g. McMechan and Mooney 1980; Cassell 1982), the advantages of a seismogram routine based on the Whittall and Clowes (1979) ray tracer are its speed of execution and its model flexibility. The latter is especially important when interpreting a possibly complex region such as the subduction zone of the western Canadian margin.

In Chapter 4, the interpretation of the onshore-offshore dataset is presented. The seismic constraints provided by the

interpretation of Waldron (1982) and McMechan and Spence (1983) were honored, as was the more general constraint that the data should be consistent with a subduction zone model. The interpretation techniques included application of the ray trace traveltime inverse procedure developed in Chapter 2, and the calculation of synthetic seismograms using the ART routine of Chapter 3. Finally, the interpreted seismic model and its tectonic implications are discussed.

CHAPTER 2. RAY TRACING AND TRAVELTIME INVERSION IN LATERALLY VARYING MEDIA

2.1 Introduction

Much information about the earth's interior is provided by traveltime data from both earthquakes and explosions. Laterally homogeneous velocity models have been obtained from such data using a number of sophisticated techniques, such as extremal inversion (Bessonova et al. 1974), linearized inversion (Johnson and Gilbert 1972) and linear programming inversion (Garmany et al. 1979). However, many geophysically interesting regions are strongly two- or three-dimensional, such as spreading ridges, subduction zones, transform faults and accreted terranes. One-dimensional methods may in fact be used to infer information about laterally varying structures, if the structure is uniform along strike or if the lateral variation is limited in extent and uniform structures on either side of the perturbed zone may be compared. But more detailed information may be obtained by directly examining the laterally varying region, and so two- or three-dimensional interpretation methods are required.

Ray tracing provides a relatively simple method for calculating traveltimes of seismic energy through complex geological models. In forward modelling procedures, traveltimes calculated by the ray tracer are matched to the observed data by varying the model in either a trial-and-error or systematic fashion. Numerous examples exist in the literature, such as Jacob (1970), Sorrells et al. (1971), Scott (1973), Gebrande

(1976), Aric et al. (1980) and Clowes et al. (1981). Some form of ray tracing is also required for inverse traveltime modelling in two- or three-dimensions. In these schemes, the model is linearized and perturbations to a starting velocity model are then estimated from the data in a matrix inversion approach utilizing a least squares criterion. Calculation of traveltimes in the original model still requires that the ray path be known.

In three-dimensional velocity inversions utilizing teleseismic data, ray paths may be calculated using a three-dimensional ray tracer. Alternatively, ray paths through a laterally varying earth model may be approximated by assuming they are the same as for a spherically symmetric velocity model. That is, starting with a spherically symmetric model, the velocity in a given block of the model may change from iteration to iteration of the inversion procedure, but so long as the lateral variations in velocity are not large, the ray path is assumed to remain the same. This method has been applied in teleseismic array studies to determine the laterally varying structure beneath the array (Aki et al. 1977). It has also been applied in whole earth studies, where massive numbers of ISC traveltimes have been used to determine lower mantle heterogeneities; examples are Dziewonski et al. (1977), who represented velocity perturbations in terms of spherical harmonics, and Clayton and Comer (1983), who used a tomographic technique.

In velocity inversions from local earthquakes, it becomes more difficult to avoid multiple iterations of a three-dimensional ray tracer. The situation is further complicated by

the need to simultaneously determine the earthquake hypocenters. Crosson (1976) tackled the problem for one-dimensional velocity models only, parameterizing the structure in terms of flat-lying constant velocity layers. Aki and Lee (1976), in what is perhaps the most widely used 3D inversion routine, subdivided the flat layers into rectangular blocks, and calculated a velocity perturbation for each block. But for simplicity in determining the ray path, they used a homogeneous half space as an initial model and iterated only once for their least-squares parameter adjustments. However, Hawley et al. (1981) were able to extend the method of Aki and Lee (1976) by introducing three-dimensional ray tracing through the plane layer block model and thus removing the restriction of a homogeneous initial model. Using the 3D ray tracer of Julian and Gubbins (1976), Spencer and Gubbins (1980) applied an iterative inversion technique to simultaneously solve for velocity structure and hypocenter location; they assumed that the velocity model in the region could be described by a simple function of the space coordinates and a small number of parameters. In the Backus-Gilbert approach to 3D velocity inversion, developed by Chou and Booker (1980), the inversion formalism does not require the explicit form of the velocity structure to be known, but rather assumes that it is an unknown function which can be viewed through a smoothing window. Nevertheless, the implementation requires specific ray paths along which integrals may be evaluated.

This chapter is concerned mainly with the development of an inversion procedure for the two-dimensional interpretation of seismic refraction traveltime data from explosions. In

experiments where multiple shots are recorded on the same set of multiple receivers, forward modelling of the traveltimes by ray tracing becomes cumbersome. It is thus desirable to invert the traveltime data for a velocity model, using a procedure in which perturbations to the ray trace model are automatically calculated. The advantages are: (1) many of the time-consuming manipulations of the forward procedure are eliminated, and (2) there is better assurance of having a model which fits the data in a least-squares sense.

The ray tracing method used in the inversion procedure is the simple, efficient scheme presented by Whittall and Clowes (1979). The velocity model is represented by large blocks with arbitrary boundaries, and within each block the velocity gradient is constant and of arbitrary orientation. The major advantages of this ray tracing method are its speed of execution and its flexibility. Speed is necessary in inverse modelling because several iterations are usually required and in each iteration the ray paths corresponding to many shot/receiver combinations must be calculated. Flexibility in ray tracing is even more important in explosion refraction surveys than in velocity modelling involving earthquake sources, where only the direct ray path is usually assumed. In a refraction interpretation, the critical first step is to identify the arrivals, usually as reflections from a particular boundary or as refractions (or head waves) in the region below the boundary. The ray tracer needs to be sufficiently flexible to allow adjustments in the depth and shape of interfaces and to accommodate velocity distributions varying both laterally and

vertically.

The need for flexibility is also related to one of the shortcomings of refraction modelling procedures, either forward or inverse, which utilize ray tracing. That is, the identification of the arrival type and the nature of the ray path involves a subjective decision about model parameterization. With a different parameterization or even different starting values for a given set of parameters, the final model may be different in many significant details. Unfortunately, there exists no method at present to overcome this fundamental problem for two- or three-dimensional interpretations.

The inverse procedure described in this chapter differs from previous velocity inversion methods for laterally varying media primarily in the nature of the ray tracer. In particular, the depth of specified interfaces may be varied in addition to the velocity of a region. The inverse routine is most similar to that of Wesson (1971), who, in crustal interpretations of explosion refraction data, also used seismic ray computations in determining least-squares adjustments to a set of velocity model parameters. However, the velocity model was a simple function of a few parameters, similar to the velocity model of Spencer and Gubbins (1980), and so was limited in its flexibility.

With the exception of the ray tracer, the inverse routine discussed in this chapter has many characteristics in common with other velocity inversion techniques, either in the general type of parameterization or in the method used to perform the matrix inversion. As will be shown, the depth to a specific

boundary plays a role which is in many ways analogous to the hypocenter depth in the routines which simultaneously invert for velocity and earthquake location. Inversion is accomplished using the damped least squares technique (Levenberg 1944), which is the procedure followed by Aki and Lee (1976) and is one of the procedures considered by Crosson (1976) and Spencer and Gubbins (1980).

2.2 Velocity Model and Ray Tracing

A complete description of the ray tracing routine is given in Whittall and Clowes (1979), and only a brief outline of the procedure is repeated here.

To define the velocity structure, there are two types of boundaries, model boundaries and divider boundaries. A model boundary is a straight line of arbitrary dip, assigned a constant velocity along its length and a non-zero velocity gradient normal to its length. A divider boundary, assigned a velocity of zero, separates a region with one velocity and gradient from a laterally adjacent region with a different velocity and gradient. Blocks may thus be defined in which the velocity and both the magnitude and direction of the velocity gradient are arbitrary. The ray path within a given block is a circular arc, for which the traveltime and distance travelled may be calculated using very simple analytical expressions (Gebrande, 1976). The source may be located along any model boundary, and rays travelling upwards or downwards from the source may be considered. If a ray is incident to a boundary at an angle which is within a specified range of the critical

angle, then head waves may be produced. Beyond the point of intersection of the critical ray with the boundary, the head waves are simulated by shooting critically refracted rays off the boundary at regular intervals along its length.

The ray path from a specific shot to a specific receiver must be found in order to calculate a model traveltime corresponding to the observed traveltime. For finding ray paths, the Whittall and Clowes (1979) ray tracer employs a shooting method, in which a shot location and a range of take-off angles are specified. It was thus necessary to extend the ray tracer to perform multiple iterations which converged on the receiver location. For reflected and turning rays, this simply requires an estimate of the rate that the shot/receiver range for the ray changes with starting angle. For head waves, an estimate is required of the rate of change of range with respect to distance along the head wave boundary. These estimates are then updated with the most current ray in the iteration.

2.3 Theory

It is assumed that there are sound geophysical reasons for choosing a particular starting model to describe the velocity structure of a region. Some of the reasons may be of a general nature, based on well-established geological or tectonic principles such as the existence of a subduction zone, a sedimentary basin, or a fault zone. Constraints on the velocity structure may also come from other reflection or refraction surveys in the area; for example, there may be tie lines crossing the profile to be interpreted, or there may be smaller

offset surveys in the area which describe the upper layers in detail. Finally, the choice of certain features in the model may be guided by a general examination of the refraction data set under consideration; as discussed in the introduction to this chapter, a given arrival must be associated with a particular boundary or a particular region of the model.

Whatever the reasons guiding the choice of a starting model, not all features of the velocity structure are to be determined by the inverse procedure. Only a few well-chosen parameters, which should be well-sampled by multiple rays with different paths, are allowed to vary.

2.3.1 The forward problem

In general, the traveltime T_{ij} between the i-th shot and the j-th receiver for a set of observed data is

$$T_{ij} = \int_{L_{ij}} \left(\frac{1}{v(x,z)}\right) ds \qquad (2.1)$$

where v(x,z) is the actual velocity structure and ds is the element of arc length along the raypath L_{ij} from shot i to receiver j. For the Whittall and Clowes (1979) ray tracer, the velocity model is specified in terms of blocks with constant velocity gradient and arbitrary boundaries. The velocity v within a given block is given by

$$v = v_0 + k\,z \qquad (2.2)$$

where v_0 is the velocity along the top boundary of the block, k is the vertical velocity gradient, and z is the vertical distance from the top boundary. Boundary position is specified

by the coordinates of the endpoints of the boundary.

Perturbations to the velocity structure produce changes in both the velocity v and the raypath L_{ij}. To first order, the traveltime can be approximated using a Taylor series expansion:

$$T_{ij} = T^{c}_{ij} + \sum_{m=1}^{M}\left[\left(\frac{\partial T}{\partial v_0}\right)_m \Delta v_{0_m} + \left(\frac{\partial T}{\partial k}\right)_m \Delta k_m\right] + \sum_{n=1}^{N}\left(\frac{\partial T}{\partial h}\right)_n \Delta h_n \qquad (2.3)$$

T^{c}_{ij} is the calculated traveltime through the starting model. The ray passes through M blocks within which velocity is allowed to vary. Δv_{0_m} and Δk_m are the unknown corrections for the velocity at the top of the m-th block and the velocity gradient in the block. N is the number of endpoints corresponding to the variable boundaries intersected by the ray, and Δh_n is the unknown correction for the depth of the n-th boundary endpoint. The partial derivatives in equation 2.3 are calculated for the starting model, and represent the rate of change of traveltime per unit change of parameter value.

From equations 2.1 and 2.2 the partial derivative of traveltime with respect to velocity at the top of the m-th block is

$$\left(\frac{\partial T}{\partial v_0}\right)_m = \int_{L_{ij}} \frac{\partial}{\partial v_0}\left(\frac{1}{v}\right) ds$$

$$\therefore \quad \left(\frac{\partial T}{\partial v_0}\right)_m = \int_{L_{ij}} \left(\frac{-1}{v^2}\right) ds \qquad (2.4)$$

Similarly, the partial derivative of traveltime with respect to velocity gradient is given by

$$\left(\frac{\partial T}{\partial k}\right)_m = \int_{L_{ij}} \left(\frac{-z}{v^2}\right) ds \qquad (2.5)$$

Thus, both partial derivatives may be simply obtained by numerical integration along the ray. The integration was implemented for the Whittall and Clowes (1979) ray tracer by dividing the circular ray path within each block into a large number of segments of equal length and assuming constant velocity along each segment.

The partial derivative of traveltime with respect to the depth of the n-th boundary endpoint was calculated analytically using a simple expression derived from geometrical arguments. Figure 2.1a shows a ray between shot and receiver, reflected at an angle α from a boundary. When the boundary is perturbed by a distance dD normal to its length, the ray path between the same shot and receiver is changed, but the reflection point on the boundary remains the same; i.e. it moves through space with the boundary. Thus, the length of the ray path changes by a distance (2 dD cosα). If the velocity immediately above the boundary is v_α, then the extra traveltime dT taken by the perturbed ray is (2 dD cosα / v_α), and

$$\frac{\partial T}{\partial D} = \frac{2 \cos\alpha}{v} \qquad (2.6)$$

For a refracted ray (Fig. 2.1b), the corresponding derivative is

$$\frac{\partial T}{\partial D} = \frac{\cos\alpha}{v_\alpha} - \frac{\cos\beta}{v_\beta} \qquad (2.7)$$

where α is the incident angle, β is the emergent, and v_α and v_β are the velocities along the incident and emergent portions of

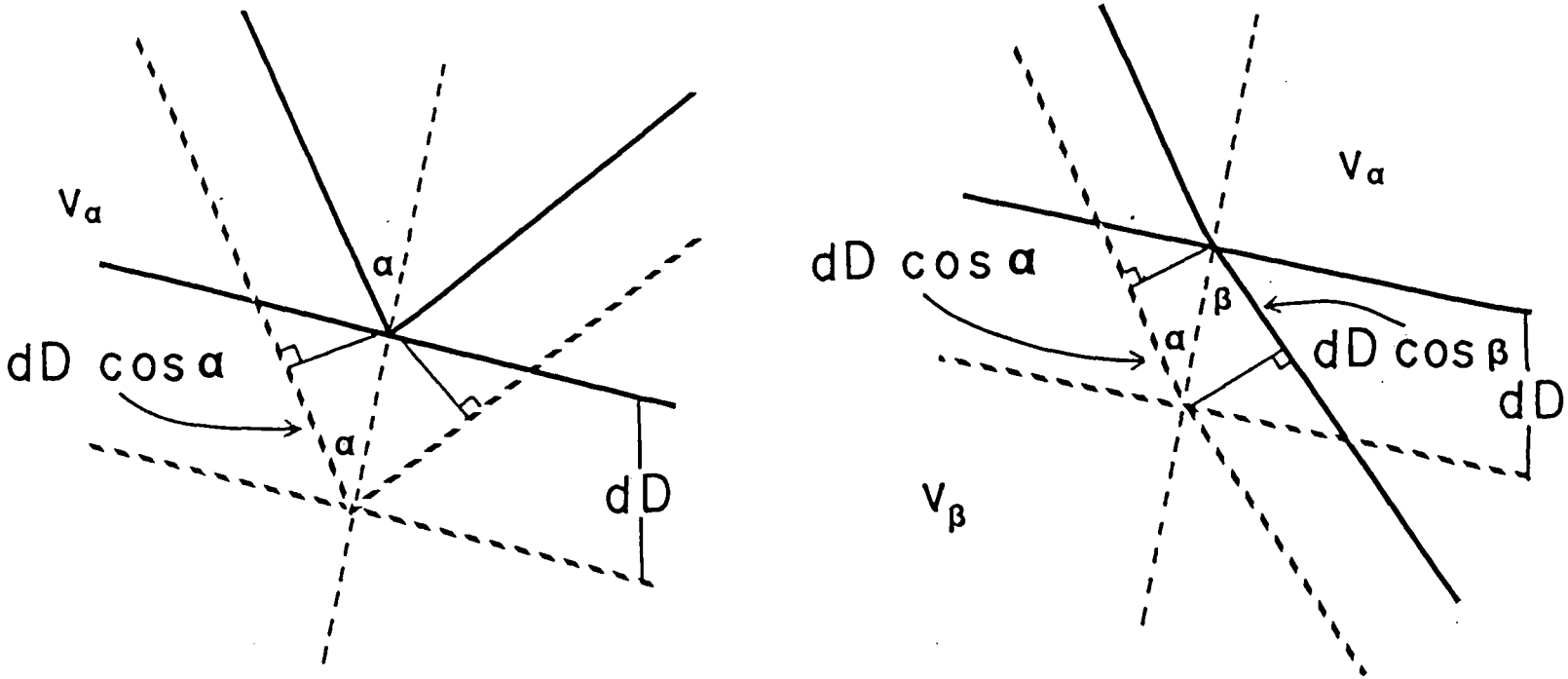

FIG. 2.1. (a) When a boundary is moved by an infinitesimal distance dD, the reflected ray path between a fixed shot and receiver is also changed. The heavy solid lines show the positions of boundary and ray path before the perturbation, and the heavy dashed show the new positions. The ray path increases in length by an amount 2 dD cosα. (b) For a refracted ray, the ray path length increases by an amount dD(cosα - cosβ).

the raypath, respectively. Note that equation 2.7 is more general and reduces to equation 2.6 if the angle β is consistently measured from the normal below the boundary. A simple geometric correction is required to convert the derivative from distance measured normal to a boundary to distance measured vertically at a boundary endpoint (Fig. 2.2). If the boundary endpoints are at h_n and h_{n+1}, then using the geometric relations for dD/dh and dh/dh_n shown in Figure 2.2, the chain rule may be applied to find

$$\left(\frac{\partial T}{\partial h}\right)_n = \left(\frac{\cos\alpha}{v_\alpha} - \frac{\cos\beta}{v_\beta}\right) \cos\gamma \left(\frac{h - h_n}{h_{n+1} - h_n}\right) \qquad (2.8)$$

where γ is the dip of the boundary measured from the horizontal and h is the depth at which the ray intersects the boundary. All of these quantities are found by the ray tracer, since full details of the ray path for the starting model are known.

In simultaneous inversions for velocity and earthquake locations, the partial derivatives with respect to hypocenter coordinates may be found by the same geometrical method. If the intersection point of the ray with the boundary were regarded as the terminating point of the ray (i.e. a source), then either equation 2.6 or 2.7 becomes

$$\frac{\partial T}{\partial z} = \frac{\cos\alpha}{v_\alpha} \qquad (2.9)$$

where z is the coordinate in the vertical direction and $\cos\alpha$ is the vertical direction cosine. In two dimensions, the partial derivative with respect to the horizontal coordinate simply involves the horizontal direction cosine.

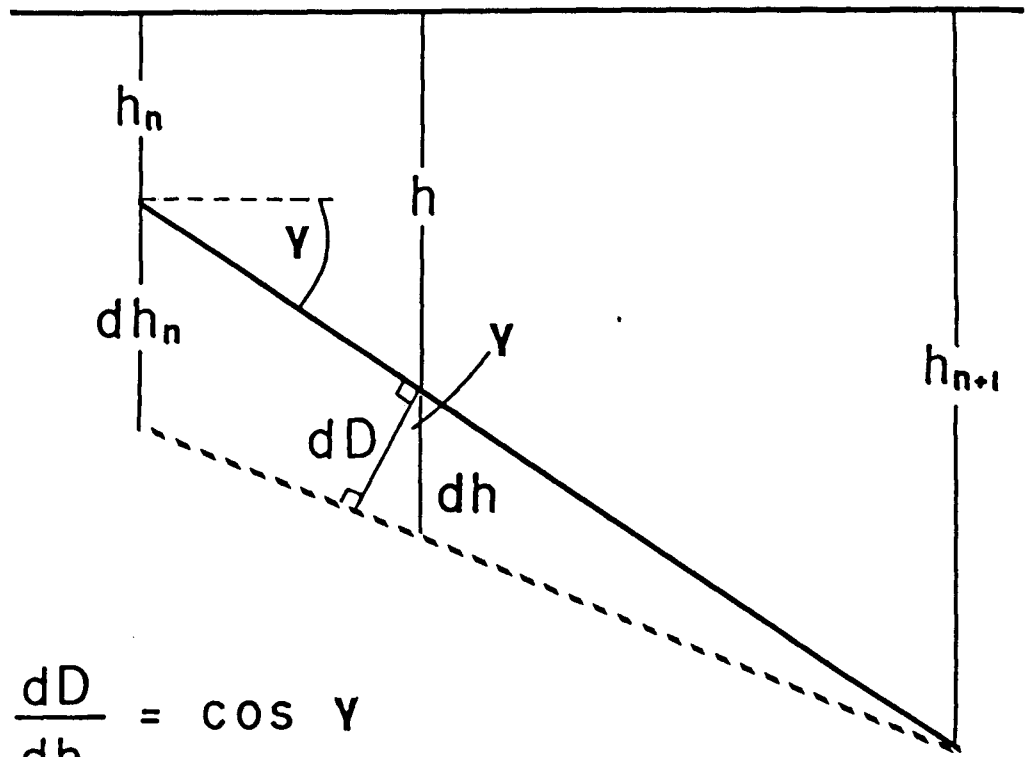

$$\frac{dD}{dh} = \cos \gamma$$

$$\frac{dh}{dh_n} = \frac{h - h_n}{h_{n+1} - h_n}$$

FIG. 2.2. With one endpoint of a boundary fixed, an infinitesimal change dh_n in the depth at the other endpoint is related by simple geometry to the infinitesimal change dD normal to the boundary at an arbitrary point along its length.

2.3.2 Damped least squares inversion

Equation 2.3 may be written in matrix notation as

$$A\Delta x = \Delta t \qquad (2.10)$$

where A is a matrix of partial derivatives, Δx is the solution vector containing the (M+N) parameter adjustments, and Δt is the traveltime residual vector, $\Delta t_{ij} = T_{ij} - T^{c}_{ij}$, corresponding to the q observations. The non-linear problem has been linearized by the use of equation 2.3, and so the solution must be computed iteratively. The current solution Δx is applied to the starting model, rays are traced through the new starting model to find a new matrix A and data vector Δt, and a new set of parameter adjustments are calculated. The procedure is repeated until convergence is reached to within the required accuracy.

With many more traveltime observations than parameters, the problem is overdetermined. The classical least-squares solution of the overdetermined problem (equation 2.10) involves minimizing the traveltime residuals with respect to the parameter variations. This leads to the calculation of the normal equations,

$$A^{T} A\Delta x = A^{T} \Delta t \qquad (2.11)$$

However, difficulties arise with this solution because the normal equation matrix $A^{T}A$ may be singular or near-singular, due to a fundamental lack of constraint on certain parameters. Symptoms of the lack of constraint would be large variations in the parameter solution from iteration to iteration. The method used here to overcome this difficulty is to apply a standard damped least-squares solution, first described by Levenberg (1944); in the context of traveltime inversion, I closely follow

the approach described by Aki and Lee (1976) and Crosson (1976). Large variations in the parameters are damped out by minimizing the weighted sum of the traveltime residuals and the parameter solution vectors, leading to a system of modified normal equations,

$$(A^T A + \Theta)\ \Delta x = A^T \Delta t \qquad (2.12)$$

Θ is a diagonal weighting matrix, given by

$$\Theta = \theta \begin{pmatrix} \sigma^2/\sigma_1^{\,2} & 0 & 0 & \cdots \\ 0 & \sigma^2/\sigma_2^{\,2} & 0 & \cdots \\ 0 & 0 & \sigma^2/\sigma_3^{\,2} & \cdots \\ \cdots & \cdots & \cdots & \cdots \end{pmatrix} \qquad (2.13)$$

Here, θ is an overall damping factor, σ^2 is an estimate of the variance of the traveltime residuals and $\sigma_i^{\,2}$ is an estimate of the variance of the i-th component of the parameter vector. Equation 2.12 has as its solution the estimated correction vector

$$\Delta x = (A^T A + \Theta)^{-1} A^T \Delta t \qquad (2.14)$$

The resolution and covariance matrices are given by

$$R = (A^T A + \Theta)^{-1} A^T A \qquad (2.15)$$

$$C = \sigma^2\ (A^T A + \Theta)^{-1} R^T \qquad (2.16)$$

The magnitude of the diagonal element of R is a good measure of the resolution of the corresponding parameter (Wiggins 1972).

Damping is increased by increasing the magnitude of the elements of Θ. Since the individual weighting factors are inversely proportional to the variance $\sigma_i^{\,2}$, a parameter adjustment with a small variance will have a large damping factor. This is significant since the magnitude of the parameter

adjustments may differ by more than a factor of 10; for example, velocity adjustments may be less than 0.1 km/s whereas depth adjustments may be several kilometres. But a parameter adjustment with a small variance implies that a small change in parameter produces a large change in traveltime, so the corresponding partial derivative is large. As well, the related diagonal element of the normal equations matrix A^TA is large, and so a relatively large damping factor is required to have any effect on that diagonal element. Thus, the purpose of the individual weighting factors is to balance the effects of the order of magnitude differences in parameter adjustment values.

As damping is increased, the covariance values decrease and the resolution values also decrease, exhibiting the standard trade-off between resolution and variance. It is desirable to have the overall damping factor θ as small as possible to maintain maximum resolution but large enough to achieve reasonable stability and variance estimates. Usually, damping may be decreased from iteration to iteration of the inversion procedure.

2.4 Tests with Artificial Data

Testing the ray trace inversion procedure using synthetic data serves two purposes. First, since the "true" model is known, it is obviously necessary to confirm that the procedure will correctly reproduce that model to within a specified degree of certainty. This is particularly important to confirm the validity of the linearizing approximation to the traveltime (equation 2.3). Second, synthetic tests may be useful in

assessing the significance of the results from real data. That is, if a synthetic model is used which is as close as possible to the model used with the actual data, the performance of the inversion procedure may prove applicable to the real interpretation.

The first test of the ray trace inversion procedure was an attempt to recover a simple two-layer model for which the depth of the boundary between the layers varied laterally. Figure 2.3 shows the synthetic model and the ray paths used to generate synthetic "observed" traveltimes. Parameter values for the synthetic model are given in Table 2.1. The model may be considered analogous to a simplified crustal model. The upper layer corresponds to the crust with constant velocity 6.5 km/s, while the second layer is the mantle; the boundary between the layers corresponds to the Moho, below which the velocity is 8.0 km/s with constant velocity gradient 0.01 km/s/km. The Moho boundary is at a depth of approximately 30 km, but there are variations in the Moho depth as large as 3 km. Shots at either end of the model result in a forward and a reversed profile, recorded on 9 receivers spaced every 20 km between 70 km and 230 km (Fig 2.3). Arrivals included wide-angle reflections from the boundary and turning rays through the gradient layer. Not all receivers recorded both arrivals, either because the shot-receiver offset was less than the critical distance or because of the effect of the corner in the boundary at 120 km, which produced a shadow zone for the reflections. The total number of traveltime observations was 31. No random noise was added to the synthetic traveltimes. However, the ray tracing scheme involved

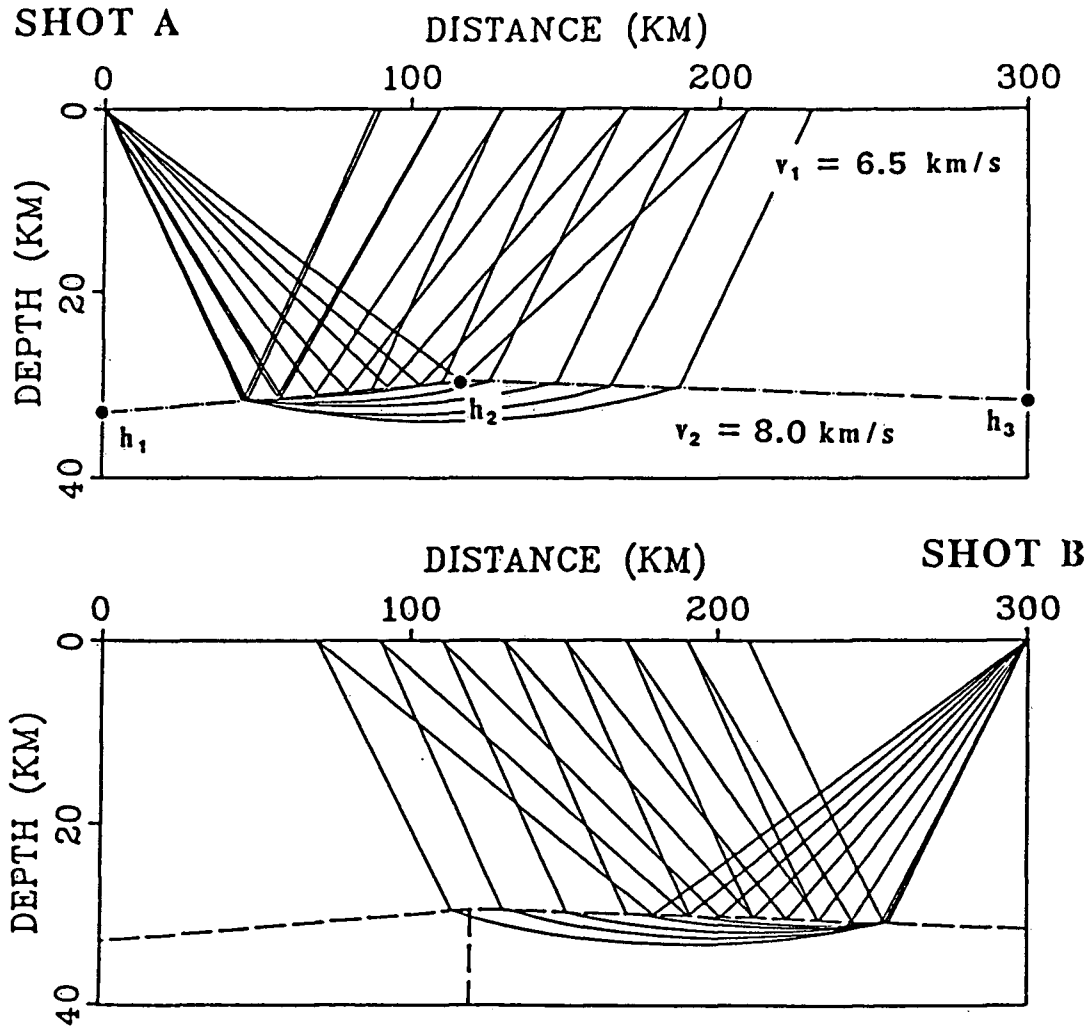

FIG. 2.3. Simple two-layer model used to generate synthetic traveltimes for testing the ray trace inversion procedure. Velocity gradients are 0 in the upper layer and 0.01 km/s/km in the lower layer. The five variables v_1, v_2, h_1, h_2 and h_3, are to be recovered in the inversion (see Table 2.1).

iteration to a specific receiver location to within a tolerance of 0.1 km, and so the traveltime error due to error in location could be as large as (0.1 km)/(6.5 km/s), or 15 ms.

For the inversion procedure, five parameters of the model were allowed to vary: the velocity of the first layer, the velocity at the top of the second layer, and the depths of the boundary at 0 km, 120 km and 300 km. Although the variance σ^2 of traveltime errors was quite small, a value of 50 ms was assumed to evaluate the performance of the damping scheme. A priori guesses were made for the values of the parameter variances to be used in the weighting matrix, and the guesses were confirmed by looking at the subsequent solution. In any case, exact values for the variances were not required, since their main purpose was to eliminate the effect of order of magnitude differences. A value of 0.015 km/s was chosen as an estimate of the rms error of the velocity variations. For a velocity of 8.0 km/s, this is

	Synthetic Value	Starting Value	Final Model Value	Res.	σ
v_1	6.50 km/s	6.00 km/s	6.49 km/s	0.93	0.007 km/s
v_2	8.00 km/s	7.80 km/s	7.97 km/s	0.72	0.013 km/s
h_1	33.0 km	23.0 km	32.9 km	0.96	0.38 km
h_2	30.0 km	23.0 km	29.3 km	0.92	0.46 km
h_3	31.5 km	23.0 km	31.5 km	0.99	0.23 km

TABLE 2.1. Synthetic test using a simple two-layer model (Fig. 2.3). Synthetic model, starting model, and characteristics of final model are shown. Resolution and standard error σ for the final model give relative measures of parameter certainties. Overall damping factor θ for the final iteration was 0.25.

a precision of about 1 part in 500, which is comparable to the precision assumed for the traveltimes (50 ms out of a typical traveltime of about 25 s). For depths, the rms error was estimated as ~1 km. The overall damping coefficient θ was set to 1.0 for the first iteration and reduced to 0.25 for subsequent iterations.

As a starting model, the Moho boundary was assumed to be flat-lying at a depth of 23 km, with the velocity set to 6.0 km/s above the boundary and 7.8 km/s just below the boundary (Table 2.1). In Figure 2.4, curve 1 (long dashed lines) represents the traveltime curve for the starting model. The synthetic traveltimes are shown by the solid dots in Figure 2.4, and the rms difference between the starting model traveltimes and the synthetic traveltimes was 1.035 s. This was reduced to 0.266 s after one iteration of the inversion procedure (curve 2 in Fig. 2.4), to 0.030 s after the second iteration (curve 3 in Fig. 2.4), and to 0.019 s after the third and final iteration. The final rms difference was comparable to the value of 0.015 s due to location error in the ray tracing procedure.

The final inverted model reproduced the original synthetic model very closely, as shown in Table 2.1. The diagonal elements of the resolution matrix and the standard errors obtained from the diagonal of the covariance matrix give relative measures for the parameter certainties in the final solution. The most poorly determined parameter was the velocity v_2 at the top of the second layer, although the difference compared to the synthetic model velocity was only 0.03 km/s. The resolution for the

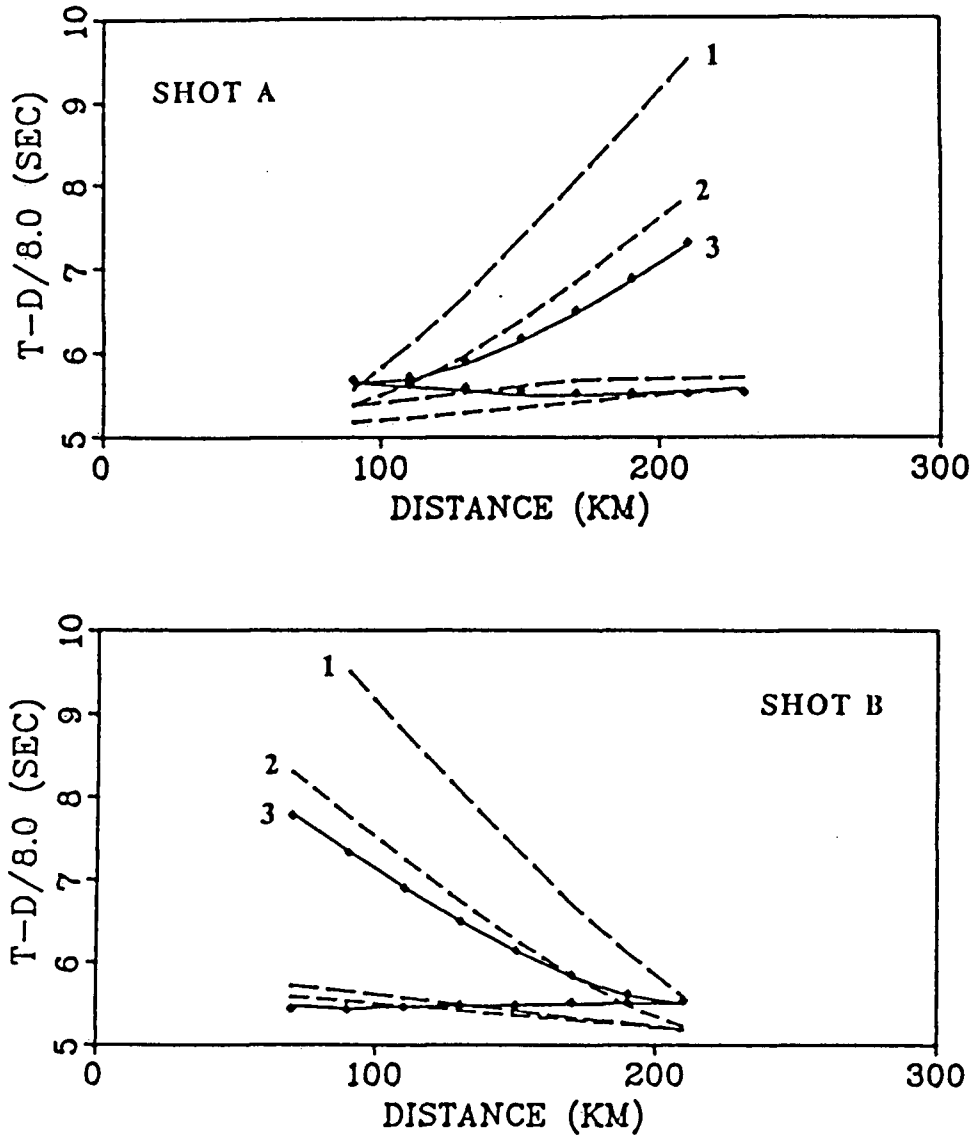

FIG. 2.4. Performance of the inversion procedure for the two-layer model of Fig. 2.3. Solid dots are the synthetic traveltimes, curve 1 is the starting model traveltime curve, curve 2 is after the first iteration and curve 3 is after the third iteration. Rms difference between the synthetic and curve 3 traveltimes is 30 ms; a further iteration reduced the difference to 19 ms.

velocity v_2 was 0.72, compared to values above 0.9 for the other parameters, and the standard error was nearly twice as large as for the velocity v_1 in the top layer. Similarly, the next most poorly determined parameter was the depth h_2, which had a resolution of 0.92 and the largest standard error (0.46 km) of all the depth parameters. The overall damping factor θ was 0.25 for the final iteration. If θ is reduced for a given iteration so that damping is further reduced, then the standard trade-off between resolution and variance is observed. For example, if θ was reduced to 0.1 for the final iteration, the resolution for parameter v_2 increases to 0.86 while the standard error also increases to 0.013 km/s. In this case, however, parameter values change only slightly and the rms traveltime difference decreases insignificantly to 0.018 s.

A fundamental limitation in the success of the inversion procedure is the subjective choice of parameterization of the starting model, including the choice of ray paths used to calculate model traveltimes. For the two-layer test example, the true model would not have been accurately recovered if the depth parameter h_2 in the starting model had been specified at a distance 200 km from shot A instead of at 120 km as in the true model. Similary, if the velocity gradient in a layer had been chosen as a variable parameter in addition to the velocity at the top of the layer, then it would have been possible to find other models which also fit the data. That is, the velocity gradient is a very poorly constrained parameter, especially in the first layer where all of the ray paths penetrate to the same depth (i.e. the bottom of the layer) and there are no rays which

independently sample only the top of the layer.

The model may be over-parameterized not only by allowing the velocity gradient to vary but also by specifying many velocity blocks and many boundary segments. In this case, another problem arises in addition to the problem of non-uniqueness for most of the parameters. With many variable blocks and boundaries, the ray tracing becomes very unstable, since no smoothing is done in the ray trace program either of boundaries or of velocities between blocks. Ray paths would tend to scatter, and it would be difficult to find ray paths between many shots and receivers. That is, the inverse procedure is not very robust because of the instability of the ray tracing. Also, the use of the inverse routine gives no added assurance that the correct choice of parameterization was made, just as in the case of using the ray tracer in a forward modelling scheme.

In the second test of the ray trace inversion procedure, a model was constructed to represent the subduction zone velocity structure beneath line I of the Vancouver Island Seismic Project, which is interpreted in Chapter 4. The test model was very similar to the preliminary model of Ellis et al. (1983), modified by the addition of an upper mantle reflector (boundary 3-4 in Fig. 2.5a). To generate the synthetic dataset, rays were traced from locations corresponding to the three main shots of the experiment (P19, P13 and P8; see Fig. 1.3) to the same 32 receiver locations as used during the recording of line I. To approximate the errors of a real traveltime dataset, random Gaussian noise with a standard deviation of 75 ms, the same as the estimated picking error of the traveltimes, was added to the

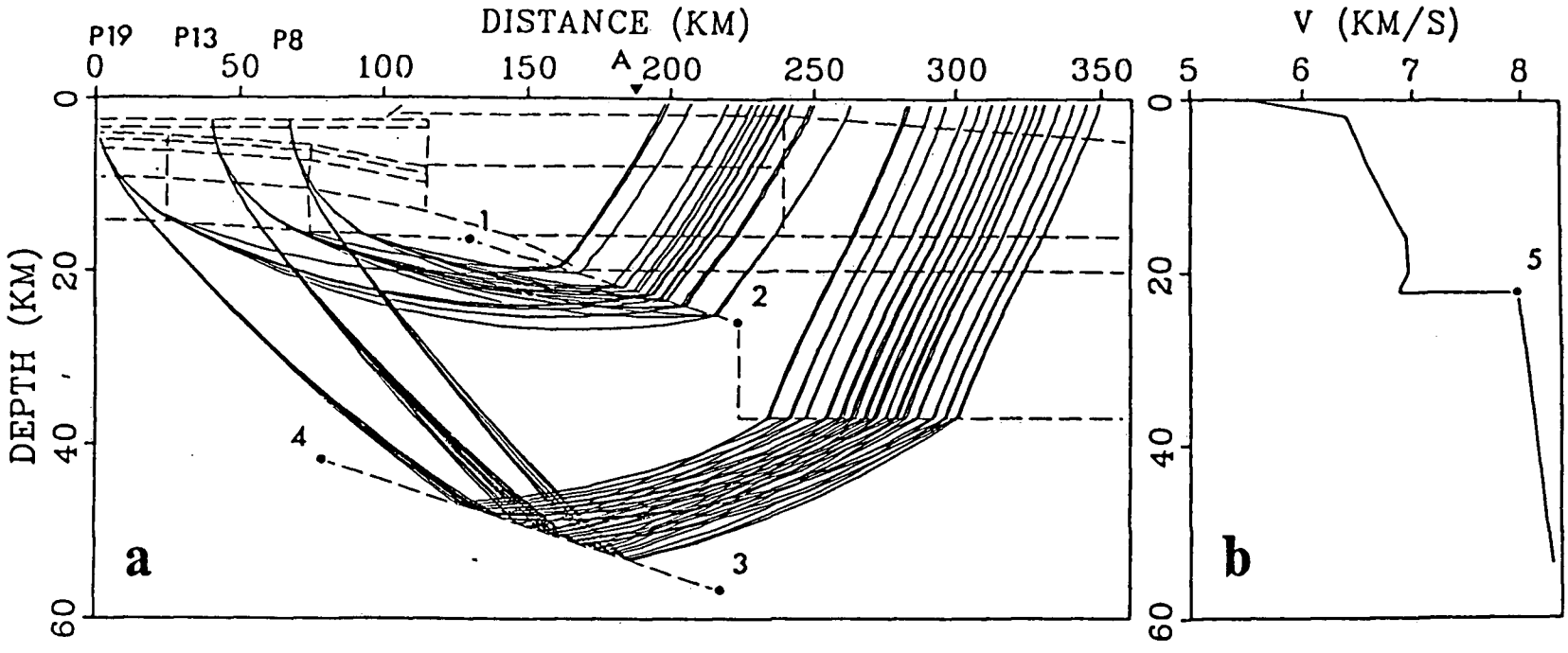

FIG. 2.5. (a) Ray paths through a test starting model using the same shot and receiver locations as in the interpretation of line I of the Vancouver Island Seismic Project. Variables in the inversion procedure include the depth of the subducting Moho at points 1 and 2 and the depth of an upper mantle reflector at points 3 and 4. (b) Velocity-depth profile at location A on the ray trace model. A fixed mantle gradient of 0.01km/s/km is assumed. Only the velocity below the Moho (point 5) is variable.

artificial data.

For the test procedure, the arrivals to the near offset receivers were modelled as turning rays through the mantle, while the far offset arrivals were modelled as reflections from the upper mantle boundary. Figure 2.5a shows the starting model and the ray paths through it. The parameters to be recovered, which are the variables in the inverse method, included the depths of the Moho at positions 1 and 2, the depths of the upper mantle reflector at locations 3 and 4, and the Moho velocity (point 5 in Fig. 2.5b). A fixed mantle velocity gradient of 0.01 km/s/km was assumed. This model was actually not much more complicated than the first test model discussed previously. Although the crustal portions of the subduction zone test model were complex, nearly all parameters related to the crust were considered fixed and did not enter into the inverse procedure.

The same values as in the first test were used for the elements of the weighting matrix, that is, 0.015 km/s for the standard error of the velocity and 1 km for the depths. The standard error of the time measurements was 75 ms, the level of the random noise added to the data. As before, the overall coefficient θ was set to 1.0 for the first iteration and subsequently reduced to 0.25.

The performance of the inverse procedure is demonstrated in Figure 2.6, Figure 2.7 and Table 2.2. Figure 2.6 shows a blowup of the central portion of the velocity model. The dashed lines correspond to the starting model while the heavy solid lines outline the final model after two iterations. The final model compares well with the "true" model, shown by the dotted lines,

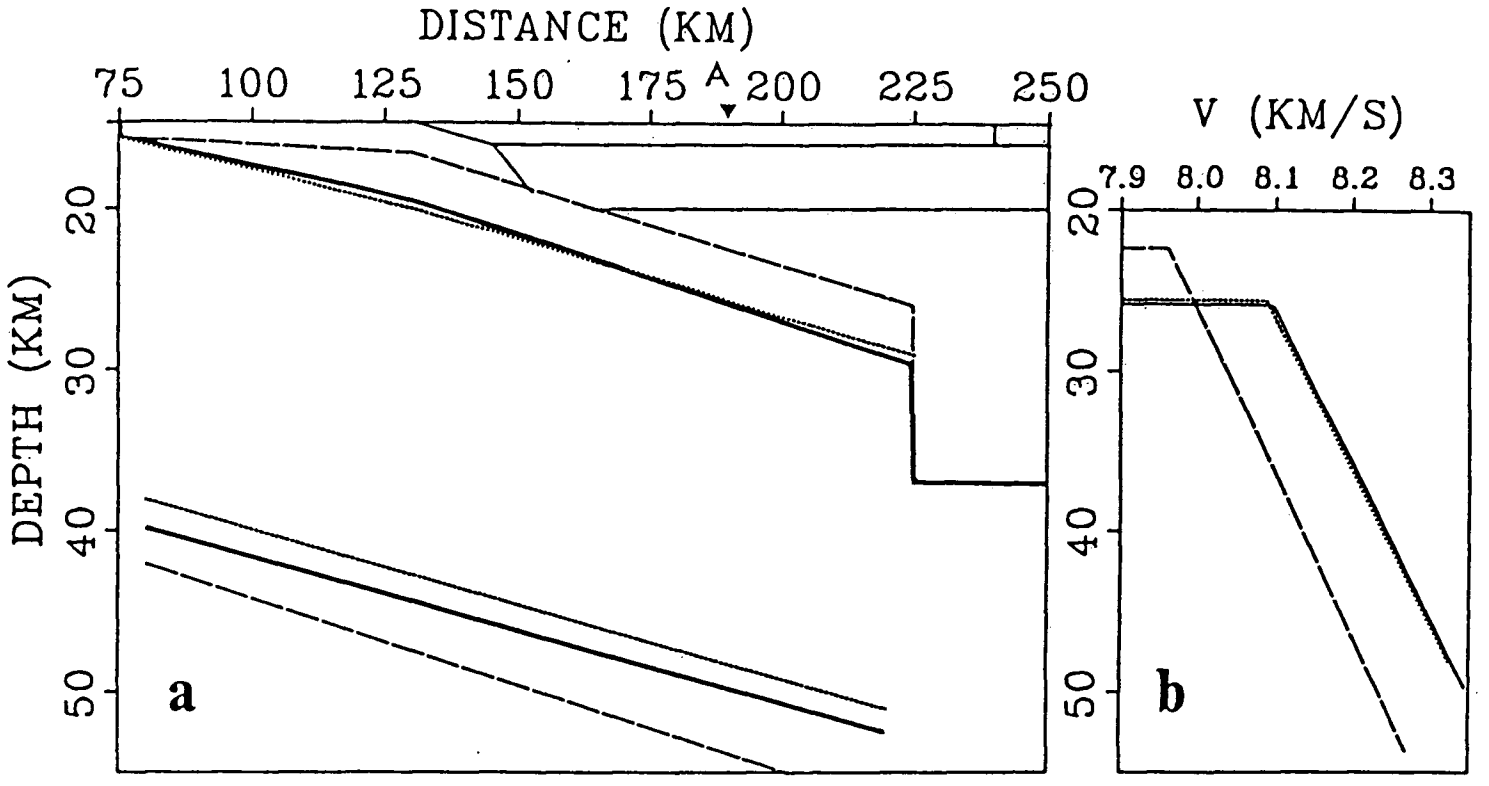

FIG. 2.6. (a) Dashed lines show the boundary positions of the starting model (Fig. 2.5). Heavy solid lines outline the final positions after two iterations of the inversion procedure. Dotted lines show the "true" positions of the subducting oceanic Moho and upper mantle reflector. (b) Final (solid line), true (dotted line) and starting (dashed line) upper mantle velocity. No change in velocity gradient was permitted. Location of velocity profiles is at A.

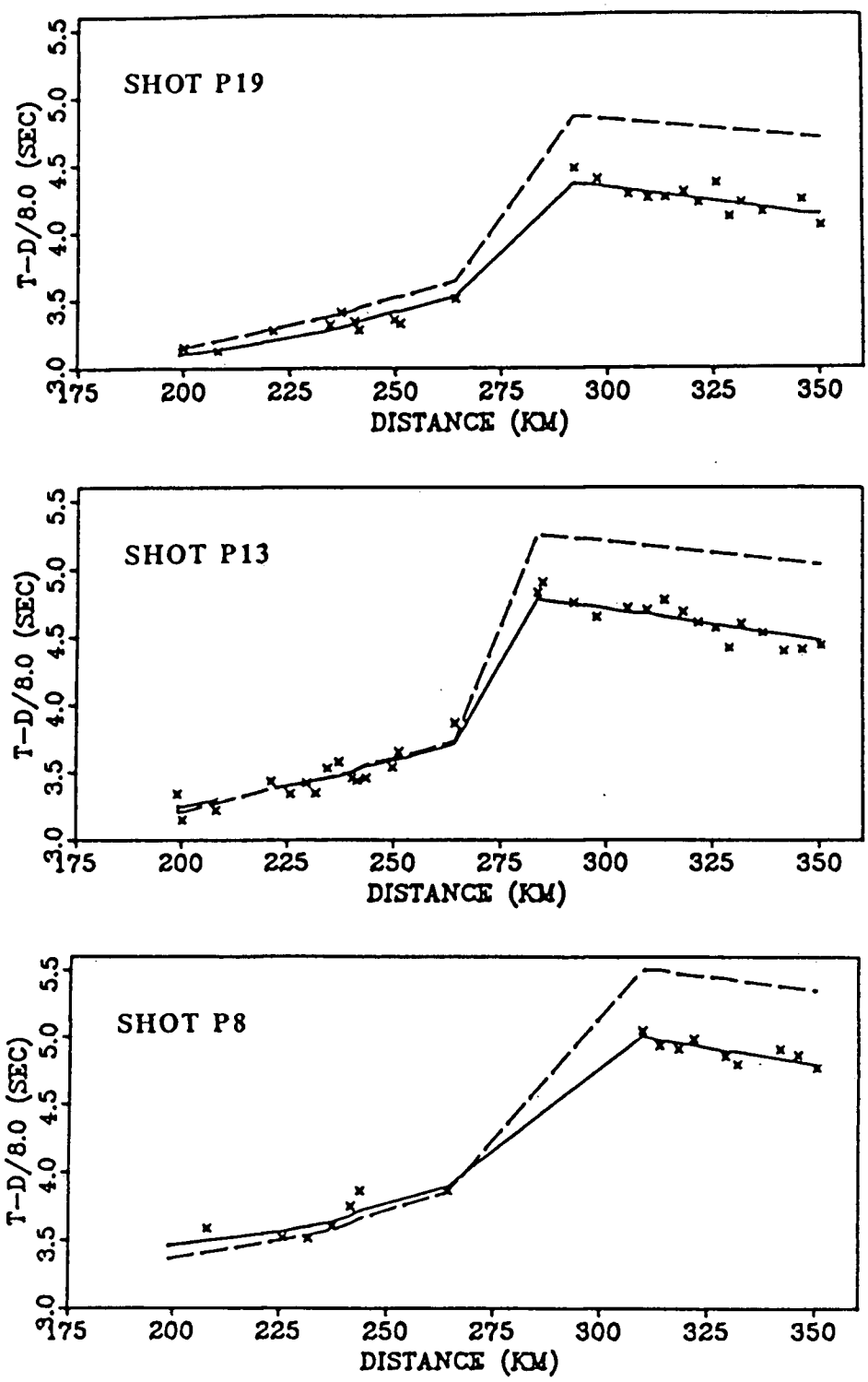

FIG. 2.7. Performance of the ray trace inversion procedure applied to the subduction zone test model. Dashed lines are the traveltime curves for the starting model of Fig. 2.5, and solid lines are the final model traveltime curves after 2 iterations. Crosses are the synthetic traveltimes, to which 75 ms random noise has been added. Rms difference beween synthetic and model traveltimes is 405 ms for the starting model and 74 ms for the final model.

the only significant difference being an error of about 1.6 km for the endpoints of the upper mantle reflector (Fig. 2.6a and Table 2.2). Figure 2.7 indicates how the traveltime fit is improved by the inverse procedure. For each of the three shots, the dashed lines are the traveltime curves corresponding to the starting model, the solid lines are the traveltime curves for the final model, and the crosses are the synthetic "observed" traveltimes. The rms difference between starting model traveltimes and synthetic traveltimes was 405 ms. This was reduced to 80 ms after one iteration and to 74 ms after the second and final iteration. Subsequent iterations produced only small parameter perturbations and reduced the rms traveltime difference only marginally; since the final rms value was already below the level of the noise, perturbations from subsequent iterations could not be considered significant.

	Synthetic Value	Starting Value	Final Model Value	Res.	σ
v	8.00 km/s	7.90 km/s	8.02 km/s	0.94	0.007 km/s
h_1	20.0 km	16.5 km	19.5 km	0.87	0.66 km
h_2	29.0 km	26.0 km	29.7 km	0.93	0.48 km
h_3	38.0 km	42.0 km	39.8 km	0.73	0.84 km
h_4	51.0 km	57.0 km	52.5 km	0.29	0.84 km

TABLE 2.2. Synthetic test using a subduction zone model (Fig. 2.5). Variable parameters included Moho velocity v, depths h_1 and h_2 of the subducting Moho, and depths h_3 and h_4 of the upper mantle reflector. Overall damping factor θ was 0.25.

From Table 2.2, the best resolved parameter was the mantle velocity v, with a resolution of 0.94. The location of the upper mantle reflector was very poorly resolved, in particular the depth at point 4 where the resolution was 0.29. The reason the reflector position was poorly determined is because the traveltimes to the far offset receivers were not very sensitive to reflector depth. This is evident upon examination of the partial derivatives of traveltime with respect to the depth of point 4; a 1 km change in depth typically produces a traveltime change of only ~15 ms, which is small compared to the random noise level of ~75 ms. On the other hand, the positions of the Moho boundary at points 3 and 4 are better resolved. Here, a 1 km perturbation in depth causes a traveltime difference of typically ~60 ms.

I feel that not too much emphasis should be placed on the absolute values of the covariance estimates and, more specifically, that they should be considered as minimum values for parameter estimates. Additional and perhaps more significant errors may arise because of the dependence of the final model on the starting model; in particular, there is no assurance that the parameterization chosen is valid for the real earth. A simple example of the non-uniqueness implied by this problem is shown in Figure 2.8. The heavy solid lines in the figure are the boundary positions for the "true" model from the previous subduction zone test, in which the depth of the continental Moho (the boundary east of 225 km) was considered fixed at 37 km. If the continental Moho is changed to 32 km depth, the same synthetic traveltimes are fit within the statistical error by

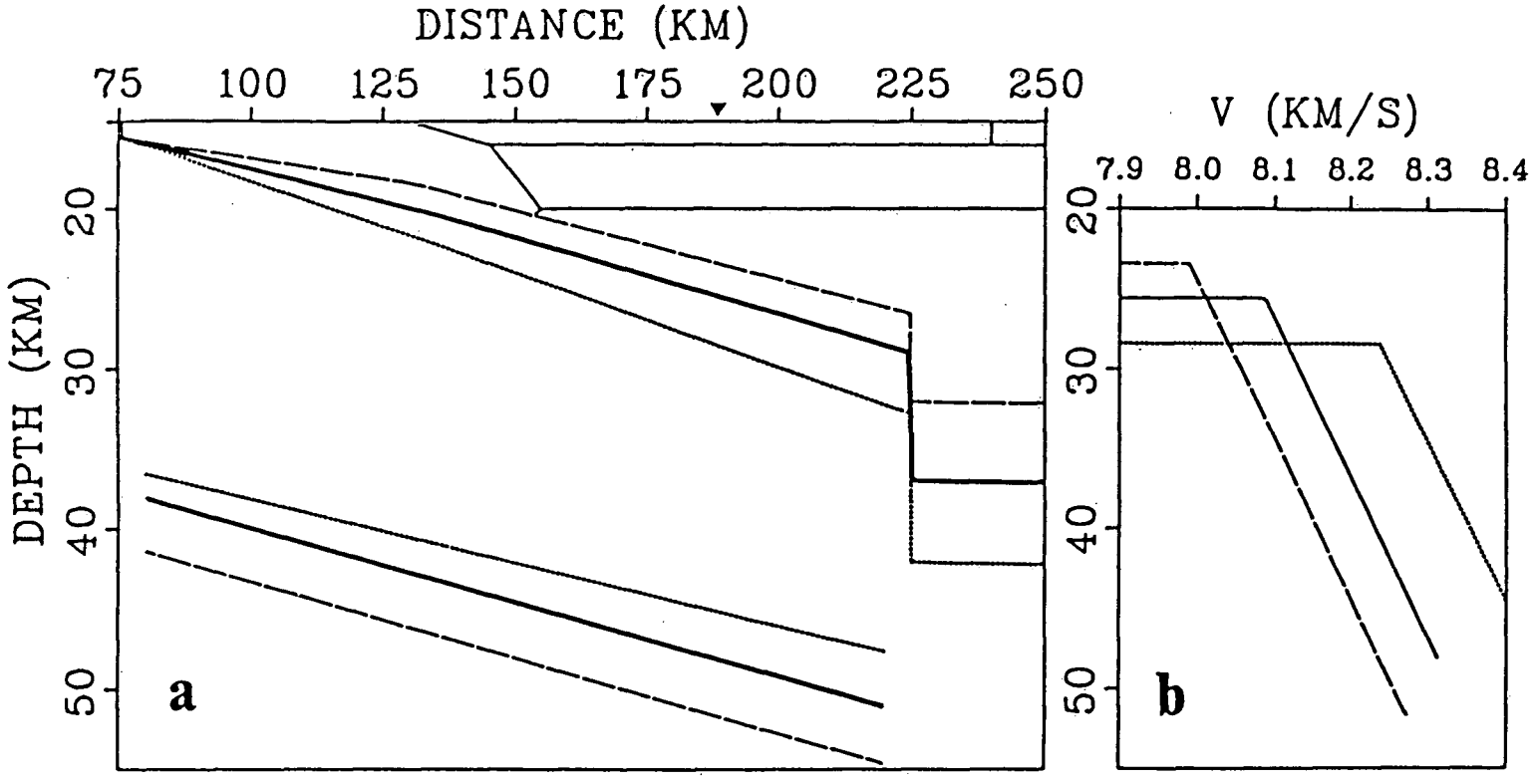

FIG. 2.8. Three different models which fit the synthetic traveltimes of the subduction zone test model. Heavy solid lines are the boundary positions assuming a continental Moho (east of 225 km) fixed at 37 km depth. Dashed lines assume a Moho fixed at 32 km depth, and dotted lines assume a Moho fixed at 42 km depth.

the model indicated by the dashed lines in Figure 2.8. Similarly, the dotted lines show a model which fits the traveltimes assuming a continental Moho fixed at 42 km depth. That is, the depth of the continental Moho cannot be determined uniquely with the other 5 parameters. If the Moho depth had been included as a variable parameter in the inversion, then the starting value assumed for the depth would control the values calculated for the other parameters.

In section 4.4 of Chapter 4, the ray trace inversion procedure is applied to the traveltime dataset recorded along the onshore-offshore line I of the Vancouver Island Seismic Project. The model used is a variant of the subduction zone test model. To illustrate the basic nonuniqueness of the interpreted model, two alternative models which fit the observed traveltimes equally as well are presented in section 4.6. One of the alternative models is the subduction zone test model itself, but with the actual observed traveltimes replacing the synthetic traveltimes of the previous example.

CHAPTER 3. PRACTICAL SYNTHETIC SEISMOGRAMS FOR LATERALLY VARYING MEDIA CALCULATED BY ASYMPTOTIC RAY THEORY

3.1 Introduction

For many years, seismologists have made use of both the kinematic and dynamic characteristics of seismic refraction data to better model the velocity-versus-depth structure of the earth. Such interpretation requires the calculation, for a specific model, of theoretical seismograms which are compared to the observed seismograms. Through a trial-and-error process different models are proposed, the synthetic seismograms are generated, and comparisons are made until an acceptable fit has been achieved. This procedure of incorporating both traveltime and amplitude information into the interpretation of seismic data has enabled more realistic models of the earth's structure to be derived.

However, until very recently the procedure could only be applied to one-dimensional earth models because the theoretical bases for synthetic seismogram computation assumed that velocity varied with depth only (e.g. Helmberger, 1968; Fuchs and Müller, 1971; Chapman, 1978). But many of the most interesting problems to which refraction seismology is applied (e.g. spreading ridges, subduction zones, cordilleran structures, rift basins) are strongly two-dimensional and require a cross-sectional model to describe them. Ray tracing following a variety of methods has provided a means of calculating traveltimes in laterally inhomogeneous media (e.g. Cerveny et al., 1977; Julian and

Gubbins, 1977; Gebrande, 1976; Whittall and Clowes, 1979). However, experience with the interpretation of one-dimensional models indicates that it is essential to have a means of calculating amplitudes as well as traveltimes.

What is required by the interpreting seismologist is an algorithm which combines ray tracing with the generation of synthetic seismograms for two-dimensional structures. An effective algorithm must be able to accept realistic structures, and reliably generate synthetic seismograms for those arrivals commonly identified on the observed record sections. At the same time, a practical computer algorithm must be fast and economical to run, and should have a simple method for the input of model parameters. Thus, the desire for great generality in a computer routine must be balanced against its speed and simplicity of use.

The most general of two-dimensional synthetic seismogram routines take into account the wave nature of the propagating energy. Examples are the Gaussian beam method (Cerveny et al., 1982), the generalization of the WKBJ seismogram to laterally-varying media (Chapman and Drummond, 1982), and the various Kirchoff integral methods (e.g. Haddon and Buchen, 1981). In these methods, ray tracing is still used as a common first step to generate a full system of rays throughout the model. Traveltimes are obtained from ray arrival times, and the calculation of amplitudes then proceeds by combining many rays at each receiver using various weighting schemes. However, practical, efficient computer algorithms based on these theoretical methods are not readily available to the

interpreting seismologist.

In this chapter, two-dimensional synthetic seismograms are calculated by a direct application of asymptotic ray theory (ART). The method has the advantage of simplicity, in that a single ray path is used to determine the amplitude of a particular arrival. Although this characteristic implies that ART cannot model certain types of signals, such as diffractions and caustics, the method has proved applicable in a wide range of models and a number of ART algorithms have recently appeared in the literature. In the method described by Cerveny et al. (1974) and Cerveny et al. (1977), a set of differential equations involving amplitude parameters was solved simultaneously with a set of differential equations for the tracing of rays. Because a solution must be obtained for each of the many points along each ray, the numerical solutions are excessively time-consuming. McMechan and Mooney (1980), in what apparently was the first application of ART to real refraction data, calculated amplitudes by using the end points of two neighboring rays to estimate the elementary ray tube area. However, they used the ray tracing code described in Cerveny et al. (1977), which employs the time-consuming point-by-point computations. Marks (1980) and Cassell (1982) avoided these cumbersome numerical calculations by parameterizing the velocity model into small rectangular or triangular regions with constant velocity or constant velocity gradient, so that simple analytical expressions could be used. For calculating amplitudes, Marks (1980) used neighboring rays to estimate ray tube area at the receiver for reflection and refraction phases.

Cassell (1982) used simple expressions for amplitudes of reflected, refracted and head waves in models with homogeneous layers and plane dipping boundaries, as given in Cerveny and Ravindra (1971).

A simple, efficient ray trace method for laterally varying media was presented by Whittall and Clowes (1979). The velocity model is represented by large blocks with arbitrary boundaries, and within each block the velocity gradient is constant and of arbitrary orientation. The model is very simple to specify and to modify, and the algorithm is very fast. The procedure has proved sufficiently flexible to allow its application in a number of refraction interpretations, for example Clowes et al. (1981), Delandro and Moon (1982), Ellis et al. (1983), Green et al. (1983) and Horn et al. (1984). The widespread use of the routine has provided encouragement to develop a method of determining amplitudes as well as traveltimes within the algorithm. In this chapter, amplitudes are calculated for the Whittall and Clowes (1979) ray tracer by a combination of the ART approaches applied by Marks (1980) and Cassell (1982). The amplitude calculation adds only a modest amount to the cost of the ray tracing, so the advantages of a simple, easily modified input and efficient computations are maintained. The resulting algorithm is a user oriented program for calculating synthetic seismograms in laterally inhomogeneous media.

3.2 Velocity Model and Ray Tracing

A brief description of the Whittall and Clowes (1979) ray tracer is given in section 2.2 of Chapter 2. However, extensions to the routine as described in section 2.2 have been added in the course of developing the synthetic seismogram algorithm.

The Whittall and Clowes (1979) algorithm was extended so as to allow ray tracing for pre-critically reflected and multiply reflected waves. Converted phases are still not considered. For the pre-critical and multiple reflections, only the boundary or boundaries at which reflection is desired need to be specified. At all other boundaries encountered by the ray, the behavior of the ray is controlled by the angle of incidence at the boundary. If the incident angle is less than the critical angle, then the ray refracts through the boundary; otherwise, it reflects from the boundary. Thus, if no pre-critical or multiple reflections are desired, then a single specification of the range of take-off angles gives all wide-angle reflections, turning rays and head waves. The corresponding traveltime curve is divided into branches such that the distance along each branch increases or decreases monotonically with distance. The family of rays associated with each traveltime branch is labelled with a unique identification number, which is used in the synthetic seismogram routine for purposes of interpolation within a given ray family.

3.3 Calculation of Amplitudes and synthetic seismograms

3.3.1 Reflected and Refracted Rays

In a medium with an arbitrary inhomogeneous velocity distribution, zero-order asymptotic ray theory provides a connection formula between the source at M_0 and any point M for the amplitude of a reflected or refracted wave (Cerveny and Ravindra, 1971, p.74).

$$U(M) = \frac{1}{L}\left(\frac{v(M_0)\rho(M_0)}{v(M)\rho(M)}\right)^{1/2} \prod_{i=1}^{N}\left(\frac{v'(O_i)\rho'(O_i)}{v(O_i)\rho(O_i)}\right)^{1/2} R_i \qquad (3.1)$$

The ray geometry is shown in Figure 3.1. O_i is the point of incidence of the ray at the i-th interface it encounters. Primed quantities are evaluated on the side of the interface from which the ray emerges. The relationship between P-wave velocity v and density ρ is approximated by (Birch,1964)

$$\rho = 0.252 + 0.3788v \ .$$

Zoeppritz amplitude cofficients R_i for transmission or reflection are taken from Cerveny and Ravindra (1971, p.63), and are calculated using a routine described by Young and Braile (1976) and Cassell (1982). The Zoeppritz algorithm assumes that the medium has a Poisson's ratio of 0.25 except if the P-wave velocity is less than 1.5 km/s, where the material is assumed to be water with a density of $1.0*10^3$ kg/m^3 and an S-wave velocity of zero. The Zoeppritz routine also allows the calculation of surface reflection and surface conversion coefficients if desired.

In equation 3.1 the geometrical spreading function L is

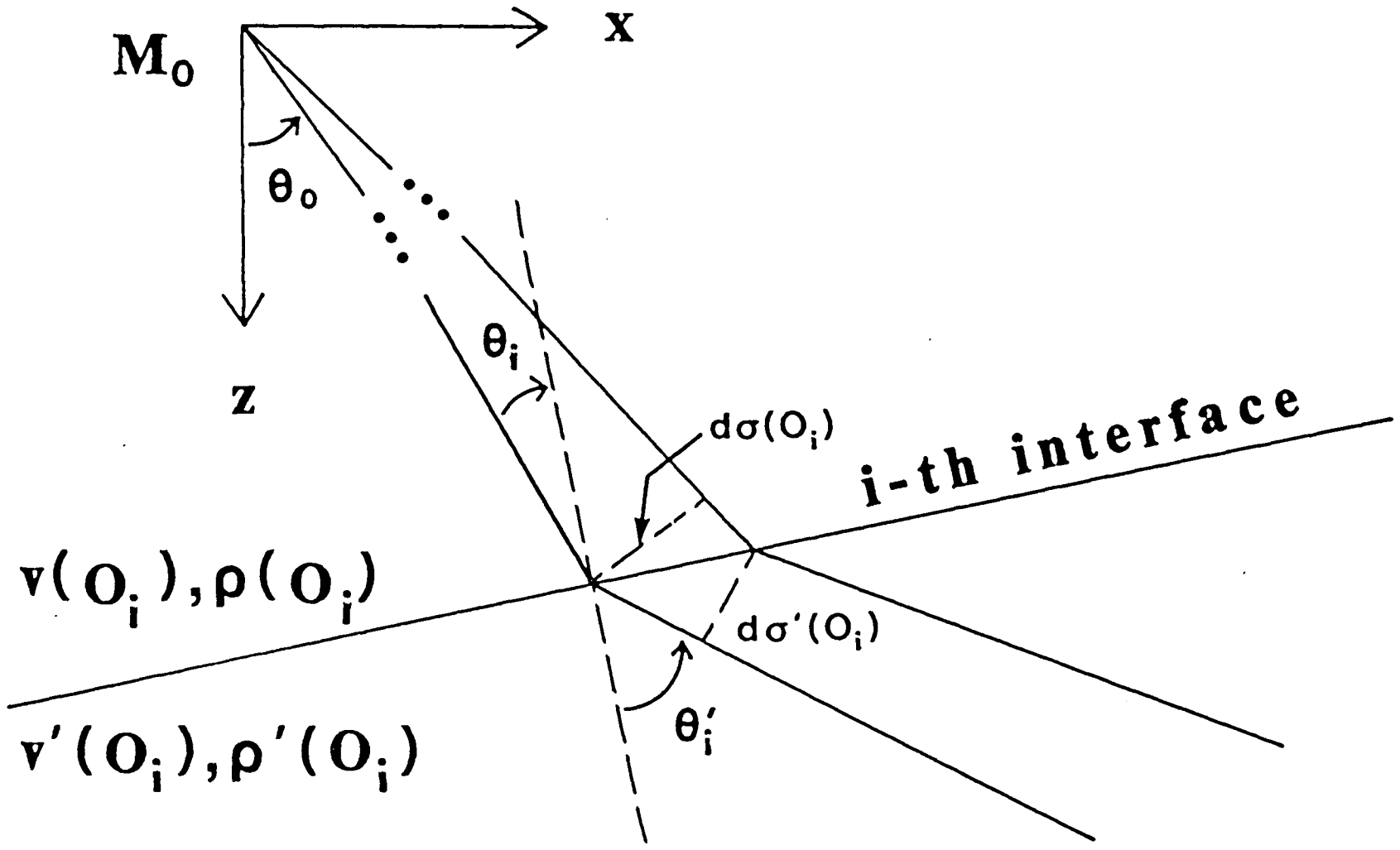

FIG. 3.1. Geometry of the ray tube at the source M_0 and at the i-th interface, where the point of intersection is O_i. The properties of the medium are laterally varying in the x-z plane but are uniform in the y-direction.

given by Cerveny and Ravindra (1971, p.74) as

$$L = \left(\frac{d\sigma(M)}{d\sigma(M_0)}\right)^{1/2} \prod_{i=1}^{N} \left(\frac{d\sigma(O_i)}{d\sigma'(O_i)}\right)^{1/2} \qquad (3.2)$$

Here, $d\sigma$ denotes the elementary ray tube area at points M, M_0, or O_i. The product term in equation (3.2) represents the influence of interfaces on geometrical spreading (see Figure 3.1). The change in ray tube area at a given plane boundary can be evaluated as the ratio of the cosine of the angle of incidence to the cosine of the angle of emergence (Cerveny and Ravindra, 1971, p.79). On the other hand, the first term in equation 3.2 represents the change in ray tube area between interfaces, which is calculated as follows. The point M_0 is commonly assumed to be on the unit sphere, within which the velocity is homogeneous, so that the elementary area on the sphere is

$$d\sigma(M_0) = \sin\theta_0 \, d\theta_0 \, d\phi_0 \qquad (3)$$

where θ_0 and ϕ_0 are the angular coordinates of the ray at the source: θ_0 is the angle measured from the vertical or z-direction, and ϕ_0 is the angle measured from the x-z plane. For a general three-dimensional velocity distribution, an element of area on the wavefront at point M is

$$d\sigma(M) = \left|\frac{\partial \bar{r}}{\partial \phi_0} \times \frac{\partial \bar{r}}{\partial \theta_0}\right| d\theta_0 d\phi_0$$

where $\bar{r}$ is the vector pointing from the source M_0 to receiver M. Cerveny et al. (1974) and Wesson (1970) obtained expressions for the time derivatives of $\partial\bar{r}/\partial\phi_0$ and $\partial\bar{r}/\partial\theta_0$, which were then integrated from known starting values to the point M. However,

for less complex velocity distributions, the expressions for $d\sigma(M)$ simplify, and analytic expressions can be used instead of time-consuming numerical integration.

With the assumption that the velocity structure is two-dimensional, varying only in the x-z plane, Marks (1980) showed that

$$d\sigma(M) = \left(\frac{\partial r}{\partial \theta_0} \cos\theta(M) d\theta_0\right)\left(\frac{\partial y}{\partial \phi_0} d\phi_0\right) \qquad (3.4)$$

Here, y is the out-of-plane coordinate and r is the magnitude of $\bar{r}$. The first factor in equation (3.4) is the width of the ray tube in the x-z plane. In our algorithm, we estimate $\partial r/\partial\theta_0$ at each departure angle θ_0 by shooting a second ray at a small angular increment $\Delta\theta_0$ greater than θ_0, and using the difference in epicentral distance Δr to calculate $\Delta r/\Delta\theta_0$. A similar procedure was followed by Marks (1980), who splined seven rays at each receiver to estimate $\partial r/\partial\theta_0$, and by McMechan and Mooney (1980), who used the two rays at successive departure angles θ_0. The second factor in equation 3.4 is the width of the ray tube in the out-of-plane direction. For a one-dimensional structure varying only in the z-direction, the quantity $g=\partial y/\partial\phi_0$ is simply the epicentral distance r, as discussed by Cerveny and Ravindra (1971, p.78). But for laterally varying media, the expression for g becomes more complex. With the second simplifying assumption that the model is parameterized in terms of blocks with constant velocity gradient, Marks (1980) solved for g by integrating an expression for dg/dt from Cerveny et al. (1974) to obtain

$$\frac{\partial y}{\partial \phi_o} = \frac{\sin\theta_o}{v_o} \sum_{i=1}^{N} \frac{v_{oi}^2(1 + \tan^2\theta_{oi}/2)}{2k_i} \left(e^{2k_i(t_i - t_{i-1})} - 1 \right) \left(1 + \tan^2\frac{\theta_{oi}}{2} e^{2k_i(t_i - t_{i-1})} \right)^{-1} \qquad (3.5)$$

where N = number of blocks

v_{oi} = velocity on entering the i-th block

k_i = velocity gradient in the i-th block

θ_{oi} = ray angle on entering the i-th block, measured with respect to the velocity gradient direction in the block

t_{i-1}, t_i = total traveltime upon entering and upon leaving the i-th block

We may express $\partial y/\partial \phi_o$ in terms of the epicentral distance calculated by the Whittall and Clowes (1979) ray tracer, by noting that the distance r_i travelled within the i-th block, measured perpendicular to the velocity gradient k, is given by (Marks, 1980)

$$r_i = \frac{v_{oi}}{k_i} \tan\frac{\theta_{oi}}{2} \left(e^{2k_i(t_i - t_{i-1})} - 1 \right) \left(1 + \tan^2\frac{\theta_{oi}}{2} e^{2k_i(t_i - t_{i-1})} \right)^{-1}$$

The above expression for r_i may be substituted into equation (3.5), after utilizing the trigonometric identity $1+\tan^2\theta_{oi}/2 = (2\tan\theta_{oi}/2)/\sin\theta_{oi}$. Equation (3.5) then reduces to

$$\frac{\partial y}{\partial \phi_o} = \frac{\sin\theta_o}{v_o} \sum_{i=1}^{N} \frac{v_{oi}}{\sin\theta_{oi}} r_i \qquad (3.6)$$

Combining equations 3.3, 3.4 and 3.6, we have

$$\frac{d\sigma(M)}{d\sigma(M_0)} = \frac{\partial r}{\partial \theta_0} \frac{\cos\theta(M)}{v_0} \sum_{i=1}^{N} \frac{v_{0i}}{\sin\theta_{0i}} r_i \qquad (3.7)$$

which is substituted into equation 3.2 for the geometrical spreading function L.

3.3.2 Head Waves

The scheme outlined above is based on the zero order asymptotic expansion, and is valid for reflected and refracted rays, including turning rays. For head waves, which represent the first-order coefficient in the ray expansion, a different scheme is used. The critical angle ray path toward and away from the head wave boundary is described by the Whittall and Clowes (1979) ray tracer in terms of circular arcs. Within each block, we divide the circular ray path into a large number of segments of equal length, and assume a constant velocity along each segment. Thus, the velocity model is re-parameterized in terms of a series of thin homogeneous layers, whose boundaries are parallel within a given block but may be non-parallel from block to block. We then apply expressions from Cerveny and Ravindra (1971, equations 5.22 and 5.29) for the amplitude of head waves in a model of homogeneous layers with plane dipping interfaces:

$$U^*(M) = \frac{\bar{v}\Gamma \tan\theta(O^*_k)}{i\omega l^{3/2} (v_k/\bar{v})^{1/2} L_1 L_2} \prod_{\substack{j=1 \\ j=k}}^{s-1} R^*_j$$

$$L_1 = \left(\frac{v_k}{v_1}\right)^{1/2} \prod_{j=1}^{k-1} \frac{\cos\theta(O^*_j)}{\cos\theta'(O^*_j)} \qquad (3.8)$$

$$L_2 = \left(1 \frac{\bar{v}}{v_1} + \sum_{j=1}^{s} \frac{l_j v_j}{v_1}\right)^{1/2}$$

where $\theta(O^*_j)$ = angle of incidence at the j-th boundary.

$\theta'(O^*_j)$ = angle of emergence at the j-th boundary.

v_j = velocity between boundaries (j-1) and j.

l_j = length of the j-th segment of the ray (j=1,2,...s).

$\bar{v}$ = velocity just below the head wave boundary (boundary k).

l = length of the ray path along the head wave boundary.

ω = estimate of dominant frequency head waves.

The head wave coefficient Γ_k is given by Cerveny and Ravindra (1971, pp. 108-109) as

$$\Gamma_k = \frac{1}{2} R^*_{13} \left(R_{31}/P_3 \right)_{\Theta=1/\bar{v}}$$

where $P_3 = (1-\bar{v}^2\Theta^2)^{1/2}$ and $\Theta = \sin\theta(O^*_k)/\bar{v}$.

R^*_{13} is the transmission coefficient at the head wave boundary for the ray incident at the critical angle, and R_{31} is the coefficient for the emergent ray.

3.3.3 Alternative Approach for Reflected and Direct Rays

Although the parameterization of the model in terms of thin homogeneous layers was made in order to calculate head wave amplitudes, the parameterization is also applicable for calculating amplitudes of reflected rays and of direct rays (i.e. refracted rays having no turning points). Thus, with very little added effort or cost, an independent check may be obtained on the reflected and direct ray amplitudes found by the previous method in which an estimate of the ray tube area is

made. For a model of homogeneous layers with plane dipping interfaces, the spreading function L is given by (Cerveny and Ravindra, 1971, equation 2.174)

$$L = \left[\left(\sum_{j=1}^{s} \frac{l_j v_j}{v_1} \right) \left(\sum_{j=1}^{s} \frac{l_j v_j}{v_1} \prod_{i=1}^{j-1} \frac{\cos^2\theta(O_i)}{\cos^2\theta'(O_i)} \right) \right]^{1/2} \qquad (3.9)$$

where s is the number of ray segments and the product factor equals 1 for j=1. This method was applied by Cassell (1982). The parameterization in terms of homogeneous layers and the use of equation 3.9 should not be applied in the case of turning rays. If a ray contains a turning point due to the velocity gradient, the ray path and its traveltime are well approximated by treating the ray as a reflection from the base of a stack of thin homogeneous layers. However, the amplitude of the turning ray is not well approximated by just the amplitude of the single basal reflection, but rather is due to constructive interference from the entire stack of layers (McMechan and Mooney, 1980; Wiggins and Helmberger, 1974).

3.3.4 Seismogram Synthesis

After amplitudes for the desired reflections, refractions and head waves are calculated, synthetic seismograms are generated by superimposing the displacements of all arrivals at a particular distance. The seismograms are produced at a set of equally spaced distances using the same algorithm as McMechan and Mooney (1980). Associated with each ray that reaches the surface is a traveltime, an epicentral distance, a complex amplitude and a traveltime branch ID number. For a given branch,

amplitude and traveltime are linearly interpolated to the desired distance. A phase-shifted impulse is then constructed by a linear combination of a unit impulse and its Hilbert transform. The seismogram synthesis is completed by convolution with an apparent source function.

3.4 Results

As a first test of the synthetic seismogram routine, ray amplitudes are calculated for a two-layer laterally homogeneous model which could represent, for example, the earth's crust over the mantle. The first layer is 30 km thick with a velocity of 6.4 km/s. The velocity at the top of the second layer is 8.0 km/s, below which is a small velocity gradient of 0.0226 km/s/km.

Figure 3.2a shows the vertical component amplitudes of rays reflected from the base of the first layer and of rays refracted in the second layer. As well, amplitudes are shown for the pure head wave that would propagate along the interface between the layers under the assumption that the velocity gradient is zero immediately below the interface; the dominant frequency of the head wave is assumed to be 6.4 Hz. Because the velocity model is one-dimensional, ART amplitudes of reflected, refracted and head waves may also be calculated directly from simple analytic expressions (Cerveny and Ravindra, 1971, Figure 6.6). As shown in Figure 3.2a, the analytic values and the values calculated by our algorithm agree very well. In this algorithm we make one of two approximations to asymptotic ray theory, depending on the type of ray. Either (1) we approximate $\partial r/\partial\theta_0$,the derivative of

FIG. 3.2. (a) Vertical component amplitudes of reflected, refracted and head waves for a two-layer model. The first layer is 30 km thick and has constant velocity 6.4 km/s; the second layer has velocity 8.0 km/s at the top and a linear velocity gradient of 0.0226 km/s/km. The head wave amplitudes, calculated for a dominant frequency of 6.4 Hz, are those that would be produced assuming that the velocity gradient is zero for a short distance immediately below the interface between the layers. The analytic values were calculated using simple expressions for a laterally homogeneous two-layer model and were taken from Cerveny and Ravindra (1971, Figure 6.6). No surface conversion coefficients have been included. (b) Vertical component amplitudes for the two-layer model using the algorithms of McMechan and Mooney (1980) and Cassell (1982).

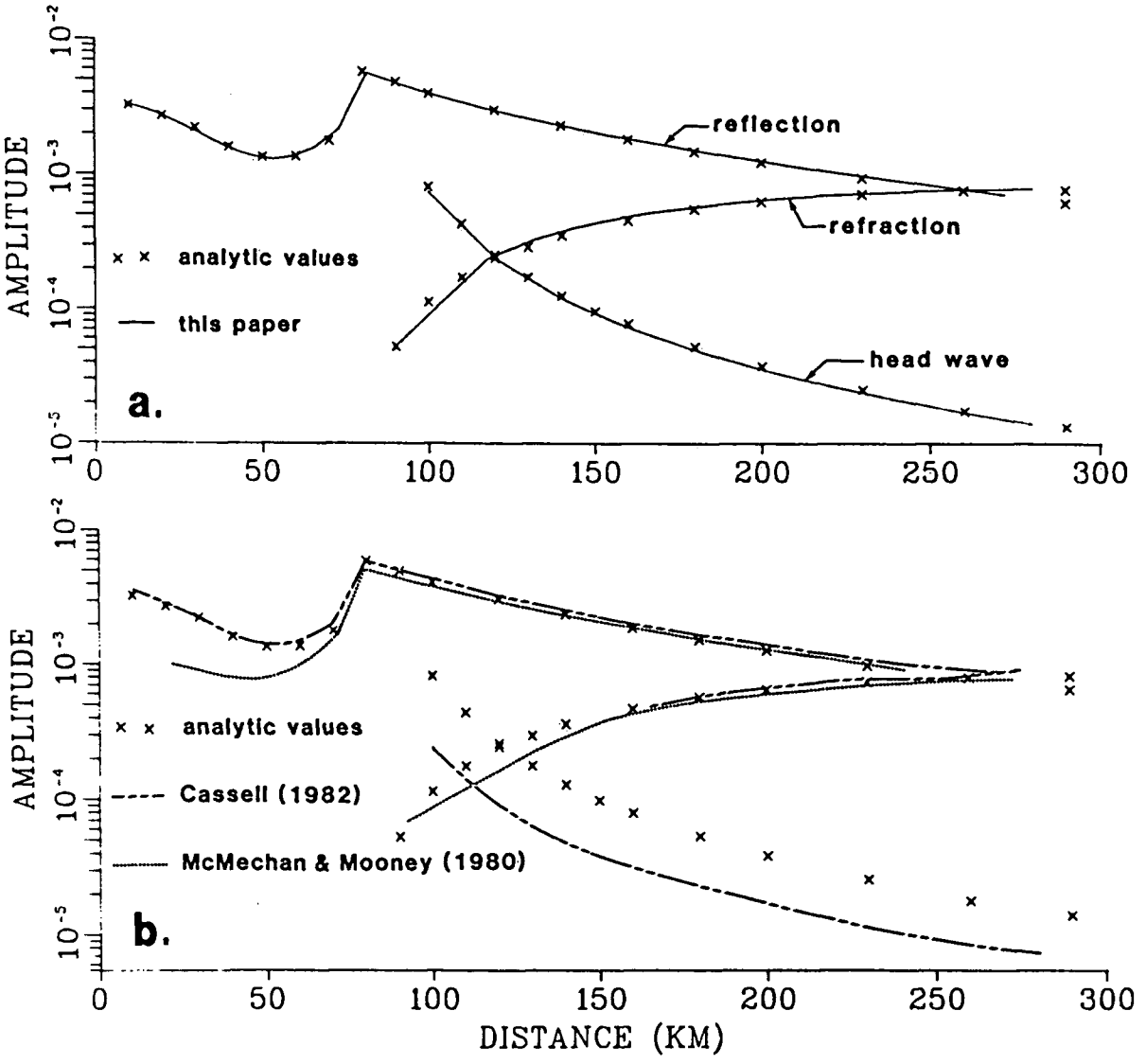
AMPLITUDE
10^{-2}
10^{-3}
10^{-4}
10^{-5}
reflection
refraction
head wave
× × analytic values
this paper
a.
0
50
100
150
200
250
300
AMPLITUDE
10^{-2}
10^{-3}
10^{-4}
10^{-5}
× × analytic values
---- Cassell (1982)
McMechan & Mooney (1980)
b.
0
50
100
150
200
250
300
DISTANCE (KM)

range with respect to starting angle, by estimating its value from two neighboring rays or (2) we approximate a smooth velocity gradient in a block by a large number of thin homogeneous layers. The agreement between the analytic values and those calculated by our algorithm thus assures that the effect of our approximations to ART is minimal.

Figure 3.2b shows amplitudes for the two-layer model calculated using the algorithms of McMechan and Mooney (1980) and Cassell (1982). The amplitude values for the Cassell routine, which was recently updated, were supplied by Cassell (pers. comm., 1983). For both algorithms, the amplitudes of the refracted waves and of the wide-angle reflections agree quite well with the analytic values. However, the pre-critical reflection amplitudes for the McMechan and Mooney algorithm diverge from the analytic values, the difference becoming greater as the distance becomes less. Part of this difference is due to different values calculated for the pre-critical reflection coefficients, which possibly arises because the McMechan and Mooney routine uses a different velocity/density relationship than the one used in this paper (McMechan, pers. comm., 1983). Head waves are not computed by the McMechan and Mooney method. The amplitudes of the head waves calculated by the Cassell algorithm are different from the analytic values in Figure 3.2b. Cassell's values underestimate the analytic values by a nearly constant factor of about 2.5. This difference arises because Cassell (1982) uses an approximation for the head wave geometrical spreading function, and not the exact expressions from Cerveny and Ravindra (1971).

For a more complex laterally homogeneous model, an additional check of our algorithm compares the amplitudes with those calculated by the reflectivity method. Since the reflectivity method produces the full wave response from the model, the comparison also tests the validity of the approximations inherent in asymptotic ray theory. The velocity model used is the HILDERS model (Figure 3.3a) of Fuchs and Müller (1971). Reflectivity seismograms, shown in Figure 3.3c, were originally calculated for this model by Fuchs and Müller (1971) and have been used as a basis of comparison in the ART methods of Cerveny et al. (1977), McMechan and Mooney (1980) and Cassell (1982). To determine the reflectivity response, the velocity gradient in the depth range 11-27 km was represented by a stack of 10 homogeneous layers, and the deeper gradient in the depth range 34-36 km was represented by 3 layers. The CPU time required to calculate the reflectivity seismograms on an Amdahl 470 V/8 was approximately 3 minutes.

In Figure 3.3b the seismograms calculated by our procedure are displayed. The calculation took approximately 14 seconds of CPU time on the Amdahl 470 V/8. The agreement with the reflectivity seismograms (Figure 3.3c) is satisfactory for interpretational purposes. The seismograms produced by our algorithm are also consistent with those produced by other ART algorithms. However, for any ART algorithm, ray theory itself is inherently limited, and so some differences exist compared to the reflectivity results. For example, a cusp appears on the ART section at approximately 4.5 s and 160 km (point C), where the amplitudes change abruptly from a large value to zero at greater

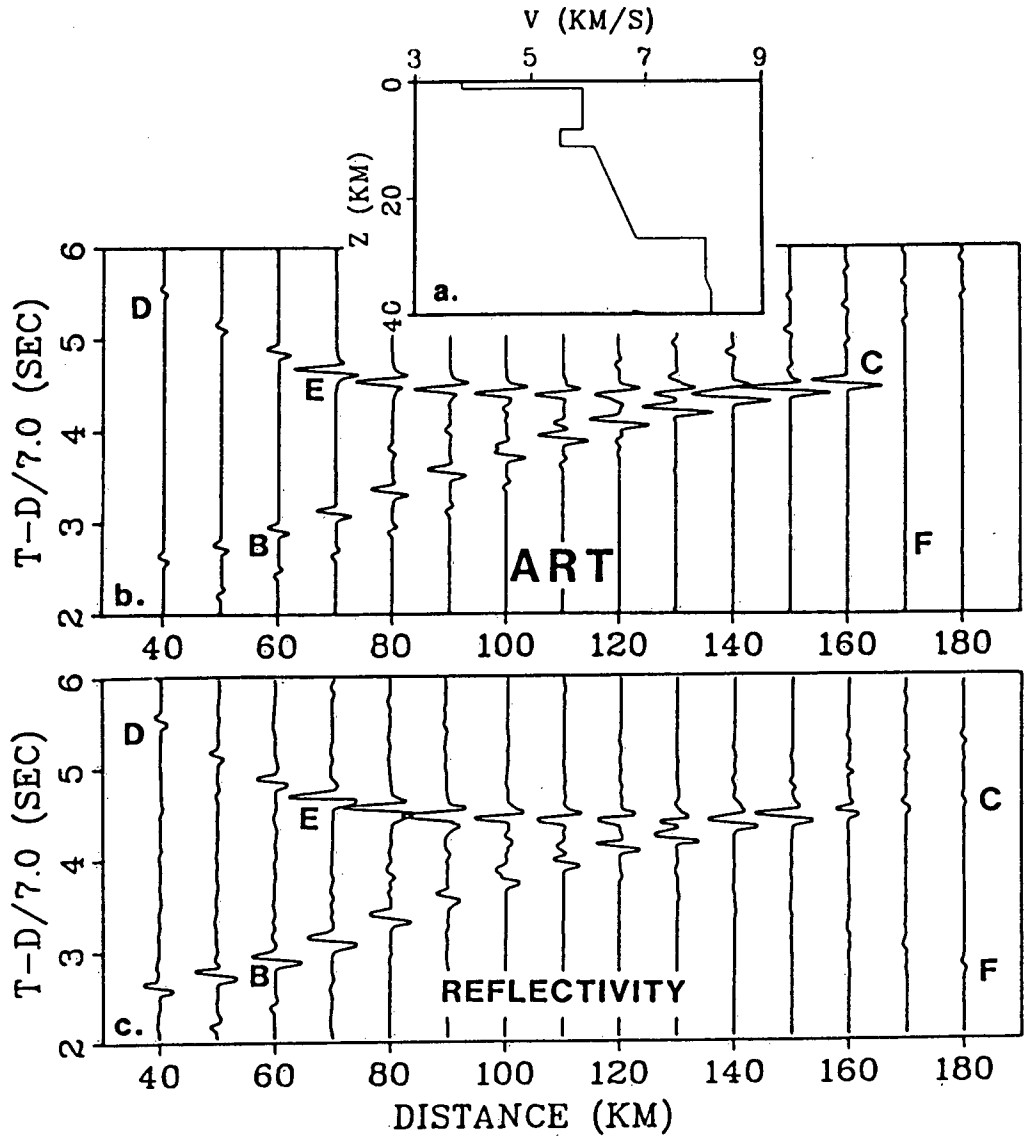

FIG. 3.3. Synthetic seismograms for the HILDERS velocity-depth model (a). Response shown in (b) is the synthetic section calculated by our ART method, while that in (c) is calculated by the reflectivity method. All traces are multiplied by a factor proportional to their distance.

distances. On the reflectivity section the amplitude is smaller at 160 km and is non-zero at greater distances. The cusp in ART occurs when the branch of rays reflected from the interface at 27 km depth (branch CD) joins the branch of turning rays in the gradient zone above 27 km (branch BC). The turning ray which just grazes the interface corresponds to a sharp termination of the branches in ART but not in wave theory, where non-Fermat rays are present in the "shadow zone". A second difference between the ART and reflectivity sections concerns the small amplitude branch (EF) from approximately 120 to 180 km with velocity of about 8.0 km/s. On the reflectivity section, the amplitude of the branch increases with distance. The amplitudes are due to pre-critical reflections from the layers approximating the deeper gradient at 34-36 km depth. On the ART section, the branch EF has been modelled simply as a head wave along the interface at 27 km depth, and so the amplitude decreases with distance. That is, there is no effect present on the ART section due to the deeper gradient structure, since turning rays within this zone only reach the surface at distances greater than 190 km. However, by replacing the gradient zone by one or more small step discontinuities, the ART algorithm could also generate pre-critical reflections at distances less than 190 km, for which amplitudes increase with distance; this was done by Cassell (1982) and Cerveny et al. (1974). Alternatively, the 8.0 km/s branch could be modelled for interpretational purposes as turning rays produced by a weak velocity gradient in the entire region below 27 km depth.

In Figure 3.4, rays and vertical component amplitudes are

displayed for a simple laterally varying model. The model (Figure 3.4a) consists of a block of constant velocity 5.0 km/s next to a dipping layer in which the velocity at the upper dipping boundary is 6.0 km/s. The dipping layer has a constant velocity gradient of 0.08 km/s/km perpendicular to the boundary. The model is actually laterally homogeneous but has been tilted clockwise from the vertical by 30°. The calculation of ray amplitudes thus exercises the two-dimensional aspects of our algorithm, and the amplitude values have been checked against exact ART analytical values determined for the corresponding one-dimensional model. As shown in Figure 3.4b, the agreement is excellent, the program-calculated values differing from the analytic values by less than 0.1% for the set of rays shown in Figure 3.4a.

A more complex laterally varying model, the Imperial Valley model discussed in McMechan and Mooney (1980), is shown in Figure 3.5. In the ray tracing routine employed by McMechan and Mooney (1980), lateral as well as vertical velocity gradients are allowed. In the Whittall and Clowes (1979) ray tracing routine utilized in our algorithm, the velocity gradients within a given block are uniform and perpendicular to one of the block boundaries. Thus the lateral velocity gradients in the Imperial Valley model are approximated in Figure 3.5 by crudely dividing each of the 3 top layers into either 2 or 3 blocks.

In Figure 3.6a, we display ray paths through our Imperial Valley model, and in Figure 3.6b the corresponding synthetic seismogram section calculated by our algorithm is shown. Figure 3.6c contains the synthetic seismograms for the Imperial Valley

FIG. 3.4. (a) Ray tracing diagram for a simple two-dimensional model. The two dashed lines represent the boundaries of a layer dipping at 30°, within which the velocity increases linearly from 6.0 km/s at the upper boundary to 8.0 km/s at the lower boundary. The region above the dipping layer has constant velocity 5.0 km/s. The model is actually laterally homogeneous but tilted from the vertical by 30°. (b) Vertical component amplitudes for the model in (a). The solid line represents the amplitudes calculated by the two-dimensional synthetic seismogram routine. The crosses are the exact ART values determined for the equivalent laterally homogeneous model using simple analytic expressions. Amplitudes, which are relative to the amplitude on the unit sphere, should be multiplied by 10^{-3}.

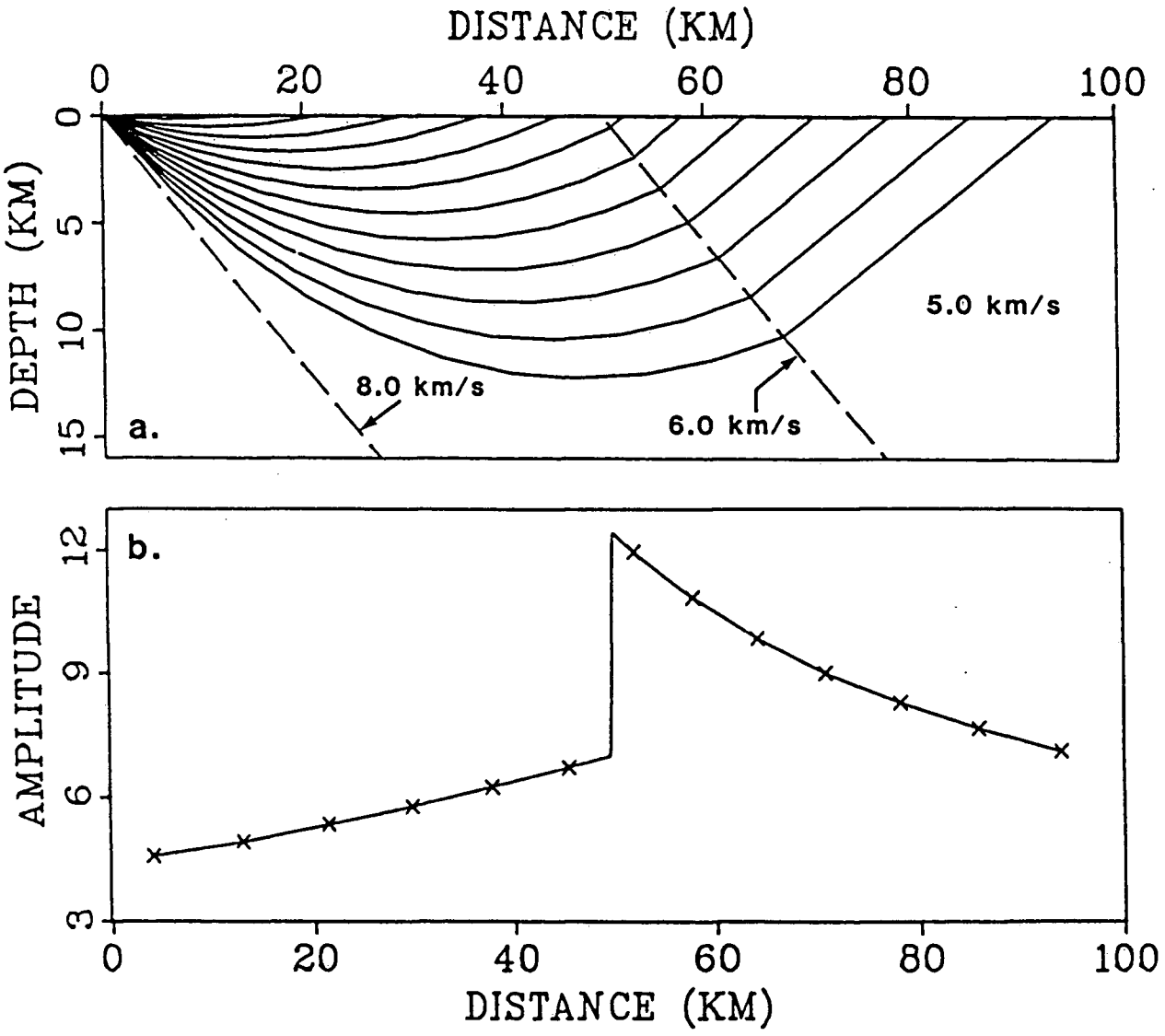
DISTANCE (KM)
0
20
40
60
80
100
DEPTH (KM)
0
5
10
15
a.
5.0 km/s
8.0 km/s
6.0 km/s
b.
AMPLITUDE
3
6
9
12
0
20
40
60
80
100
DISTANCE (KM)

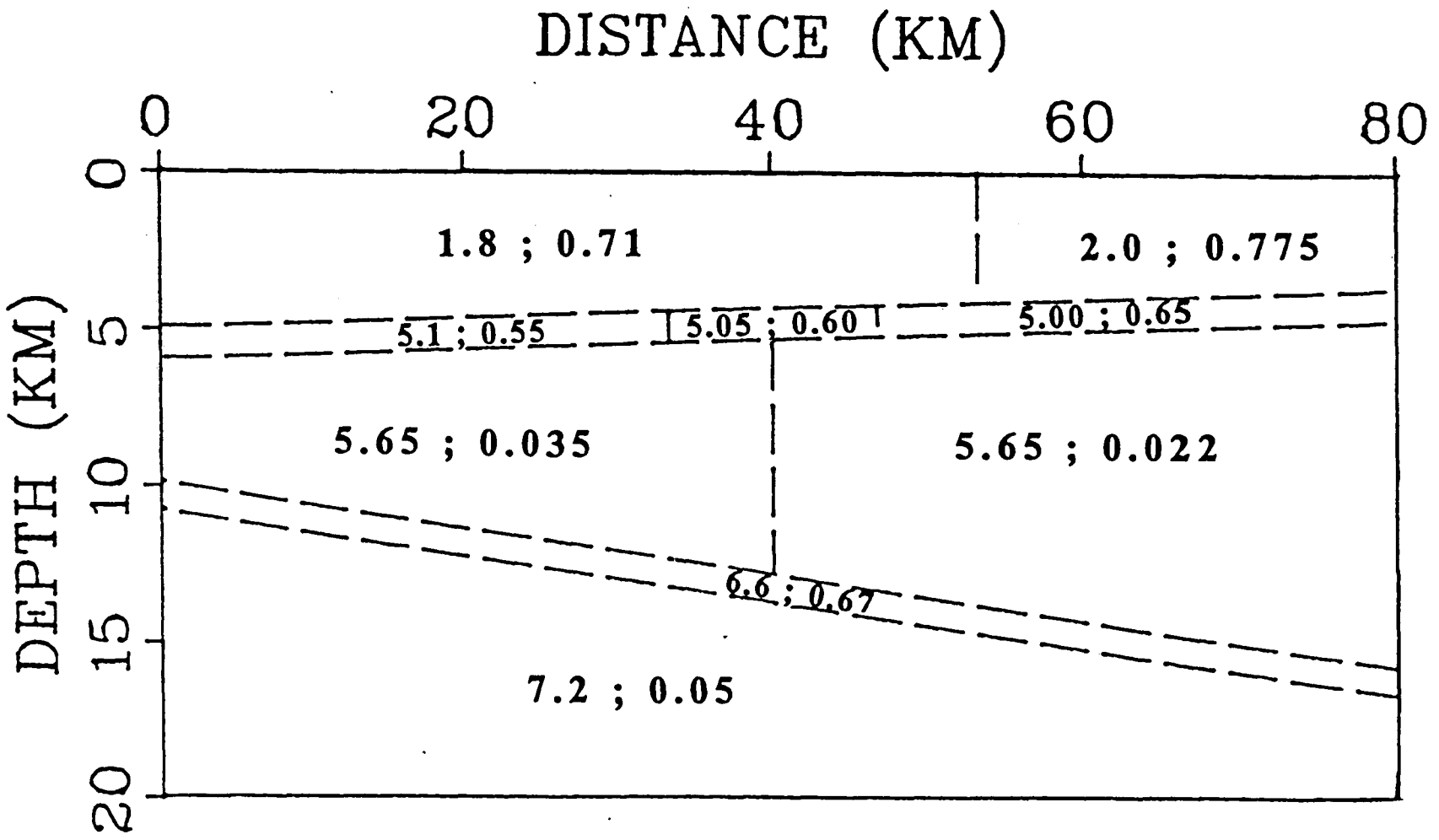

FIG. 3.5. The Imperial Valley model similar to that used by McMechan and Mooney (1980). Lateral velocity gradients in the top 3 layers have been approximated by dividing each layer into blocks. Velocities (km/s) are given for the top of each layer followed after the semicolon by the velocity gradient (km/s/km).

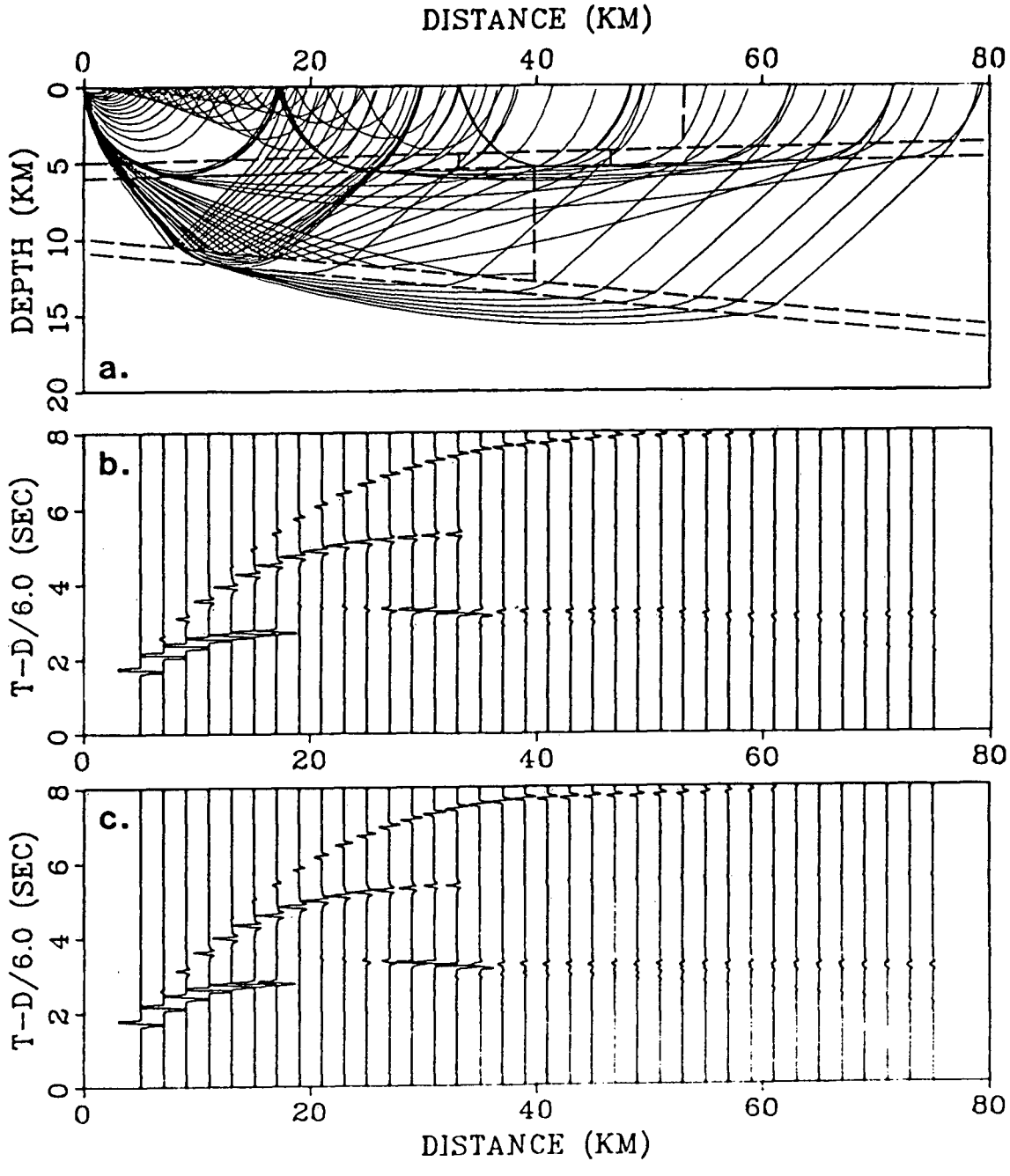

FIG. 3.6. (a) Ray paths through the Imperial Valley model of Figure 3.5. (b) Synthetic seismograms calculated by our algorithm. (c) Synthetic seismograms calculated by the routine of McMechan and Mooney (1980) for their Imperial Valley model, in which laterally varying velocity gradients are allowed. Amplitude scaling in (b) and (c) is proportional to square root of distance.

model calculated by the routine of McMechan and Mooney (1980). The seismograms determined by our routine (Figure 3.6b) agree closely with those determined by the McMechan and Mooney (1980) algorithm (Figure 3.6c). The corresponding CPU times to calculate ray amplitudes on an Amdahl V/8 were 5 seconds and 19 seconds respectively, with an additional 8 seconds for each to produce the seismograms. The types of arrivals modelled include pre- and post-critical reflections, turning rays in 5 layers, and the free-surface multiples PP and PPP.

An important aspect of the synthetic seismogram algorithm is that it allows the modelling of complex structures. An example is shown in Figure 3.7. The data upon which the model is based and preliminary interpretations of the data are discussed in Ellis et al. (1983) and Clowes et al. (1983b). The main purpose of presenting this example is not to show agreement between observations and synthetics or to discuss the interpretation, but rather to illustrate the type of lateral changes in structure that can arise in seismic refraction interpretations, especially in regions where tectonic activity has occurred. The model in Figure 3.7 depicts the subduction zone across the margin between the oceanic Juan de Fuca plate and the continental America plate in the region of Vancouver Island. The large two-dimensional variations in structure are necessary because of the great difference between oceanic and continental crustal thicknesses, each of which is controlled within limits by other independent interpretations. The most important features of the model are thus the details of the transition between oceanic and continental crusts. These

FIG. 3.7. (a) Schematic diagram of the subduction zone between the oceanic Juan de Fuca plate and the continental America plate in the region of Vancouver Island. The range of velocities in km/s is indicated for each layer. The diagram does not include the details of all layers or blocks that were used for the ray tracing. (b) Ray tracing diagram for the Vancouver Island subduction model. (c) Synthetic seismograms for the subduction model. Far-offset arrivals are reflections from the dipping upper mantle horizon. Near-offset arrivals include turning rays in the upper mantle, and large upper mantle reflections as secondary arrivals.

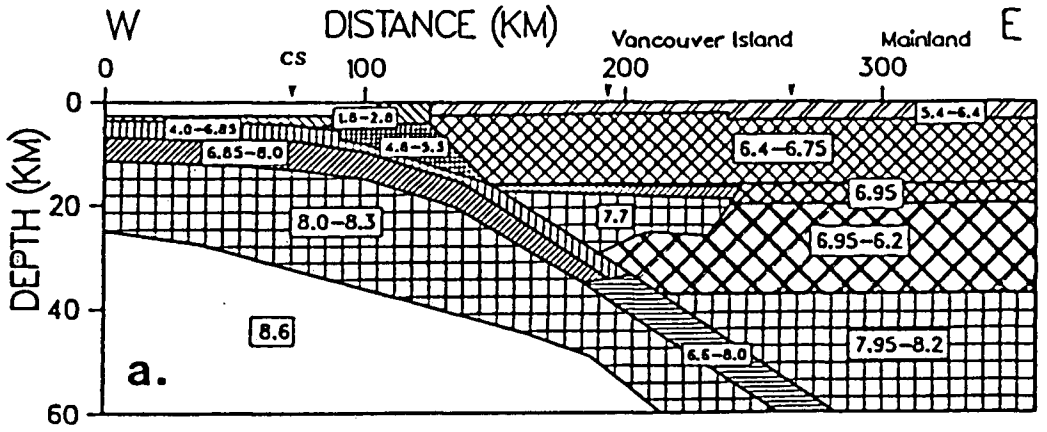
W
DISTANCE (KM)
E
CS
Vancouver Island
Mainland
0
100
200
300
DEPTH (KM)
0
20
40
60
1.6–2.8
4.0–6.85
4.6–5.3
6.85–8.0
8.0–8.3
8.6
5.4–6.4
6.4–6.75
6.95
7.7
6.95–6.2
6.6–8.0
7.95–8.2
a.

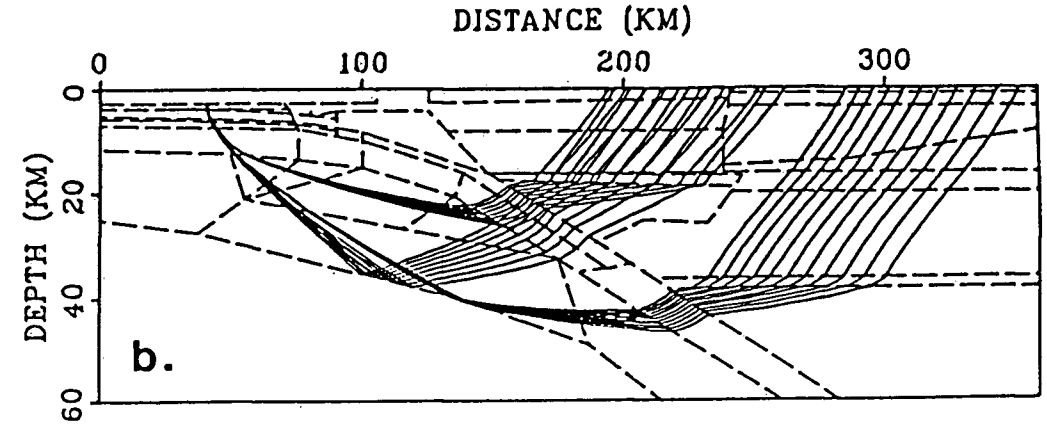
DISTANCE (KM)
0
100
200
300
DEPTH (KM)
0
20
40
60
b.

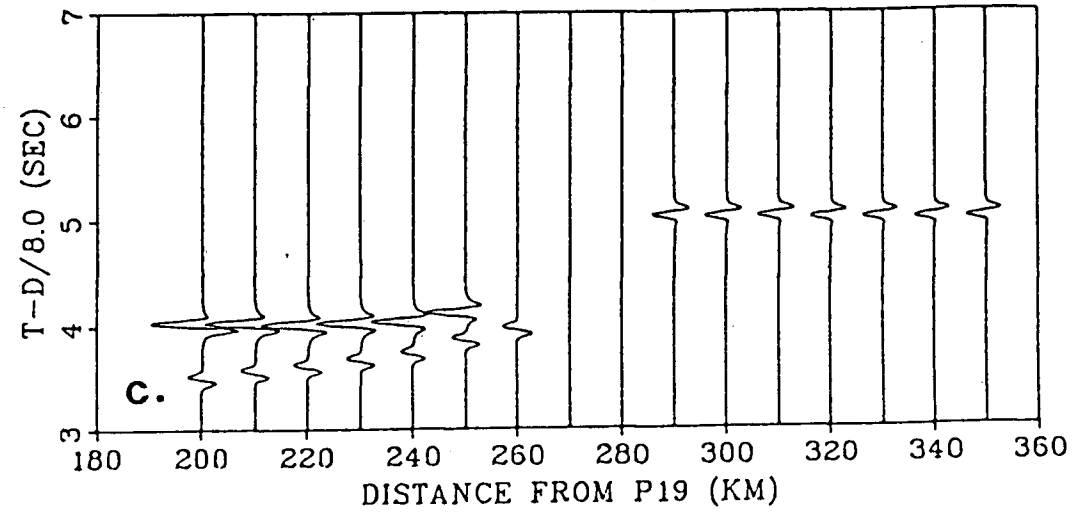
T–D/8.0 (SEC)
7
6
5
4
3
c.
180
200
220
240
260
280
300
320
340
360
DISTANCE FROM P19 (KM)

include: (1) the shallow-dipping high-velocity finger (7.8 km/s) at 20-26 km depth over the distance range 150-240 km, and (2) the upper mantle velocities of 8.0-8.3 km/s below the subducting oceanic crust. The subducting oceanic crust is itself not well-defined, since all rays take a similar amount of time to pass through it and this time is only a small portion of the total traveltime. Only three types of rays - two sets of reflections and one set of turning rays - are traced (Figure 3.7b) because these represent the arrivals of most interest for the interpretation. The resultant seismograms are thus very simple (Figure 3.7c), but model the kinematic and dynamic characteristics of the observed data reasonably well.

3.5 Discussion

A fast, practical method of calculating asymptotic ray theory amplitudes has been implemented utilizing an efficient technique for ray tracing through laterally varying structures. The types of arrivals which may be modelled include head waves, refractions, pre-critical and wide-angle reflections, surface reflections and multiples. Amplitudes calculated by this method in a one-dimensional medium are consistent with those determined by the reflectivity method, with the exception of certain types of arrivals arising from wave phenomena which any asymptotic ray theory method cannot directly handle. However, this limitation is overshadowed by the capability of the routine to be applied in two-dimensional structures.

The routine is intended as a practical tool for use by interpreters of seismic refraction data. In comparison with

other asymptotic ray theory methods, the major advantages of the algorithm are its speed and ease of use. These characteristics arise because of the nature of the velocity model, which is defined by arbitrary polygonal blocks, each with its own velocity and linear velocity gradient. Such model specification is particularly appropriate for some types of tectonic features, e.g. wedges or fault blocks. On the other hand, the parameterization is somewhat limiting for models where the velocity or its gradient vary continuously in a lateral sense, e.g. a passive continental margin problem. However, such models can be adequately approximated by several laterally adjacent blocks. A scheme which automatically divides a block into several sub-blocks could be incorporated into the program without great difficulty.

A number of modifications to the algorithm could be implemented to further enhance its applicability. To compensate for limitations in ray theory, it is possible to incorporate additions to ART which account for certain types of wave behavior. These include corrections to ray theory amplitudes in the region of critical points and caustics, and high frequency approximations for waves such as diffractions. On a more practical basis, the program could be adapted for interactive use, where speed is a primary requirement. Changes to the input velocity structure could thus be made even more quickly, and the effect of the change on the amplitude and traveltime behavior seen within a few seconds.

CHAPTER 4. INTERPRETATION OF ONSHORE-OFFSHORE PROFILE ACROSS VANCOUVER ISLAND

4.1 Introduction

Seismic refraction line I was directed across the strike of the British Columbia continental margin (see Fig. 1.3). The onshore-offshore line provides the basic data to test the structural model of Riddihough (1979), in which the oceanic Juan de Fuca plate subducts beneath the continental America plate. Seventeen shots (the P series) were fired over the continental slope and ocean basin, and were recorded on an array of 32 land seismographs located on Vancouver Island and the British Columbia mainland. An additional two shots separated by ~7 km (shots J1 and J2) were fired at shot points near the eastern end of the profile. For the oceanic shots, the minimum shot-receiver distance was 93 km and the maximum was 350 km. Since oceanic crust typically has a thickness of about 10 km or less, rays from the oceanic shots are expected to travel through upper mantle material for at least a portion of their paths. Thus, the interpretation of line I provides information about upper mantle velocity and the location of the contact between upper mantle and crustal material.

The distribution of shots and receivers along line I allows a two-dimensional interpretation to be made of the subduction zone velocity structure. In this thesis, data are displayed either as common shot gathers or common receiver gathers. In common shot gathers, recordings on all 32 receivers from a

particular shot are shown and the variation in the data from receiver to receiver tends to provide information about the structure beneath the receivers. On common receiver gathers, the seismograms from all 17 shots recorded on a particular receiver are displayed; in this case the variation from shot to shot tells us more about the structure beneath the shots. Furthermore, we may already have independent information about the uppermost layers beneath the shots and beneath the receivers, so the interpretation is then reduced to finding the variation in the structure of the deeper layers.

For the interpretation of the onshore-offshore portion of line I, the uppermost layers about which information is known include much of the oceanic crust (Waldron 1982) and a portion of the continental crust (McMechan and Spence 1983). For the oceanic crust, the structure to about 9 km depth was relatively well-determined beneath the deep oceanic basin and somewhat less constrained under the continental slope, where thick sediments and a possible low-velocity melange were found. For the continental crust, the structure was controlled at its intersection point with line IV, which was roughly parallel to the continental margin and perpendicular to line I (Fig. 1.3). Here, the upper continental crust was well-determined to a depth of about 20 km while the lower continental crust was poorly constrained. The preferred interpretation for the lower crust included a low-velocity zone and a crustal thickness of 37 km; however, alternative interpretations allowed the thickness to be as large as 52 km.

4.2 Interpretation of shots J1 and J2

Shots J1 and J2, which were detonated in a deep inlet and recorded on the land receivers, provide additional control for the continental crustal structure. Since the maximum shot-receiver offset was less than 170 km, only upper crustal information is obtained from these shots. The seismic section for shot J1 is shown in Figure 4.1b; amplitudes are multiplied by a factor proportional to distance. The section for shot J2 is very similar (see Appendix 1, Fig. A1.1), although there appears to be some indication of clipping even on some of the more distant traces. For both shots J1 and J2, the shots and receivers have been corrected to sea level by using a replacement velocity of 5.5 km/s for both the water-column and the near surface material at the receivers. Because of the similarity of the shot J1 and J2 record sections, an interpretation for the shot J1 data will also be valid for the shot J2 data.

A preliminary interpretation of first arrival traveltimes for shot J1 was presented in Ellis et al. (1983). An initial one-dimensional starting model was determined by a linear programming inversion of the first arrival times (Garmany et al. 1979). The initial model was then modified using the two-dimensional ray tracing routine of Whittall and Clowes (1979), for which the preferred model of McMechan and Spence (1983) was incorporated west of the intersection point of lines I and IV.

The interpretation of shot J1 presented in Ellis et al. (1983) has been further refined in an effort to model amplitudes and to account for secondary arrivals. In particular, an attempt

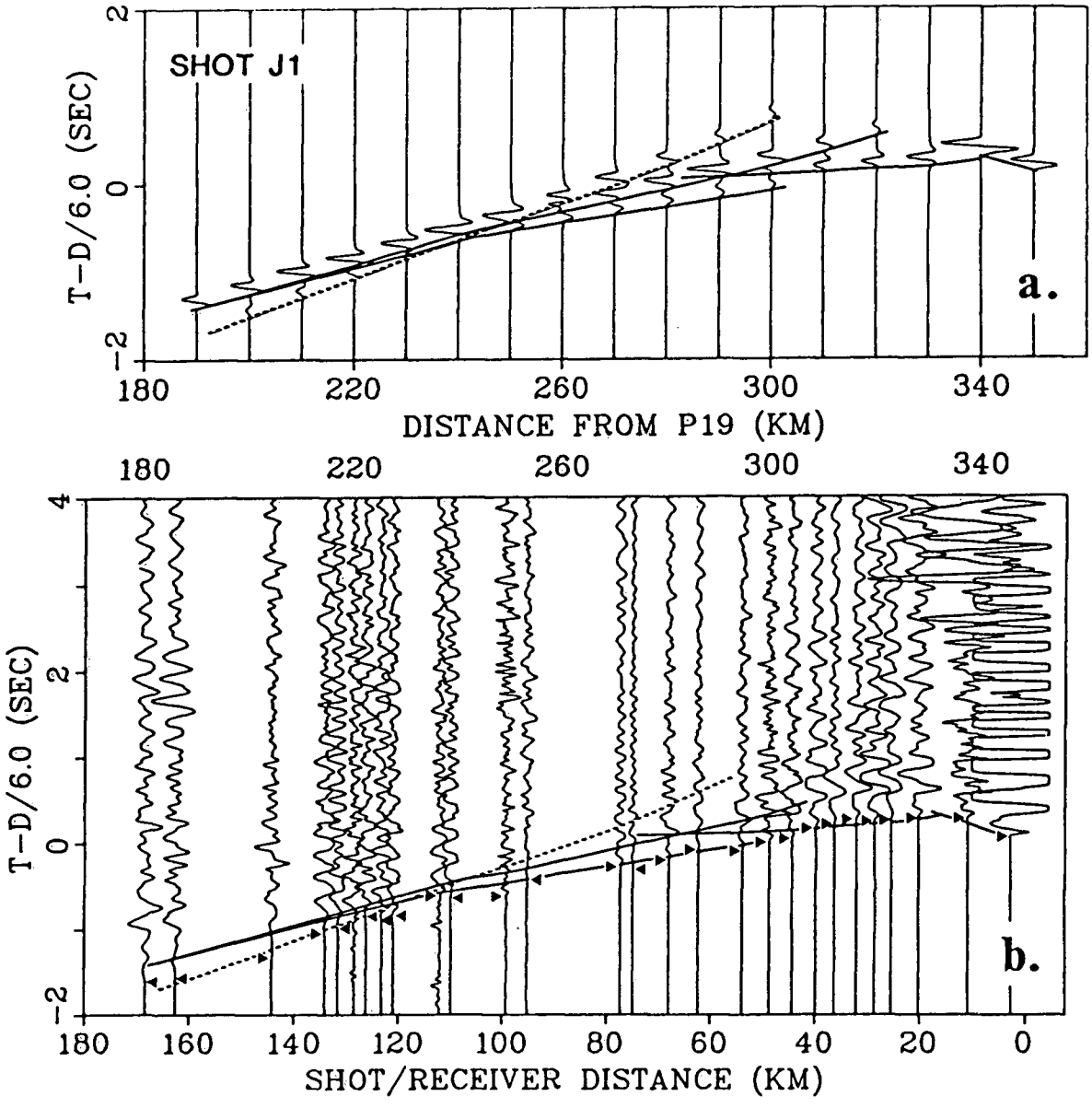

FIG. 4.1. Synthetic seismograms and observed data for shot J1, which is located on the right hand side of the sections. The first arrival traveltime picks are indicated by arrowheads. The theoretical traveltime curve from the synthetic seismograms is superimposed on the observed record section. The dashed line corresponds to reflections from the base of the 6.7 km/s constant velocity layer in Fig. 4.2. All amplitudes have been multiplied by a factor proportional to distance. The distance scale in (a) and the top scale in (b) are measured relative to shot P19, the westernmost of the P series shots in the deep ocean.

was made to model the low-amplitude first arrivals and the higher amplitude second arrivals occurring at distances from shot J1 greater than about 110 km (Fig. 4.1b). The apparent velocity of the first arrival phase, which is denoted by a dashed line in Figure 4.1, is about 6.7 km/s while the apparent velocity of the secondary phase is about 6.5 km/s. A similar set of arrivals, but with velocities 6.9 km/s and 6.75 km/s, had been found for some of the Vancouver Island shots along line IV (McMechan and Spence 1983).

The final velocity model for shot J1 is shown in Figure 4.2a. West of 240 km, the McMechan and Spence (1983) interpretation is incorporated in the model, except for the portion below ~16 km which originates from the interpretation of the P series shots considered in the following section. In Figure 4.2b, rays are traced throughout the model, and the theoretical model traveltimes are superimposed on the J1 record section in Figure 4.1b. Synthetic seismograms corresponding to the traced rays were calculated using the routine described in Chapter 3 of this thesis and by Spence et al. (1984), and are displayed in Figure 4.1a.

In the interpreted model, the velocity of the near surface material is 5.3 km/s, somewhat less than that determined on Vancouver Island by McMechan and Spence (1983). The velocity of the upper layers is determined by the first arrivals at receivers near shot J1. This portion of the model is poorly constrained because ray paths were not reversed in this region and because the receivers were far from the intersection with line IV, where some two-dimensional control was available. For

FIG. 4.2. Velocity model determined from shot J1 data, and ray paths traced through the model. Interpretation of McMechan and Spence (1983) to a depth of 16 km is used west of 240 km distance. Details in the model below that depth are derived fom interpretation of the P series shots. Distances are measured relative to shot P19, the westernmost shot in the deep ocean basin. The arrowheads indicate the west and east coasts of Vancouver Island. Velocities (km/s) are given for the top of each block, followed after the colon by the velocity gradient (km/s/km) if one was used.

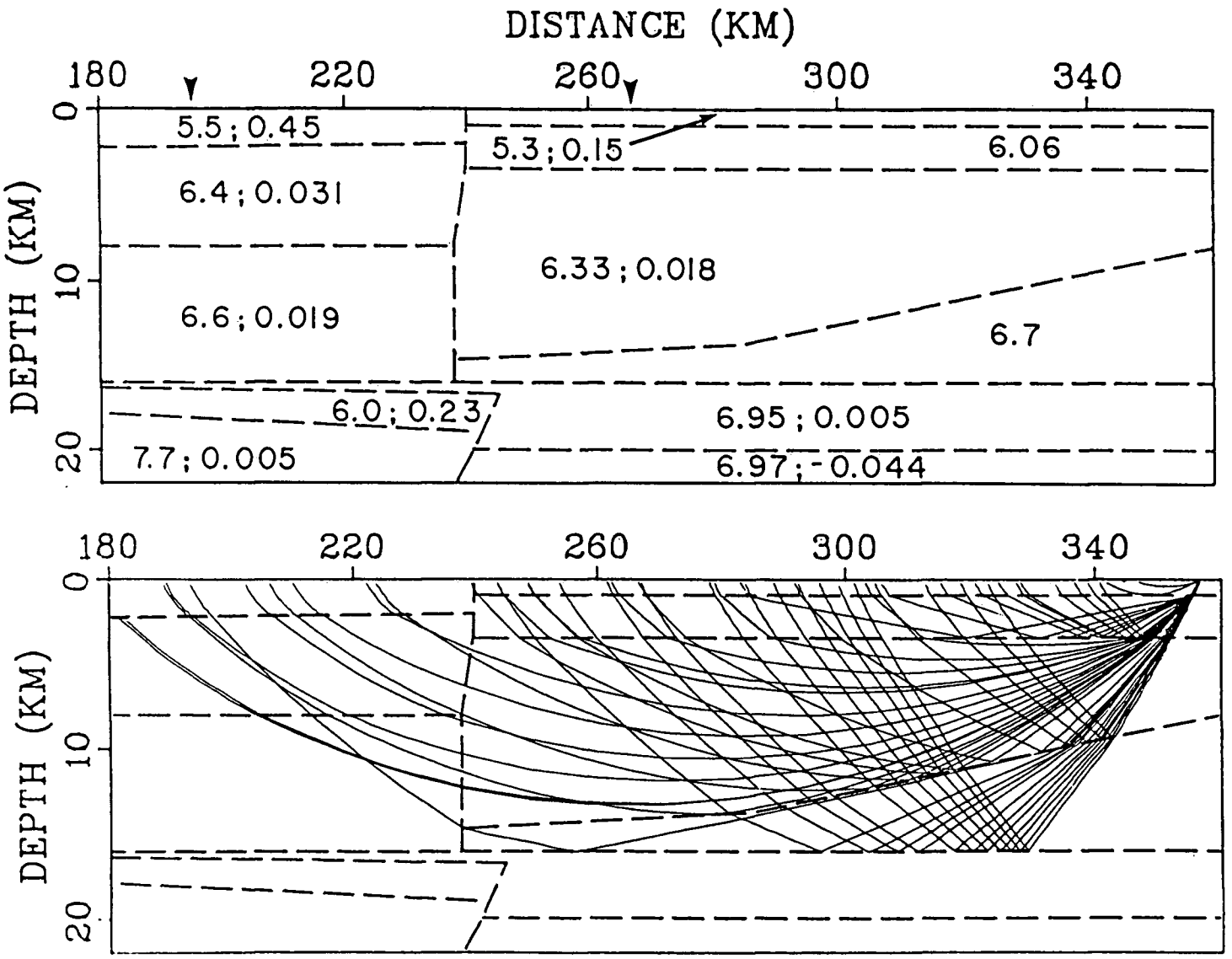
DISTANCE (KM)
180
220
260
300
340
0
10
20
DEPTH (KM)
5.5 ; 0.45
6.4 ; 0.031
6.6 ; 0.019
5.3 ; 0.15
6.06
6.33 ; 0.018
6.7
6.0 ; 0.23
7.7 ; 0.005
6.95 ; 0.005
6.97 ; -0.044

simplicity, the region from 1.0 km to 3.5 km was modelled as a constant velocity layer with velocity just over 6 km/s, so that arrivals in the distance range of 20-50 km from J1 corresponded to reflections from the bottom of this layer. But because of the indeterminacy, different velocity structures would also be valid; for example, the upper 3 or 4 km of the model could have been modelled equally as well by a layer with constant velocity gradient, with the first arrivals corresponding to turning rays.

Below 3.5 km depth in the interpreted model, the velocity increases from 6.33 km/s with a velocity gradient of 0.018 km/s/km. Turning rays in this region form the first arrivals in the distance range of 50-120 km from J1, and are the secondary, large amplitude arrivals past 120 km.

The interpretation of the small amplitude primary arrivals past 120 km is somewhat speculative. They were interpreted in a fashion similar to that employed by McMechan and Spence (1983) for line IV on Vancouver Island. There, a small amplitude first arrival phase with velocity 6.95 km/s was modelled as turning rays below a discontinuity at 16 km depth, across which the velocity increased from 6.75 km/s to 6.95 km/s (Fig. 1.5). For shot J1, a discontinuity is similarly inferred, across which velocity increases from 6.4-6.5 km/s to 6.7 km/s, and the small amplitude phase is interpreted as a set of arrivals which turn back to the surface within the region of 6.7 km/s velocity. In the ray tracing diagram of Figure 4.2b, these arrivals are for convenience modelled as <u>reflections</u> from the bottom of the 6.7 km/s velocity region; but with a small gradient in the region, the corresponding turning rays to the greater offset distances

would also have small amplitudes and almost the same traveltimes as the reflections.

The top of the 6.7 km/s constant velocity zone is inferred to be shallower in the east than in the west. The depth in the east is 8 km and is controlled by the location of the crossover point between the primary and secondary arrivals which occurs 120 km from the shot (at 240 km in the model of Figure 4.2). If the depth was greater, then the traveltimes for the reflections would be greater, and the crossover point would be at an even greater distance from the shot. The discontinuity needs to be deeper at its western end because the large amplitude turning rays above the boundary, which are present in the data out to the maximum shot-receiver offset, need to penetrate to depths near 14 km.

The top of the 6.7 km/s velocity region has been modelled as a discontinuity, but could just as well be a narrow gradient zone. On the synthetic record section (Fig. 4.2a), the reflections from the discontinuity are sufficiently close in traveltime to the turning rays above the discontinuity that their waveforms overlap. That is, the reflections are not expected to form a very distinct phase which can be easily identified on the observed record section (Fig. 4.2b), and thus there is not direct support for the existence of the discontinuity. This contrasts with the evidence on Vancouver Island for the existence of the discontinuity at ~16 km depth in the interpretation of McMechan and Spence (1983), where reflections were more easily picked on some (though not all) of the observed record sections.

Perhaps one of the more interesting features of the J1 data set is what is not seen in the data: no major offset or perturbation of traveltimes or amplitudes is observed on crossing the Strait of Georgia, which corresponds to the distance range 60-95 km from shot J1 (Fig. 4.1b). This implies that down to a depth of almost 14 km there is no evidence for a major velocity discontinuity across Georgia Strait. Thus, the inferred fault (Muller 1977) separating the Coast Plutonic Complex on the mainland from the Insular Belt on Vancouver Island is not observable in terms of velocity contrast. An interpretation of a detailed sonobuoy refraction survey across Georgia Strait (White and Clowes 1984) also concluded that there was no seismic evidence for such a fault down to depths of 3 to 4 km.

4.3 Description of P series shots

The 17 P shots were corrected for sea bottom topography and detonation depth by placing all shots at an equivalent datum depth of 2600 m. In addition to a time correction, this also involved a distance offset of each shot toward the receivers. The corrections were found by ray tracing from each shot to the datum depth through the model of Waldron (1982), who determined the sedimentary structure along the marine portion of line I using CSP and OBS data. The topographic variation was only significant for the first six shots on the continental slope (shots P1 to P6) where the water depth ranged from 500 to 2100 m; for the remaining shots in the ocean basin (P8 to P19), depths were between 2425 and 2625 m. Variation in topography at

the receivers was corrected in the same manner as for shot J1, by adjusting receiver elevation to sea level using a velocity of 5.5 km/s.

A correction for basement topography and varying thickness of sediments was also calculated for the 11 shots in the ocean basin, where the sedimentary structure down to the basement was well-determined in the interpretation of Waldron (1982). The corrections were found by equalizing the sediment thickness to 1 km and the sediment velocity to 1.8 km/s. No basement correction was performed for shots P1 to P6 on the continental slope.

Figure 4.3 displays the record sections for three representative shots in the ocean basin. All sections show true amplitudes multiplied by a factor proportional to shot/receiver distance, and corrected for charge size using the $W^{2/3}$ relationship between charge weight and amplitude determined experimentally by O'Brien(1960). Shots P19 and P13 are 825 kg charges, and shot P8 is 200 kg. On all three record sections, the gap in the middle corresponds to the location of Georgia Strait (265-285 km from shot P19). Common receiver gathers for two land seismograph stations, X45 on the mainland at the eastern end of the profile and X22 located on Vancouver Island ~15 km west of Georgia Strait, are shown in Figure 4.4. Note that the westernmost shot P19 is on the left of the common receiver sections, i.e. the shot/receiver distance increases from right to left.

The most prominent phases in the entire data set are the large amplitude first arrivals from the ocean basin shots recorded on the stations to the east of Georgia Strait (see

FIG. 4.3. Observed record sections for shots P19, P13 and P8. Record sections are true amplitude, so that amplitudes may be compared from shot to shot. All amplitudes have been multiplied by a factor proportional to distance. Traveltime picks are indicated by arrowheads, and include secondary arrivals for shots P19 and P13. Times and distances are adjusted to place the shot at a depth of 2.6 km, and to correct the sediment layer to a thickness of 1 km and velocity of 1.8 km/s. The gap near the middle of all sections indicates the location of Georgia Strait (at 265-285 km from shot P19).

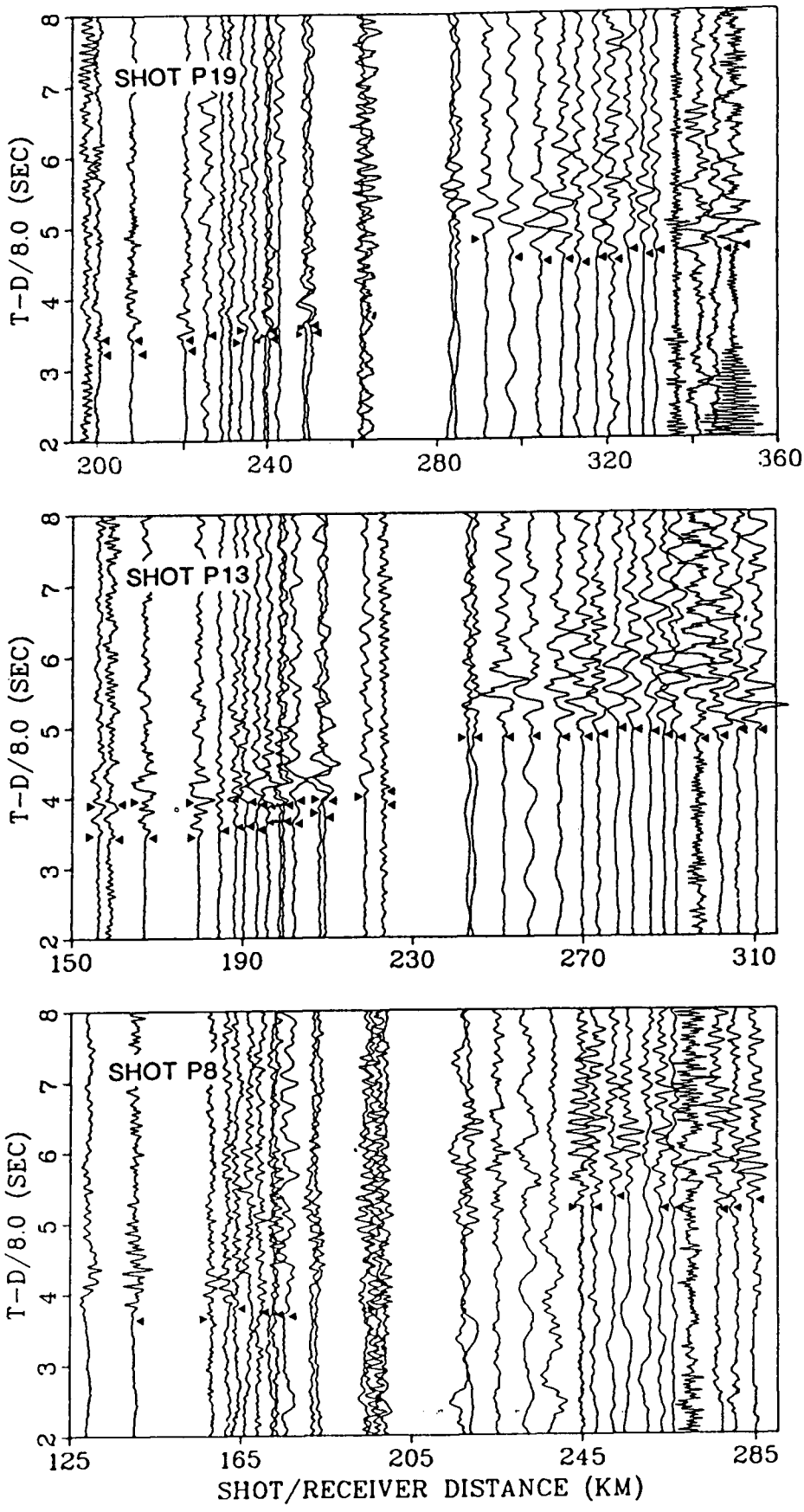
SHOT P19
SHOT P13
SHOT P8
T-D/8.0 (SEC)
2
3
4
5
6
7
8
200
240
280
320
360
150
190
230
270
310
125
165
205
245
285
SHOT/RECEIVER DISTANCE (KM)

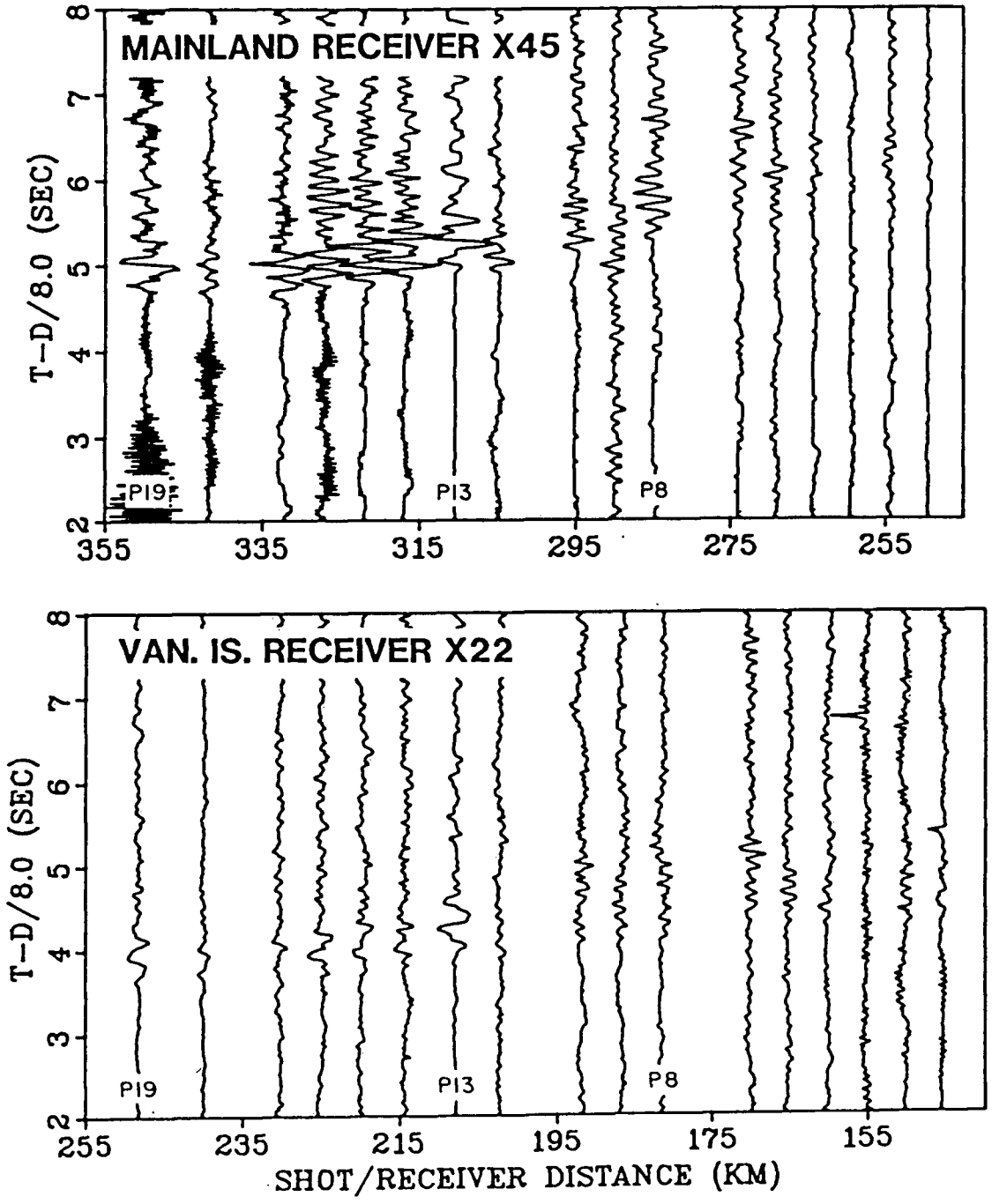

FIG. 4.4. Observed record sections showing all shots (three are identified) recorded on receivers X45 and X22, which are located to the right of the sections. Record sections are true amplitude, with all amplitudes multiplied by a factor proportional to distance. Times and distances are adjusted to place the shots at 2.6 km depth, and for shots P19-P8 to correct the sediment layer to a thickness of 1 km and velocity of 1.8 km/s.

shots P19 and P13 in Figure 4.3 and receiver X45 in Figure 4.4). These arrivals have an excellent signal-to-noise ratio and a sharp onset, with an apparent velocity of 8.1-8.2 km/s across the receivers (Fig. 4.3) and a reversed apparent velocity of 8.3-8.5 km/s across the shots (Fig. 4.4). The large amplitudes from these more distant ocean basin shots contrast markedly with the diminished amplitudes from the closer shots P1-P6 on the continental slope, as seen for receiver X45 in Figure 4.4. Because the amplitudes for shots P1-P6 are quite small, it is difficult to pick the apparent velocities across these shots, but an estimate is about 8 km/s.

For the stations on Vancouver Island, which are closer to the shots than the mainland stations, the data quality is poorer than that of the prominent phases seen on the mainland stations. The signals are less consistent from trace-to-trace, having a more complex wave form and lower signal-to-noise ratio. However, a second arrival can be discerned on some of the Vancouver Island stations, and its amplitude is somewhat larger than that of the primary arrival. The best examples of these arrivals are seen on shot P13 (Fig. 4.3) and receiver X22 (shots P13 to P19, Fig. 4.4). A consistent characteristic of the secondary arrivals is that their traveltimes approach the primary arrival traveltimes for greater shot/receiver offsets.

The apparent velocity of the first arrivals across the Vancouver Island receivers is 7.5-7.7 km/s (Fig. 4.3), while that of the second arrivals is nearly 8 km/s. The apparent velocity of the first arrivals across the shots for a Vancouver Island station is ~8.3 km/s (Fig. 4.4), which is comparable to

that for a mainland station, while the secondary arrival apparent velocity approaches 9 km/s.

Finally, the most prominent traveltime characteristic of the data is a traveltime delay of about 1 s occurring on all shots for the stations east of Georgia Strait relative to the stations west of Georgia Strait. The actual location where the delay occurs is the same on all shot record sections and is not dependent on shot/receiver offset. This is suggestive of a fixed structural feature in the model, such as a fault, rather than simply a depth-dependent feature such as a low-velocity zone. But from the interpretation of shot J1, we know that there is no major two-dimensional disruption in structure beneath Georgia Strait down to a depth of 14 km. Thus, the structural feature causing the traveltime offset must be at greater depths.

4.4 Ray tracing and traveltime inversion: shots P19, P13 and P8

The 17 shots of the P series recorded on up to 32 receivers form a large number of shot-receiver combinations, especially when secondary arrivals are considered. A model of the data should simultaneously fit all the traveltimes. To achieve this, the ray trace inversion procedure described in Chapter 2 was applied. In this procedure, two-dimensional ray tracing is used to determine traveltimes and the partial derivatives of traveltime with respect to selected parameters of the velocity model. Adjustments to the model are then found using the damped least-squares matrix inversion technique.

Of the 17 shots in the P series, ocean basin shots P19, P13 and P8 were selected in the ray trace inversion procedure. None

of the continental slope shots P1-P6 were used because consistent arrivals were difficult to pick and because sedimentary and upper crustal structures (including a possibly thick low velocity melange) were not as well constrained as the ocean basin structure in the interpretation of Waldron (1982). Only the three shots P19, P13 and P8 were used because (1) shots P19 and P13 were the largest charges and their arrivals the best recorded, and (2) first arrival traveltimes show no major offsets from shot P8 to shot P19, and so it was felt that the three shots adequately represented the variation among all the ocean basin shots.

In the following example, the behavior of the ray trace inversion procedure is demonstrated using a model which is close to the final onshore-offshore refraction model. The development of the model and the details of the final model will be discussed in later sections. Figure 4.5 shows ray paths through the model from the shots to the receivers. The observed traveltimes which were used in the inverse procedure are marked by arrowheads on the P19, P13 and P8 record sections in Figure 4.3. In this example, turning rays through the upper mantle give rise to the first arrivals at the near stations, reflections from an upper mantle horizon form the second arrivals, and reflections from the same horizon correspond to the sole arrivals at the far stations.

Only six parameters of the structure shown in Figure 4.5 are allowed to vary: the velocity in region I where the turning ray paths to the near receivers are located, the velocity in region II where ray paths to the far receivers are located, and

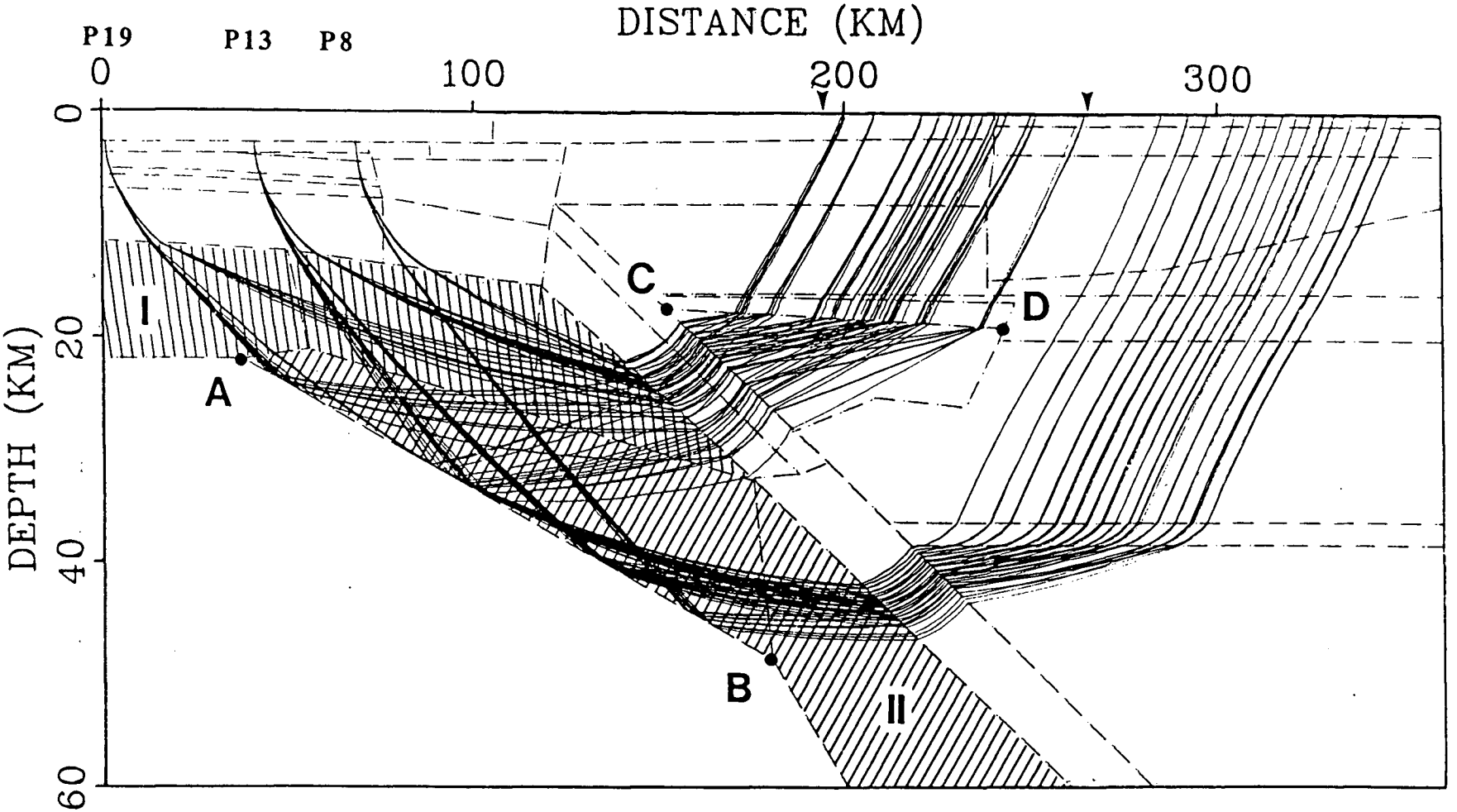

FIG. 4.5. Ray paths through a preliminary model for shots P19, P13 and P8. Observed traveltime picks shown in Fig. 4.3 are used in the ray trace inverse procedure, by which adjustments to specified ray trace parameters are automatically calculated so that model traveltimes fit observed traveltimes. Parameters that are adjusted are upper mantle velocities in regions I and II, and the depths of boundaries at points A, B, C and D. Arrowheads indicate the coasts of Vancouver Island. Vertical exaggeration is 3:1.

the depths at four points A, B, C and D which represent the ends of two boundaries in the model. Variations in these parameters affect the traveltimes through the model in different ways. For example, if the velocity increases in one of the regions, then the total traveltime decreases and the apparent velocity increases in both the forward and reverse directions. If the reflecting boundary becomes deeper, then the total traveltimes for the reflections also increase. If the dip of the boundary increases, then the apparent velocity across the receivers becomes smaller and the apparent velocity across the shots becomes larger; however, for the particular set of rays shown in Figure 4.5, the change in apparent velocity across the receivers would be smaller than that across the shots, because the reflecting points for all rays from a shot to its receivers all lie within a very small region on the boundary.

The performance of the ray trace inverse routine is shown in Figure 4.6. The perturbations determined from a single iteration of the routine were applied to the initial model, and final model traveltimes were then found by retracing the rays. In each panel of Figure 4.6, the crosses indicate the observed traveltimes, the dashed line represents the initial model traveltimes, and the solid line represents the final model traveltimes. For the initial model,the residual between observed and calculated traveltimes had an rms value of 222 ms, due mainly to the misfit in traveltimes to the far stations. The rms traveltime residual for the final model was 79 ms, which is close to the estimated error on the observed traveltime picks of ~75 ms.

FIG. 4.6. Performance of the ray trace inversion procedure is indicated by the traveltime fit before and after the procedure is applied. Observed traveltimes are shown by crosses for first arrivals and plus signs for secondary arrivals. The dashed lines for each shot are the traveltime curves for the initial model of Fig 4.5; the rms residual is 222 ms. The solid lines are the traveltime curves for the final model after the parameter adjustments have been applied; the rms residual is 79 ms.

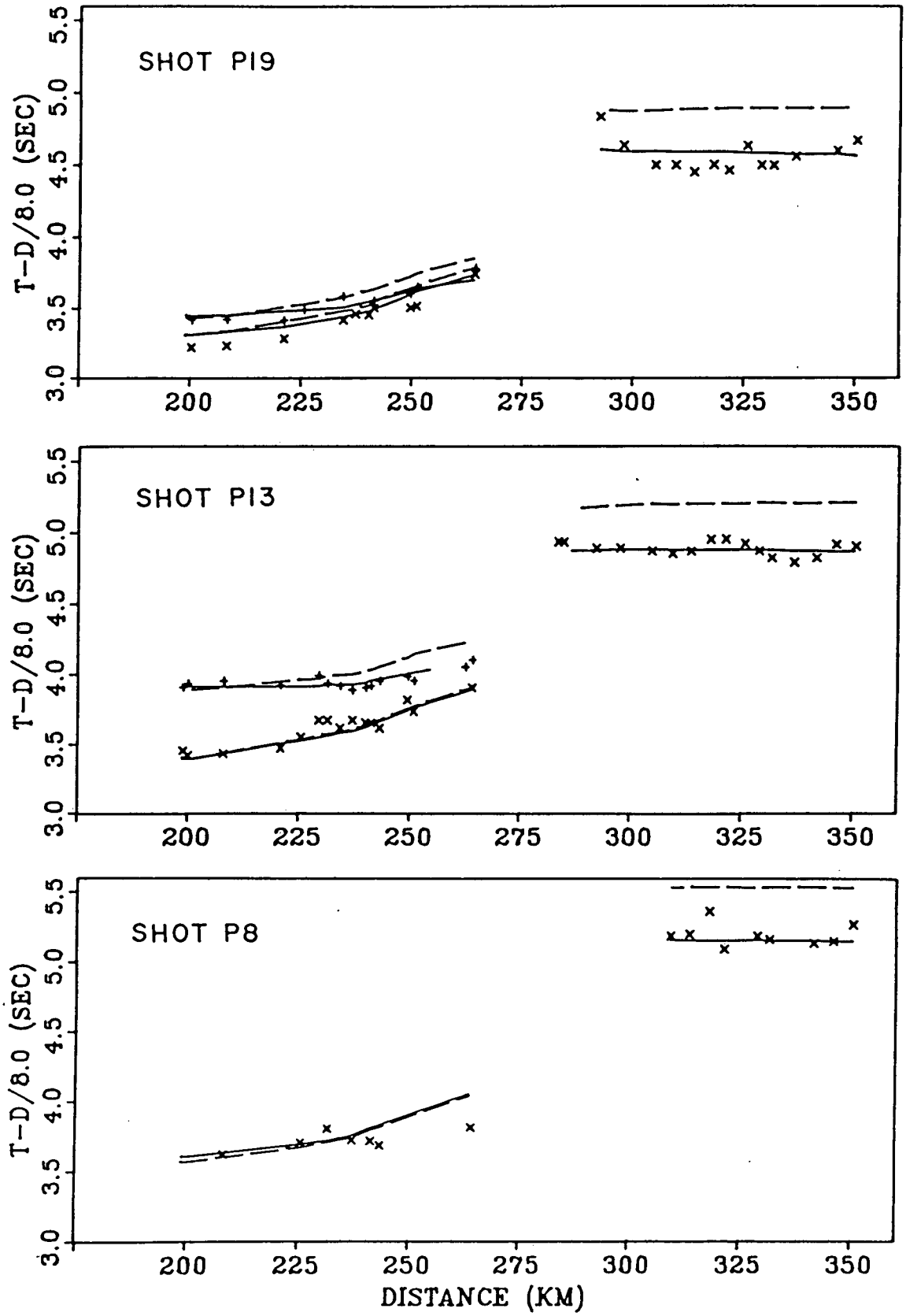
SHOT PI9
SHOT PI3
SHOT P8
T-D/8.0 (SEC)
3.0
3.5
4.0
4.5
5.0
5.5
200
225
250
275
300
325
350
DISTANCE (KM)

The changes in parameters for the iteration shown in Figure 4.6 were as follows:

velocity, region I	:	Δv_I =	+0.045 km/s
velocity, region II	:	Δv_{II} =	+0.107 km/s
depth, point A	:	Δh_A =	+2.11 km
depth, point B	:	Δh_B =	-2.99 km
depth, point C	:	Δh_C =	+1.39 km
depth, point D	:	Δh_D =	+0.21 km

Thus, the most significant changes were the increase in the velocity of region II and the decrease in dip of the reflecting boundary (i.e. point A became deeper and point B shallower). The velocity increased in order to reduce the total traveltime to the far stations. Because a larger model velocity also implied a larger apparent velocity, the dip of the reflection decreased to counterbalance the velocity change, i.e. to act in such a way as to reduce the apparent velocity across the shots.

It should be clear that the logic could become quite convoluted if a manual or trial-and-error method were used to find the proper adjustments to a ray trace model. Using the ray trace inversion procedure, least-square adjustments are automatically calculated which enable us to directly find a ray trace model which fits the data. This has the following advantages: (1) we are assured that the model and observed data agree in an objective least-squares-sense, and not in a more subjective manner which would be involved in a manual procedure, and (2) compared to a strictly trial-and-error method, we are able to test a much larger range of starting models with different choices of either fixed or variable parameters.

4.5 Final onshore-offshore refraction model

4.5.1 Interpretation procedure

As described in the previous section, the method of fitting traveltimes for multiple shots and multiple receivers is largely automated through the ray trace inversion procedure. However, once a satisfactory traveltime fit is obtained, modifications to the corresponding model may still be desired in order to obtain a better fit to the amplitudes on the observed sections. Changes may also be introduced in order to try different starting models and so find alternate models which also fit the data; such alternate models will be discussed in the following section.

Whatever the reason for the change, the major difficulty that arises is related to the stability of the ray tracing. That is, the change may have the result that the ray path from shot to receiver no longer exists. This would occur, for example, if the "shadow zone" due to a low velocity zone or to a corner moved over the receiver, or if the critical point on a boundary was changed so that the corresponding critical ray surfaced beyond the receiver.

Amplitudes through two-dimensional structures were calculated with the asymptotic ray theory algorithm of Spence et al. (1984), also described in Chapter 3. The algorithm incorporates a modified version of the ray tracing routine of Whittall and Clowes (1979), and so the identical model input file may be used for both the ray trace inversion procedure and the amplitude algorithm. To obtain a model which fits both amplitudes and traveltimes, the two routines are applied in

conjunction. For example, starting with a model that fits the traveltimes, changes may be made such that the amplitude fit improves, which also has the likely side effect that the traveltime fit deteriorates. Using the ray trace inversion procedure, adjustments are then found so that model and observed traveltimes again match, in the hope that the amplitude behavior is not much affected. In practice, amplitudes are not very sensitive to small changes in the overall velocity of a block, whereas traveltimes naturally are. On the other hand, amplitudes may be altered by varying the velocity gradient in a block, the velocity contrast across a boundary, and the angle at which a ray and a boundary intersect.

Amplitude variations were modelled for different arrivals on the same trace and for different traces on the same record section. However, only the general amplitude trends between different groups of traces were modelled, and not the individual variations from trace to trace. The detailed trace-to-trace variations were not considered because of uncertainties both in the data and in the modelling procedure. For the data, some of the variations in amplitude from receiver to receiver could be caused by site-dependent characteristics. For a given model, the calculation of amplitudes was limited by the use of asymptotic ray theory, which cannot directly handle wave phenomena, and by possible effects from unknown two- or three-dimensional structures.

The final onshore-offshore refraction model is displayed in Figure 4.7. In Figure 4.8, the full details of the velocity model are given, including the velocities and velocity gradients

of all blocks in the model. The final ray trace through the model for shots P19, P13 and P8 is shown in Figure 4.9. The rms traveltime residual for the three shots is 79 ms. If a further iteration of the ray trace inversion procedure is applied, the residual is reduced insignificantly to 78 ms. From the values of resolution and standard error for the final iteration of the inversion procedure (Table 4.1), the most poorly determined parameter is the depth h_A at point A (Fig. 4.5) on the upper mantle reflector. The resolution is 0.46 and the standard error is nearly 1 km. This is consistent with the results from the subduction zone test model in section 2.4 of Chapter 2, where the poor resolution of the upper mantle reflector was related to the lack of sensitivity of traveltime with respect to the depth of the reflector. It should again be emphasized that the standard errors given in Table 4.1 should not be considered as absolute measures of certainty for the parameters. As will be shown in section 4.6, there are alternate models with slightly different parameterizations which also satisfy the observed traveltimes, and the equivalent parameters for the various models differ by amounts greater than the calculated standard errors.

The final model also incorporates amplitude information from the continental slope shots P1-P6, as well as from the main ocean basin shots P19, P13 and P8. Only the observed traveltimes from the ocean basin shots were included in the ray trace inversion procedure. To obtain a traveltime fit for the continental slope shots, the shallow structure beneath the shots was varied in a trial-and-error manner, which had no effect on

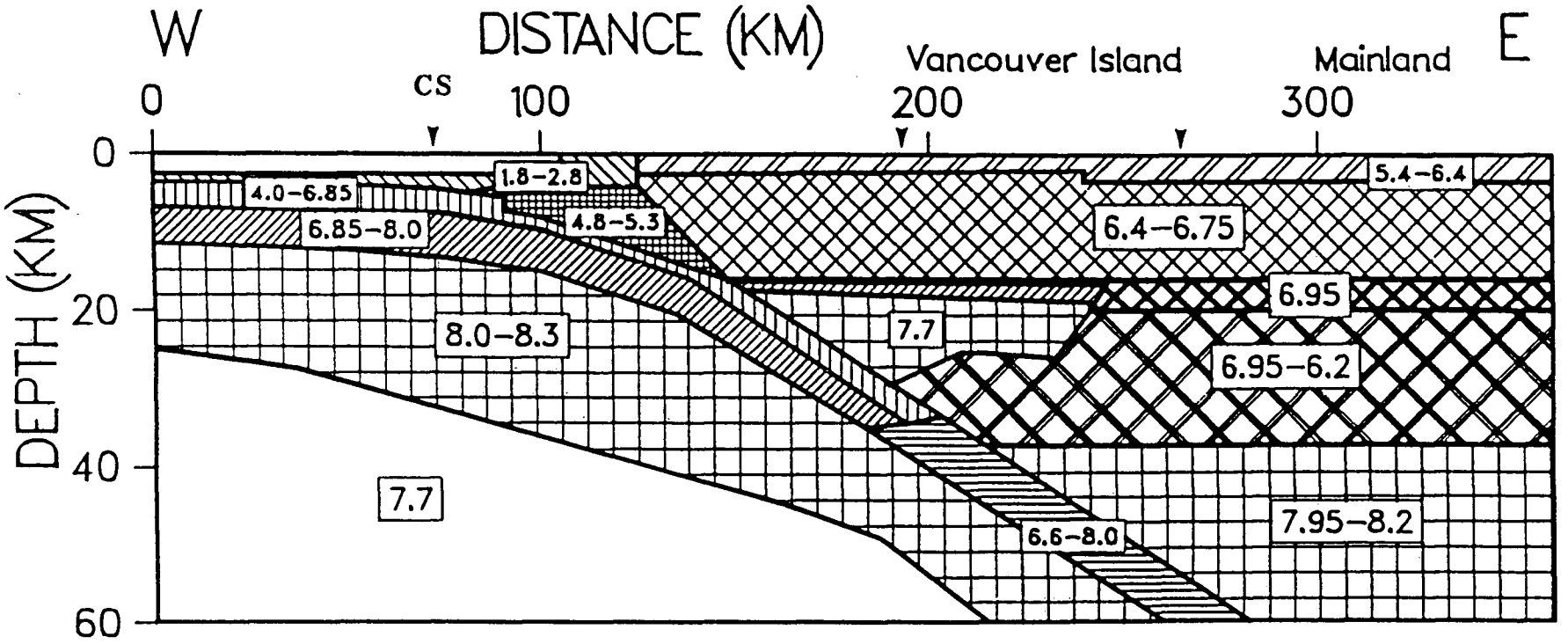

FIG. 4.7. Final velocity model interpreted from the onshore-offshore dataset along line I. Numbers indicate the velocities (km/s) at the shallowest and deepest points in each block. CS is the location of the foot of the continental slope. Oceanic crustal model was determined by Waldron (1982). The subducting ocean crust is arbitrarily represented by only a single layer below about 30 km depth. Continental crustal model was constrained by the preferred low-velocity zone interpretation of McMechan and Spence (1983) which applies at the intersection of line I and line IV (230 km from shot P19).

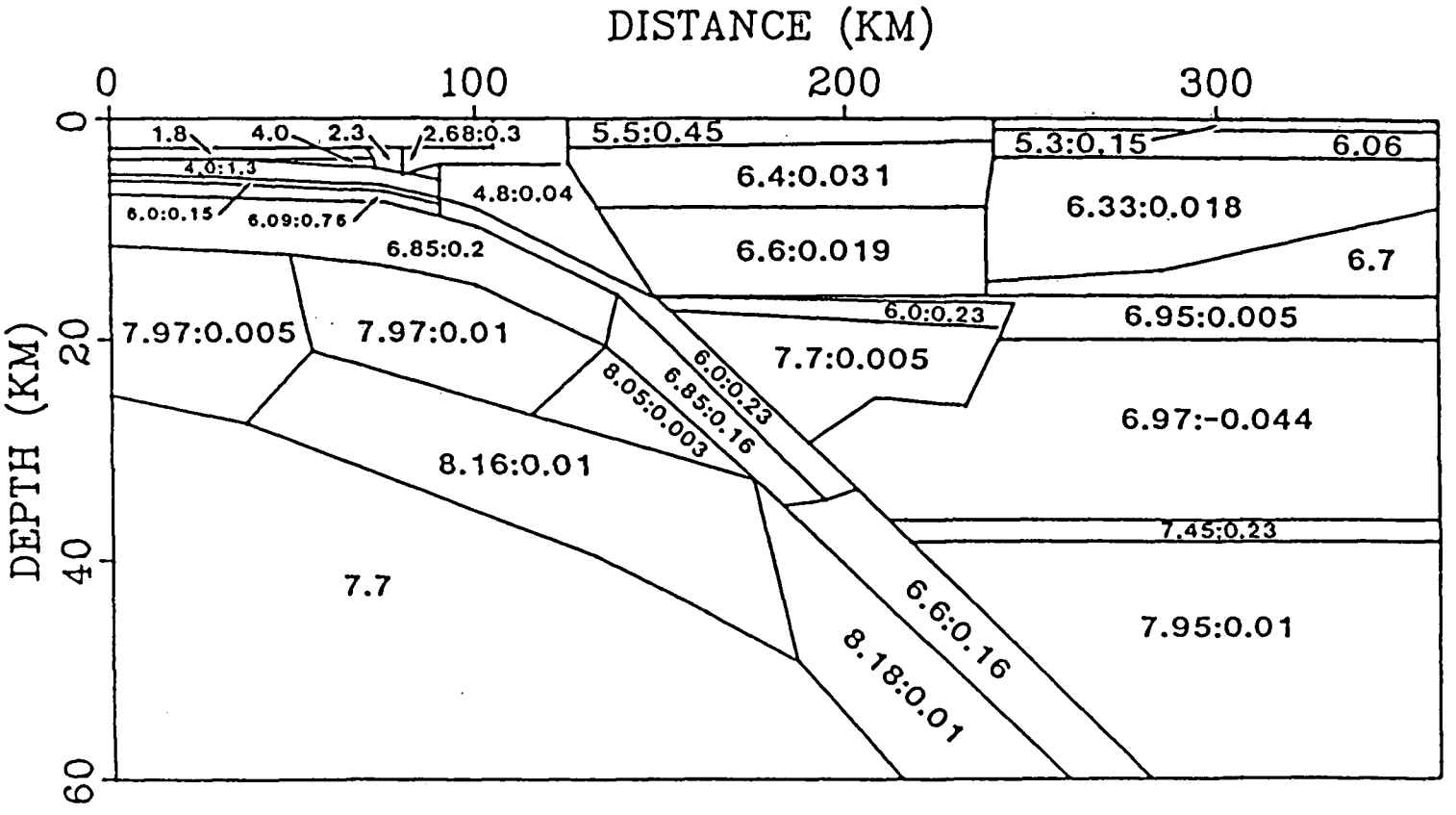

FIG. 4.8. Details of the velocity model shown in Fig. 4.7. Velocities (km/s) are given for the top of each block, followed after the colon by the velocity gradient (km/s/km) if one was used.

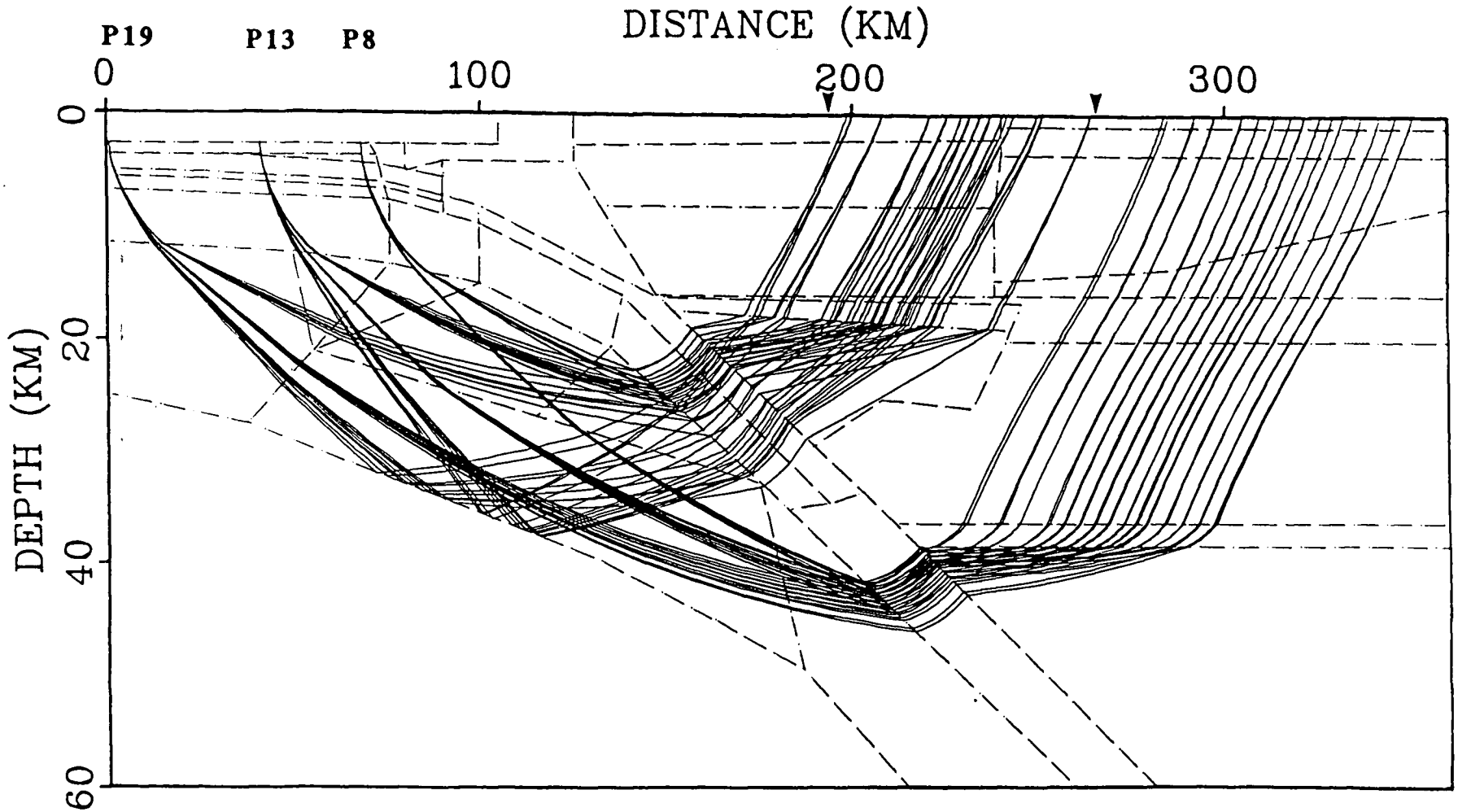

FIG. 4.9. Ray paths from shots P19, P13 and P8 through the final velocity model shown on Fig. 4.7 and Fig. 4.8. The rms residual for the three shots is 79 ms; if a further iteration of the ray trace inversion procedure is applied, the residual is reduced insignificantly to 78 ms.

Parameter	Final Value	Resolution	Standard Error
v_I	7.97 km/s	0.68	0.013 km/s
v_{II}	8.16 km/s	0.93	0.007 km/s
h_A	27.5 km	0.46	0.93 km
h_B	39.6 km	0.83	0.67 km
h_C	17.3 km	0.90	0.54 km
h_D	18.9 km	0.93	0.45 km

TABLE 4.1. Parameter values, resolution and standard error for the final iteration of the ray trace inversion procedure, applied to the traveltime dataset of the onshore-offshore line I (Fig. 4.9). Resolution and standard error give approximate relative measures of certainty for the parameters. The overall damping factor θ was 0.25.

the traveltime fit for shots P19, P13 and P8. Traveltimes from the continental slope shots were not included in the more automated ray trace inversion procedure because of the poor data quality from the shots, and because oceanic crustal structure in the interpretation of Waldron (1982) was not as well-constrained beneath the continental slope and shelf as beneath the deep ocean basin.

In Figure 4.8, the melange has been modified slightly from that shown in Figure 1.6, which was derived by Waldron (1982). The major change was a reduction in the velocity gradient within the melange from 0.2 km/s/km to 0.04 km/s/km. With this change, a better fit was obtained for the data recorded on OBS 5 (located at 125 km in Fig. 4.8), compared to the interpretation presented by Waldron (1982); that is, the amplitudes of turning rays within the melange to OBS 5 were reduced and thus compared more favorably with the data. An additional cosmetic change to

the model of Figure 1.6 was that an extra layer was added at the base of the melange above the lower ocean crust. The ocean crust still appears to thin beneath the melange (Fig. 4.7). This effect is related to the formation of the melange itself; as a response to their resistance to subduction, the upper layers are compressed and deformed and their velocity is reduced (Waldron 1982).

In the final ray trace diagram for the ray trace inversion procedure (Fig. 4.9), it should be noted that turning rays are used to the mainland receivers, in contrast to the reflected rays in Section 4.4 where the ray trace procedure was first demonstrated. In terms of traveltimes, the two types of rays are almost equivalent, with a maximum time difference of ~150 ms for shot P8. The major difference between the ray types is that turning rays to the far stations are much more unstable with respect to changes in the ray trace model, since they intersect the continental Moho at a shallower angle than the reflected rays. Thus, much of the development of the ray trace model was done using reflected rays as the only arrivals at the far receivers. However, no claim is made that both the turning and reflected rays can be separately observed at the mainland stations. Either could be recorded and would contribute to the observed arrivals.

4.5.2 Synthetic seismograms for the final model

Figures 4.10 to 4.17 contain theoretical and observed vertical component seismograms for representative shots and representative receivers. The synthetic seismograms were

calculated using the final refraction model of Figure 4.7, and the theoretical traveltimes of the synthetics are superimposed on the observed record sections. Both observed and synthetic seismograms are multiplied by a factor proportional to distance. All record sections are true amplitude, so amplitudes may thus be compared from trace-to-trace. In addition, amplitudes may be compared between shot record sections and between receiver record sections.

The sections are presented unfiltered (except for a 1 Hz lowcut filter on the observed record section for receiver X34), since filtering did not appear to significantly enhance either first breaks or continuity of arrivals from trace-to-trace. On Figures 4.10 to 4.17, the location of a seismogram may be referred either to its appropriate shot/receiver distance, or to its location on the final velocity model which has the location of shot P19 as its origin; both distance scales are presented.

The main characteristics of the synthetic seismograms and their related features on the final velocity model are as follows:

(1) Turning rays through the upper mantle give rise to the first arrivals at all receivers. The velocity at the Moho of the subducting slab is approximately 8.0 km/s, with a velocity gradient perpendicular to the Moho of 0.01 km/s. As in the preliminary interpretation of Ellis et al. (1983), the value of the gradient is not well-constrained. The value used is comparable to that given by Steinmetz et al. (1977) for lithosphere beneath 9 Ma oceanic crust and by Fuchs (1979) for lithosphere beneath continents.

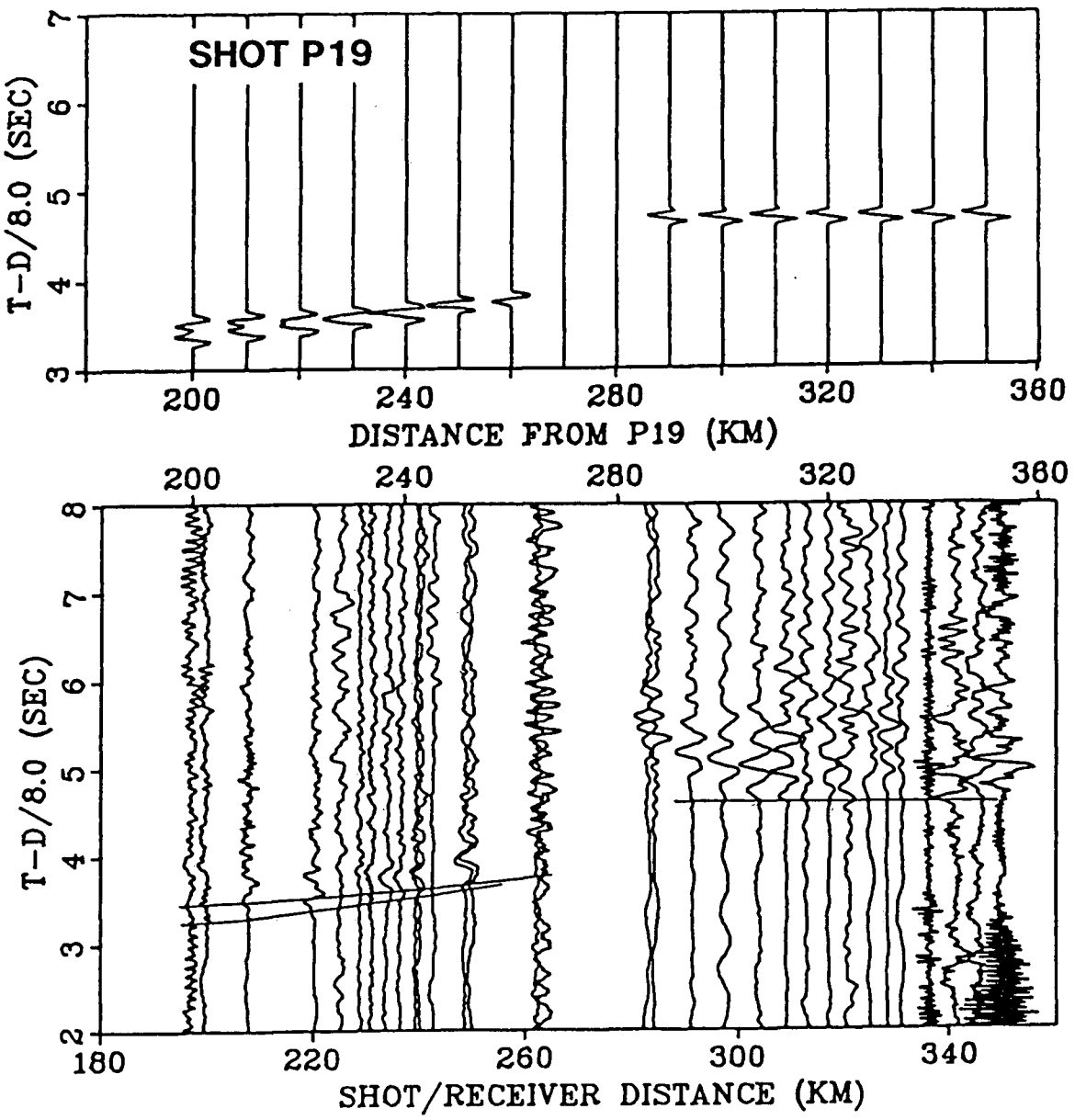

FIG. 4.10. Synthetic seismograms and observed data for shot P19. Model traveltimes from the synthetic seismograms are superimposed on the observed record section. Primary arrivals are turning rays through the mantle. Secondary arrivals correspond to rays reflected from an upper mantle boundary, with the velocity below the boundary smaller than the velocity above. For shot P19, the model traveltimes to the mainland stations (290-350 km) are almost the same for both turning rays and reflected rays.

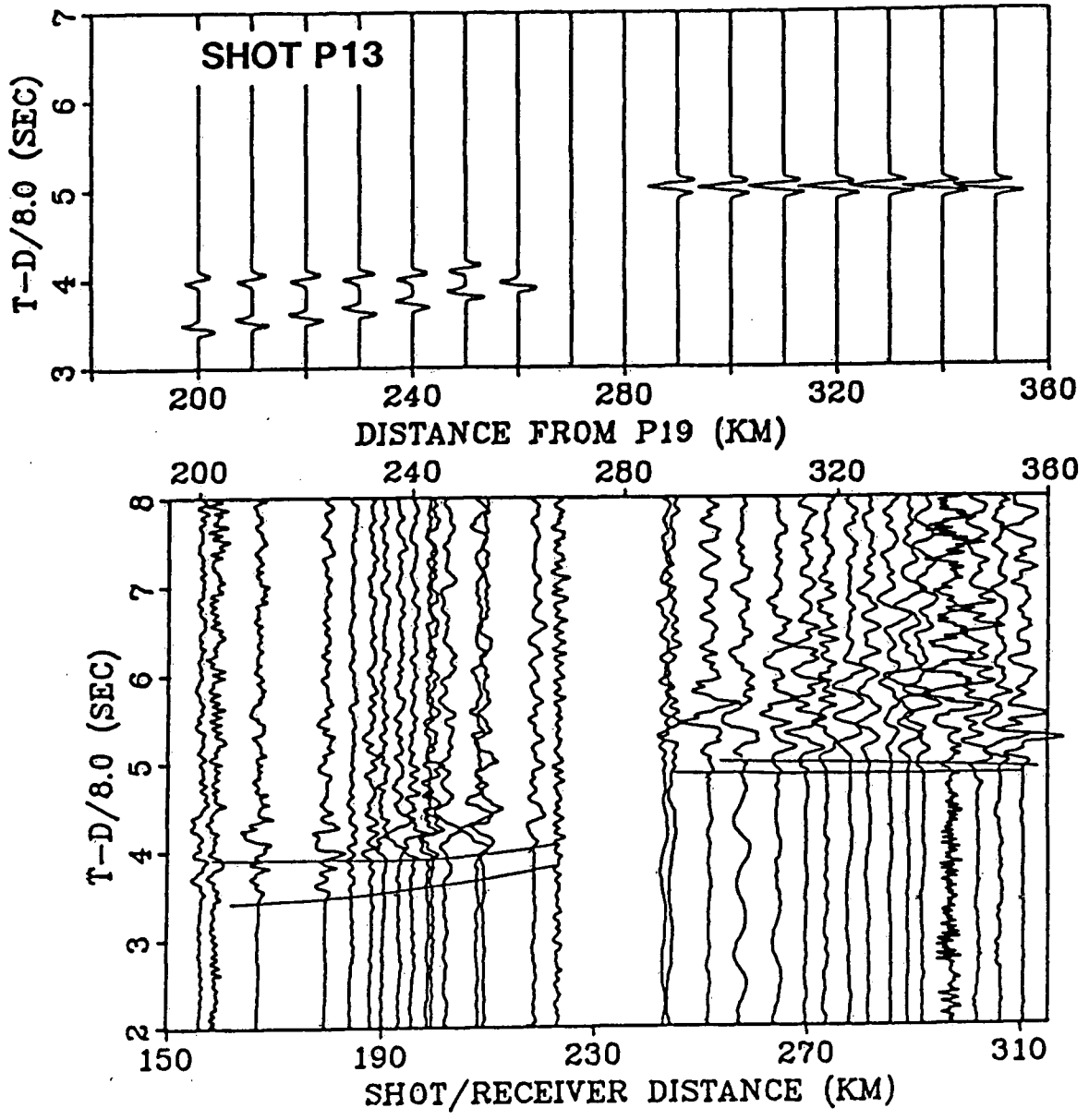

FIG. 4.11. Synthetic seismograms and observed data for shot P13, located 40 km east of shot P19. See caption for Fig. 4.10.

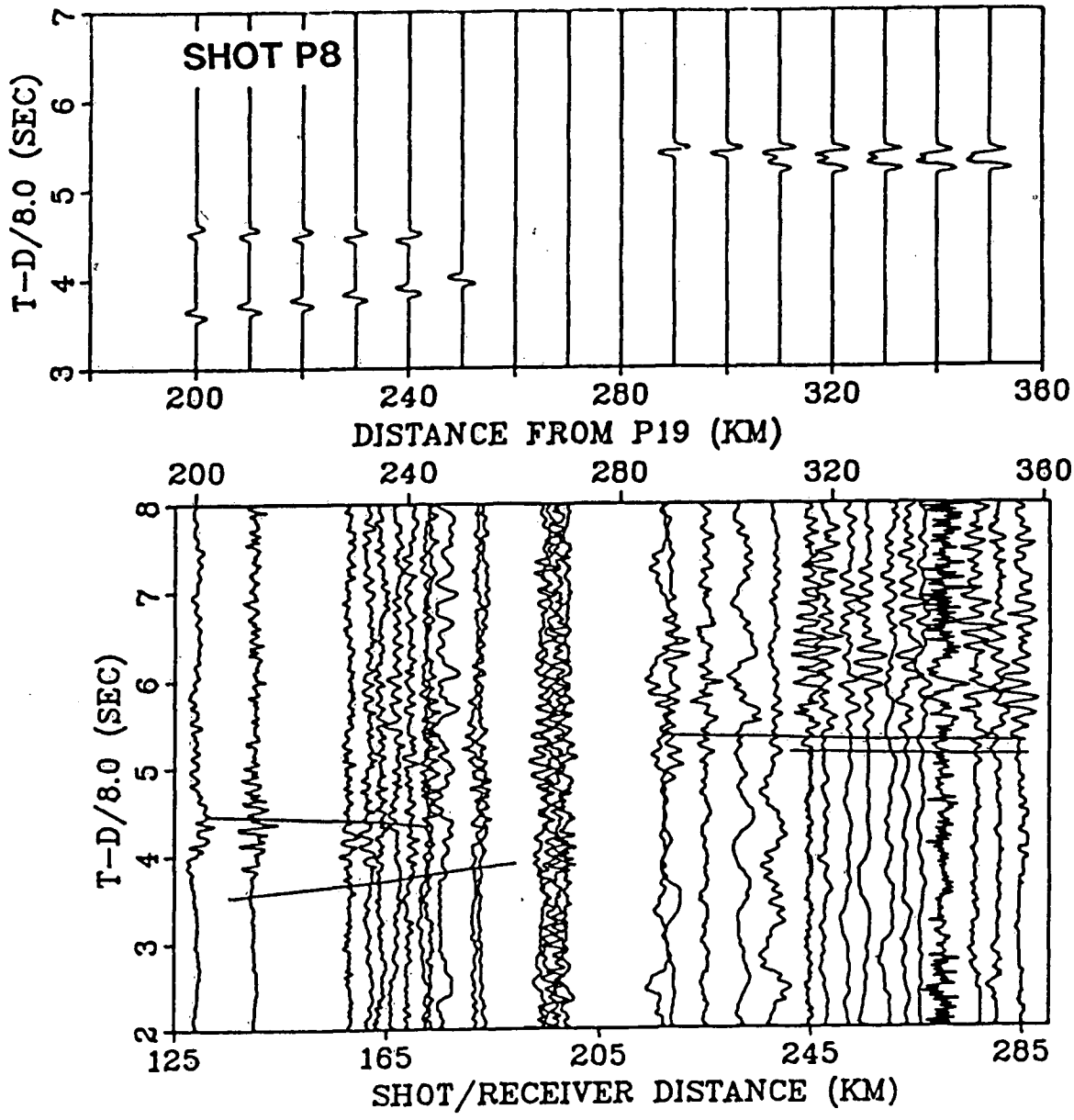

FIG. 4.12. Synthetic seismograms and observed data for shot P8, located 67 km east of shot P19. See caption for Fig. 4.10. On the synthetic seismograms, note that the first arrival branch to the mainland stations is truncated; these arrivals are turning rays through the upper mantle, some of which are blocked by the corner formed at the intersection of continental Moho and subducting oceanic crust (see Fig. 4.18).

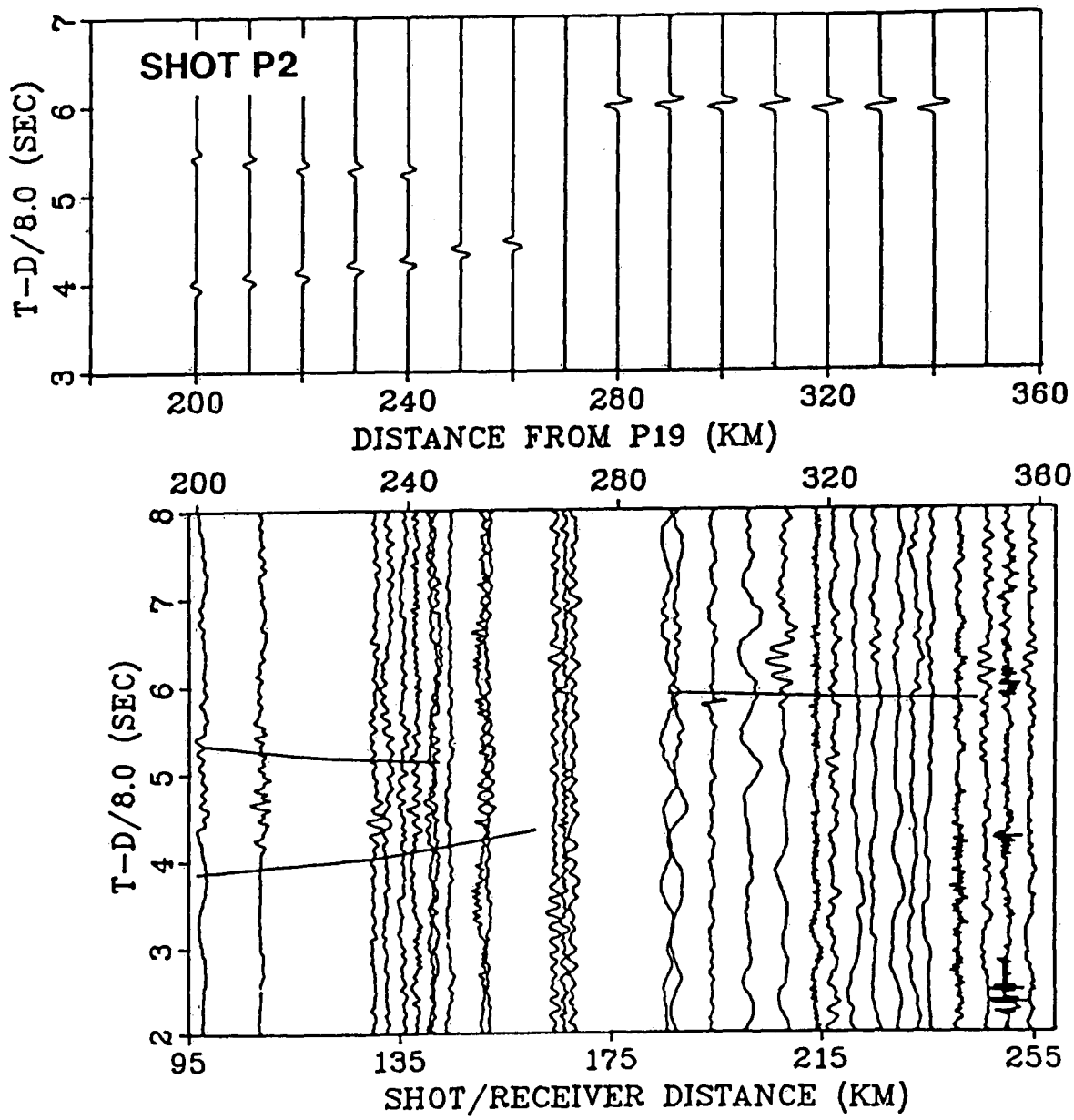

FIG. 4.13. Synthetic seismograms and observed data for shot P2, located 99 km east of shot P19. See caption for Fig. 4.10. On the synthetic seismograms, the only branch present at the mainland stations is the branch of rays reflected at the upper mantle boundary. All turning rays to the mainland stations are blocked by the corner formed at the intersection of continental Moho and subducting oceanic crust (see Fig. 4.18).

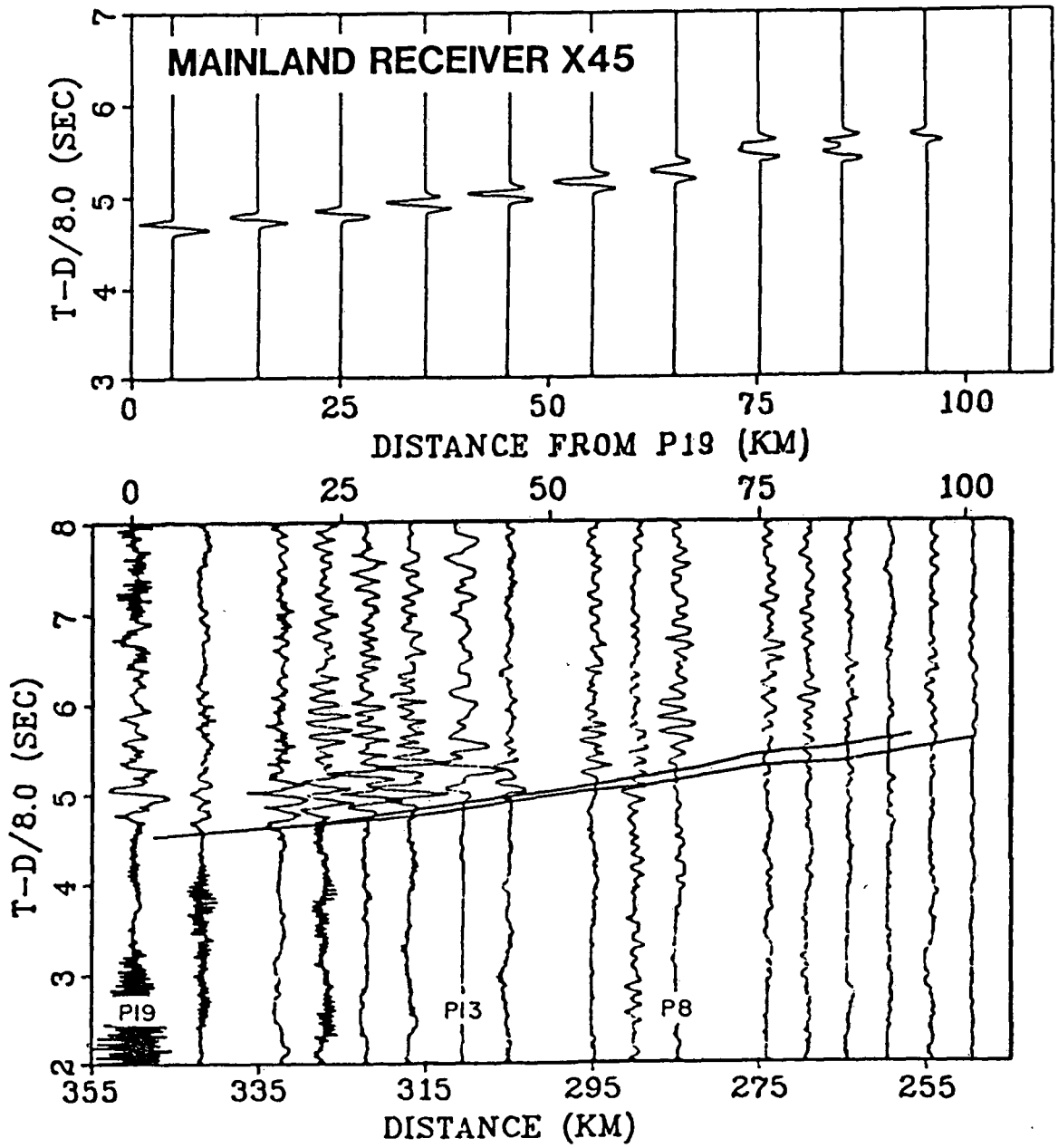

FIG. 4.14. Synthetic seismograms and observed data for mainland receiver X45, located at the easternmost end of the onshore-offshore profile. See caption for Fig. 4.10. The first arrival branch of turning rays is truncated (no arrivals beyond 99 km on the synthetic section) due to the effect of the corner where the continental Moho meets the subducting oceanic crust (see Fig. 4.18). The secondary arrival branch of reflected rays is also truncated; but this is due to a poorly controlled feature of the velocity model (Fig. 4.7), in which the dip of the reflector east of about 200 km distance from P19 suddenly increases.

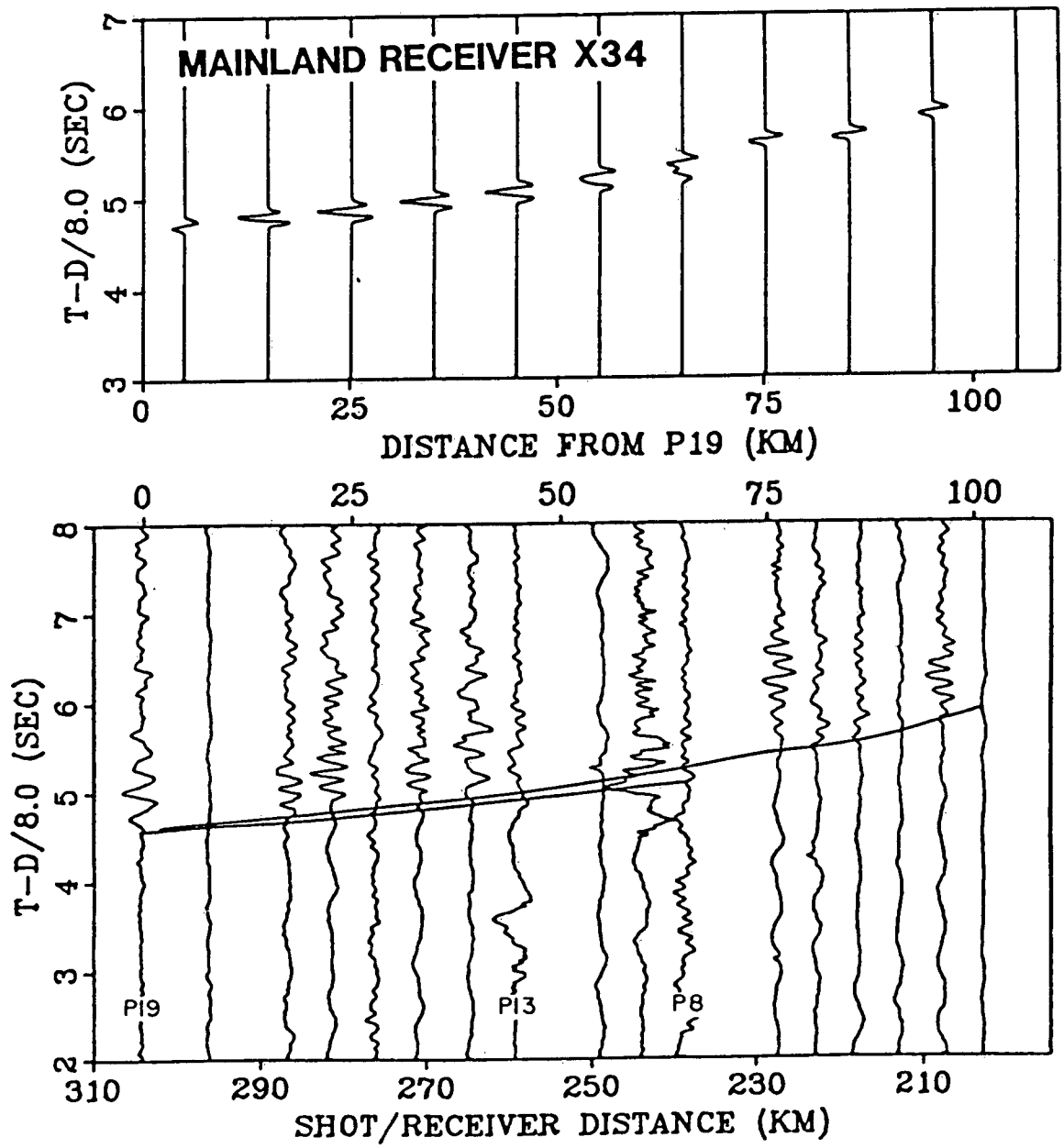

FIG. 4.15. Synthetic seismograms and observed data for mainland receiver X34. See caption for Fig. 4.10. Note that the first arrival branch of turning rays is truncated due to the effect of the intersection of the continental Moho and subducting oceanic crust (see Fig. 4.18).

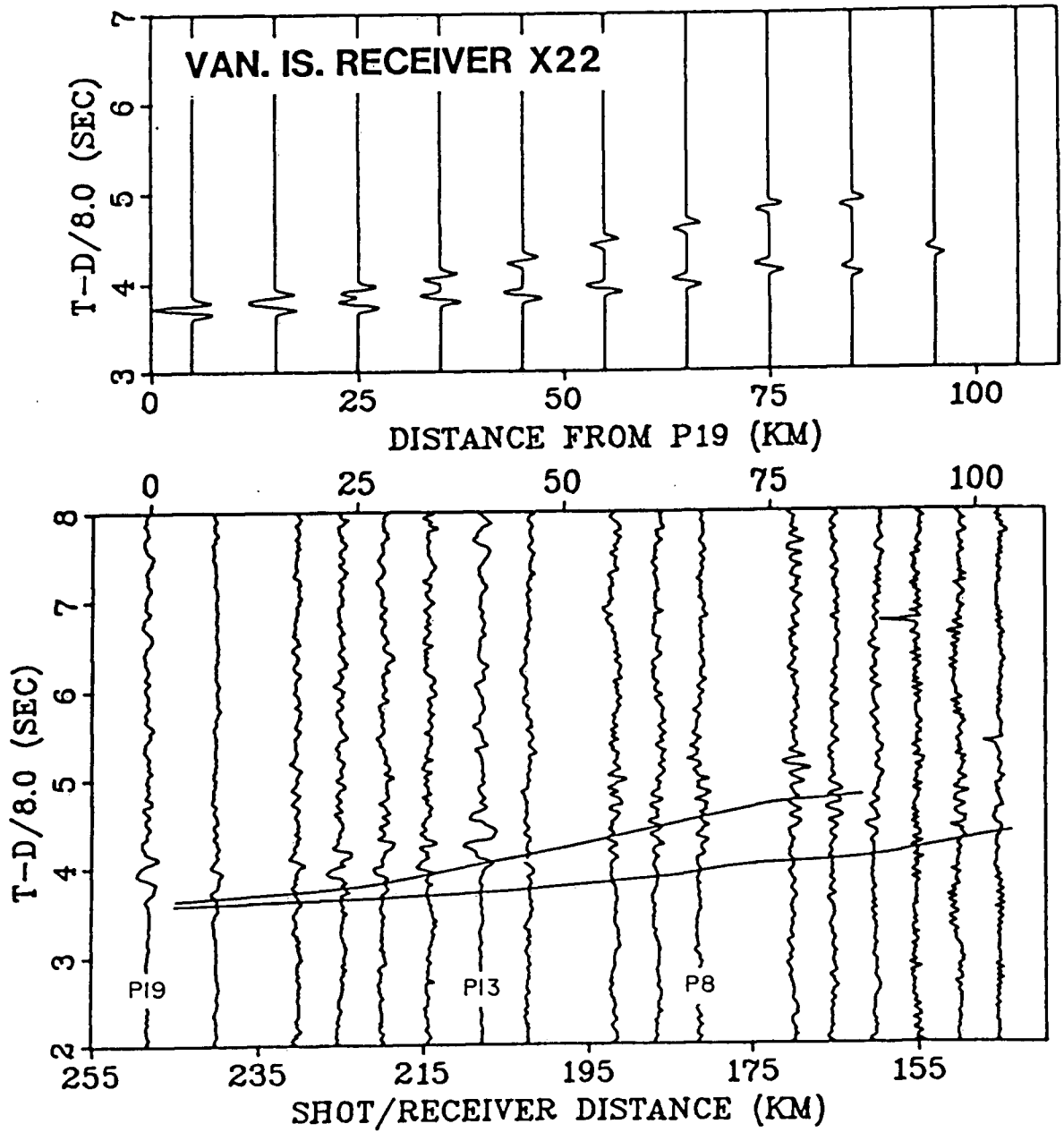

FIG. 4.16. Synthetic seismograms and observed data for mainland receiver X22. See caption for Fig. 4.10.

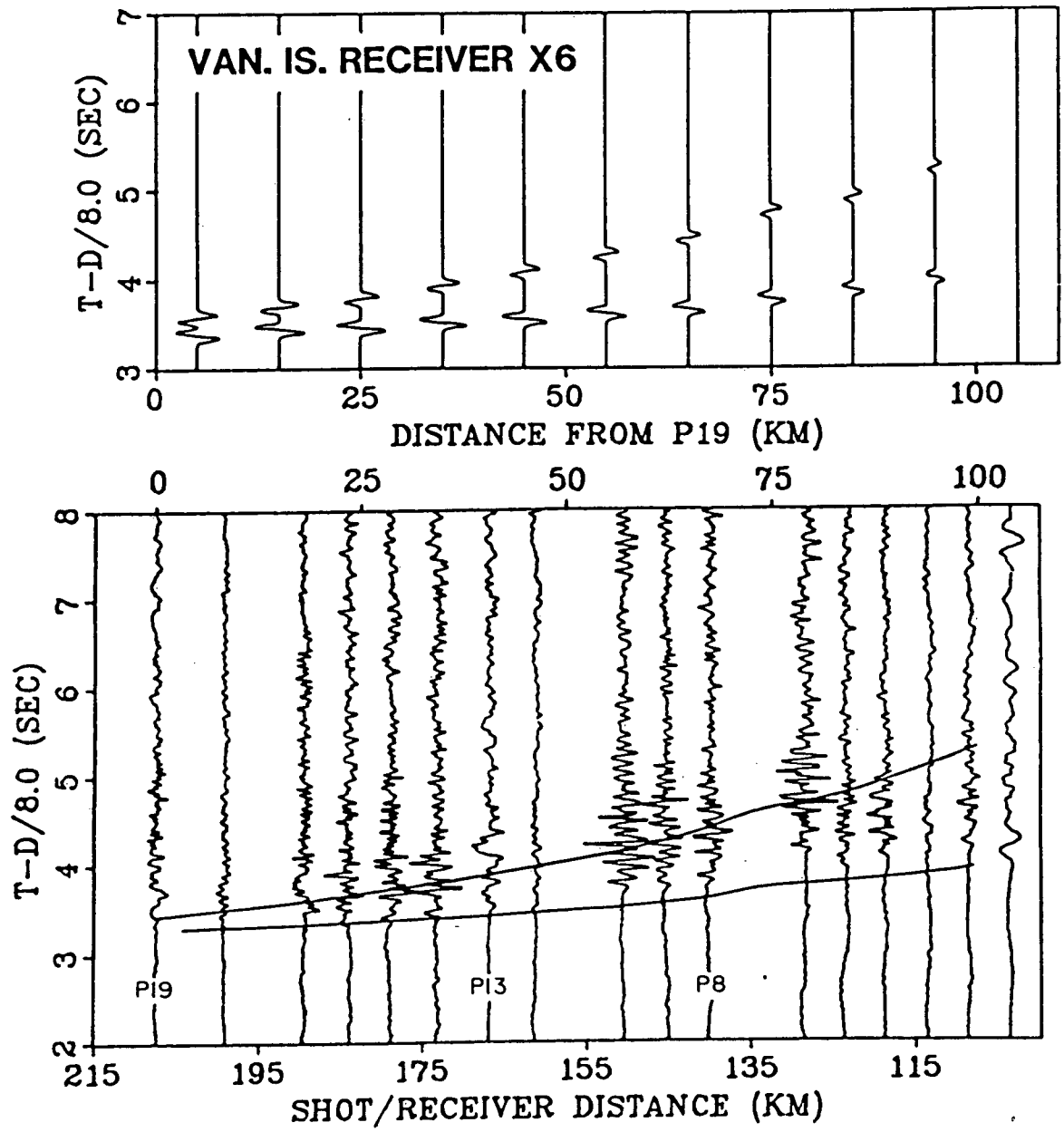

FIG. 4.17. Synthetic seismograms and observed data for mainland receiver X6. See caption for Fig. 4.10.

It was hoped that the amplitude modelling would provide more control on the mantle gradient, at least on the relative values between shallower and deeper mantle, since the two regions were sampled by different ray paths (see ray trace diagram, Fig. 4.9). However, as discussed below, the shallow mantle gradient was not the decisive factor in determining the amplitudes of the turning ray arrivals to the near stations, and so the gradient was not well-controlled by the amplitudes.

(2) An anomalous feature in the velocity model, and a feature through which all rays to the Vancouver Island stations pass, is the mantle-like sliver at ~20 km depth above the downgoing oceanic crust (Figs. 4.7 to 4.9). The sliver velocity of 7.7 km/s was determined mainly by amplitude considerations, in particular for the nearest offset shots. Amplitudes are sensitive to the value of sliver velocity because the velocity controls the ray path angle through the sliver, and ray path angles are near zero. Thus, a decrease in velocity implies that ray paths are directed more steeply towards the surface and a resultant increase in amplitude. On the other hand, an increase in velocity may result in ray paths that are directed downwards, never to intersect the upper boundary of the sliver or to reach the surface. This effect is most pronounced for the nearest offset shots, which have the steepest downward angle through the mantle below the ocean crust.

(3) For the oceanic basin shots, the apparent velocity of turning rays across the mainland receivers is approximately 8.1 km/s. Since this is the velocity of mantle material, it implies that the dip of the boundary through which rays enter the

continental crust is near zero. That is, the boundary is interpreted as approximately flat-lying continental Moho, and not a boundary related to the subducting oceanic crust. This contrasts with the results of Taber (1983) for a similar onshore-offshore profile acrosss the Washington margin only 250-300 km south of the Vancouver Island profile. Taber (1983) found an apparent velocity of 7.4 km/s across his mainland receivers from deep ocean shots and interpreted a subducting oceanic Moho dipping at ~9°.

(4) For the ocean basin shots, the apparent velocity of turning rays across the Vancouver Island receivers is 7.5-7.7 km/s (Figs. 4.10 to 4.12). This apparent velocity is controlled primarily by the high-velocity sliver above the downgoing crust. That is, with a sliver velocity of 7.7 km/s, the observed apparent velocity implies that the dip of the upper boundary of the mantle sliver is near zero.

(5) The traveltime offset of ~1 s seen for the first arrivals on shot profiles across Georgia Strait (Figs. 4.10 to 4.13) is caused by different ray paths to the Vancouver Island stations compared to the mainland stations. For the Vancouver Island arrivals, rays pass through the high-velocity sliver beneath western Vancouver Island and the inner continental shelf at depths as shallow as 20 km. These arrivals are thus advanced in traveltime compared to the mainland arrivals, which must enter the continental crust through the Moho at 37 km depth.

(6) For a given receiver, the apparent velocity of turning rays across the ocean basin shots is 8.3-8.5 km/s, only slightly higher than mantle velocity. This is consistent with a shallow

dip of <2° for the oceanic crustal layers west of the continental rise. The dip of the crustal layers was constrained by the marine interpretation of Waldron (1982) for the oceanic crust.

(7) The first break apparent velocity across the continental shots P1-P6 on the receiver gathers is difficult to pick, but appears to be approximately 8.0 km/s. This apparent velocity is sensitive primarily to the dip at the base of the sub-sediment melange block beneath shots P1-P6, labelled with velocity 4.8-5.3 km/s in the velocity model of Figure 4.7. Assuming that oceanic layers are parallel to the base of the melange, the apparent velocity thereby provides control on the dip of the Moho beneath shots P1-P6. On the synthetic profiles (Figs. 4.14 to 4.17), the apparent velocity may actually be somewhat larger than in the observed data; so beneath shots P1-P6, the base of the melange and the oceanic layers should probably dip at a smaller angle than shown in the velocity model of Figure 4.7. However, the important implication is that the point at which the subducting oceanic slab significantly increases in dip must occur east of the continental slope. This is consistent with the results of Taber (1983) in an onshore-offshore experiment across the Washington margin. Taber (1983) observed an increase in apparent velocity from 8 km/s for the more westerly shots to 11 km/s for the easterly shots. He interpreted this increase as direct evidence of the bend in the subducting slab at a point nearly 50 km landward of the beginning of the continental slope.

(8) The amplitudes of the first arrivals at the mainland

receivers are large from the ocean basin shots (see shots P19 and P13) and relatively small from the continental slope shots (see shot P2 and receiver X45). The reduced amplitudes could possibly be due to large attenuation losses from the thick and probably complexly deformed continental slope sediments. However, decreased amplitudes are also expected due to structural features in the velocity model. Figure 4.18 shows turning rays from a continental slope shot to the mainland receivers, and the reverse set of rays from a mainland receiver to the continental slope and ocean basin. All rays are separated by equi-angular increments, and for each set of rays there is a "shadow zone" due to the corner where the continental Moho meets the subducting oceanic crust. No turning ray arrivals occur within the shadow zone; thus, on the synthetic section for shot P2 (Fig.4.13), there is no turning ray branch present, and the branch is truncated on the synthetics for shot P8 (Fig. 4.12), receiver X45 (Fig.4.13), and receiver X34 (Fig 4.14). However, due to the wave nature of the propagating energy, diffractions would be predicted within the shadow zone, so that reduced amplitude arrivals are expected within the region.

(9) Secondary arrivals at the Vancouver Island stations, which are most clearly seen on the observed sections for shot P13 (Fig. 4.11) and receiver X22 (Fig. 4.16), are interpreted as reflections from an upper mantle reflector. Receiver X6 (Fig. 4.17) also shows evidence of a secondary arrival, although the model traveltimes are somewhat late compared to the observed traveltimes. However, the difference is not considered serious since its magnitude is not too much larger than the average

FIG. 4.18. Ray paths showing shadow zones due to the corner at 215 km distance and 37 km depth, where the subducting oceanic crust intersects the continental Moho. Arrowheads indicate the coasts of Vancouver Island. (a) A continental slope shot at 85 km distance produces a shadow zone over the distance range 285-335 km. (b) A receiver at 305 km distance records no arrivals from shots on the continental slope east of 70 km distance.

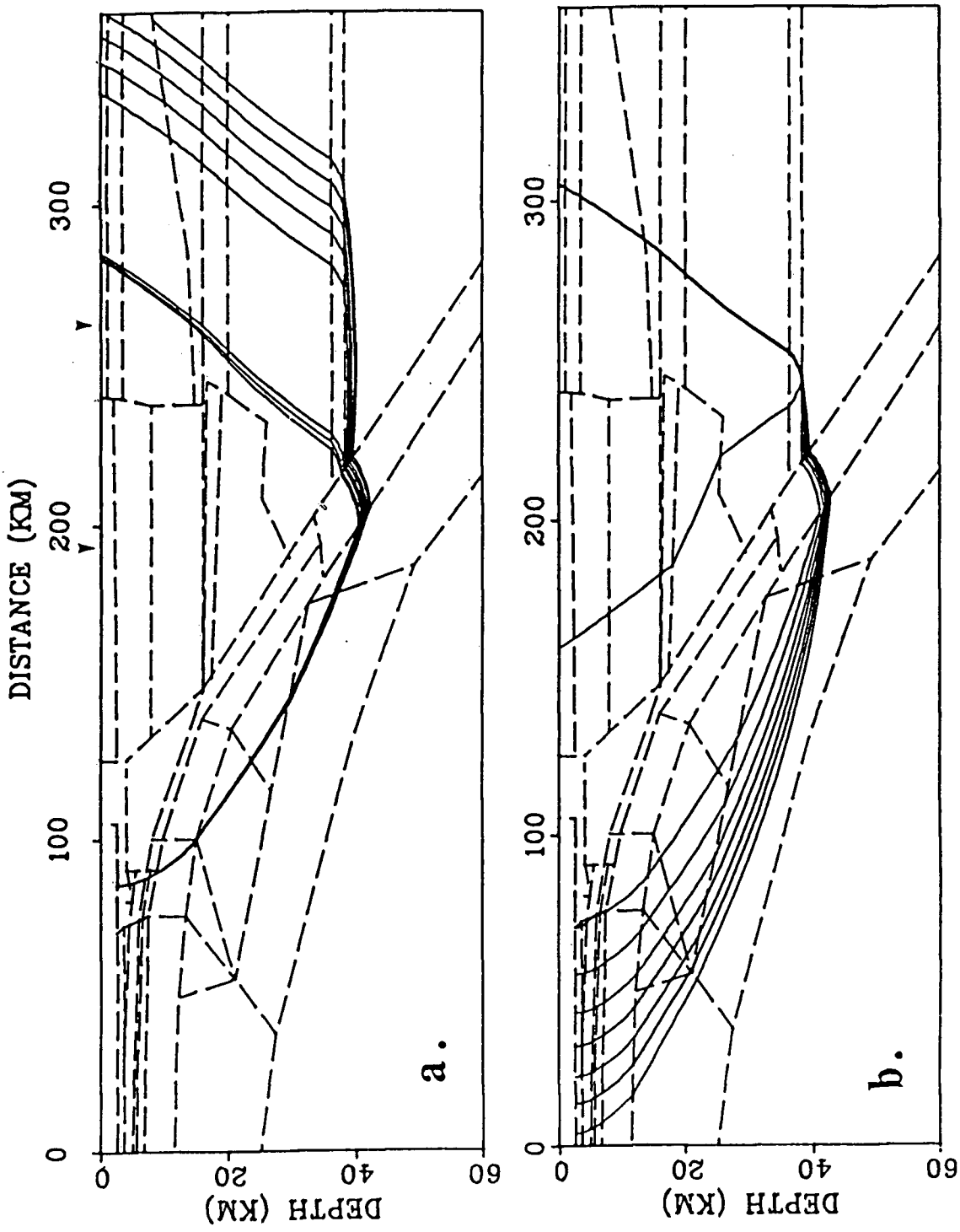
DISTANCE (KM)
0
100
200
300
0
20
40
60
DEPTH (KM)
a.
b.

picking error for all arrivals (~75 ms) and because only the secondary arrival times for shots P13 and P19 (and not receiver X6) were used in the ray trace inversion procedure which determined the overall traveltime fit.

The amplitudes of wide-angle reflections are not very sensitive to the magnitude of the velocity contrast at the boundary from which they are reflected (Braile and Smith 1975). However, the amplitudes do depend on whether the velocity contrast is positive or negative, with larger amplitudes produced from a positive contrast. Figure 4.19 shows the synthetics for shots P19 and P13 through a model identical to the final model except that the velocity below the reflector is 8.6 km/s instead of 7.7 km/s. When compared to the synthetics and observed data in Figures 4.10 and 4.11, it is seen that the reflected arrivals at the Vancouver Island stations in Figure 4.19 are too large in comparison to the arrivals at the mainland stations. It is on this basis that a low velocity of 7.7 km/s is the preferred velocity in the final model for the region below the upper mantle reflector.

(10) Upper mantle reflections to the mainland receivers have been included on all synthetic sections. Based on the data, they are not <u>necessary</u> to the modelling, since only reflections to the Vancouver Island receivers are observed as distinct arrivals. However, reflections to the far stations are <u>possible</u> arrivals and so they are included for completeness and to show their possible effect as an additional arrival at a time slightly delayed from that of the mantle turning ray. But it should be emphasized that the existence of the upper mantle

FIG. 4.19. Synthetic seismograms for shots P19 and P13 for rays through the same velocity model as the final model (Fig. 4.7), except that the velocity below the upper mantle reflector is 8.6 km/s instead of 7.7 km/s. The amplitudes of the reflections at the Vancouver Island stations, which are the secondary arrivals for distances 200-260 km from shot P19, are too large in comparison with the observed record sections (Fig. 4.3).

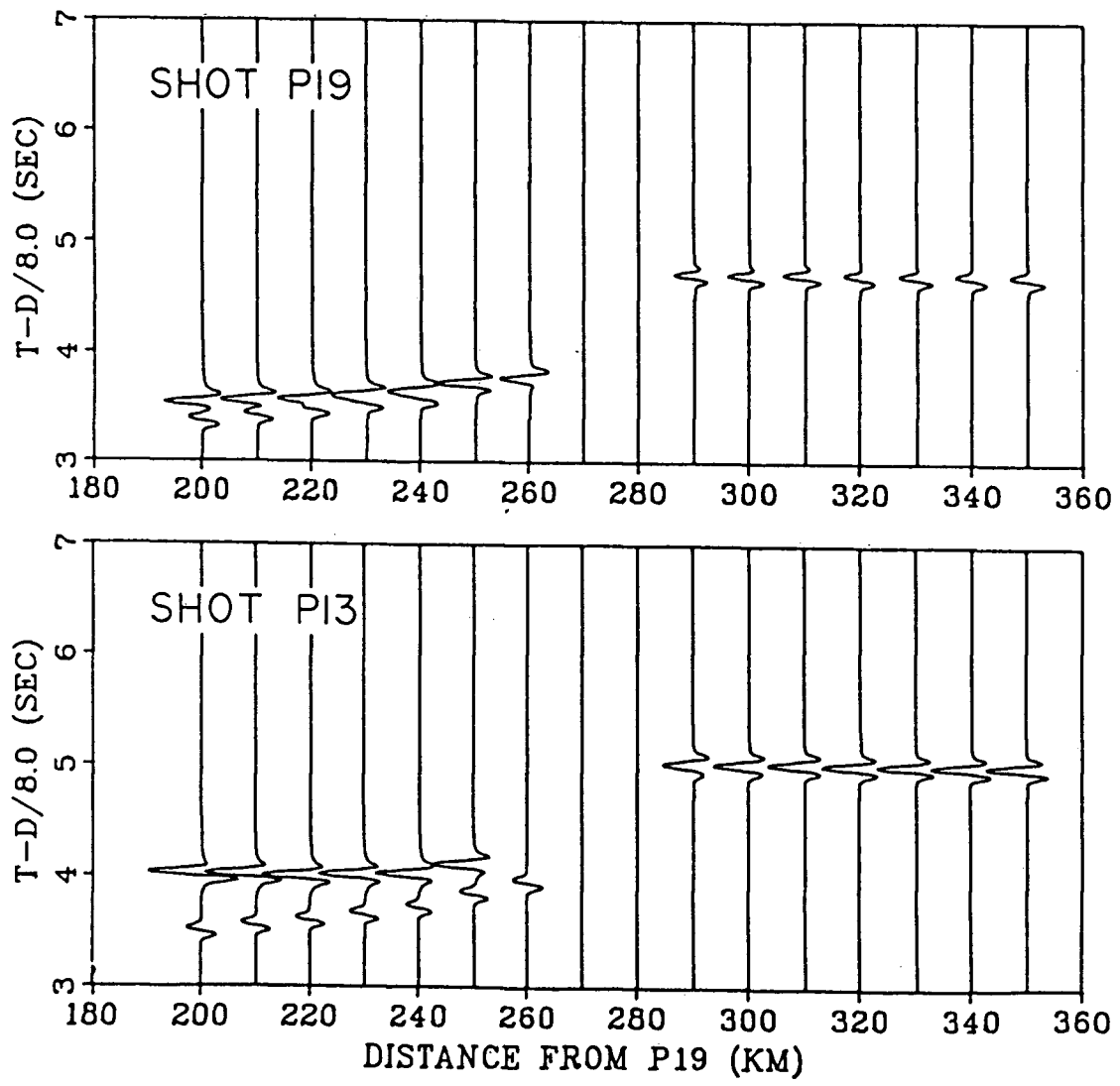
V = 8.6 KM/S
SHOT P19
SHOT P13
T-D/8.0 (SEC)
3
4
5
6
7
180
200
220
240
260
280
300
320
340
360
DISTANCE FROM P19 (KM)

boundary is speculative for distances greater than 110 km, which corresponds to the reflection point for the easternmost Vancouver Island station (see ray trace diagram, Fig. 4.9).

With the velocity below the reflecting boundary lower than the velocity above, the phase of reflection is opposite to that of the mantle turning ray. Thus, for shot P19 (Fig. 4.10), where the arrival times of the reflected and turning rays differ by less than 20 ms, the effect of the reflection on the synthetics is to decrease the amplitude of the turning ray alone. For shot P13 (Fig. 4.11), the difference is ~75 ms and, assuming a source wavelet of length 200 ms, the combined arrival is elongated and has a main peak amplitude larger than that of the turning ray alone. For shot P8 (Fig. 4.12), the reflected and turning ray wavelets start to separate, although the reflected ray is the only arrival on the synthetics at 290 and 300 km distance from P19 because the turning ray expected at those distances is stopped by the corner between the continental Moho and the subducting ocean crust. For shot P2 (Fig. 4.13), the reflected wave is the only arrival on the synthetics, with the turning ray being completely blocked by the corner.

4.6 Alternate models consistent with the seismic data

In the final onshore-offshore model discussed in the previous section, certain features were introduced which were not controlled by the refraction seismic data but rather were suggested by more general tectonic or geological principles. In particular, most features of the downgoing oceanic crust and even its very existence in the model are not necessary to

satisfy the refraction seismic constraints, but are included because the weight of the other geophysical evidence, both locally and worldwide, lends strong support to its presence (Keen and Hyndman 1979). The uncertainty of the characteristics of the downgoing crust in the seismic model will be illustrated with two alternate models which fit the traveltimes for P19, P13 and P8 equally as well as the final model and have similar amplitude behavior. The purpose of presenting two alternative models is to show the variability permitted by the seismic data and also to emphasize those features common to all models.

The simplest model consistent with the seismic data is essentially the preliminary model of Ellis et al. (1983) modified by the addition of an upper mantle reflector (Fig. 4.20). The oceanic crust is shown as terminating against the continental crust, and the structure below Vancouver Island as determined by McMechan and Spence (1983) is extrapolated to the region below the continental shelf. The features of the preliminary model (Fig. 4.20) in common with the final model (Fig. 4.7) are (1) the mantle velocity and gradient (8.0 km/s and 0.01 km/s/km), (2) a flat-lying continental Moho at a depth of 40 km or less, (3) the geometry of the upper mantle reflector (the depth of the boundary when extrapolated beneath P19 is ~22 km for the preliminary model and ~25 km for the final model, and the corresponding dips are ~8° and ~7°), and (4) a shallow high-velocity pathway at depths of 30 km and less beneath western Vancouver Island and the continental shelf. The major difference between the models, apart from the termination of the oceanic crust, is that the high-velocity pathway in the final model

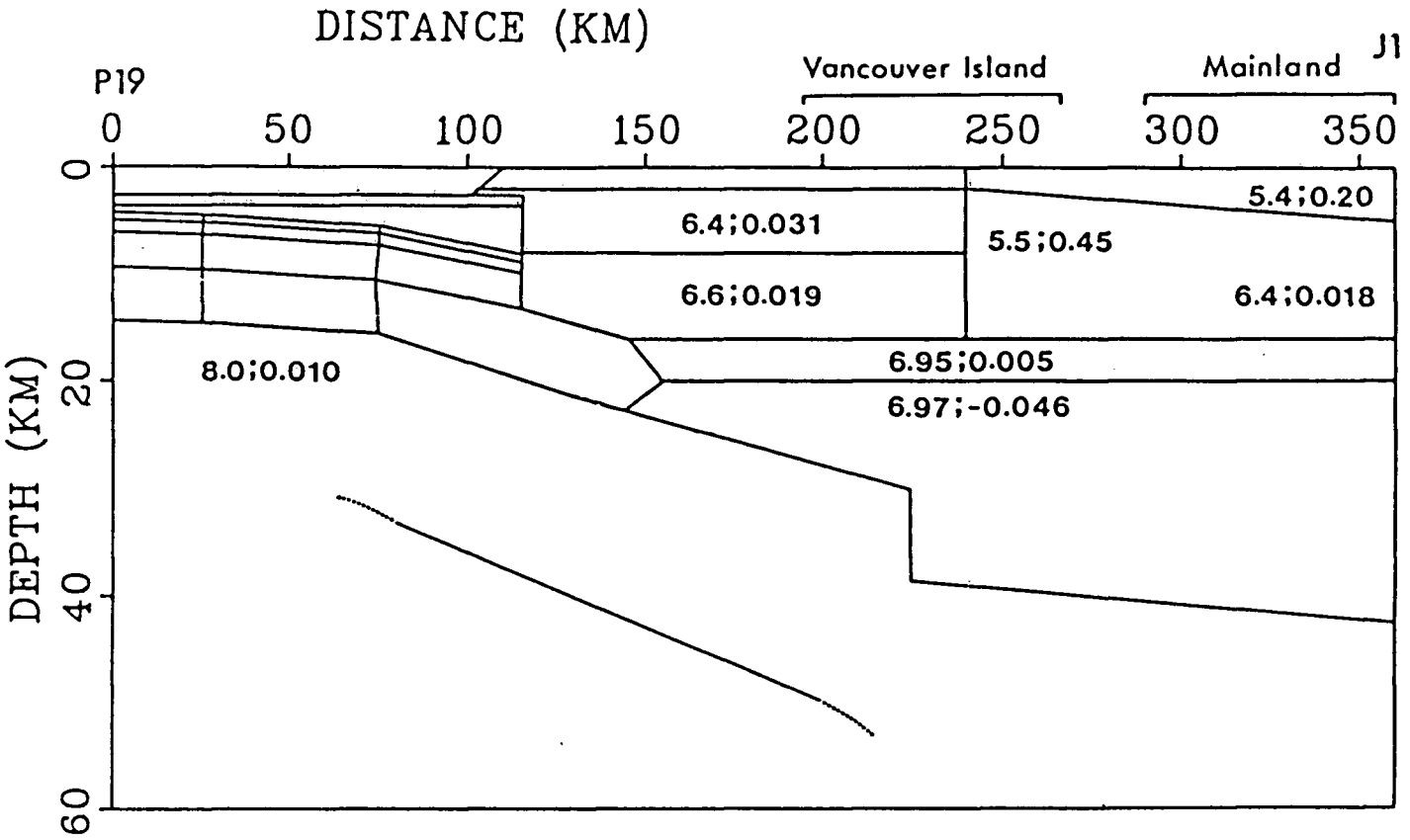

FIG. 4.20. The preliminary velocity model of Ellis et al. (1983), modified by the addition of an upper mantle reflector. The oceanic layers are shown terminating against the continental crustal layers. The ray trace inversion procedure has been applied to the model, and the model traveltimes for shots P19,P13 and P8 fit the observed traveltimes with an rms residual of 73 ms, equivalent to that for the final model.

appears as a sliver of mantle material at 20-25 km depth, whereas in the preliminary model the depth to mantle suddenly increases from ~29 km to ~39 km in a fault-like feature under central Vancouver Island.

To better satisfy tectonic principles, the preliminary model may be modified by requiring that the oceanic crust should be continuously subducting throughout the region, instead of terminating abruptly against the continental crust. In the intermediate model of Figure 4.21, the oceanic layers are extrapolated eastward, instead of the continental layers being extrapolated westward as in the preliminary model of Figure 4.20. Because the slab of subducting oceanic crust is parallel-sided, all rays to a set of receivers are affected equally, and the major structural characteristics of the preliminary model are not significantly changed. Dips of boundaries are comparable in the two models, and the sudden increase in thickness of the continental crust beneath central Vancouver Island appears as a kink in the subducting oceanic crust. The intermediate model also incorporates considerations from pressure-temperature data that basalt in the oceanic crust transforms to eclogite, with associated increases in density and velocity to values greater than those of normal mantle. The stability field of basalt-eclogite as shown by Grow and Bowin (1975, Fig. 5) indicates that the phase change occurs at depths as shallow as 30 km. Thus, an elevated velocity of 8.2 km/s is used in the intermediate model for the portion of oceanic crust below approximately 30 km depth. It should be noted that this effect is not incorporated in the final refraction model, since there

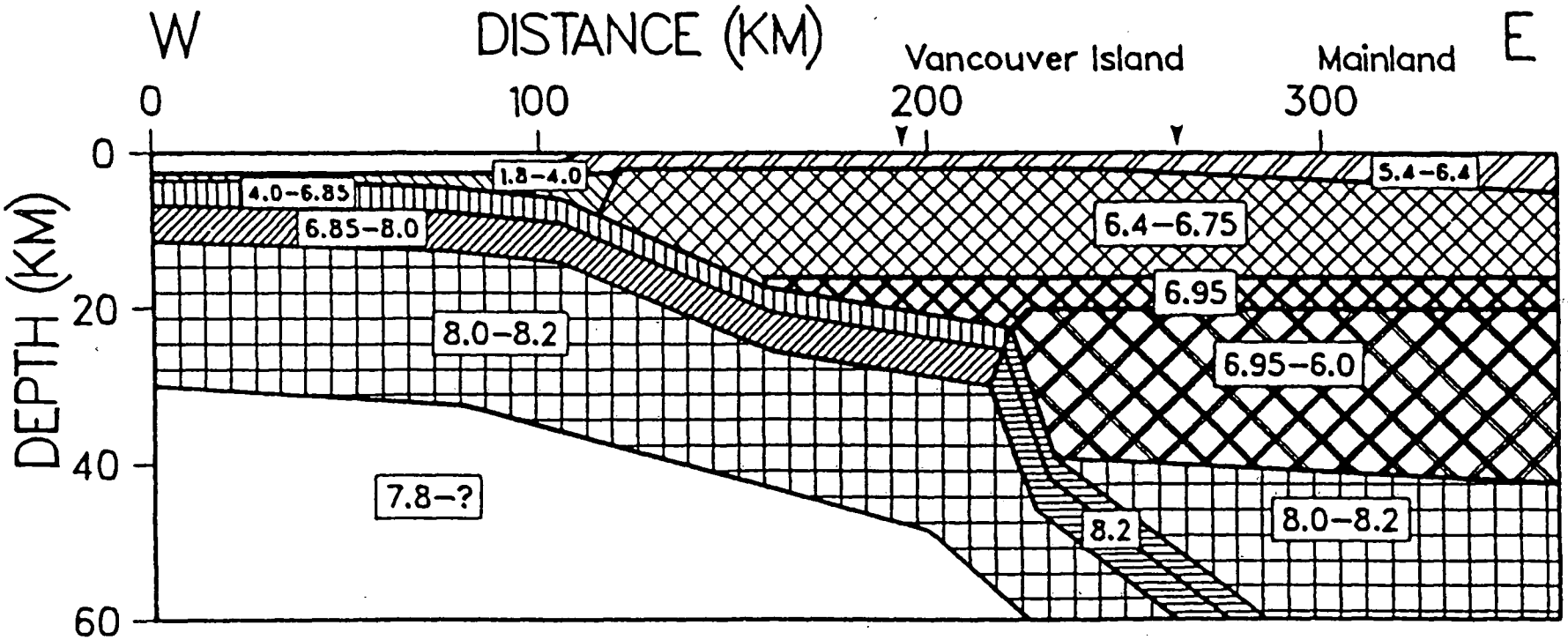

FIG. 4.21. Intermediate velocity model in which the oceanic layers determined by Waldron (1982) are extrapolated under the continental crust. The ray trace inversion procedure has been applied to the model, and the rms residual for shots P19,P13 and P8 was 75 ms, equivalent to that for the final model.

is controversy regarding the depth at which the phase transformation occurs. In particular, Fukao et al. (1983) presented more direct seismological evidence that the subducting oceanic crust remains untransformed down to a depth of about 60 km. The shallower phase change is included in the intermediate model only to illustrate that it is not inconsistent with the onshore-offshore data.

Although the intermediate model has a continuous oceanic crust and is generally consistent with the seismic data, there are still some difficulties with the model. The main problem is the existence of the kink in the downgoing crust. The kink may perhaps be interpreted as a normal fault in the ocean crust, downthrown towards the continent, and in some subduction zones such as the Aleutian arc (Spence 1977), normal faulting has been suggested as a descent mechanism for the slab. However, it is difficult to accept a fault with a throw of ~10 km, especially since there is no substantial seismicity associated with the fault, i.e. in the depth range 20-30 km beneath central Vancouver Island. Another problem with the intermediate model is that it is not totally consistent with the lower crustal portion of the McMechan and Spence (1983) model for line IV along the length of Vancouver Island. Although the models are consistent where line IV and the onshore-offshore line I intersect (at a point 230 km from shot P19; see location map, Fig 1.3), the bend in the middle of line IV causes the deeper ray paths from the southern shot point to the northern receivers to cross line I at distances up to 20-25 km west of the intersection point. Thus, the continental Moho and the low-velocity zone above the Moho

should extend as far west as ~205 km from shot P19. If this existed in the intermediate "kink" model, then the kink in the downgoing crust would become a break, and the desired continuity of the oceanic crust would be lost.

The two models evolved into the final model (Fig. 4.7) mainly by invoking the requirement that the subducting oceanic crust be continuous. With this requirement, which is itself not necessary to satisfy the refraction data but rather is implied by more general principles, a sliver of high-velocity material must then be introduced above the subducting crust on the basis of the seismic constraints. In particular, the shallow high-velocity pathway is required to allow arrivals at the Vancouver Island stations to be advanced by ~1 s relative to the arrivals at the mainland stations.

In both alternate models and in the final model discussed in section 4.5, the depth of the continental Moho was fixed at a value near 40 km. Although this depth is constrained by the preferred interpretation of McMechan and Spence (1983), alternate interpretations of the line IV dataset allow the Moho to be as deep as 52 km (Fig. 1.5). If a Moho depth >40 km were used in the onshore-offshore interpretation, then a major effect on the final model would be a larger shadow zone, due to the corner where the subducting ocean crust meets the continental Moho, for the turning rays to the far offset receivers (Fig. 4.18). It is difficult to quantify the implications of a larger shadow zone, since a 2D seismogram routine including diffraction arrivals would be required. However, it is my impression that the size of the current shadow zone is sufficiently large; with

a larger shadow zone, too many receivers would be without turning ray arrivals. Nevertheless, it is still possible to model the data using only reflections to the far-offset stations (although the fit deteriorates because amplitudes at the far stations would be too small). Thus, with a deeper continental Moho, the effect on the remainder of the model will be similar to that shown in Figure 2.8, in which different Moho depths were used in the subduction zone test model. That is, a deeper Moho implies a faster mantle velocity and also a shallower depth for the upper mantle reflector.

4.7 Gravity model across the subducting margin

As discussed in the introductory chapter, the gravity anomaly data in the Pacific Northwest exhibit a low-high couple which is similar to other subduction zones. The gravity low normally corresponds to the trench and the high to the arc-trench gap, which in the Pacific Northwest includes all of Vancouver Island. The Vancouver Island "gravity-seismic conflict", which was the main concern of Riddihough (1979), arises because the gravity high demands a relatively thin crust in which material with mantle density occurs at depths of 30 km or less, whereas seismic interpretations on Vancouver Island suggest that the crust is much thicker.

The interpretation of McMechan and Spence (1983), in which the minimum crustal thickness beneath Vancouver Island is 37 km, provides the major seismic evidence which constrains the crust to be thicker than that implied by the gravity data. The onshore-offshore seismic model must obviously be consistent with

the interpretation of McMechan and Spence (1983), and so it can immediately be recognized that a gravity model along the cross-island profile will not bring about a straightforward resolution of the gravity-seismic conflict. However, because of the presence of the high-velocity sliver beneath western Vancouver Island in the 20-25 km depth range, it can be qualitatively stated that perhaps the severity of the conflict will be reduced. The limitation of the cross-island model in resolving the conflict is that the high-velocity sliver does not extend eastwards sufficiently far.

The resolution of the conflict requires special arguments which justify the existence of anomalous lower crustal material with high density and low compressional velocity. Riddihough (1979) pointed to known basic metamorphic rocks with the required properties, and suggested that the anomalous material could originate in the wedge of material above the downgoing lithosphere due to expected conditions of low temperature, high pressure and hydrous environment. Thus, the implication of this solution is that the seismic Moho, which marks a velocity contrast, does not correspond to a discontinuity marking a density contrast.

4.7.1 Method

The observed gravity profile along a line very close to the onshore-offshore profile was quantitatively modelled utilizing the constraints of the cross-island seismic model and the concept that the lower crust may contain anomalous high-density, low-velocity material. The observed gravity values (dashed lines

in Figs. 4.22b and 4.22c) and the ocean bottom topography along the line were supplied by Riddihough (pers. comm. 1982).

The interpreted cross-island gravity model is shown in Figure 4.22a. The model incorporates most features of the gravity model of Waldron (1982), which was based on his marine seismic interpretation for the portion of the ocean crust as far east as the top of the continental slope. A few minor modifications were made to Waldron's gravity model; the number of sedimentary blocks was reduced, and an upper crustal density of 2.72 g cm^{-3} was used, instead of 2.62 g cm^{-3}. The latter change arose because outside the region of the ocean crust and shelf Waldron (1982) used the same model as Riddihough (1979), in which the positions of a number of boundaries (including the base of the lithosphere) were slightly different from those implied by the cross-island seismic interpretation. Densities in other regions of the cross-island gravity model are the same as in Riddihough (1979): crustal density is 2.92 g cm^{-3}, lithosphere mantle is 3.34 g cm^{-3}, oceanic asthenosphere is 3.295 g cm^{-3}, continental asthenosphere is 3.285 g cm^{-3}, and the anomalous material above the downgoing lithosphere is assigned a density of 3.30 g cm^{-3}. Finally, the sliver of high-velocity material embedded in the continental crust is given a density of 3.28 g cm^{-3}, somewhat less than normal mantle density.

As in the interpretation of Riddihough (1979), the density of the downgoing oceanic crust is assumed to increase to the density of the surrounding mantle. The crustal density would be expected to increase beyond that of normal lithosphere due to the basalt/eclogite phase transition. But in the gravity model,

FIG. 4.22. (a) Density model, with densities in g cm^{-3}, based on the observed gravity and on the final velocity model for the onshore-offshore profile. Arrowheads indicate coasts of Vancouver Island. The shaded region is the portion of the lower seismic crust with an anomalous low-velocity high-density relationship. The horizontal dashed line at the base of this region is the seismic Moho at 37 km depth. (b) Observed gravity values (dashed line) and theoretical gravity values (solid line) for which the shaded region of the density model is assigned a density of 3.30 g cm^{-3}. (c) Observed gravity values (dashed line) and theoretical gravity values (solid line) for which the shaded region of the density model is assigned a density of 2.92 g cm^{-3}, the normal density expected for crustal material. The misfit illustrates the basic gravity-seismic conflict.

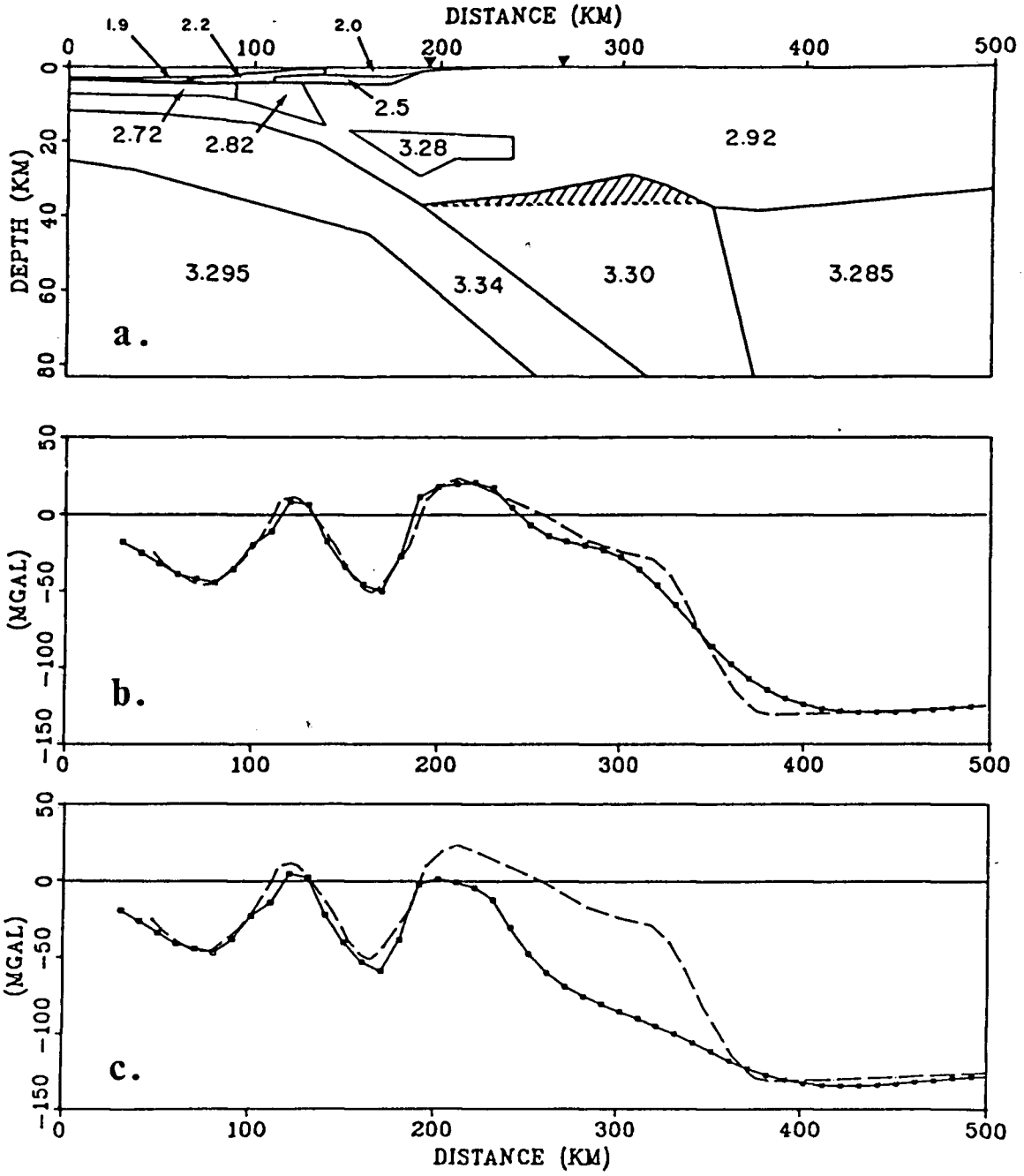
DISTANCE (KM)
1.9
2.2
2.0
0
100
200
300
400
500
2.5
2.72
2.82
3.28
2.92
DEPTH (KM)
0
20
40
60
80
3.295
3.34
3.30
3.285
a.
50
0
-50
-100
-150
(MGAL)
b.
c.
DISTANCE (KM)

as in the seismic velocity model, the depth at which the phase change occurs is assumed to be 60 km or greater. In any case, even if the oceanic crust were assigned an elevated density of 3.56 g cm^{-3} below 30 km depth, the gravity effect due to the increased density would be small and have a much longer wavelength than that in the observed gravity data.

The base of the lithosphere beneath the western ocean basin was assumed to correspond to the upper mantle reflector in the seismic velocity model. Beneath shot P19 the depth of the reflector is 25 km (although it could be as deep as 31 km without altering any part of the seismic model through which rays travel). With 2.6 km of water and ~1 km of sediments, lithospheric thickness is ~21.5 km. This value is slightly larger than the expected thickness of around 20 km for the lithosphere (aged 6-9 Ma at the continental margin), based on the age-thickness relationship of Yoshii et al. (1976). The top of the subducting lithosphere was extrapolated to 100 km depth beneath the volcanic chain, which is in accord with its depth in other active margins (Barazangi and Isacks 1976). East of the Coast Mountains, a value of 33 km was used for the Moho depth (Berry and Forsyth 1975). Below the Moho in this region, asthenospheric densities were used for the mantle; lithospheric mantle was assumed to be absent (Fulton and Walcott 1975; Riddihough 1979). The structures at the edges of the model were extended out to ±3000 km and down to 200 km depth, so that the effect of material outside these limits could be safely assumed to be negligible.

The gravity field due to the structural model was

calculated using a standard two-dimensional algorithm based on Talwani et al. (1959). The model parameters which were varied in order to match the observed and calculated gravity profiles were mainly: (1) the depth to the top of the anomalous wedge with density 3.30 g cm^{-3}, and the depth to the nearby continental Moho over the distance range 250-400 km, and (2) the boundaries of the sedimentary blocks in the distance range 110-200 km, much of which corresponds to the sediments of Tofino Basin.

4.7.2 Interpretation

The final gravity model is shown in Figure 4.22a. The shaded region in the figure corresponds to that portion of the lower seismic crust with an anomalous high-density low-velocity relationship, and is assigned a density of 3.30 g cm^{-3} for the final model. The corresponding theoretical gravity values are displayed in Figure 4.22b, together with the observed gravity values along the profile. Figure 4.22c shows the theoretical gravity values when all of the lower seismic crust, including the shaded region, is assigned a normal crustal density of 2.92 g cm^{-3}. Thus, the disagreement between these theoretical values and the observed gravity illustrates the current extent of the gravity-seismic conflict.

For the final gravity model, most of the features of the gravity profile above the ocean basin and continental shelf are due to relatively near-surface effects. As in the interpretation of Waldron (1982), the westernmost gravity low (Fig.4.22b) reflects the ocean basin sediments increasing in thickness towards the shelf. The gravity high over the outer shelf is due

to decreasing water depth along the continental slope and also to greater sediment densities there. The negative anomaly over the main portion of the shelf is related mainly to the sediments in Tofino Basin, which increase in thickness towards the center of the basin and may also be less dense than on the outer shelf. As well, a contribution to the gravity low arises from the increasing crustal thickness in this region, as the downgoing lithospheric slab begins to bend more steeply.

The main gravity high, which extends across Vancouver Island to a point east of Georgia Strait, may be explained in terms of pockets of high-density material imbedded in the lower (seismic) crust. That is, part of the positive anomaly is due to the sliver of high-density mantle under western Vancouver Island in the depth range 20-25 km, and part is due to anomalous high-density low-velocity material beneath eastern Vancouver Island and part of the mainland. The anomalous material (the shaded zone in Fig. 4.23a) extends above the seismic Moho with a maximum thickness of only 9 km. Thus, perhaps the main result of the gravity modelling is that the size of the anomalous zone has been reduced relative to that of Riddihough (1979).

Obviously, other distributions of high-density material in the lower crust will also satisfy the gravity data. For example, an even better match between observed and calculated values would be obtained if the high-density sliver at 20-25 km depth were extended eastwards. However, this is not permitted on the basis of the refraction data, unless the extended sliver had a peculiar configuration out of the plane of the cross-island profile or were fragmented so as to be undetectable at the

wavelengths of seismic energy.

4.8 Discussion

The major objective of the onshore-offshore study was to obtain a two-dimensional velocity model to upper mantle depths across the margin where the oceanic Juan de Fuca plate subducts beneath the continental America plate. Figure 4.23 shows the resultant velocity model together with a stylized tectonic model taken from the trans-Cordillera Transect B2 of Monger et al. (1984), located along a line close to the location of the onshore-offshore profile. The tectonic model incorporates the speculative concept that assemblages corresponding to older terranes are vertically stacked and are underlain by the currently descending oceanic plate. The model is based on surface geology, other geophysics and also on the seismic results from this thesis, which has provided a representation of the geometry of the subducting lithospheric plate including possible complexities associated with the subduction zone.

The final velocity model is actually a composite model, requiring the interpretation of several associated seismic datasets. The velocity structure of the oceanic crust, including the presence of a relatively low-velocity melange beneath the outer continental shelf, was determined by Waldron (1982) in a marine refraction interpretation. The basic seismic structure of the continental crust was established by McMechan and Spence (1983) in the interpretation of a refraction line along the length of Vancouver Island; the most important feature of the interpretation was a preferred value of 37 km for the crustal

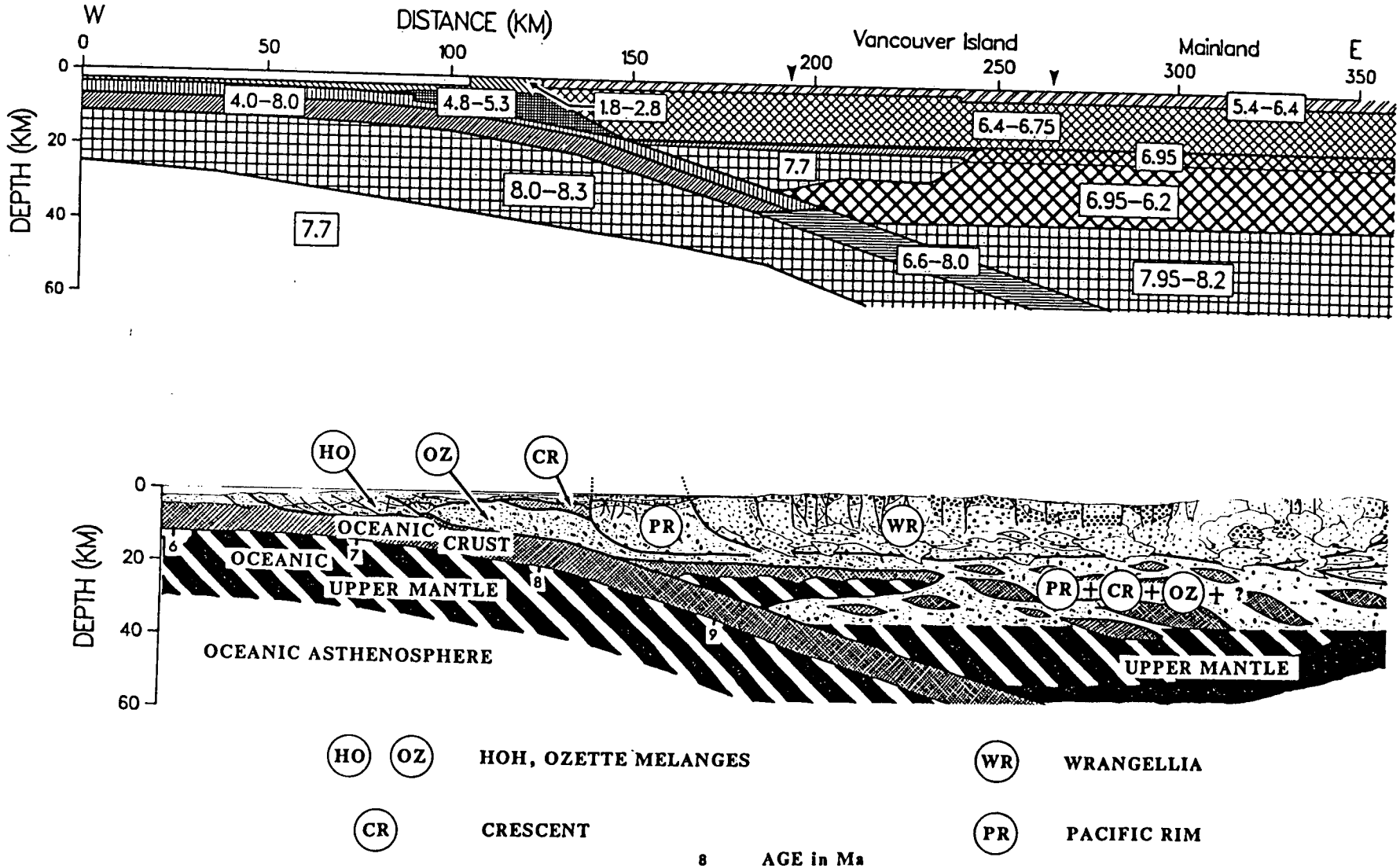

FIG. 4.23. Final velocity model for the onshore-offshore profile and stylized tectonic cross section modified from the trans-Cordillera Transect B2 of Monger et al. (1984). No vertical exaggeration.

thickness, which also implied the existence of a low-velocity zone in the lower crust. With the oceanic and continental structures as known quantities, the interpretation of the onshore-offshore profile across Vancouver Island was able to extend the crustal models to the upper mantle region.

Although the subducting oceanic crust was not directly observed, the onshore-offshore dataset provides some indirect control on the dip of the oceanic crust and the point at which it bends to dive under the continental crust. The controlling information is that the dip at the base of the melange unit is relatively small (3° or less) under all shots on the outer continental shelf. Thus, assuming the other oceanic layers dip at the same angle as the base of the melange, the bend in the subducting slab must occur landward of the easternmost shot, which is 35 km east of the foot of the continental slope. This conclusion is consistent with the results of Taber (1983), who more directly observed the bend in the slab at a point nearly 50 km landward of the beginning of the slope at the Washington continental margin. Taber (1983) suggested that large rates of sedimentation caused the foot of the slope to move seawards, and also resulted in the lack of an ocean bottom trench. With the depth of the top of the oceanic crust approximately known under the continental slope, the dip of the slab under the continental shelf may be determined because the depth of the slab under western Vancouver Island can be no shallower than 37 km, the continental Moho depth found by McMechan and Spence (1983). The average dip is 14-16°, which is larger than the value of 9-11° found by Taber (1983) from seismicity studies and from an

onshore-offshore refraction profile off the coast of Washington. However, relatively small differences in structure are perhaps to be expected, since the studies of Taber (1983) were located to the south of a bend in the continental margin at the latitude of Puget Sound (Fig. 1.1), while the present study is to the north of the bend.

The base of the subducting lithosphere in the region can be associated with the upper mantle reflector in the velocity model, dividing oceanic upper mantle from oceanic asthenosphere (Fig. 4.23). For lithosphere of age 9 Ma, the expected thickness is about 20 km, and this corresponds reasonably well with the depth of the upper mantle reflector. As well, the preferred velocity below the boundary is less than the velocity above, which is consistent with the expected relative velocities of lithosphere and asthenosphere.

The subduction zone in the Vancouver Island region appears to be complicated by an anomalous feature above the downgoing oceanic crust. On the basis of the onshore-offshore refraction dataset, a sliver of material with mantle-type velocities (7.7 km/s) is present at the 20-25 km depth range beneath western Vancouver Island and the inner continental shelf. A similar localized region of high-velocity material at 20 km depth was independently predicted from the refraction dataset along Vancouver Island, interpreted by McMechan and Spence (1983) (Fig. 1.4). A map view showing the location of these high-velocity regions and their possible interconnection is shown in Figure 4.24. Beneath the southern tip of Vancouver Island, western Washington and western Oregon, Langston (1981) found a

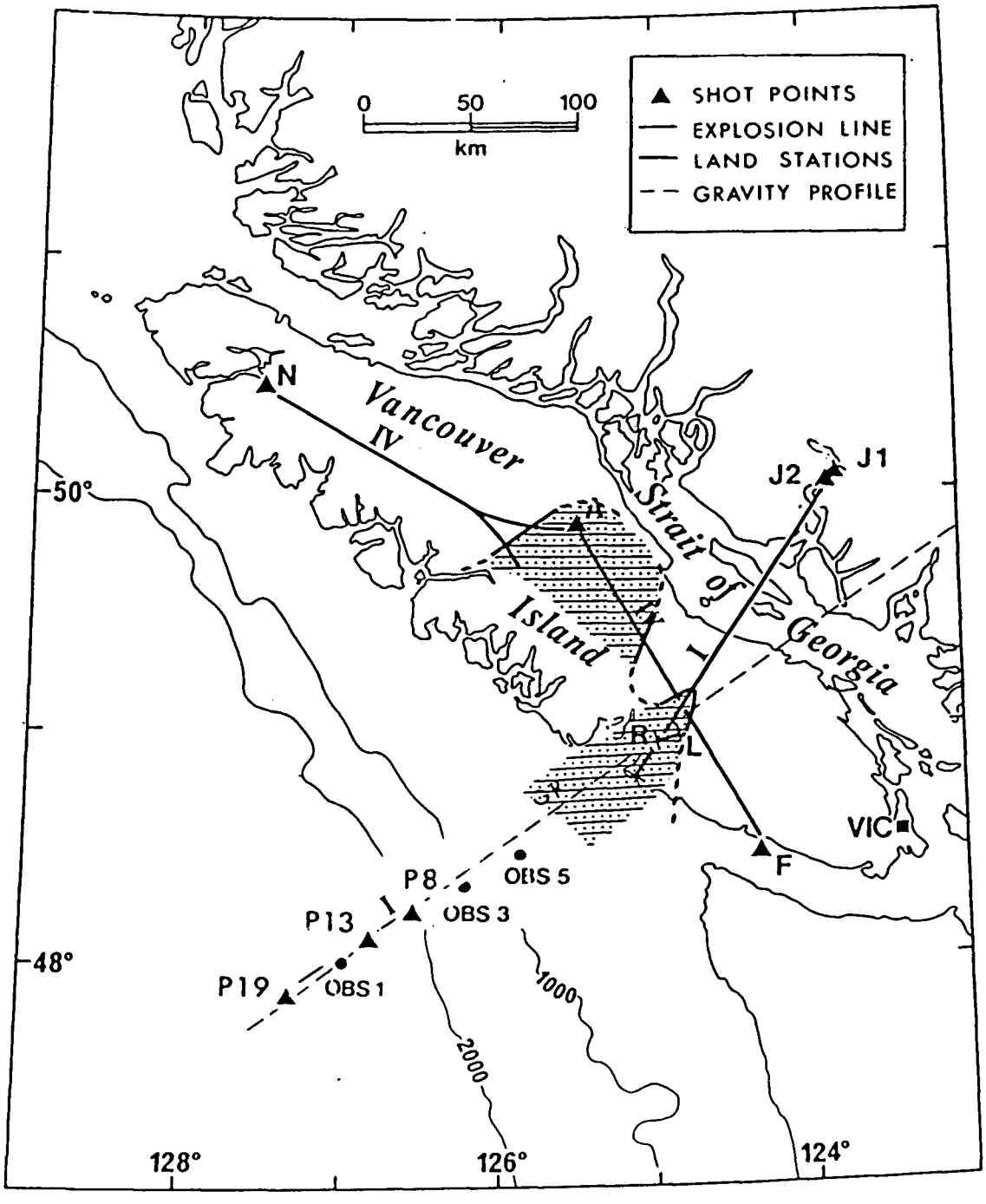

FIG. 4.24. Shaded region shows the possible extent of pockets of high-velocity material lying at 20 km depth beneath Vancouver Island. The boundary of the shaded region is indicated by a solid line where its location is reasonably well-controlled, and by a dashed line where its location is speculative.

region of mantle-type velocity at 16 km depth, below which was a low-velocity zone and a second region of high velocity starting at 40 km depth. He interpreted the shallow high-velocity region as older indigenous mantle and the lower one as mantle related to the currently subducting ocean lithosphere. Similar arguments may apply for the shallow, high-velocity regions beneath Vancouver Island. That is, the speculation can be made that the features are remnants of a subducted slab, perhaps stranded in the past when the locus of subduction jumped westward. Such a reorganization of subduction geometry has been suggested to explain the existence of Tofino Basin on the continental shelf, which may then have been the former trench (Dickinson 1976; Riddihough 1979).

The seaward jumping of a subduction zone may be related to the arrival of an accreted terrane at the continental margin (Jones et al. 1982). At the same time, thrust faulting associated with the collision process tends to thicken the crust to continental proportions. In the tectonic model of 4.23b, several adjacent accreted terranes are represented. These include the Wrangellia terrane WR on Vancouver Island and the mainland (Jones et al. 1977; Muller 1977), the Pacific Rim Complex PR on the westernmost coast of Vancouver Island and extrapolated offshore (Muller 1977), the Ozette and Hoh melanges OZ and HO under the outer continental shelf and slope (Snavely and Wagner 1981; Waldron 1982), and a fragment of Crescent volcanics CR identified as a detached slab of Eocene oceanic crust (Yorath and Currie 1980; Yorath 1980). The terranes form distinct units laterally, but in addition the speculation has

been made that the thrust faulting has resulted in vertical stacking of the terranes as well (Monger et al. 1984). Thus, beneath Wrangellia there might be a fragmented mixture of several terranes, including Pacific Rim plus more westerly terranes such as Crescent and Ozette (Fig. 4.23b).

Compared to the velocity model from the onshore-offshore refraction profile (Fig. 4.23a), the speculative region below Wrangellia corresponds to the low-velocity zone in the lower "continental" crust and also includes the high-velocity sliver above the subducting oceanic crust. The seismic low-velocity zone may thus be made up of pockets of subducted or underthrust material from a number of terranes, and the low velocities may result from the melange-like nature of the region. The sliver, which is most likely mantle material but also may consist of high-velocity lower crustal material, may be a large fragment equivalent to the detached slab of oceanic crust beneath the continental shelf (CR in Fig. 4.23b).

The interpretation of the onshore-offshore refraction data has added significant details to the original subduction zone model of Riddihough (1979), which was based on gravity, heat flow and limited seismic data. However, a gravity interpretation constrained by the new seismic model leads to similar conclusions as those of Riddihough (1979). The main conclusion from the gravity modelling is that special high-density low-velocity material is required in some portions of the lower crust. Riddihough (1979) has suggested that the formation of the anomalous material may be due to conditions of high pressure, low temperature and hydrous environment above the subducting

crust. In the new seismic model, a sliver of mantle material, with a normal velocity-density relationship, was found in the lower crust beneath western Vancouver Island. Thus, the size of the anomalous zone, relative to that of Riddihough (1979), has been reduced to a pocket of material above the seismic Moho with a maximum thickness of only 8 km (Fig. 4.22a).

An alternative origin for the unusual high-density low-velocity material may perhaps be found in the speculative tectonic model discussed previously. The properties of the anomalous material may not be due to the current environment above the subducting slab, but rather the material had formed elsewhere and been transported to the region as part of an accreted terrane, some of which was thrust under the stack of terranes already in place. If accreted terranes in fact have their modern analog in some of the plateaus present in today's oceans, then the origin of the anomalous material is related to the origin of the oceanic plateaus, the crustal structure of which is intermediate between continental and oceanic crustal structure (Ben-Avraham et al. 1981). That is, the gravity-seismic conflict in the Vancouver Island region is another manifestation of the complexity that can arise in processes involving the generation and accretion of exotic terranes.

As suggested by McMechan and Spence (1983) and Ellis et al. (1983), future studies should include reflection profiling for delineating many of the details of the seismic refraction model. A feasibility study has already been carried out, as part of the Vancouver Island Seismic Project, to determine whether coherent reflections to upper mantle depths could be acquired in this

tectonic regime (Clowes et al. 1983a). The program included a 10 km 1200% common depth point explosion survey; the location of the reflection line (RL in Figs. 1.3 and 4.24) was very close to the onshore-offshore line I. Two clear reflections were present across the record section near 4.4 s and 7.0 s two-way traveltime, and two bands of coherent energy were observed near 9.5 s and 10.8 s. These two-way traveltimes have been converted to depth using the refraction velocity model, and the corresponding depths are shown superimposed on the refraction model in Figure 4.25. The uppermost reflector A correlates well with the refractor at 16 km depth determined by McMechan and Spence (1983). The second reflector C near 24 km depth could correspond with the base of the high-velocity sliver, although it should be kept in mind that this boundary was not well-constrained in the refraction model. The third possible reflector D at 31 km depth lies in the middle of the crustal low-velocity zone of McMechan and Spence (1983). The deepest reflector E at 37 km depth possibly correlates with either the continental Moho or the top of the subducting oceanic crust.

The availability of a seismic refraction model and the encouraging results of the reflection feasibility study has led the Canadian Lithoprobe Steering Committee to designate Vancouver Island as the site of a major Vibroseis[1] reflection program to be carried out in May-June 1984. The program includes at least 150 km of 3000%-coverage profiles, the majority of which is a profile across Vancouver Island following essentially

---

[1] copyright Continental Oil Company

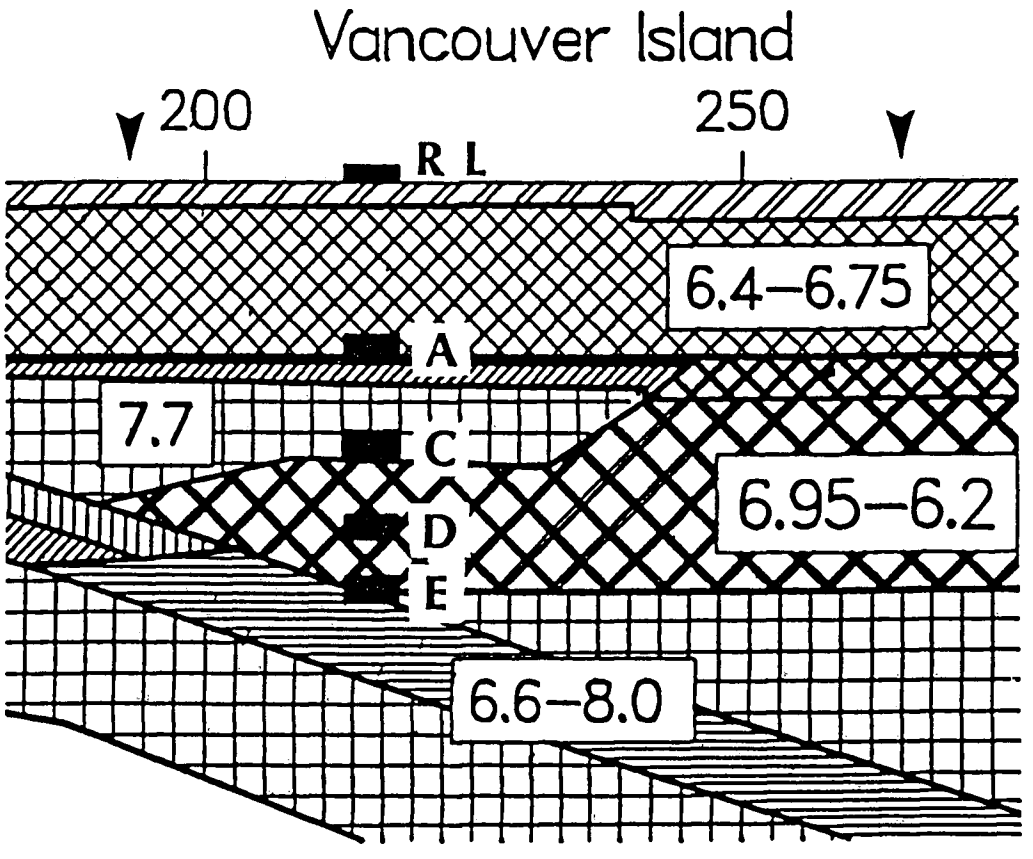

FIG. 4.25. Enlargement of the final velocity model under Vancouver Island. RL indicates the location of the 10 km explosion reflection line, also shown on the location map (Figs. 1.3 or 4.24). The equivalent depths of reflectors A, C, D and E on the reflection record section are superimposed on the model.

the same line as the cross-island refraction profile. This high-resolution study may thus provide nearly immediate confirmation (or repudiation) of many of the features of the refraction model.

REFERENCES

Aki, K. and W.H.K. Lee (1976). Determination of three-dimensional velocity anomalies under a seismic array using first P arrival times from local earthquakes, 1. A homogeneous initial model, J. Geophys. Res. 81, 4381-4399.

Aki, K., A. Christoffersson and E.S. Husebye (1977). Determination of the three-dimensional seismic structure of the lithosphere, J. Geophys. Res. 82, 277-296.

Ando, M. and E.I. Balazs (1979). Geodetic evidence for aseismic subduction of the Juan de Fuca plate, J. Geophys. Res. 84, 3023-3028.

Aric, K., R. Gutdeutsch and A. Sailor (1980). Computation of traveltimes and rays in a medium of two-dimensional velocity distribution, Pure Appl. Geophys. 118, 796-806.

Au, D. and R.M. Clowes (1982). Crustal structure from an OBS survey of the Nootka fault zone off western Canada, Geophys. J. 168, 27-48.

Barazangi, M. and B.L. Isacks (1976). Spatial distribution of earthquakes and subduction of the Nazca plate beneath South America, Geology 4, 686-692.

Ben-Avraham, Z., A. Nur, D. Jones and A. Cox (1981). Continental accretion: from oceanic plateaus to allocthonous terranes, Science 213, 47-54.

Berry, M.J. and D.A. Forsyth (1975). Structure of the Canadian Cordillera from seismic refraction and other data, Can. J. Earth Sci. 12, 182-208.

Bessonova, E.N., Y.M. Fishman, V.Z. Ryaboyi and G.N. Sitnikova (1974). The tau method for inversion of traveltimes - I. Deep seismic sounding data, Geophys. J. 36, 377-398.

Birch, F. (1964). Density and composition of the mantle and core, J. Geophys. Res. 69, 4377-4387.

Braile, L.W. and R.B. Smith (1975). Guide to the interpretation of crustal refraction profiles, Geophys. J. 40, 145-176.

Cassell, B.R. (1982). A method for calculating synthetic seismograms in laterally varying media, Geophys. J. 69, 339-354.

Cerveny, V. and R. Ravindra (1971). Theory of Seismic Head Waves, University of Toronto Press, Toronto 312 pp.

Cerveny, V. J. Langer and I. Psencik (1974). Computation of geometrical spreading of seismic body waves in laterally inhomogeneous media with curved interfaces, Geophys. J. 38, 9-19.

Cerveny, V., I. Molotkov, and I. Psencik (1977). Ray Method in Seismology, Charles University Press, Prague, 214 pp.

Cerveny, V., M.M. Popov, and I. Psencik (1982). Computation of seismic wave fields in inhomogeneous media - Gaussian beam approach, Geophys. J. 70, 109-128.

Chapman C.H. and R. Drummond (1982). Body-wave seismograms in inhomogeneous media using Maslov asymptotic theory, Bull. Seism. Soc. Am. 72, 5277-5317.

Chapman, C.H. (1978). A new method for computing synthetic seismograms, Geophys. J. 54, 481-518.

Chou, C.W. and J.R. Booker (1979). A Backus-Gilbert approach to inversion of traveltime data for three-dimensional velocity structure, Geophys. J. 59, 325-344.

Clayton, R.W. and R.P. Comer (1983). A tomographic analysis of mantle heterogeneities from body wave travel times, Eos Trans. AGU 64 , 776.

Clowes, R.M. and S.J. Malecek (1976). Preliminary interpretation of a deep marine seismic survey off the west coast of Canada, Can. J. Earth Sci. 16, 1265-1280.

Clowes, R.M., A.J. Thorleifson, and S. Lynch (1981). Winona Basin, west coast Canada: crustal structure from marine seismic studies, J. Geophys. Res. 86, 225-242.

Clowes, R.M., R.M. Ellis, Z. Hajnal and I.F. Jones (1983a). Seismic reflections from subducting lithosphere? Nature 303, 668-670.

Clowes, R.M., G.D. Spence, D.A. Waldron and R.M. Ellis (1983b). VISP II: Lithospheric structure across the Juan de Fuca/America plate margin, CGU Annual Meeting, Victoria, B.C., Program with Abstracts 8, 13.

Coney, P.J., D.L. Jones and J.W.H. Monger (1980). Cordilleran suspect terranes, Nature 288, 239-333.

Crosson, R.S. (1976). Crustal structure modelling of earthquake data, 1. Simultaneous least squares estimation of hypocentre and velocity parameters, J. Geophys. Res. 81, 3036-3046.

Crosson, R.S. (1981). Review of seismicity in the Puget Sound region from 1970 through 1978: a brief summary, in 'Earthquake Hazards of the Puget Sound Region, Washington State', J.C. Yount, editor. Open File Report, Menlo Park, California.

Delandro, W. and W. Moon (1982). Seismic structure of the Superior-Churchill Precambrian boundary zone, J. Geophys. Res. 87, 6884-6888.

Dickinson, W.R. (1976). Sedimentary basins developed during the evolution of Mesozoic-Cenozic arc-trench systems in North America, Can. J. Earth Sci. 13, 1268-1287.

Dziewonski, A.M., B.H. Hager and R.J. O'Connell (1977). Large scale heterogeneities in the lower mantle, J. Geophys. Res. 82, 239-255.

Ellis, R.M. and R.M. Clowes (1981). Acquisition of crustal reflection/refraction data across Vancouver Island, Earth Physics Branch Open File Rept. 81-11, 72pp.

Ellis, R.M., G.D. Spence, R.M. Clowes, D.A. Waldron, I.F. Jones, A.G. Green, D.A. Forsyth, J.A. Mair, M.J. Berry, R.F. Mereu, E.R. Kanasewich, G.L. Cumming, Z. Hajnal, R.D. Hyndman, G.A. McMechan, and B.D. Loncarevic (1983). The Vancouver Island Seismic Project: a CO-CRUST onshore-offshore study of a convergent margin, Can J. Earth Sci. 20, 719-741.

Fuchs, K. (1977). Structure, physical properties and lateral heterogeneities of the subcrustal lithosphere from long-range deep seismic sounding observations on continents, Tectonophysics 56, 1-15.

Fuchs, K. and G. Müller (1971). Computation of synthetic seismograms with the reflectivity method and comparison with observations, Geophys. J. 23, 417-433.

Fukao, Y., S. Hori and M. Ukawa (1983). A seismological constraint on the depth of basalt-eclogite transition in subducting oceanic crust, Nature, 303, 413-415.

Fulton, R.J. and R.I. Walcott (1975). Lithospheric flexure as shown by deformation of glacial lake shorelines in southern British Columbia, Mem. Geol. Soc. Am. 142.

Garmany, J., J.A. Orcutt and R.L. Parker (1979). Traveltime inversion: a geometrical approach, J. Geophys. Res. 84, 3615-3622.

Gebrande, H. (1976). A seismic ray-tracing method for two-dimensional inhomogeneous media, in Explosion Seismology in Central Europe: Data and Results, P. Giese, C. Prodehl, and A. Stein. eds., Springer-Verlag, Berlin, 162-167.

Green, A.G., P. Morel-à-l'Huissier, and C. Pike (1983). Interpretation of COCRUST seismic refraction data across the Superior-Churchill boundary zone and the Williston Basin, CGU Annual Meeting, Victoria, B.C., Program with Abstracts 8, 28.

Grow, J.A. and C.O. Bowin (1975). Evidence for high-density crust and mantle beneath the Chile trench due to descending lithosphere, J. Geophys. Res. 80, 1449-1458.

Haddon, R.A.W. and P.W. Buchen (1981). Use of Kirchhoff's

formula for body-wave calculations in the Earth, Geophys. J. 67, 587-598.

Hawley,B.W., G. Zandt and R.B. Smith (1981). Simultaneous inversion for hypocenter and lateral velocity variations: an iterative solution with a layered model, J. Geophys. Res. 86, 7073-7086.

Helmberger, D.V. (1968). The crust-mantle transition in the Bering Sea, Bull. Seism. Soc. Am. 58, 179-214.

Horn, J.R., R.M. Clowes, R.M. Ellis and D.N. Bird (1983). The seismic structure across an active oceanic/continental transform fault zone, J. Geophys. Res. 89, 3105-3120.

Hyndman, R.D. and D.H. Weichert (1983). Seismicity and rates of relative motion on the plate boundaries of Western North America, Geophys. J. 72, 59-82.

Hyndman, R.D., R.P. Riddihough and R. Herzer (1979). The Nootka Fault Zone - a new plate boundary off western Canada. Geophys. J. 58, 667-683.

Jacob, K.H. (1970). Three-dimensional seismic ray tracing in a laterally heterogeneous spherical earth, J. Geophys. Res. 75, 6675-6689.

Johnson, L.E. and F. Gilbert (1972). Inversion and inference for teleseismic ray data, in Methods of Computational Physics, 12, 231-266.

Jones, D.L., A. Cox, P. Coney and M. Beck (1982). The growth of western North America, Sci. Am. 247, #5, 70-84.

Jones, D.L., N.J. Silberling and J. Hillhouse (1977). Wrangellia - a displaced terrane in northwestern North America, Can. J. Earth Sci. 14, 2565-2577.

Julian, B.R. and D. Gubbins (1977). Three dimensional seismic ray tracing, J. Geophys. 43, 95-113.

Keen, C.E. and D.L. Barrett (1971). A measurement of seismic anistropy in the northeast Pacific, Can. J. Earth Sci. 8, 1056-1064.

Keen, C.E. and R.D. Hyndman (1979). Geophysical review of the continental margins of eastern and western Canada, Can. J. Earth Sci. 16, 712-747.

Langston, C.A. (1981). Evidence for the subducting lithosphere under southern Vancouver Island and western Oregon from teleseismic P wave conversions, J. Geophys. Res. 86, 3857-3866.

Levenberg, K. (1944). A method for the solution of certain nonlinear problems in least squares, Q. Appl. Math. 2, 164-168.

Marks, L.W. (1980). Computational topics in ray seismology, Ph.D. thesis, University of Alberta, Edmonton, 170pp.

McMechan, G.A. and G.D. Spence (1983). P-wave velocity structure of the Earth's crust beneath Vancouver Island, Can. J. Earth Sci. 20, 742-752.

McMechan, G.A. and W.D. Mooney (1980). Asymptotic ray theory and synthetic seismograms for laterally varying structures: theory and application to the Imperial Valley, California, Bull. Seism. Soc. Am. 70, 2021-2035.

Mitchell, H.G. and M.S. Garson (1981). Mineral Deposits and Global Tectonic Settings, Academic Press, New York, 405pp.

Monger, J.W.H. and E. Irving (1980). Northward displacement of north-central British Columbia, Nature 285, 289-294.

Monger, J.W.H., R.M. Clowes, R.A. Price, R.P. Riddihough, P. Simony and G.J. Woodsworth (1984). Continent-ocean Transect B2: Juan de Fuca plate to Alberta plains, Geol. Soc. Am. (in preparation).

Muller, J.E. (1977). Evolution of the Pacific margin, Vancouver Island and adjacent regions, Can. J. Earth Sci. 14, 2062-2085.

O'Brien, P.N.S. (1960). Seismic energy from explosions, Geophys. J. 3, 29-44.

Pavlis, G.L. and J.R. Booker (1980). The mixed discrete-continuous inverse problem: Application to the simultaneous determination of earthquake hypocenters and velocity structures , J. Geophys. Res. 85, 4801-4810.

Riddihough, R.P. (1977). A model for recent plate interactions off Canada's west coast, Can. J. Earth Sci. 14, 384-396.

Riddihough, R.P. (1979). Gravity and structure of an active margin -British Columbia and Washington, Can. J. Earth Sci. 16, 350-363.

Riddihough, R.P. (1981). Absolute motions of the Juan de Fuca plate system: resistance to subduction? Eos Trans. AGU 62, 1035.

Riddihough, R.P. (1982a). One hundred million years of plate tectonics in western Canada, Geoscience Canada, 9, 28-34.

Riddihough, R.P. (1982b). Contemporary movements and tectonics on Canada's west coast: a discussion, Tectonophysics, 86, 319-341.

Riddihough, R.P. and R.D. Hyndman (1976). Canada's active western margin -the case for subduction, Geoscience Canada, 3, 269-278.

Rogers, G.C. (1983). Seismotectonics of British Columbia, Ph.D. thesis, University of British Columbia, 247 pp.

Rona, P. (1980). Global plate motion and mineral resources, in The Continental Crust and Its Mineral Deposits, D.W. Strangway (editor), Geol. Assoc. Can. Spec. Paper 20, pp. 607-622.

Savage, J.C, M. Lisowski and W.H. Prescott (1981). Geodetic strain measurements in Washington, J. Geophys. Res. 86, 4929,4949.

Scott, J.H. (1973). Seismic refraction modelling by computer, Geophysics, 38, 271-284.

Shouldice, D.H. (1971). Geology of the western Canadian continental shelf, Bull. Can. Petr. Geol. 19, 405-436.

Snaveley, P.D.Jr. and H.C. Wagner (1981). Geological cross section across the continental margin off Cape Flattery, Washington, and Vancouver Island, British Columbia, USGS Open-File Report 81-978, 5pp.

Sorrells, G.G., J.B. Crowley and K.F. Veith (1971). Methods for computing ray paths in complex geological structures, Bull. Seism. Soc. Am. 61, 27-53.

Spence, G.D., K.P. Whittall and R.M. Clowes (1984). Practical synthetic seismograms for laterally varying media calculated by asymptotic ray theory, Bull. Seism. Soc. Am. (accepted).

Spence, W. (1977). The Aleutian arc: tectonic blocks, episodic subduction, strain diffusion and magma generation, J. Geophys. Res. 82, 213-230.

Spencer, C. and D. Gubbins (1980). Travel-time inversion for simultaneous earthquake location and velocity structure determination in laterally varying media, Geophys. J. 63, 95-116.

Steinmetz, L., R.B. Whitmarsh and V.S. Moreira (1977). Upper mantle structure beneath the Mid-Atlantic Ridge, north of the Azores based on observations of compressional waves, Geophys. J. 50, 353-380.

Taber, J.J.Jr. (1983). Crustal structure and seismicity of the Washington continental margin, Ph.D. thesis, University of Washington, 159pp.

Talwani, M., L. Worzel and M. Landisman (1959). Rapid gravity calculations for 2-dimensional bodies with application to the Mendocino submarine fracture zone, J. Geophys. Res. 64, 49-59.

Tseng, K.H. (1968). A new model for the crust in the vicinity of Vancouver Island, M.Sc. thesis, University of British

Columbia, 83pp.

Waldron, D.A. (1982). Structural characteristics of a subducting oceanic plate, M.Sc. thesis, University of British Columbia, 121pp.

Wesson, R.L. (1970). A time integration method for computation of the intensities of seismic rays, Bull. Seism. Soc. Am. 60, 307-316.

Wesson, R.L. (1971). Travel-time inversion for laterally inhomogeneous crustal velocity models, Bull. Seism. Soc. Am. 61, 729-746.

White, D.J. and R.M. Clowes (1984). Seismic investigation of the Coast Plutonic Complex-Insular Belt boundary beneath Georgia Strait, Can. J. Earth Sci. (accepted).

White, W.R.H., M.N. Bone and W.G. Milne (1968). Seismic refraction surveys in British Columbia: a preliminary interpretation, AGU Monograph 12, 81-93.

Whittall, K.P. and R.M. Clowes (1979). A simple, efficient method for the calculation of traveltimes and raypaths in laterally inhomogeneous media, J. Can. Soc. Expl. Geophys. 15, 21-29.

Wickens, A.J. (1977). The upper mantle of southern British Columbia, Can. J. Earth Sci. 14, 1100-1115.

Wiggins, R.A. (1972). The general linear inverse problem: Implication of surface waves and free oscillations for earth structure, Rev. Geophys. Space Phys. 10, 251-285.

Wiggins, R.A. and D.V. Helmberger (1974). Synthetic seismogram computation by expansion in general rays, Geophys. J. 37, 73-90.

Yole, R.W. and E. Irving (1980). Displacement of Vancouver Island: paleomagnetic evidence from the Karmutsen Formation, Can. J. Earth Sci. 17, 1210-1228.

Yorath, C.J. (1980). The Apollo structure in Tofino Basin, Canadian Pacific continental shelf, Can. J. Earth Sci. 17, 758-775.

Yorath, C.J. and R.G. Currie (1980). Some aspects of the geology and structural style of the Vancouver Island continental margin, Geological Association of Canada, Annual Meeting, Halifax, N.S., Program with Abstracts 5, p.88.

Yoshii, T., Y. Kono and K. Ito (1976). Thickening of the oceanic lithosphere, AGU Monograph 19, 423-430.

Young, G.B. and L.W. Braile (1976). A computer program for the application of Zoeppritz's amplitude equations and Knott's energy equations, Bull. Seism. Soc. Am. 66, 1881-1885.

APPENDICES: ADDITIONAL RECORD SECTIONS

A.1 Common Shot Record Sections

The following 14 figures represent the observed record sections for all shots of the Vancouver Island Seismic Project other than shots J1, P19, P13, P8 and P2, for which record sections were presented in Chapter 4. Picks on the main record sections were made in a manner consistent with the sections in this appendix. That is, the main sections are representative of the full VISP data set shown here.

Amplitudes on all sections may be compared between shots. All amplitudes have been multiplied by a factor proportional to distance. Times and distances are adjusted to place the shot at a depth of 2.6 km, and to correct the sediment layer to a thickness of 1 km and velocity of 1.8 km/s. The gap near the middle of all sections indicates the location of Georgia Strait (at 265-285 km from shot P19).

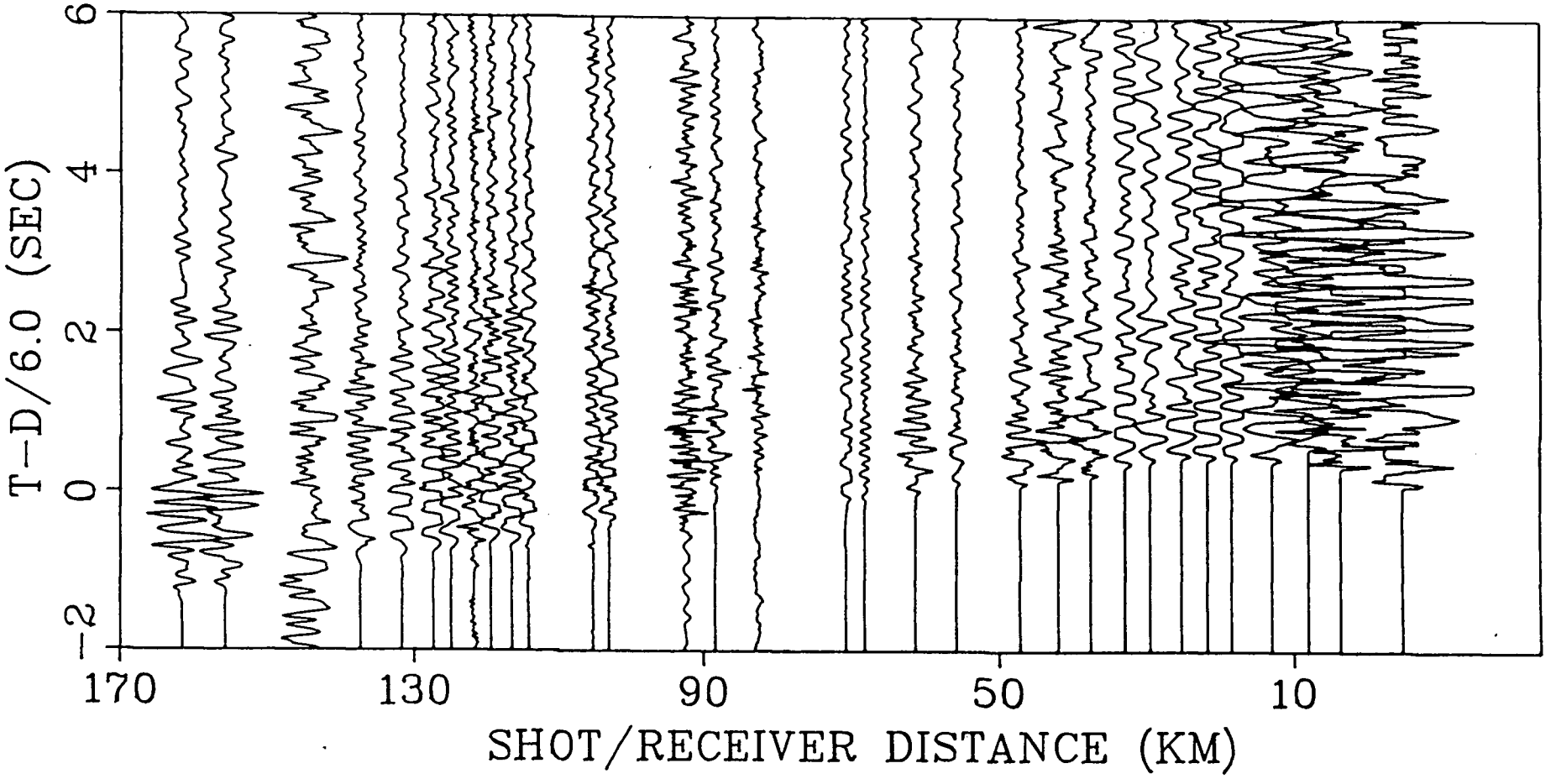

FIG. A1.1. Observed record section for shot J2.

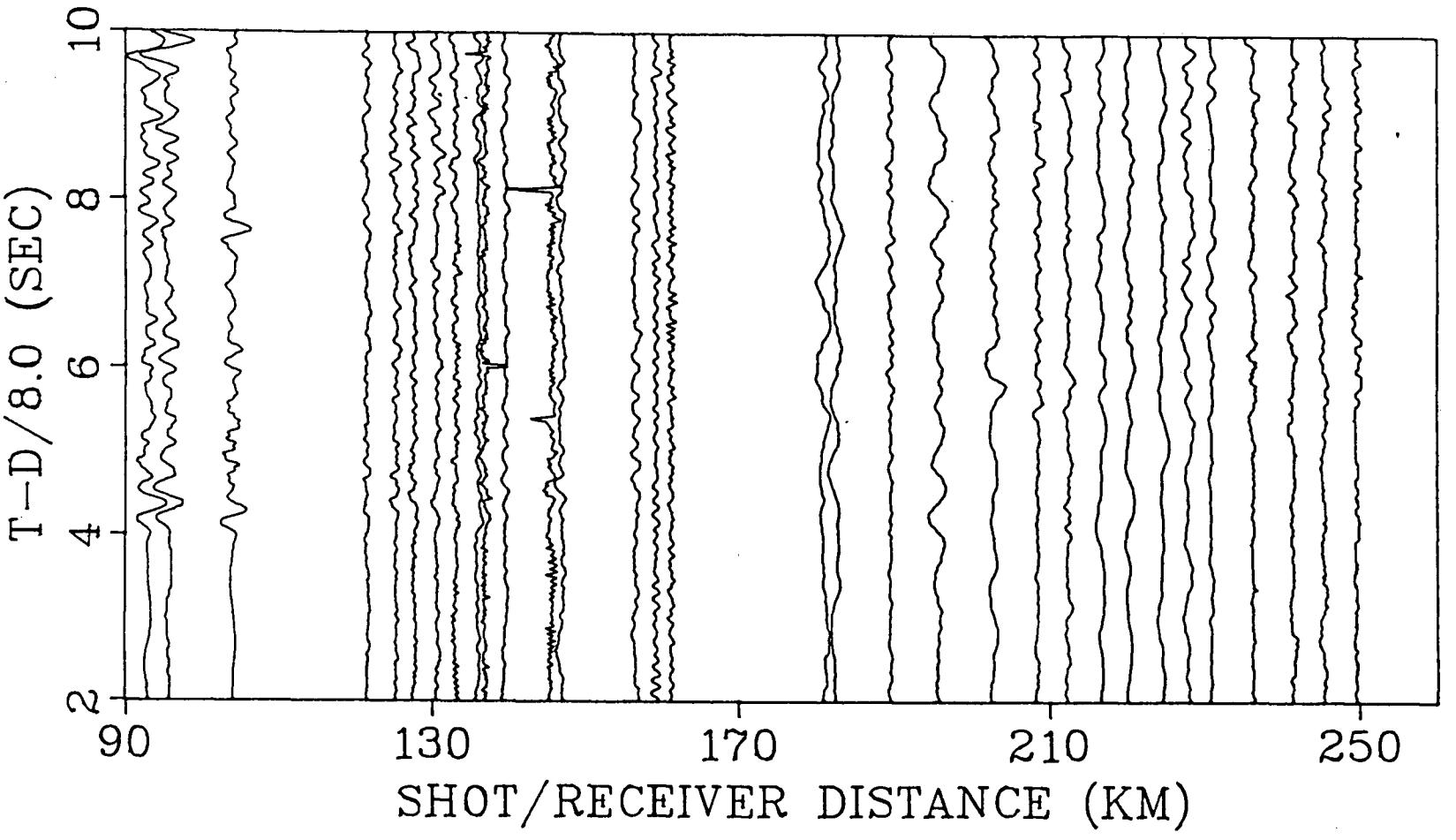

FIG. A1.2. Observed record section for shot P1, 104 km from shot P19.

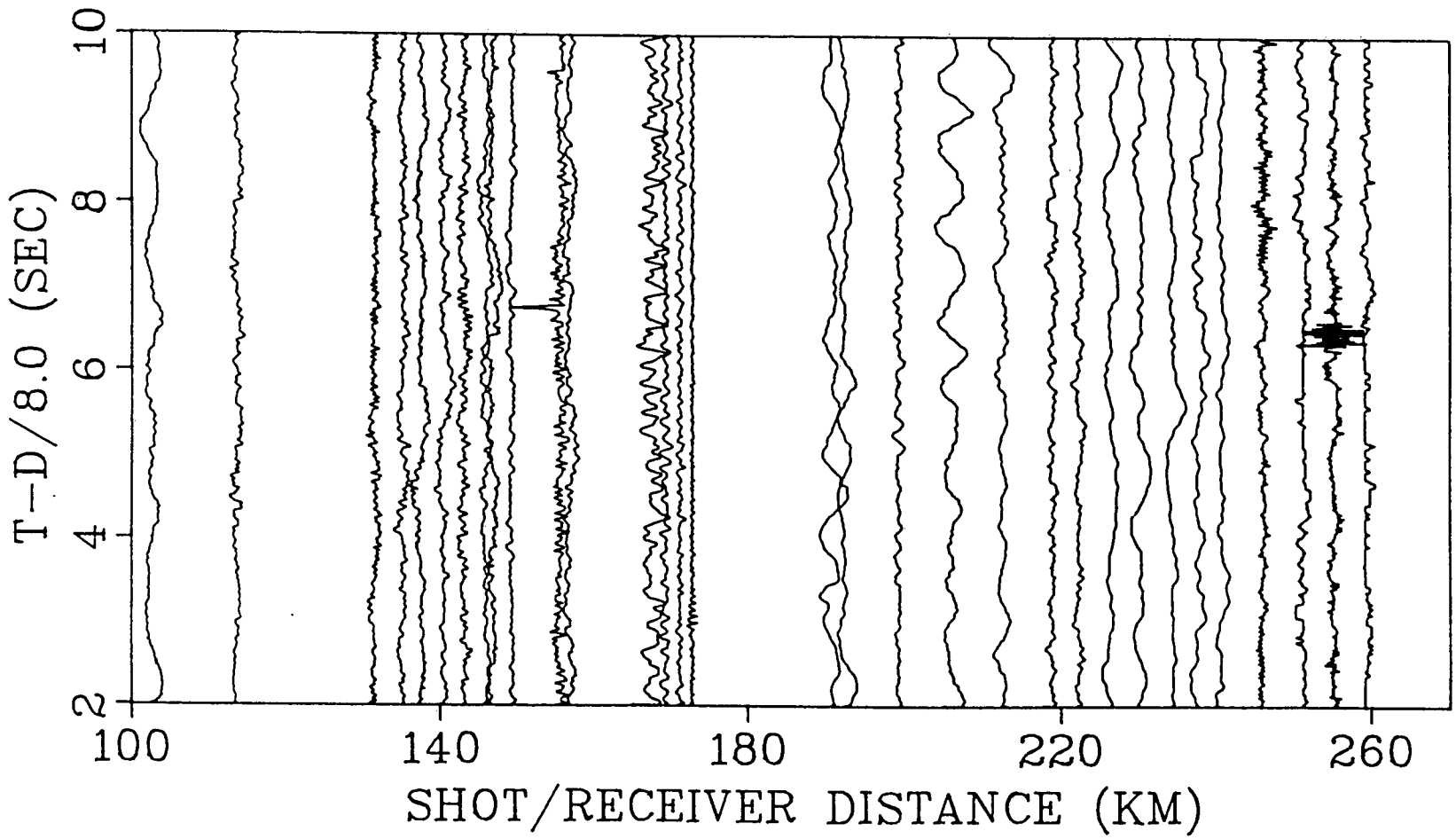

FIG. A1.3. Observed record section for shot P3, 94 km from shot P19.

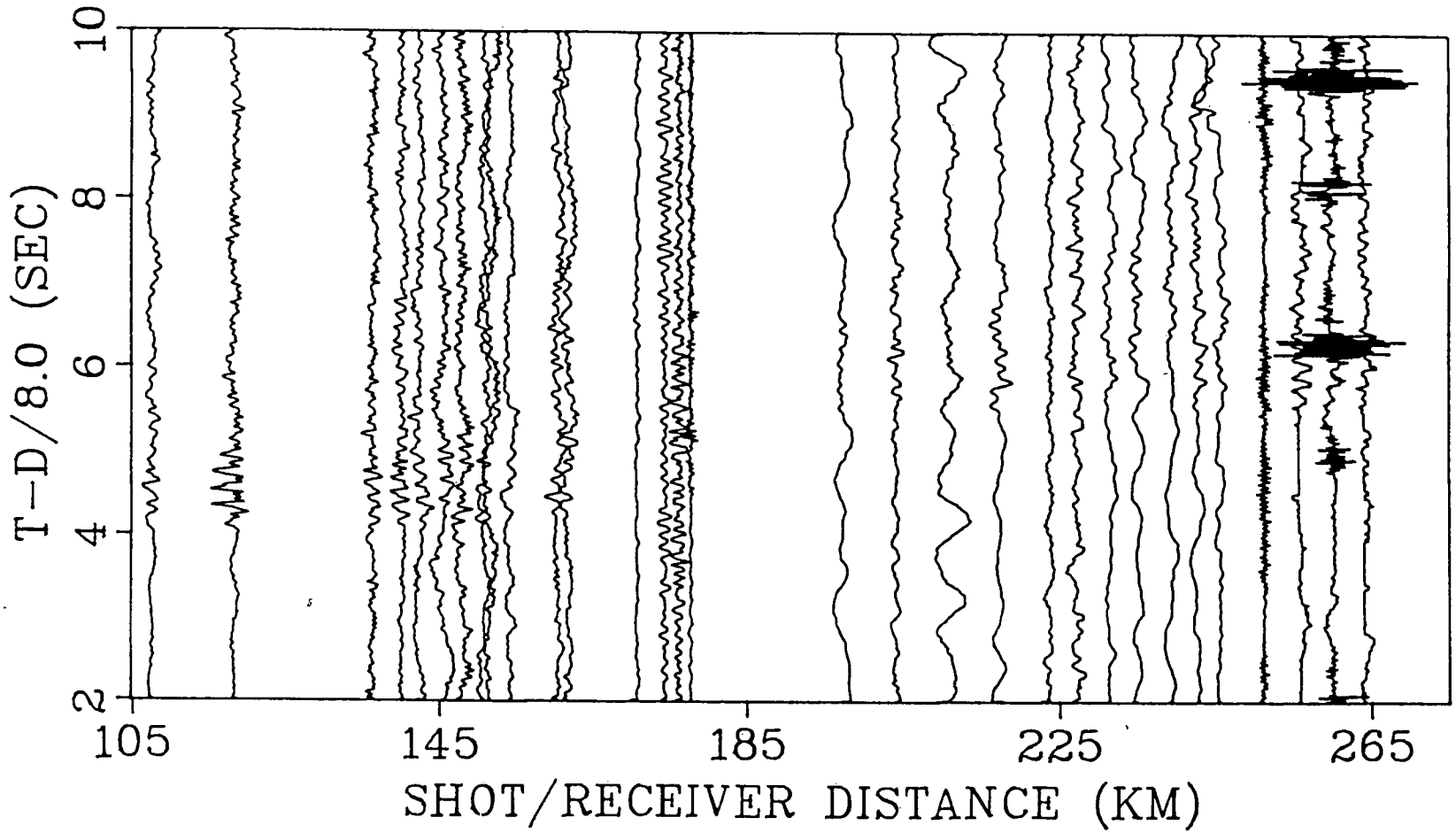

FIG. A1.4. Observed record section for shot P4, 89 km from shot P19.

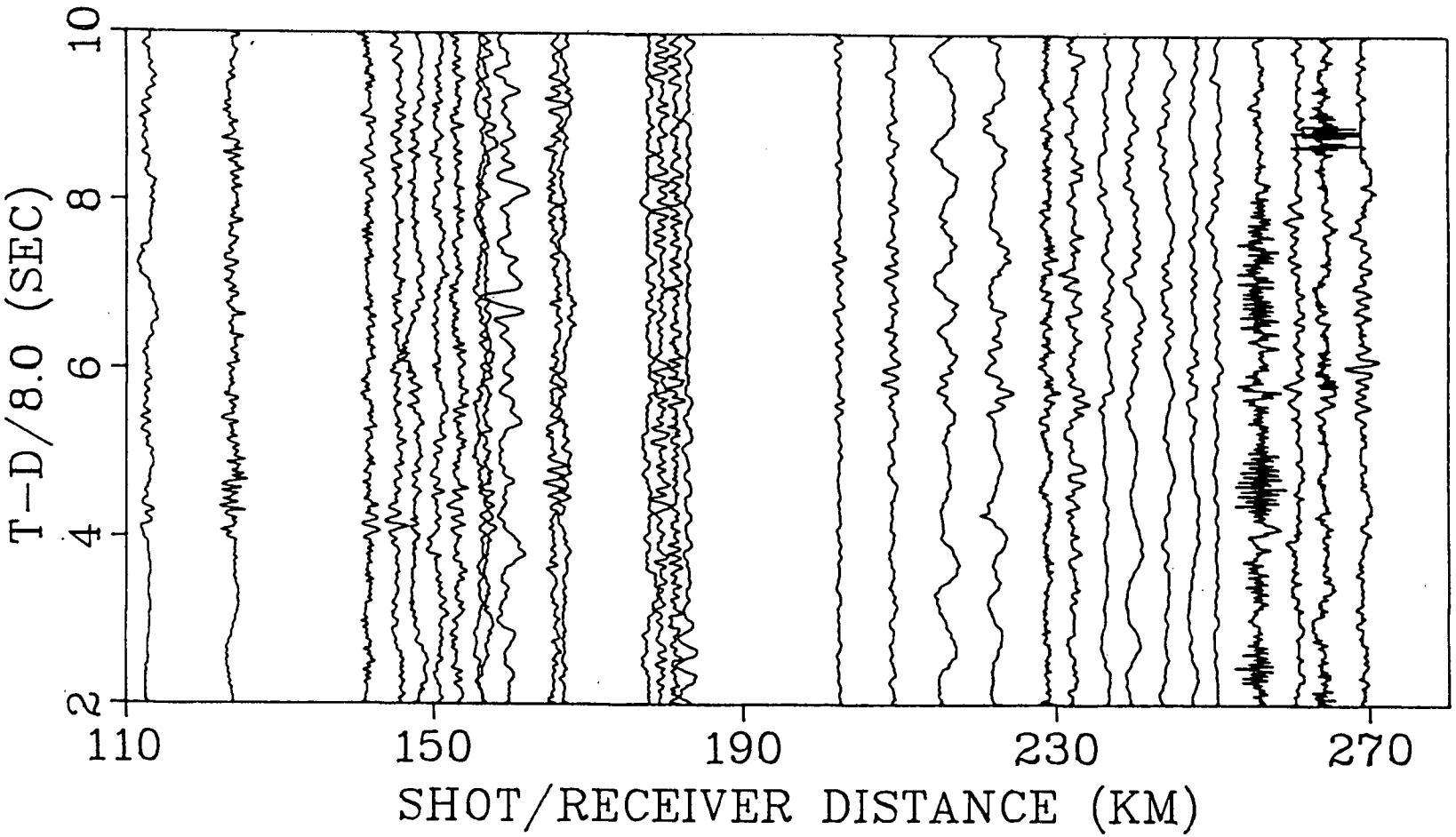

FIG. A1.5. Observed record section for shot P5, 83 km from shot P19.

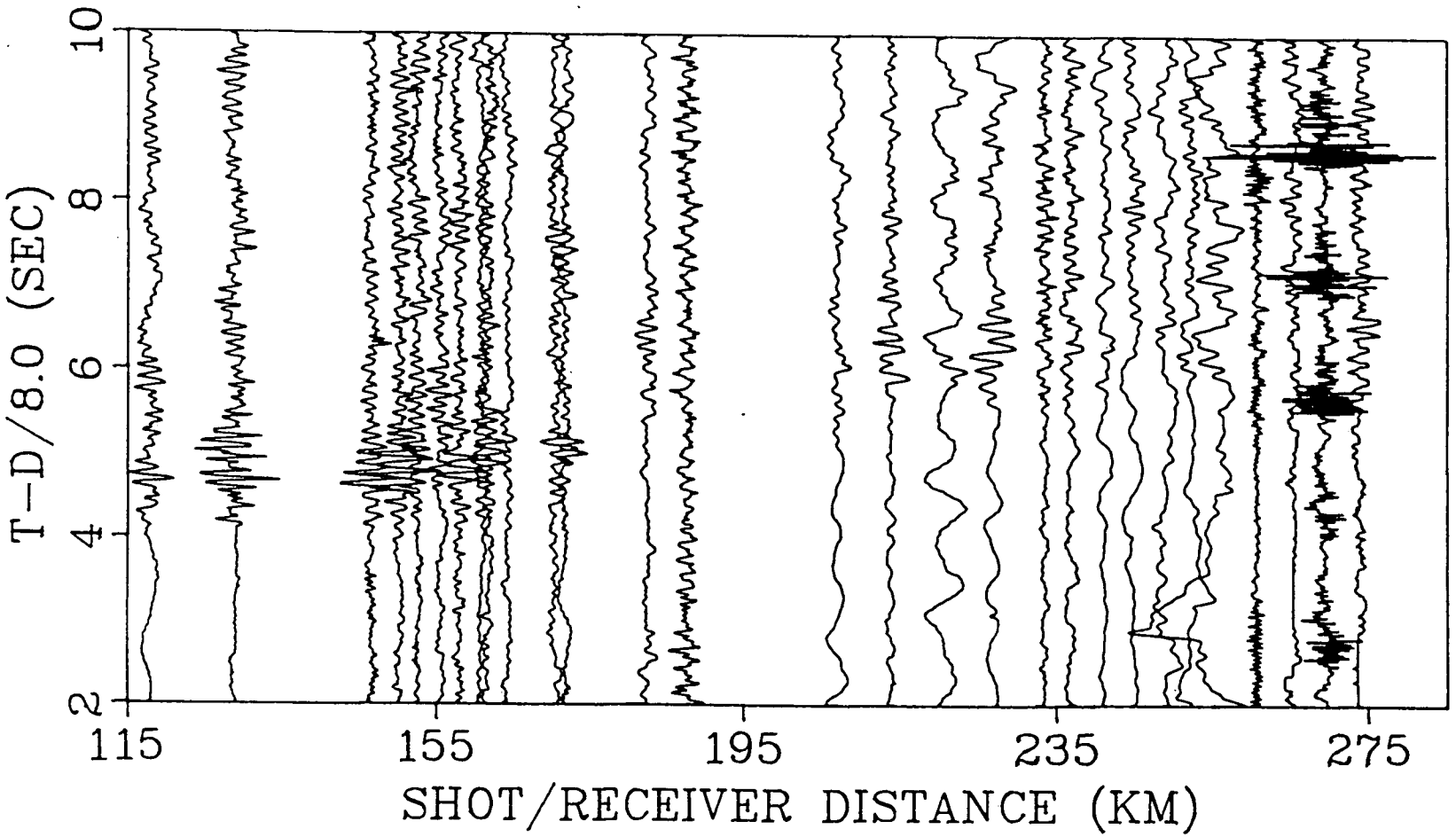

FIG. A1.6. Observed record section for shot P6, 78 km from shot P19.

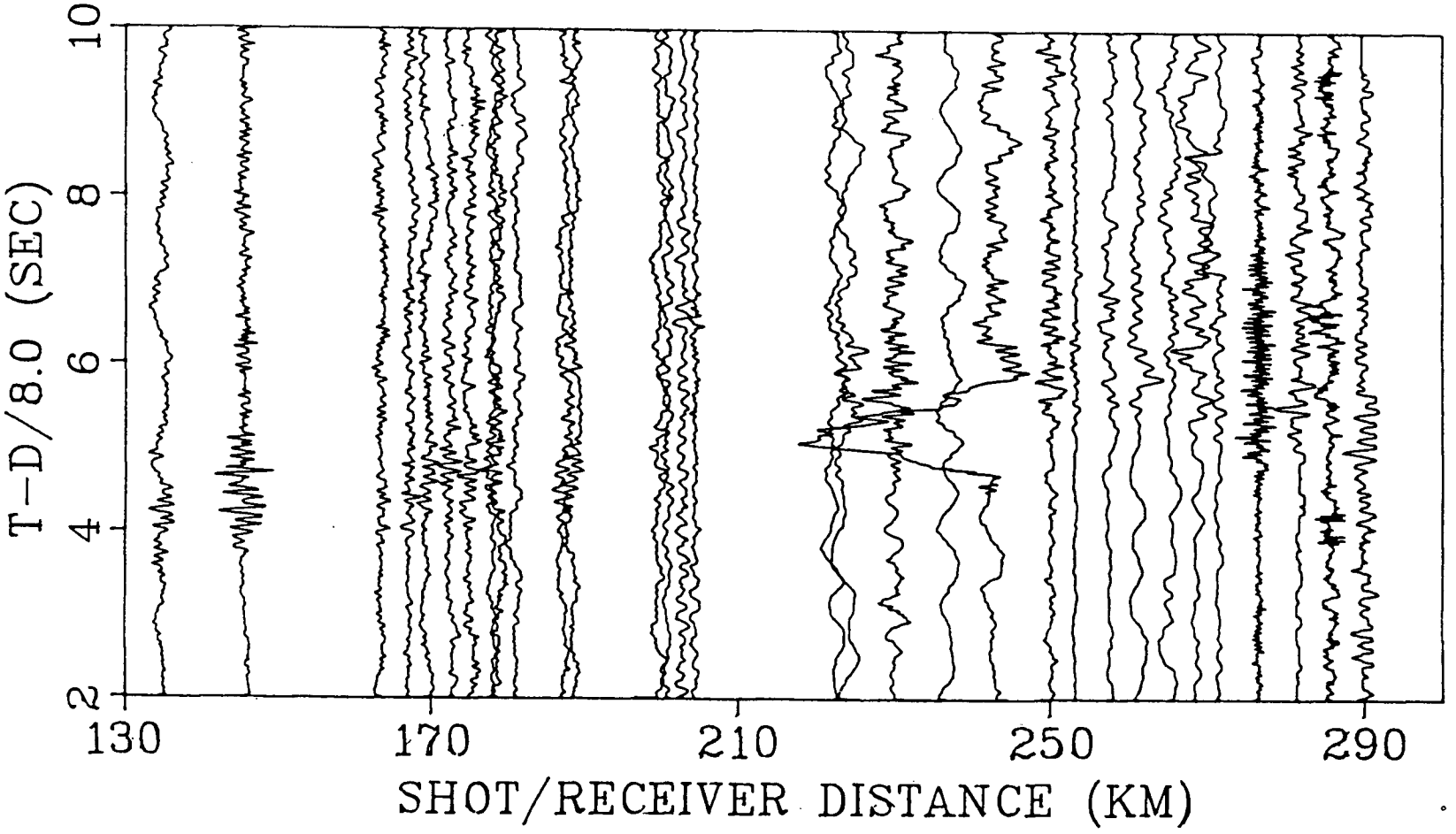

FIG. A1.7. Observed record section for shot P9, 63 km from shot P19.

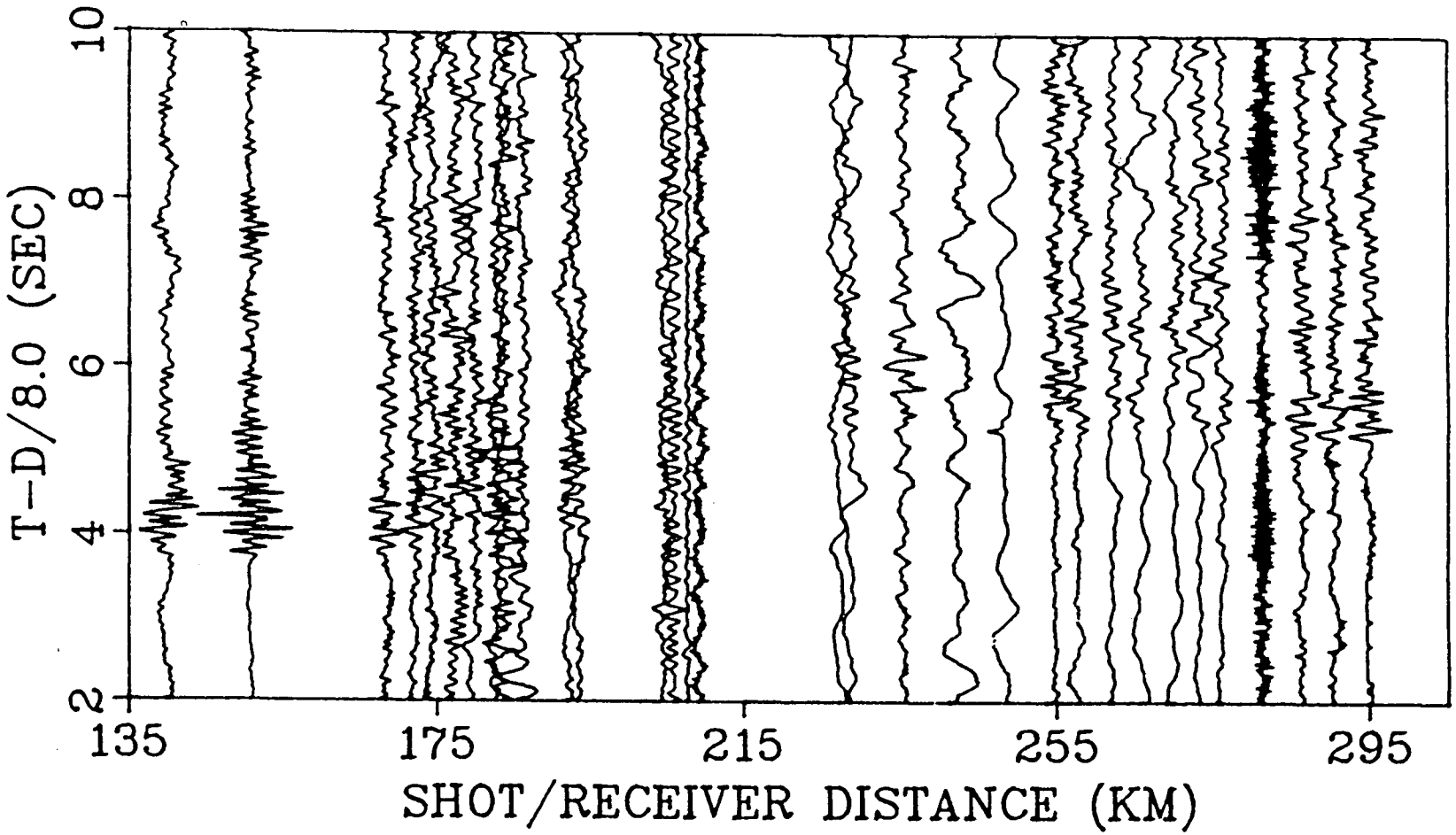

FIG. A1.8. Observed record section for shot P10, 57 km from shot P19.

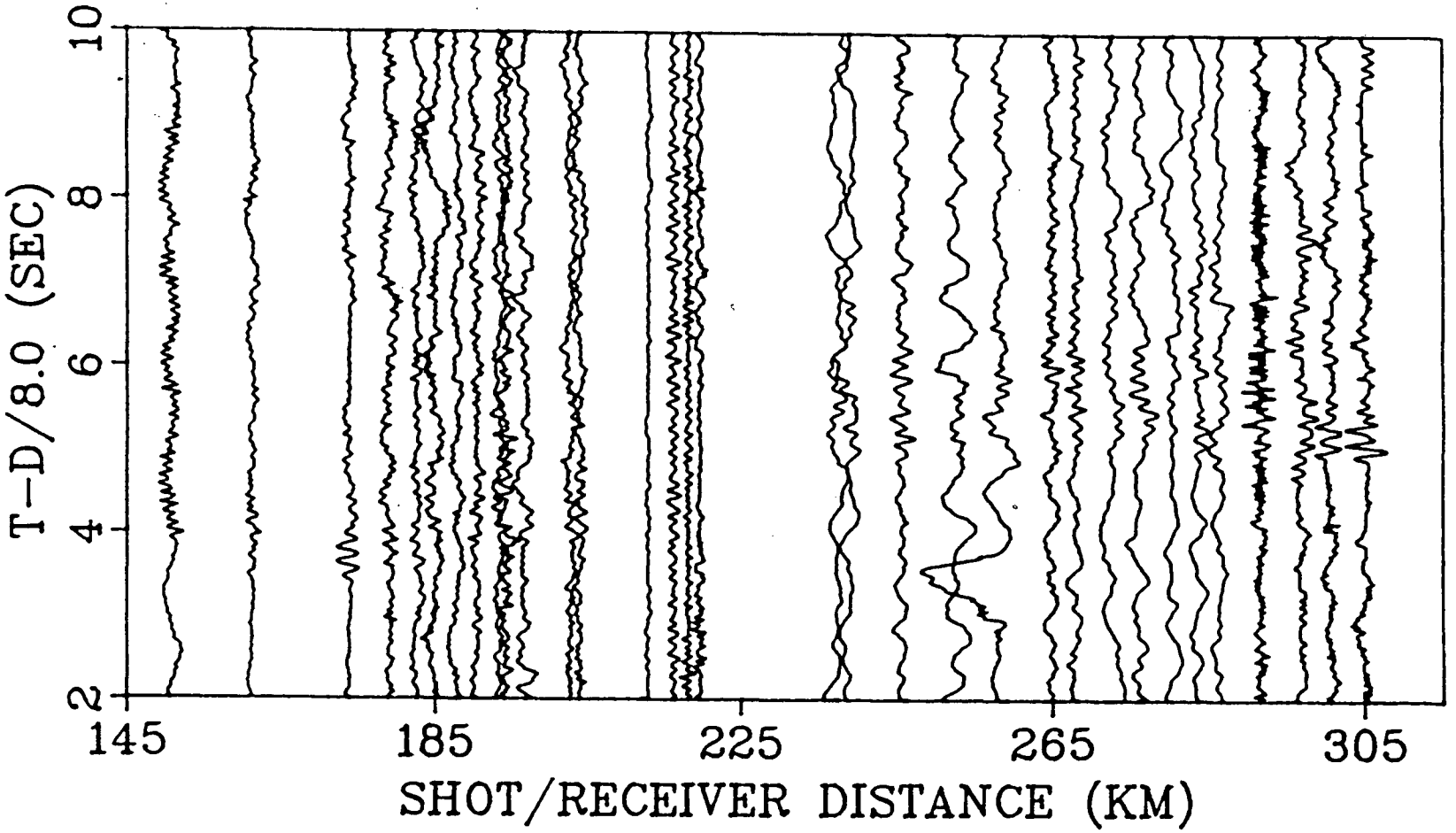

FIG. A1.9. Observed record section for shot P12, 47 km from shot P19.

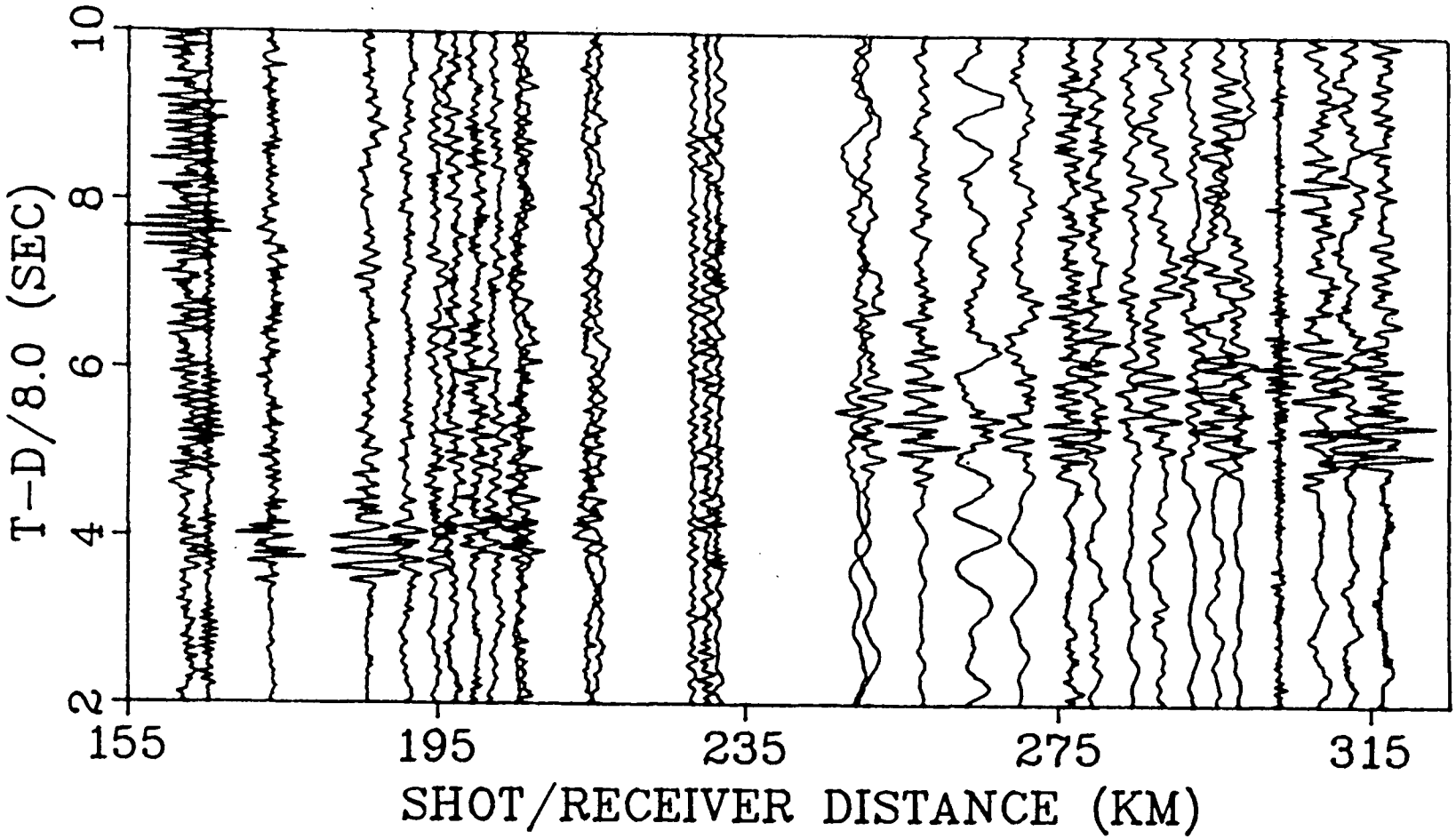

FIG. A1.10. Observed record section for shot P14, 36 km from shot P19.

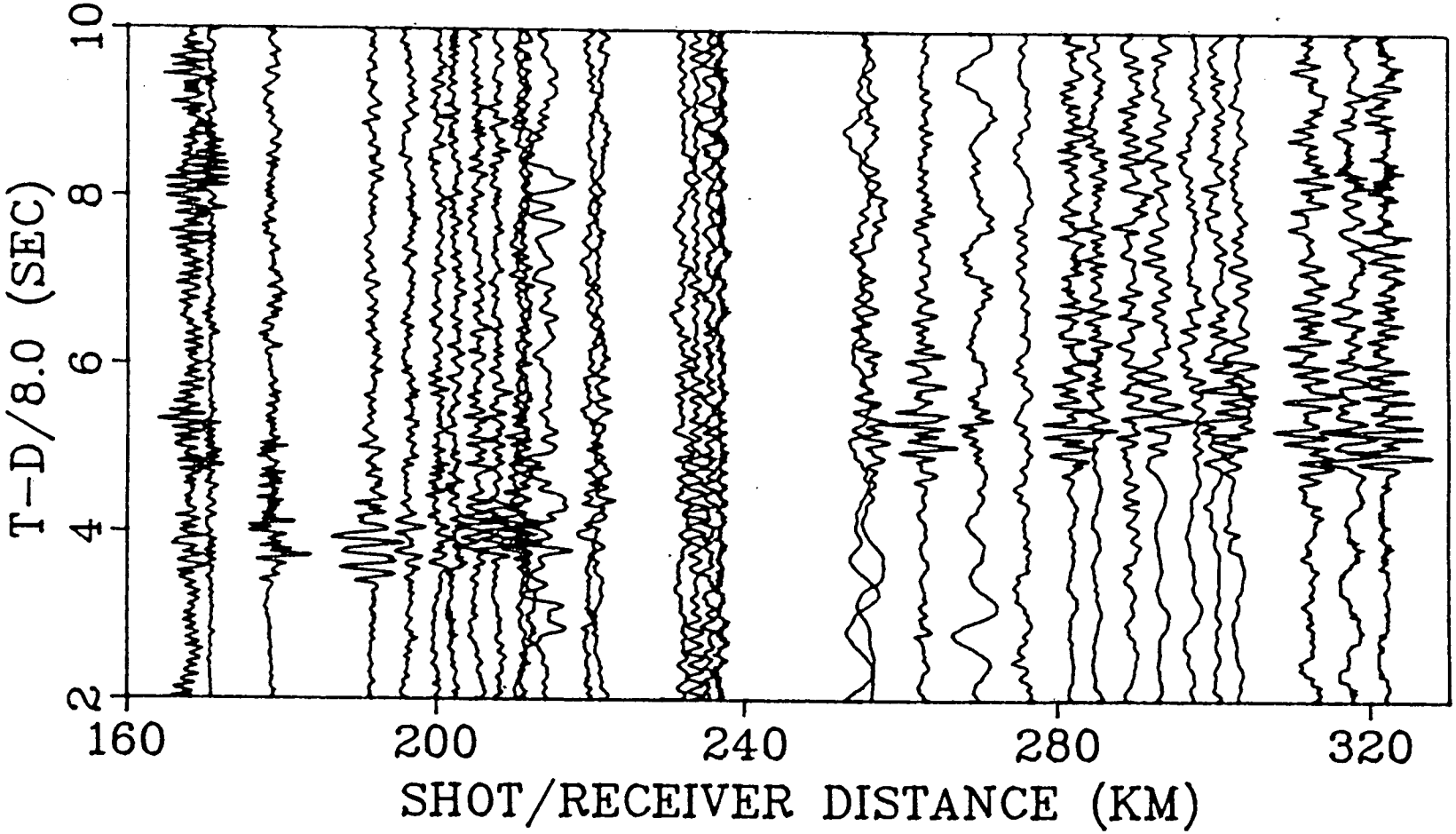

FIG. A1.11. Observed record section for shot P15, 31 km from shot P19.

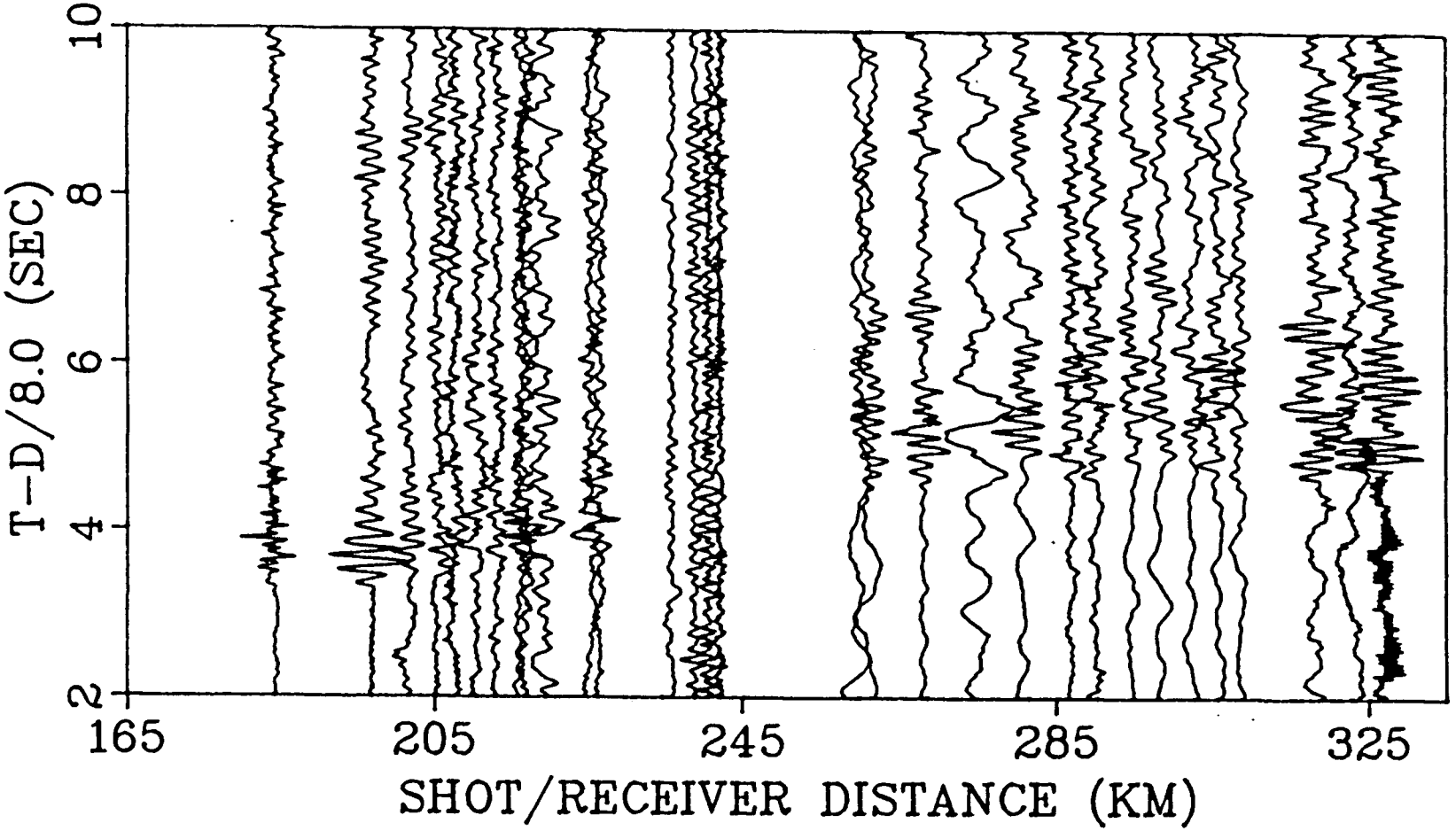

FIG. A1.12. Observed record section for shot P16, 26 km from shot P19.

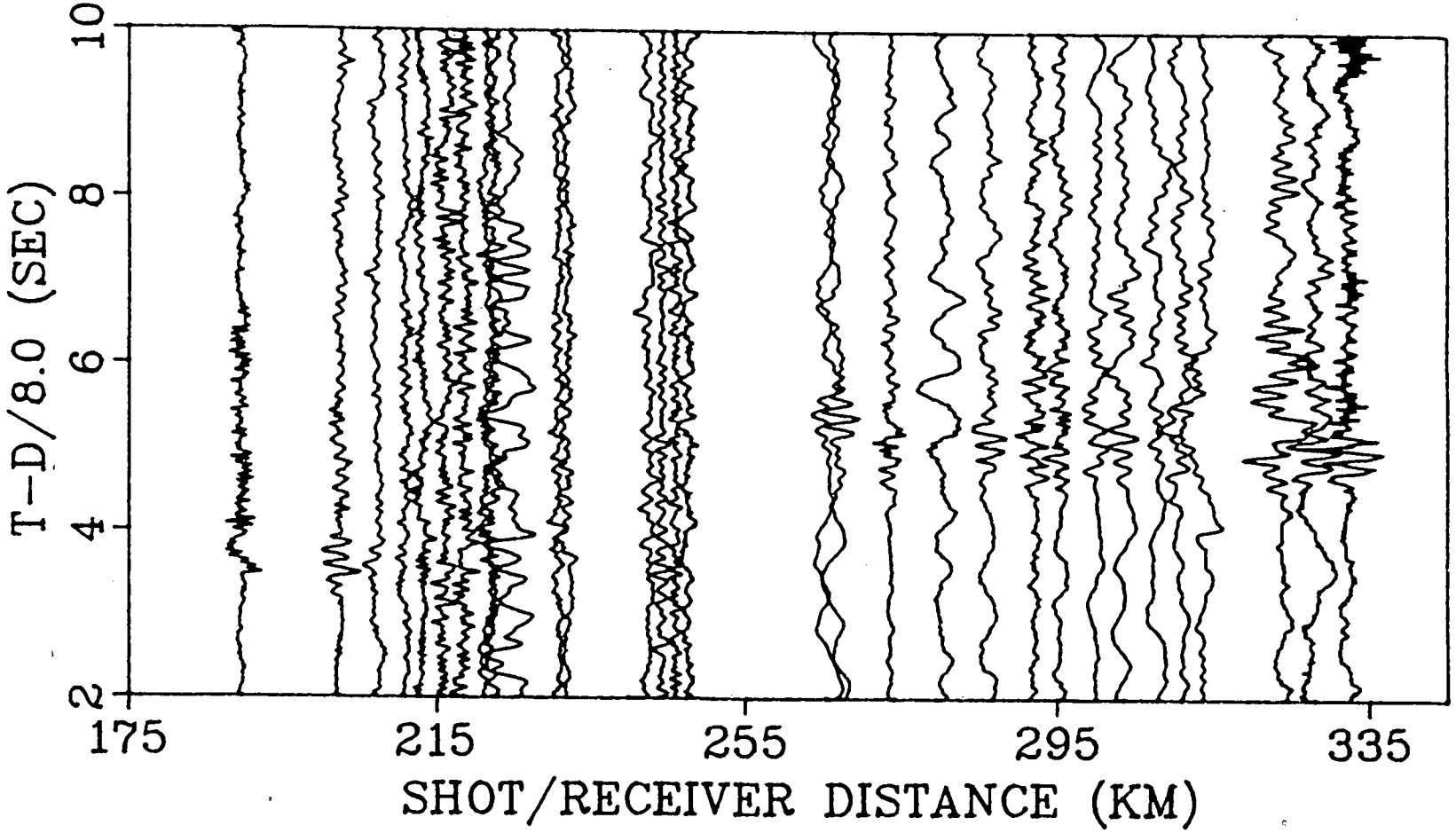

FIG. A1.13. Observed record section for shot P17, 21 km from shot P19.

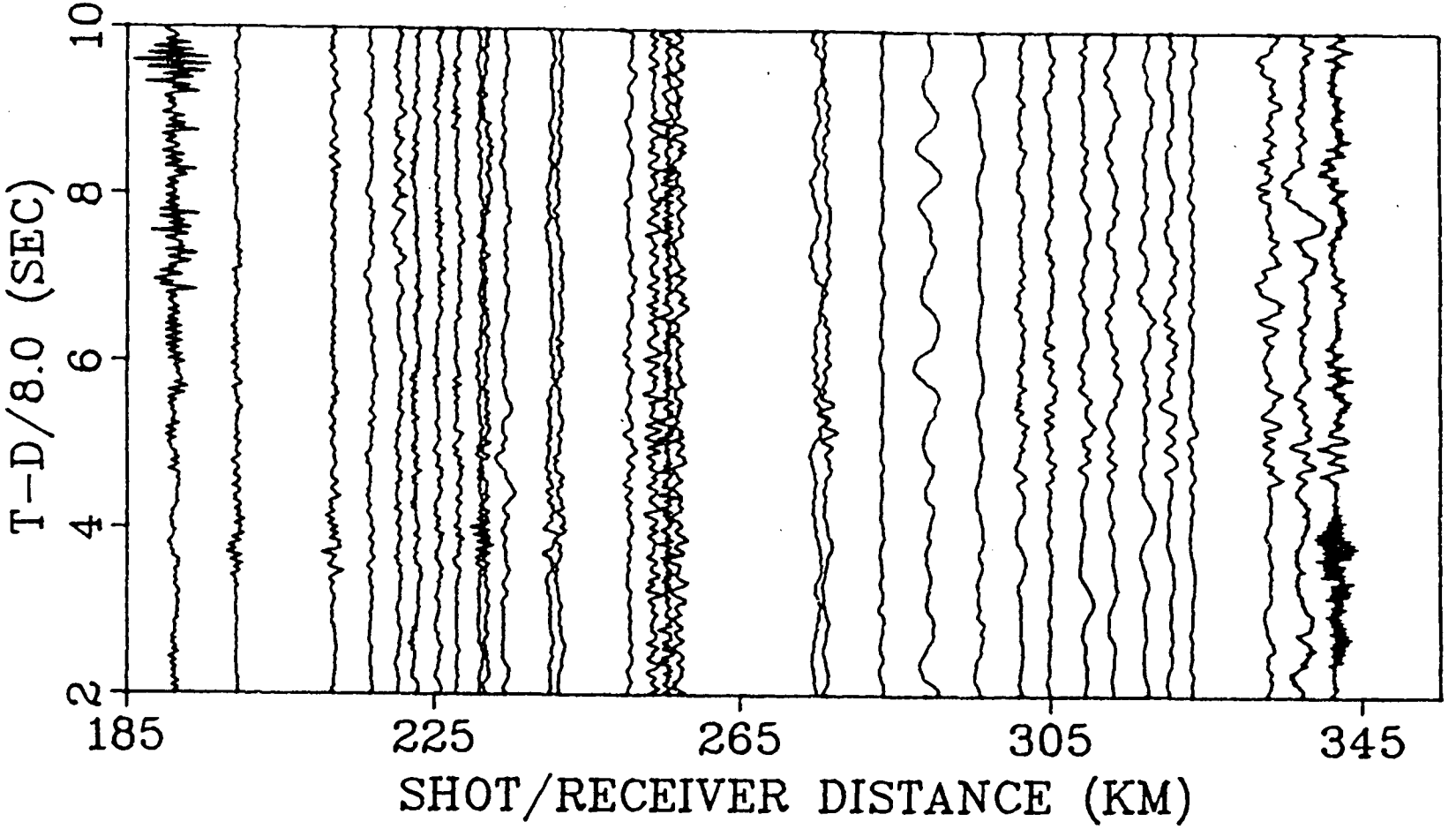

FIG. A1.14. Observed record section for shot P18, 10 km from shot P19.

A.2 Selected Common Receiver Record Sections

The following 10 figures are selected samples of observed record sections showing all 17 shots recorded on a given receiver. Shot P19 is on the left and shot P1 is on the right (P7 and P11 were misfires and so are missing). Amplitudes may be compared beween all receivers, and all amplitudes have been multiplied by a factor proportional to distance. Times and distances are adjusted to place the shots at 2.6 km depth, and for shots P19-P8 to correct the sediment layer to a thickness of 1 km and velocity of 1.8 km/s.

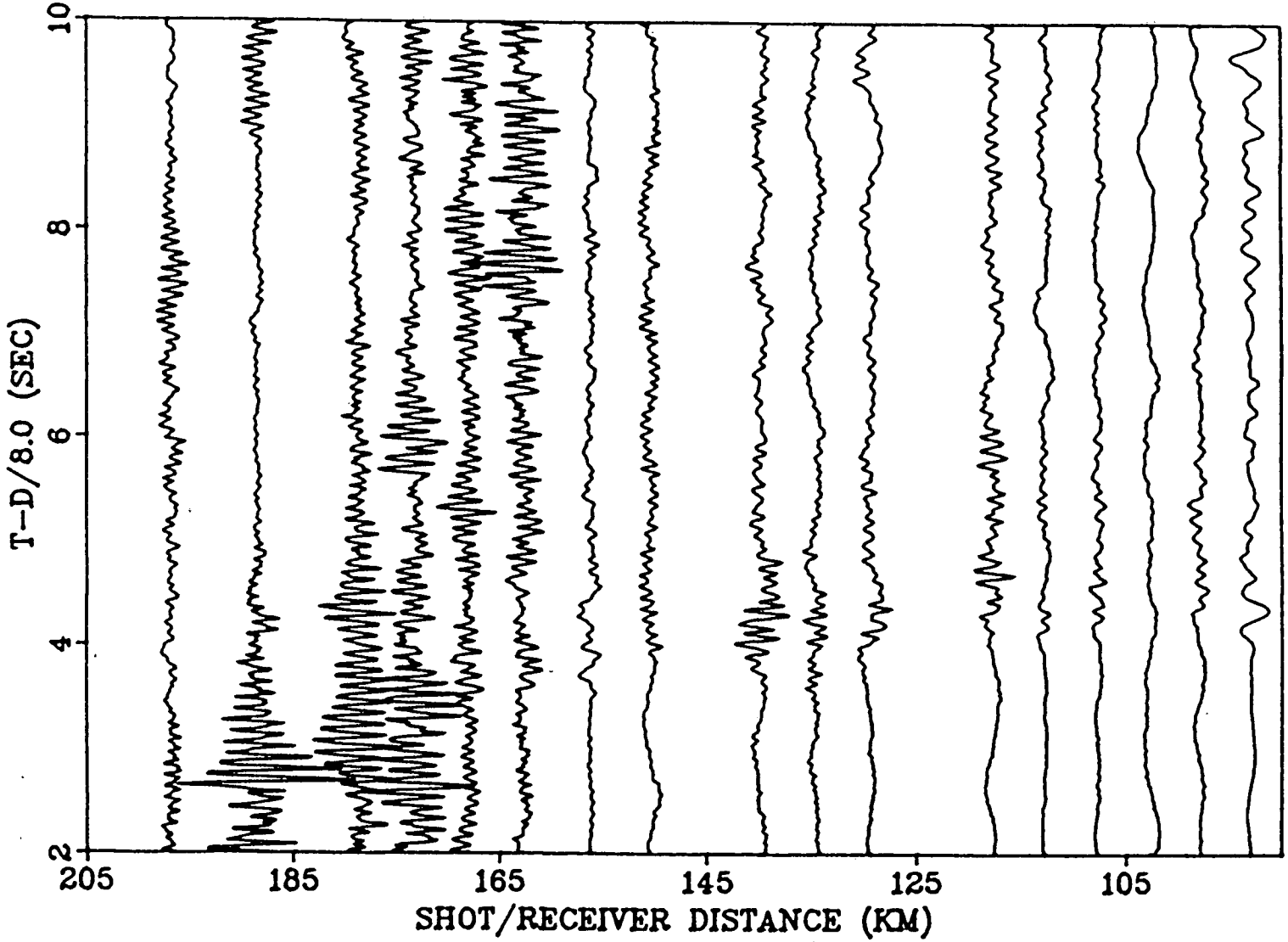

FIG. A2.1. Observed record section for receiver X2.

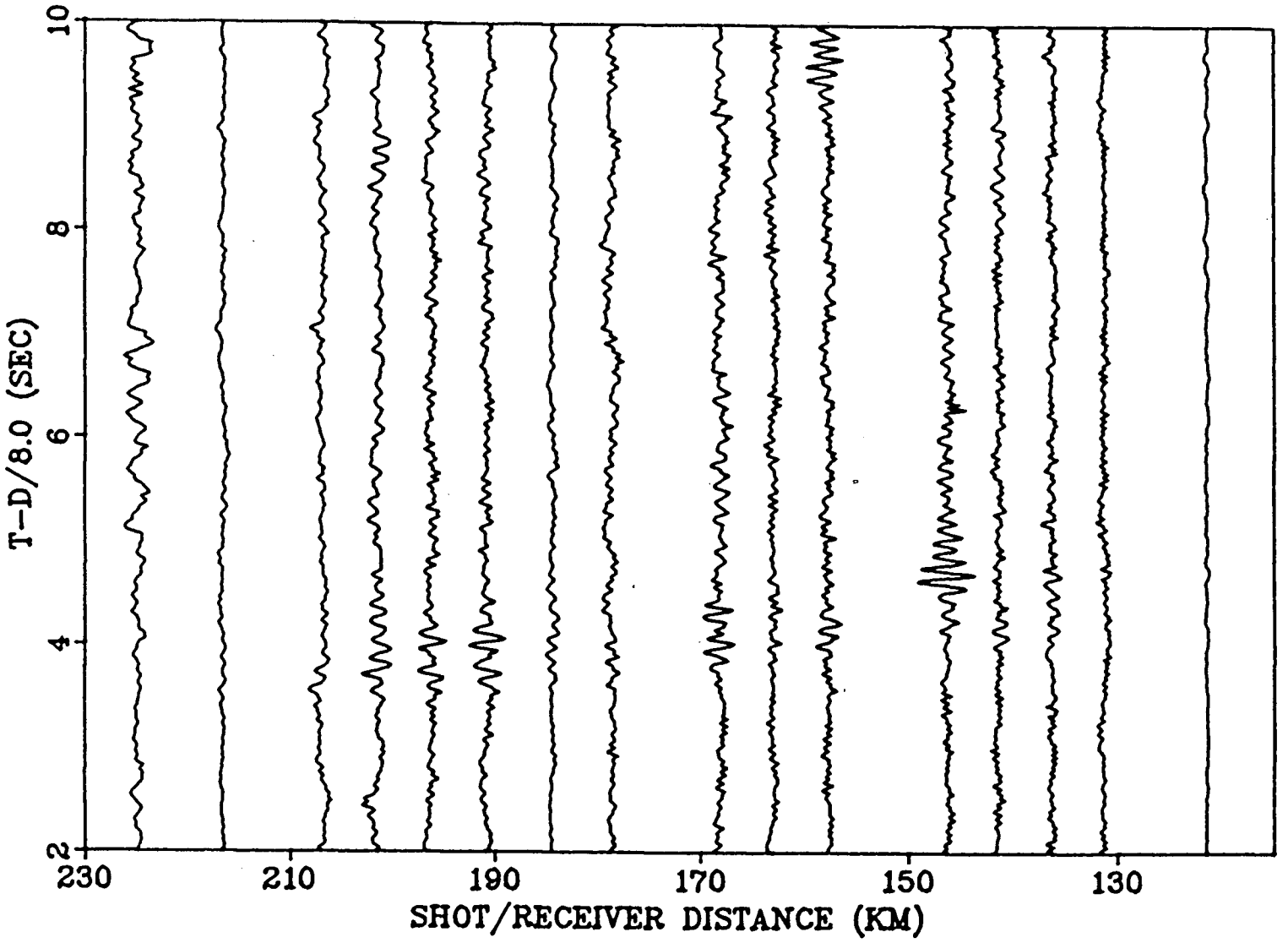

FIG. A2.2. Observed record section for receiver X13.

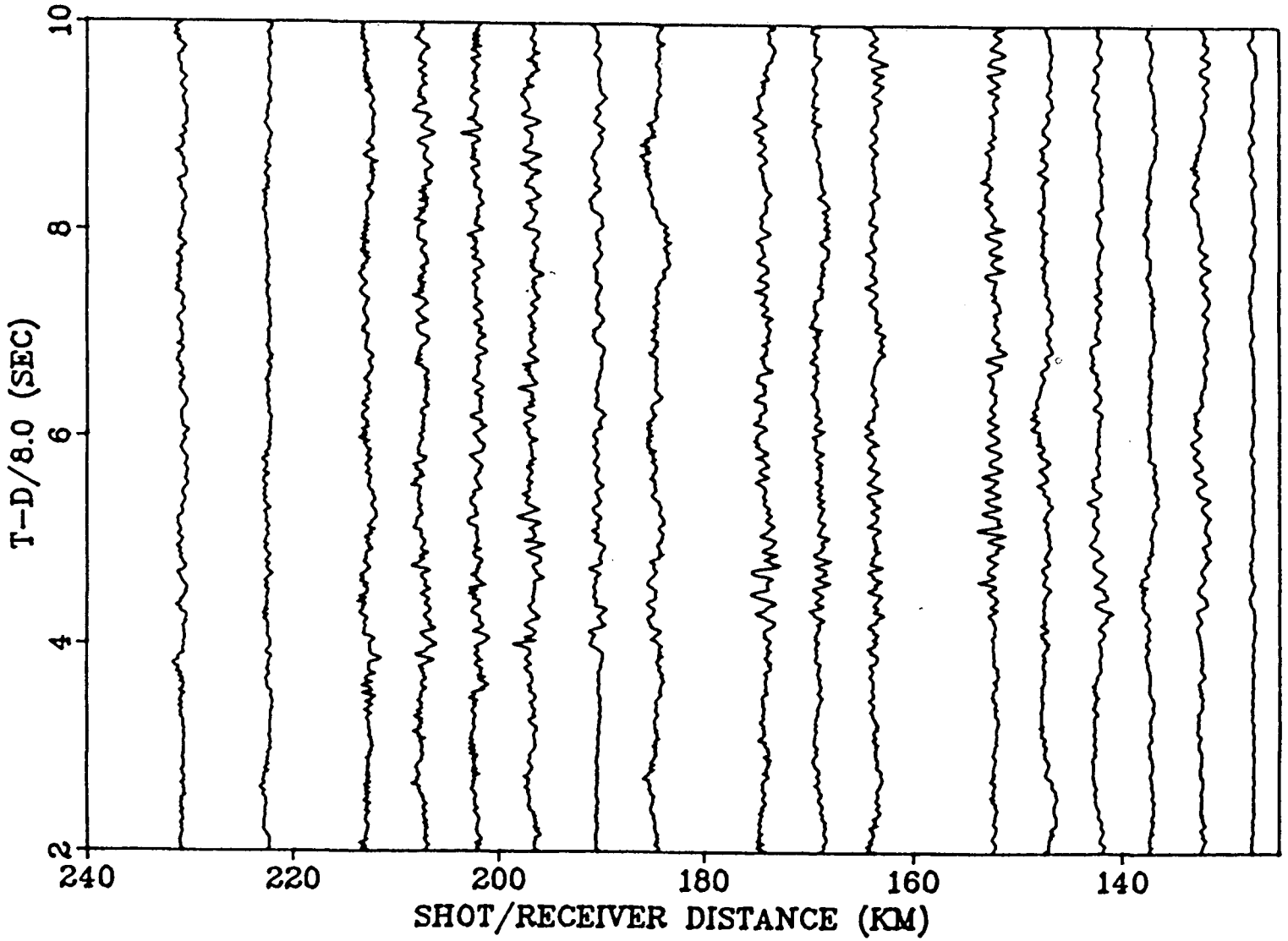

FIG. A2.3. Observed record section for receiver X15.

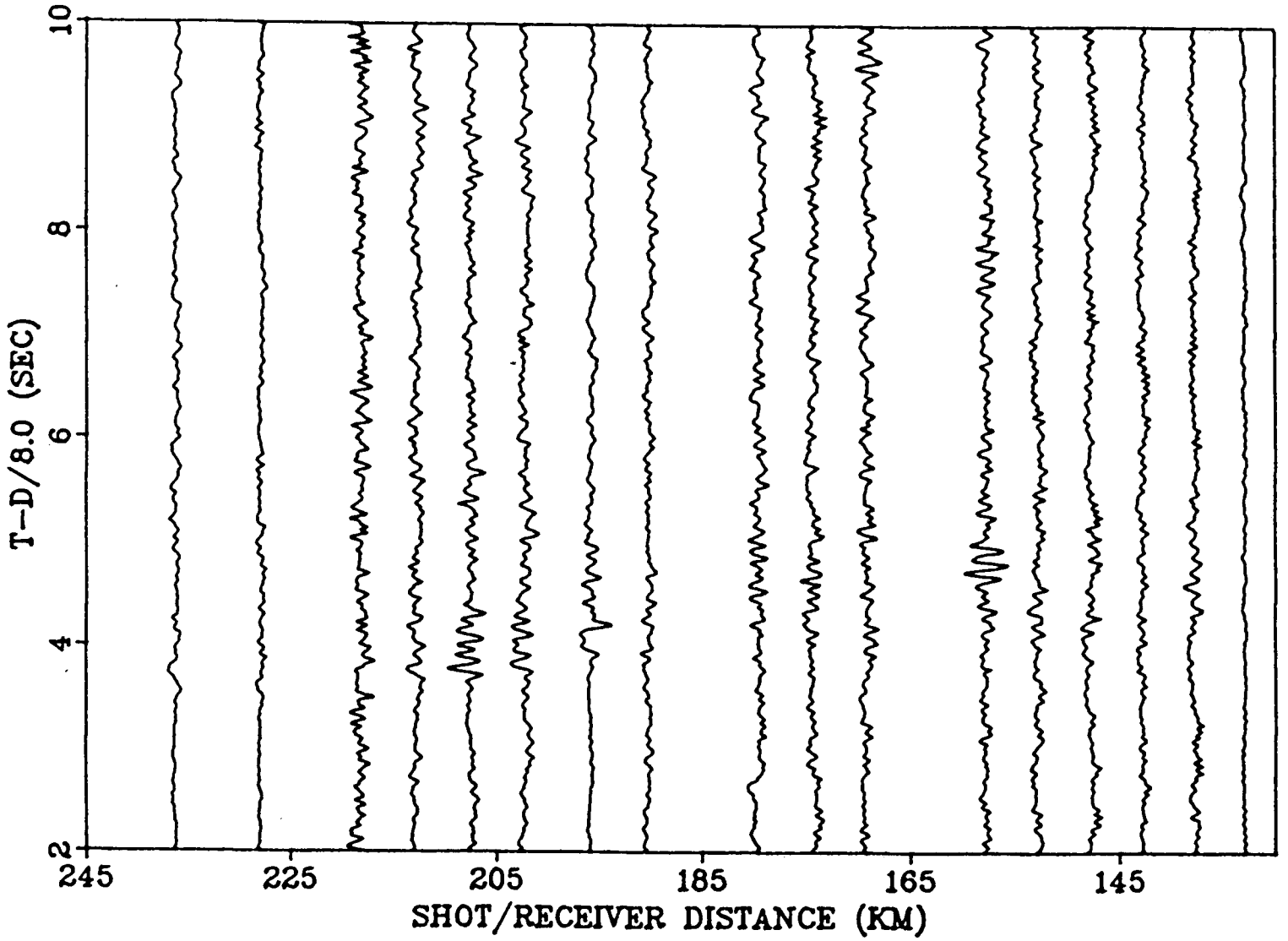

FIG. A2.4. Observed record section for receiver X17.

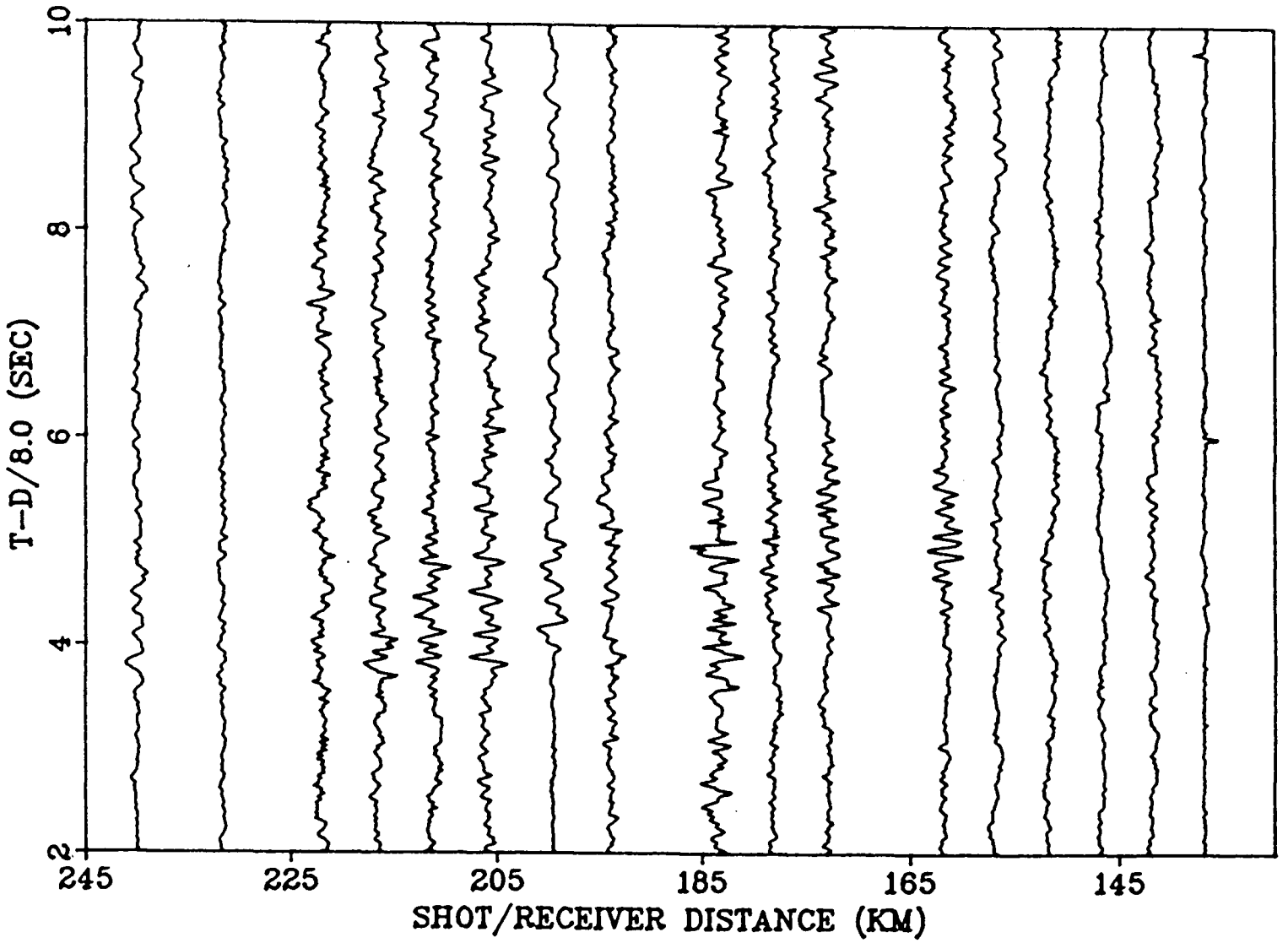

FIG. A2.5. Observed record section for receiver X19.

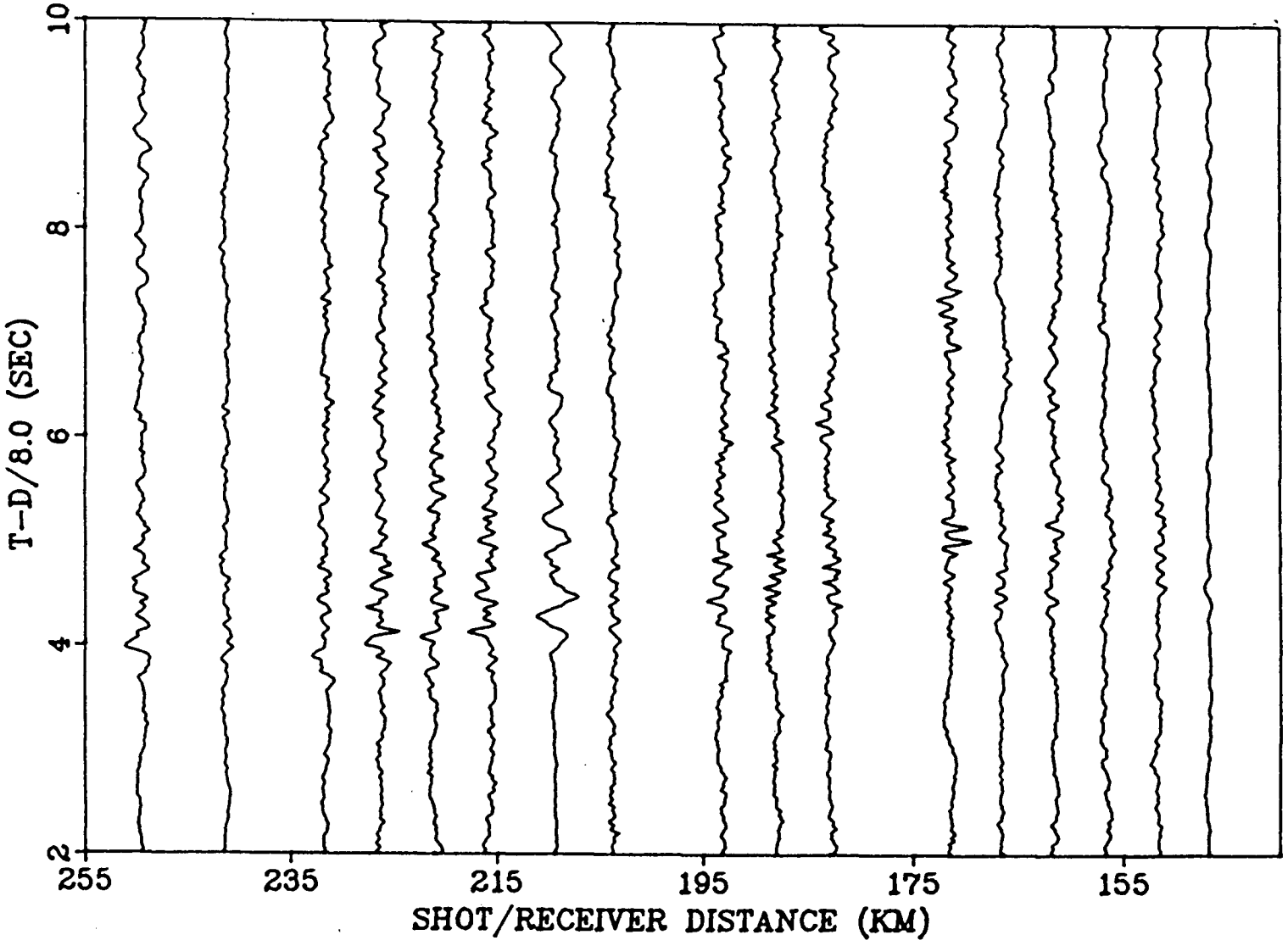

FIG. A2.6. Observed record section for receiver X23.

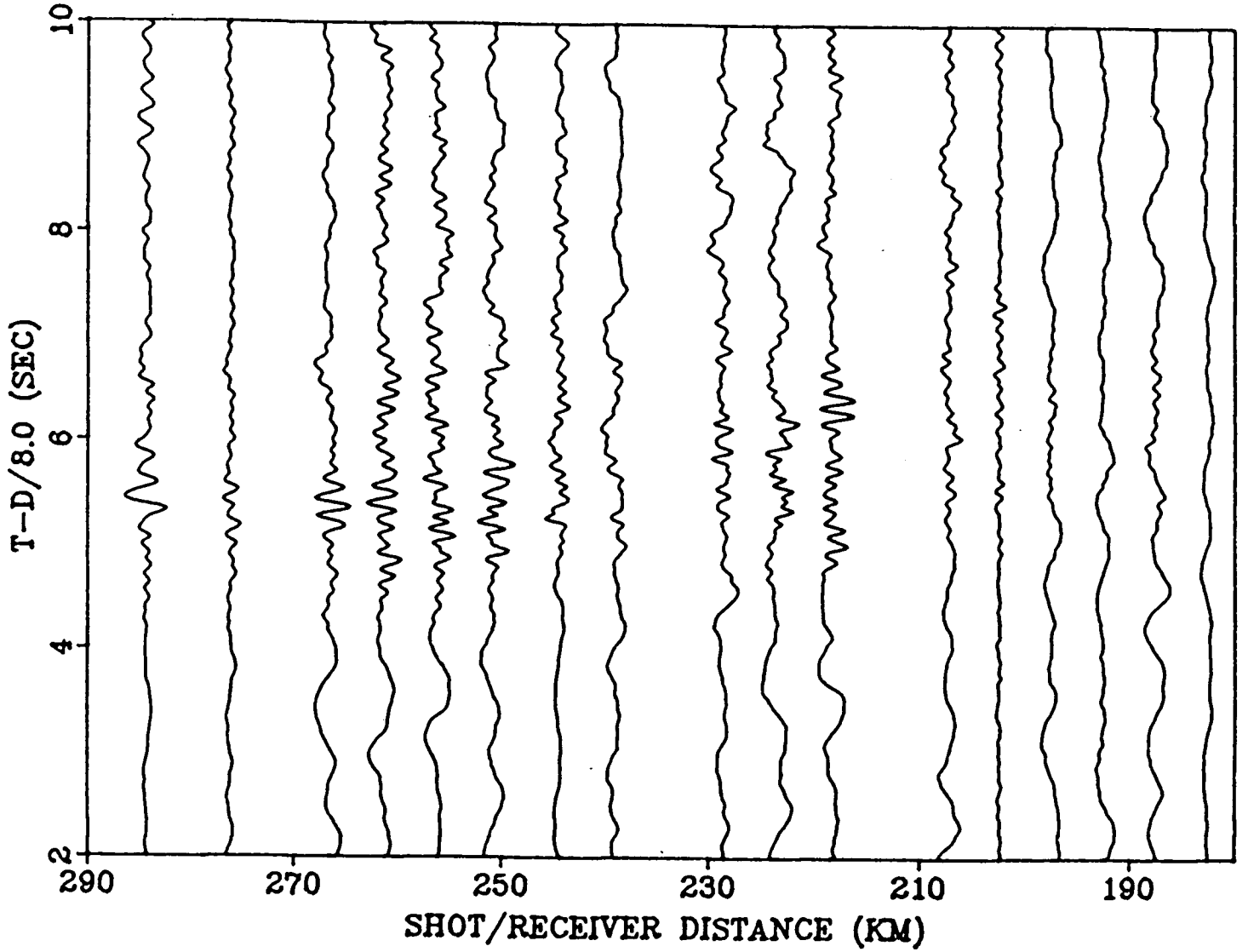

FIG. A2.7. Observed record section for receiver X31.

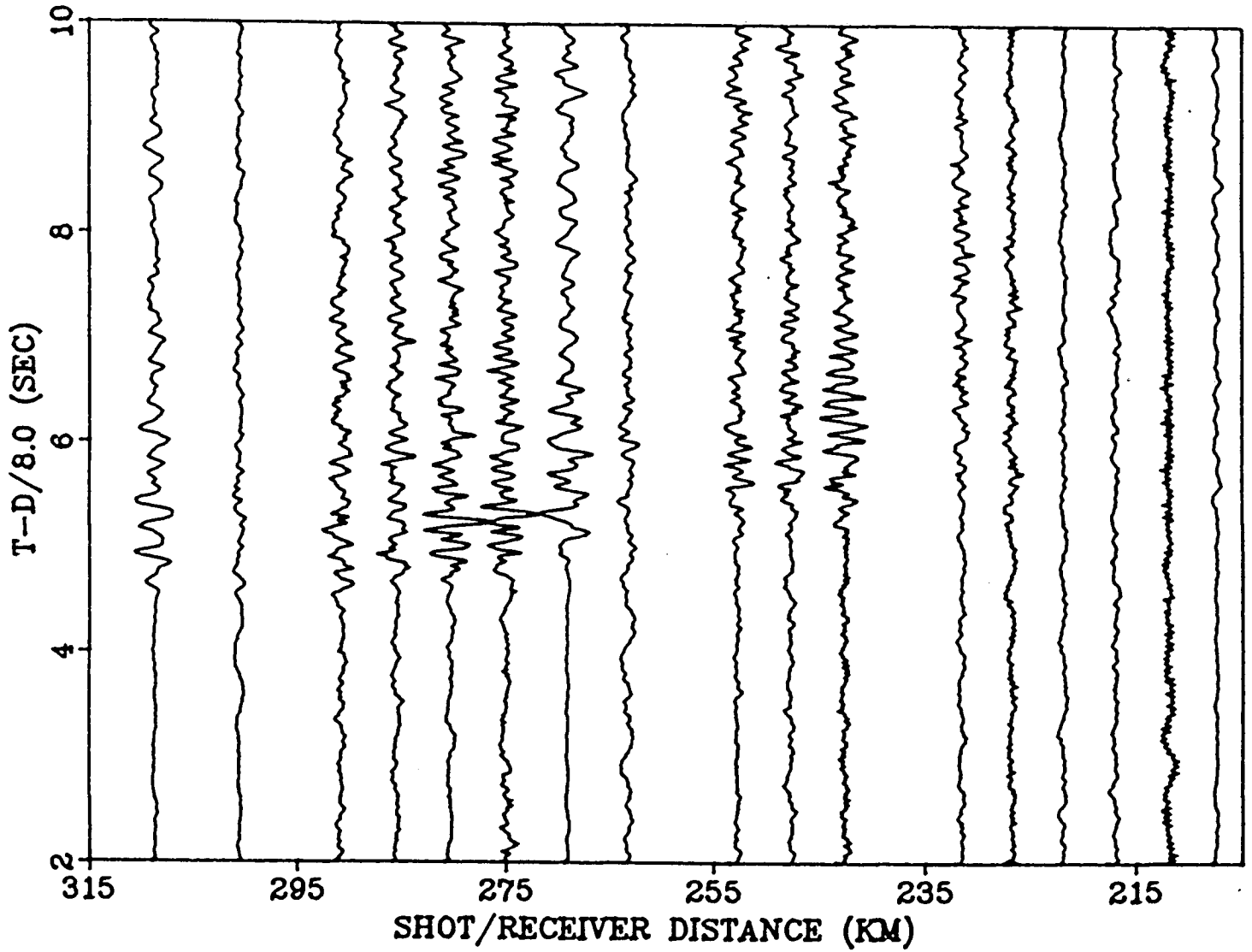

FIG. A2.8. Observed record section for receiver X35.

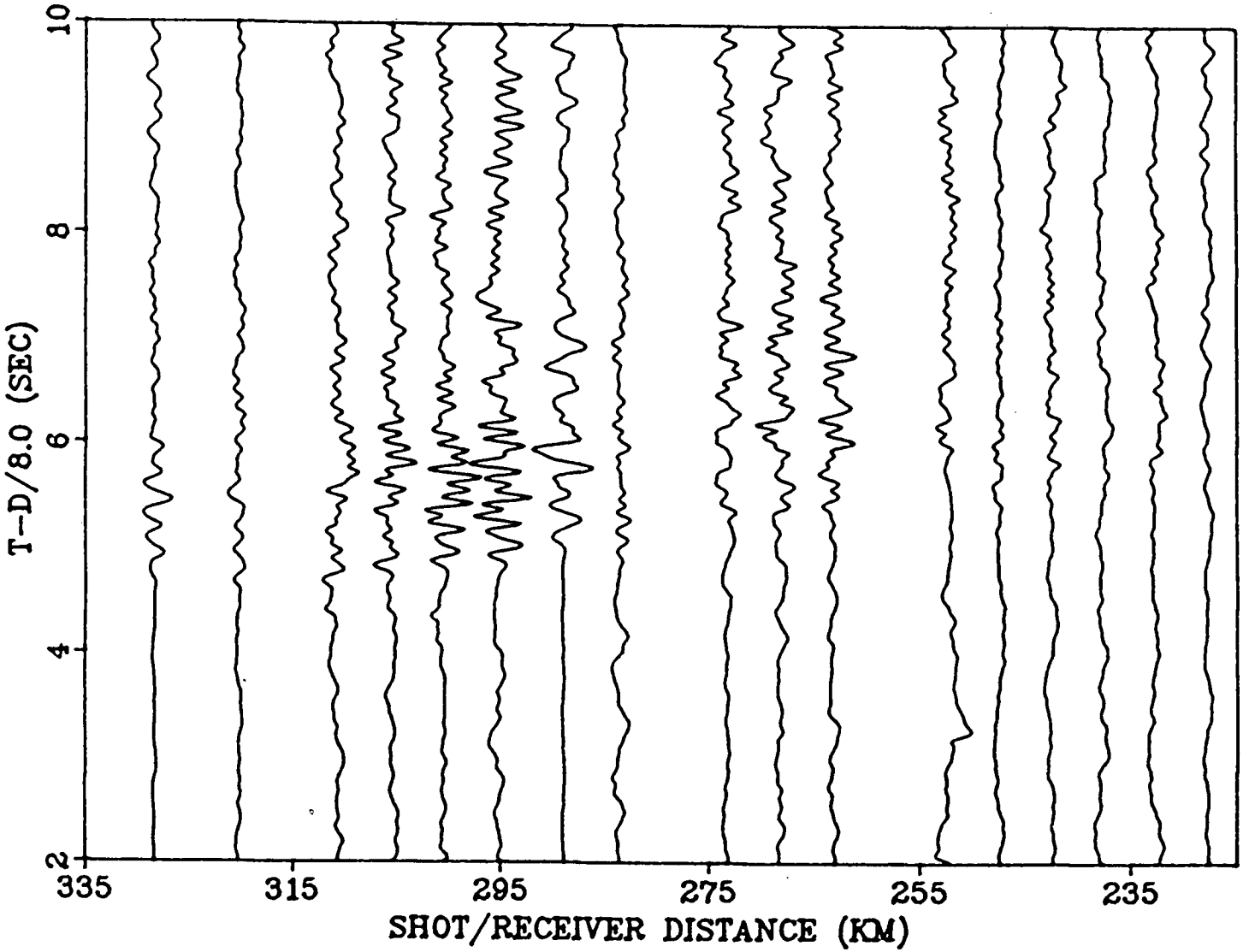

FIG. A2.9. Observed record section for receiver X40.

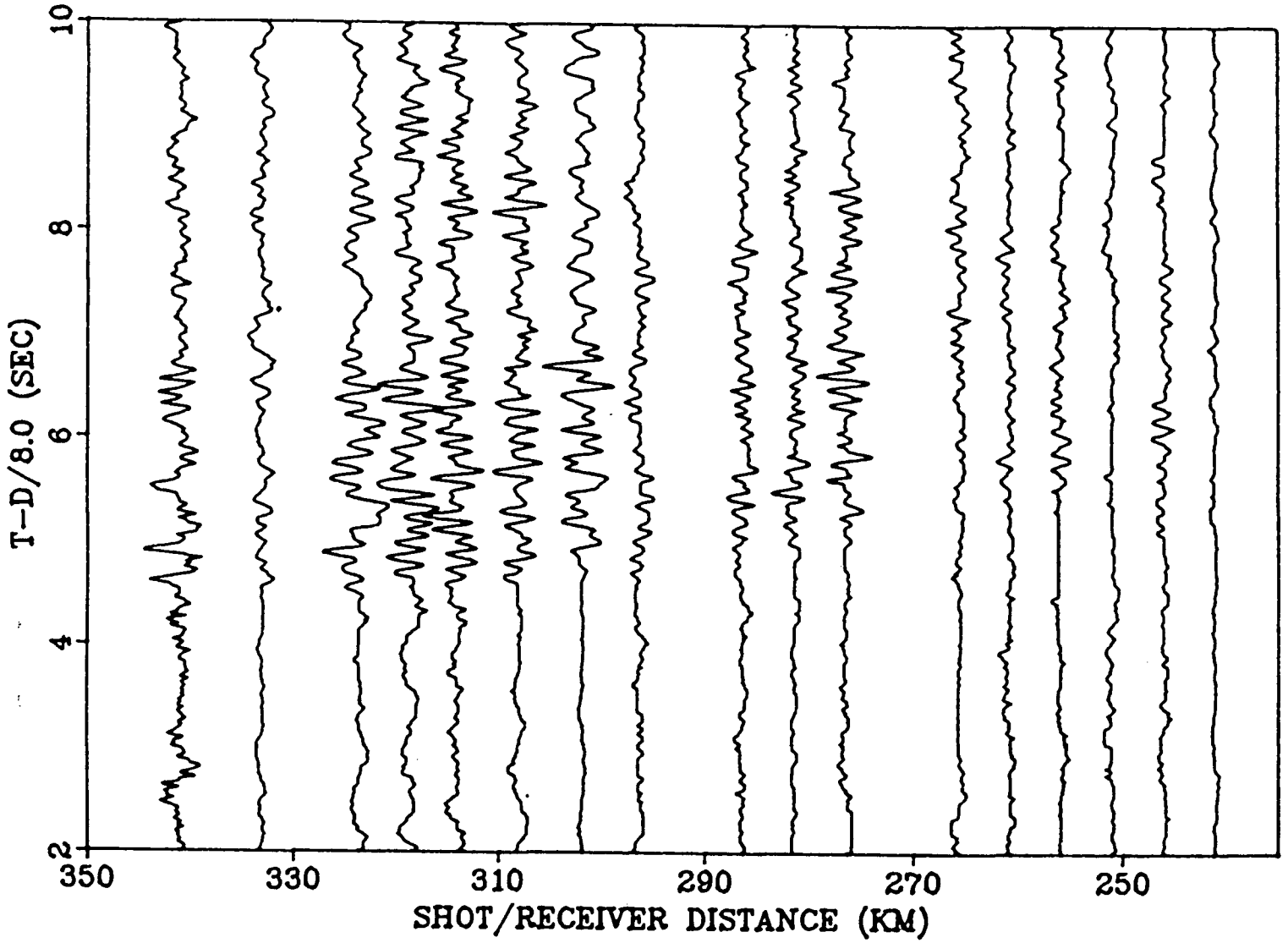

FIG. A2.10. Observed record section for receiver X43.

PUBLICATIONS

Ellis, R.M. G.D. Spence, R.M. Clowes, D.A. Waldron, I.F. Jones, A.G. Green, D.A. Forsyth, J.A. Mair, M.J. Berry, R.F. Mereu, E.R. Kanasewich, G.L. Cumming, Z. Hajnal, R.D. Hyndman, G.A. McMechan, and B.D. Loncarevic (1983). The Vancouver Island Seismic Project: A CO-CRUST onshore-offshore study of a convergent margin, Can. J. Earth Sci. 20, 719-741.

McMechan, G.A. and G.D. Spence (1983). P-wave velocity structure of the Earth's crust beneath Vancouver Island, Can. J. Earth Sci. 20, 742-752.

Spence, G.D., R.M. Clowes and R.M. Ellis (1977). Depth limits on the Moho discontinuity in the southern Rocky Mountain Trench, Canada, Bull. Seism. Soc. Am. 67, 543-546.

Spence, G.D., R.M. Ellis and R.M. Clowes (1977). Gravity evidence against a high-angle fault crossing the Rocky Mountain Trench near Radium, British Columbia, Can. J. Earth Sci. 14, 25-31.

Spence, G.D., K.P. Whittall and R.M. Clowes (1984). Practical synthetic seismograms for laterally varying media calculated by asymptotic ray theory, Bull. Seism. Soc. Am. (in press).